FRIEDRICH-SCHILLER-
UNIVERSITÄT
JENA

Stable, Conductive, and Cost-Effective Semi-Transparent Electrodes for Organic Photovoltaics and Beyond

Dissertation

zur Erlangung des akademischen Grades

doctor rerum naturalium (Dr. rer. nat.)

vorgelegt dem Rat der Chemisch-Geowissenschaftlichen Fakultät

der Friedrich-Schiller-Universität Jena

von M.Tech Aman Anand

geboren am 06.03.1993 in Indien

Gutachter:

1) PD Dr. Harald Hoppe / Institute for Organic Chemistry and Macromolecular Chemistry, Friedrich Schiller University Jena
2) Assoc.-Prof. Thomas M. Brown / Department of Electronic Engineering, University of Rome - Tor Vergata
3) Prof. Dr. Carsten Deibel / Institute of Physics, Optics and Photonics of Condensed Matter, Chemnitz University of Technology

Tag der öffentlichen Verteidigung: 21.03.2023

Printed and/or published with the support of the German Academic Exchange Service

Selbständigkeitserklärung

Ich erkläre, dass ich die vorliegende Arbeit selbständig und unter Verwendung der angegebenen Hilfsmittel, persönlichen Mitteilungen und Quellen angefertigt habe.

Jena, 07/11/2022 **Aman Anand**

Ort, Datum Unterschrift der Verfasserin/des Verfassers

Acknowledgment

In the academic world, it's common to hear that a student's journey toward a doctoral degree will be the most challenging of their lives. Although there were some ups and downs, as life often is, I am delighted to have finished this journey with a smile, and this wouldn't have been possible without a lot of individuals I met both before and during this journey.

I want to give my utmost gratitude to many individuals, but I would like to start by thanking my parents, Mr. Krishna Nandan Lal Das and Mrs. Poonam Das, for being my first teachers in life and for always being there for me. This wouldn't have been possible without them.

I would like to express my gratitude to Dr. Harald Hoppe, my research supervisor, for his unwavering support during this study. He has offered some intriguing projects, and I am really appreciative of how he has inspired and motivated me to pursue new endeavors. Thank you for giving me the opportunity to attend several conferences and summer schools, which surely helped me develop personally and meet amazing scientists from across the world. We had several insightful discussions that were both scientific and personal, and I learned a lot that I will surely use for the rest of my professional career.

I thank Prof. Dr. Ulrich S. Schubert for giving me the opportunity to pursue my Ph.D. at the Center for Energy and Environmental Chemistry Jena, where I had access to all the top-notch resources I needed to effectively carry out my research.

I would like to thank my colleagues Shahidul Alam, Rico Meitzner, Md. Moidul Islam, Jose Prince Madliamuthu, Zhuo Xu, Aurelien Sokeng Djoumessi, Chikezie Williams Ugokwe, Zekarias Teklu Gebremichael, Dr. A. Markus Anton, Josef Bernd Slowik, and Kshitij Kakad for their help, fruitful discussions, and the good times we shared both inside and outside the office.

I would like to thank my collaborators, Theo Pflug, Sandra Busse, Markus Olbrich, Alexander Horn, Maximilian Schaal, Felix Otto, Marco Gruenewald, Torsten Fritz, and Susanne Sandkuhl, for working on interesting ideas and conducting research with me.

I wish to acknowledge Ms. Ulrike Kaiser, Ms. Katja Genus, Ms. Mandy Necke, and Ms. Sylvia Braunsdorf for their assistance in helping me manage the university's bureaucracy. I would also like to thank the technical staff at Friedrich Schiller University Jena's Center for

Energy and Environmental Chemistry and Center for Applied Research for all of their assistance.

I thank the Deutscher Akademischer Austauschdienst (DAAD) for funding my Ph.D. degree. I also thank the Thüringer Ministerium für Wirtschaft, Wissenschaft und Digitale Gesellschaft (TMWWDG) for supporting the CEEC Jena, the Free State of Thuringia ("Innovation Center CEEC Jena" – 2016 IZN 0009), and the European Union within the framework of the European Regional Development Fund (ERDF) for financing the equipment at the CEEC Jena.

Last but not least, many thanks to my sister, Mrs. Shalini Sudhir Jain, brother-in-law, Mr. Sankit Jain, and friends from India and Germany (there are many to thank that I won't list here), for sharing this time with me, for taking me on all the wonderful vacations, for listening to all of my complaints, and for inspiring me to finish my Ph.D. successfully.

In the end, I would say just one thing—what a beautiful journey it was!

Jena, 07/11/2022 **Aman Anand**

Place, Date Signature

Table of Contents

Abstract

Today's lifestyle includes the daily use of electronic devices. These include smartphones, touchscreens, displays, less common solar cells, and smart windows, all of which employ transparent conductive electrodes (TCEs). TCEs are a special class of material, as they are both transparent and conductive, allowing light to enter or exit the devices and current to be drawn from or injected into them. TCEs should have both high transparency and high conductivity. In reality, however, these two important characteristics typically trade-off with one another and thus must be balanced.

In terms of the material system, the selection of the TCE with the best performance is essential, which is evaluated by the so-called “figure of merit” (FOM). Hence, researchers have suggested various FOMs to rate the TCEs over the past 50 years. However, a more straightforwardly formulated FOM may help to assess a TCE's potential specifically for photovoltaic applications. Since the requirements for the latter are distinctly different compared to other optoelectronic devices, this thesis is devoted to bridging this gap.

A novel and exact FOM is proposed that exclusively quantifies the impact of the TCE on photovoltaic performance. This exact FOM fulfills the aspired requirement of being a normalized, dimensionless, and proportional factor for the potential photovoltaic output power with respect to the Shockley-Queisser limit. Its analysis results in the discovery of two regimes of TCE operation: a) transmittance, and b) conductance limitation, which are separated by the defined transition sheet resistance. Using this FOM, a set of current state-of-the-art semi-transparent electrodes is comprehensively assessed, where the spectral range in which photovoltaic materials operate is an important factor. Based on a comment from a colleague at the National Renewable Energy Laboratory, the exact FOM is extended into formulations that allow the assessment of different solar module geometries, including the addition of serial connections and additional metal grids.

The thesis also includes a thorough study of the impact of poly (3,4-ethylenedioxythiophene) polystyrene sulfonate (PEDOT:PSS) processing conditions on its work function. Various formulations are tested with regard to relative humidity levels, annealing temperatures, and solar cell performance. The acidic and hygroscopic nature of PEDOT:PSS leads, on metallic substrates, to the release of metal ions from the latter, compromising the device's performance. Finally, literature assessments and strategies for achieving highly conductive PEDOT:PSS TCEs are conducted at the end of the thesis.

Zusammenfassung

Zum heutigen Lebensstil gehört der tägliche Gebrauch elektronischer Geräte. Dazu gehören Smartphones, Touchscreens, Displays. Weniger verbreitete Solarzellen und intelligente Fenster, die allesamt transparente leitfähige Elektroden (TCEs) verwenden. TCEs sind eine besondere Materialklasse, da sie sowohl transparent als auch leitfähig sind, so dass Licht in die Geräte eindringen oder aus ihnen austreten sowie Strom aus ihnen gezogen oder in sie eingespeist werden kann. TCEs sollten sowohl eine hohe Transparenz als auch eine hohe Leitfähigkeit aufweisen. In der Realität stehen diese beiden wichtigen Eigenschaften jedoch oft in einem Spannungsverhältnis zueinander und müssen daher ausgeglichen werden.

Im Hinblick auf das Materialsystem ist die Auswahl der TCE mit der besten Leistung, die durch die so genannte "figure of merit" (FOM) bewertet wird, entscheidend. Daher haben Forscher in den letzten 50 Jahren verschiedene FOMs zur Bewertung von TCEs vorgeschlagen. Eine gezielt gestaltete FOM könnte jedoch helfen, das Potenzial einer TCE speziell für photovoltaische Anwendungen zu bewerten. Da sich die Anforderungen für letztere deutlich von denen anderer optoelektronische Bauelemente unterscheiden, widmet sich diese Arbeit der Erschließung dieser Aufgabe.

Es wird eine neuartige und exakte FOM vorgeschlagen, die ausschließlich den Einfluss der TCE auf die photovoltaische Leistung quantifiziert. Diese exakte FOM erfüllt die angestrebte Anforderung, ein normierter, dimensionsloser und proportionaler Faktor für die potenzielle photovoltaische Ausgangsleistung im Hinblick auf die Shockley-Queisser-Grenze zu sein. Ihre Analyse führt zur Entdeckung von zwei Regimen des TCE-Betriebs: a) die Transmissions und b) die Leitwertbegrenzung, die durch definierte Übergangsflächen getrennt sind. Mit Hilfe dieser FOM wird eine Reihe von semitransparenten Elektroden, die dem Stand der Technik entsprechen, umfassend bewertet, wobei der Spektralbereich, in dem die photovoltaischen Materialien arbeiten, ausschlaggebend ist. Auf der Grundlage eines Kommentars eines Kollegen am National Renewable Energy Laboratory wird die exakte FOM zu Formulierungen erweitert, welche die Bewertung verschiedener Solarmodulgeometrien ermöglichen, einschließlich der Hinzufügung von serieller Anschlüsse und zusätzlichen Metallgittern.

Die Arbeit umfasst auch eine gründliche Untersuchung der Auswirkungen der Verarbeitungsbedingungen von Poly(3,4-Ethylendioxythiophen) polystyrolsulfonat (PEDOT:PSS) auf seine Austrittsarbeit. Es wurden verschiedene Formulierungen im Hinblick

auf relativer Luftfeuchtigkeit, Wärmebehandlung und Leistung der Solarzellen getestet. Die saure und hygroskopische Beschaffenheit von PEDOT:PSS führt beim Auftragen auf ein Metallsubstraten zur Freisetzung von Metallionen, wodurch die Leistung reduziert wird. Am Ende der Arbeit werden Literaturbewertungen und Strategien zur Erzielung hochleitfähiger PEDOT:PSS TCEs durchgeführt.

List of Figures

List of Tables

List of Acronyms

Ag	Silver
Ag_2S	Silver Sulfide
Ag_2Se	Silver Selenide
AgI	Silver Iodide
AgrOPV	Organic Photovoltaic for Agrivoltaics
Al	Aluminum
a-Si	Amorphous Silicon
Au	Gold
CdO	Cadmium Oxide
CdS	Cadmium Sulfide
CdSe	Cadmium Selenide
CdTe	Cadmium Telluride
CI(G)S	Copper Indium Gallium Selenide
CNTs	Carbon Nanotubes
C-Si	Crystalline Silicon
Cu	Copper
Cu_2O	Copper(I) Oxide
Cu_2S	Copper(I) Sulfide
CuI	Copper(I) Iodide
CuO	Copper(II) Oxide
CuS	Copper Sulfides
CuSe	Copper Selenide
CZTS	Copper Zinc Tin Sulfide
DC	Direct Conductivity
DMD	Dielectric/Metal/Dielectric
DMSO	Dimethyl Sulfoxide
EG	Ethylene Glycol

EQE	External Quantum Efficiency
eV	Electron Volt
FF	Fill Factor
FOM	Figure of Merit
GaAs	Gallium Arsenide
GaInP	Gallium Indium Phosphide
H_2SO_4	Sulfuric Acid
HCl	Hydrochloric Acid
HOPG	Highly Oriented Pyrolytic Graphite
InP	Indium Phosphide
ITO	Indium Tin Oxide
KP	Kelvin probe
LCD	Liquid Crystal Display
m-Si	Monocrystalline Silicon
N_2	Nitrogen
Na	Sodium
NIR	Near-Infrared
NW	Nanowires
OLED	Organic Light-Emitting Diode
OPV	Organic Photovoltaics
PbO	Lead(II) Oxide
PbS	Lead Sulfide Quantum Dots
PbS	Lead(II) Sulfide
PCE	Power Conversion Efficiency
PEG	Polyethylene Glycol
PV	Photovoltaic
PVD	Physical Vapor Deposition
RH	Relative Humidity
SQL	Shockley-Queisser-Limit

TCEs	Transparent Conductive Electrodes
TCO	Transparent Conducting Oxide
TGA	Thermogravimetric Analysis
TlS	Titanium(II) Sulfide
Uni.	University
UPS	Ultraviolet photoelectron spectroscopy
USD	United States Dollar
UV	Ultraviolet
Vis	Visible
XPS	X-ray Photoelectron Spectroscopy

List of Symbols

ϕ_{TC}	Figure of merit
°C	Degree Celsius
$\mu_{n,p}$	Carrier mobility
A	Absorptance
B_λ	Spectral irradiance
c	Speed of light
cm	Centimeter
E_g	Bandgap
ε_0	Permittivity of free space
h	Planck's constant
I	Current
I_0	Reverse saturation current
I_0	Dark saturation current
I_D	Diode current
I_{MPP}	Current at the maximum power point
I_{SC}	Short circuit current
I_{SH}	Shunt current
J_0	Dark saturation current density
J_{PH}	Photocurrent density
k_B	Boltzmann's constant
L	Length of the material
m*	Effective mass of the free carriers
mW	Megawatt
n	Diode ideality factor (1 for an ideal diode)
n_0	Concentration of the charge carrier
q	Elementary charge
R	Reflectance

$R_{\square}$	Sheet resistance
R_S	Series resistance
$R_{\square,c}$	Critical sheet resistance
$R_{\square,target}$	Target sheet resistance
T_k	Temperature
t	Thickness
T	Transmittance
V	Voltage
V_{MPP}	Voltage at the maximum power point
V_{OC}	Open-circuit voltage
w	Width of the material
Z_o	Impedance of the free space
α	Absorption co-efficient
$\theta R_{\square}$	Transition sheet resistance
λ	Wavelength.
ρ	Electrical resistivity
σ	Electrical conductivity
σ_{OP}	Optical conductivity
$\Phi_{BB,300K}$	Blackbody radiation photon flux density at 300 Kelvin
Ω	Ohm
Ω/□	Ohm/square
ω_p	Plasma frequency
l	solar cell length

Chapter 1

Introduction

The energy demand has risen dramatically in recent decades as a result of the rising population and industrialization. The fulfillment of energy demand relies significantly on conventional energy sources, which are limited in quantity and may not be able to fulfill our present or future global energy needs [1-3]. In the meantime, the pollution they generate has reached unprecedented heights, ranging from particulates that are hazardous to human health to greenhouse gases that harm the environment [4]. Although numerous initiatives and agreements [5] have been implemented to combat the consequences of climate change, much more work needs to be done.

Alternative renewable energy sources that are both clean and abundant are being researched to fulfill rising energy demand. Each source of renewable energy, including wind, water, sunlight, and biomass, has its own set of technological advantages and disadvantages [6]. Among all clean energy sources, harnessing solar energy and converting it into electricity is one of the most promising solutions to the global energy dilemma.

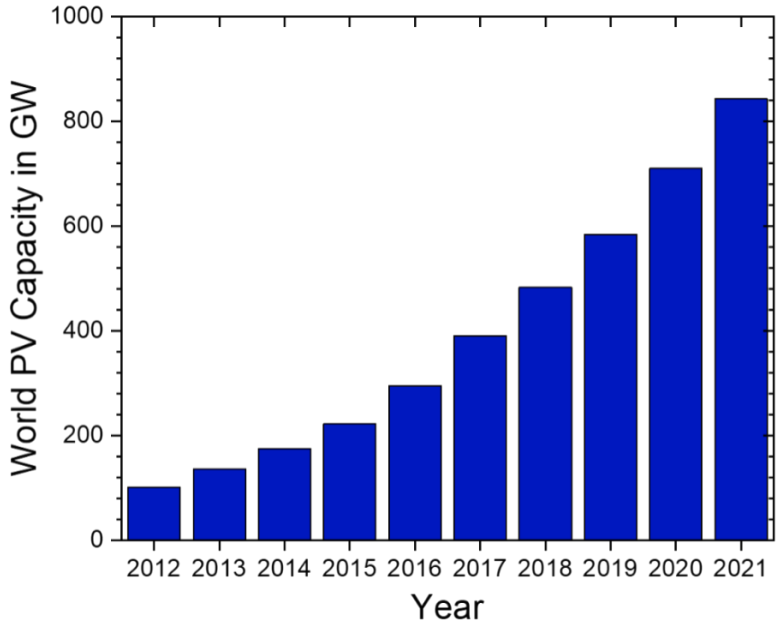

Figure 1: *World photovoltaic (PV) capacity in Gigawatt (GW) from 2012 to 2022. Data extracted from International Renewable Energy Agency (IRENA) report 2022* [7].

One of the most effective methods of converting solar energy into electricity is the photovoltaic (PV) effect [8, 9]. As a result, PV research has been stepped up to successfully capture the sun's energy by producing solar panels or cells with high conversion efficiencies while simultaneously decreasing prices. Realizing the potential of photovoltaics, the market for photovoltaics is expanding substantially (Figure 1). From 2010 to 2021, the total compound annual growth rate (CAGR) of PV installations was found to be 32% [7, 10].

From 1976 to the present year, several PV systems (multijunction cells, single-junction gallium arsenide cells, crystalline silicon cells, thin-film technologies, and emerging PVs such as organic solar cells and perovskites) have been discovered. Researchers have reached solar cell efficiencies of up to 47.1% through continuous research in the field of PVs, demonstrating the sector's remarkable development [11].

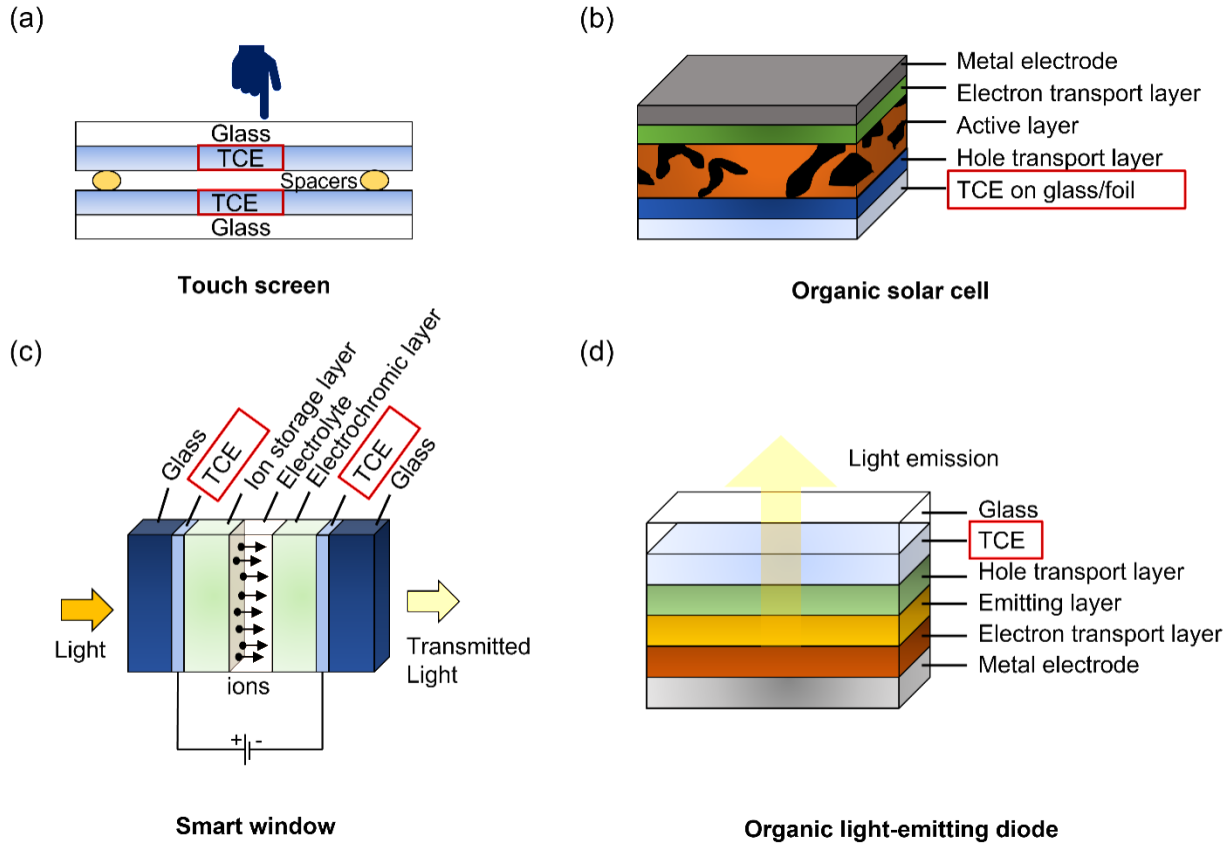

Figure 2: *Schematic representation of TCEs applications (a) touch screen, (b) organic solar cell, (c) smart window, and (d) organic light-emitting diode.*

One thing common to all these PV technologies is the incorporation of transparent conductive electrodes (TCEs). TCEs are often employed in PVs as the front electrode facing the sun, although in the case of semi-transparent systems, a TCE might be utilized as the back

electrode. TCEs have been around for 115 years, and in the present era of electronics, TCEs have become an important aspect of the information and semiconductor industries. TCEs are a unique class of materials as they exhibit both transparency and conductivity, and they are often used in several electronic devices such as touchscreens, displays, solar cells, smart windows, and organic light-emitting diodes (OLED) (Figure 2) [12-14].

The discovery of transparent conductive oxide films by Karl Wilhelm Sali Baedeker served as the impetus for the development of TCEs. Baedeker was a German scientist born in Leipzig, Germany. He earned his habilitation from the University of Jena in 1907 after finishing his Ph.D. studies at the University of Göttingen and having post-doctoral experience at several German institutions (the University of Leipzig, University of Würzburg, University of Greifswald). In 1907, he was also employed as a private lecturer at the University of Jena and held various lectures on electricity. In 1910, he was appointed as an associate professor at the University of Jena. During his tenure, he also worked on doped semiconductors as artificial metals with variable electron concentrations. In 1914, during World War I, he died during the mobilization process. It was not until the 1980s that his contributions to solid-state physics and materials research were finally recognized and his work began to be utilized in a variety of contexts. [15].

In his 1907 paper [16], Baedeker describes the fabrication of several simple metal compounds, including CdO, CdS, CdSe, CuI, Cu_2O, CuO, CuS, Cu_2S, CuSe, Ag_2S, Ag_2Se, AgI, PbO, PbS, and TlS which is an attractive list of semiconductors. The samples were developed by fabricating metal thin films on glass or mica using the sputtering technique. Air was used to accomplish oxidation, iodization happened on its own, and sulfurization and selenization were carried out at high temperatures in the relevant anion vapors. The resulting films proved to be both transparent and electrically conductive [15, 16]. Since the cathode ray tube was the state-of-the-art in display technology at the time, Baedekers' study did not focus on creating a TCE for use in displays or optoelectronic thin film devices. Following World War II, when the electronics industry began to take shape, TCEs were explored for optoelectronic applications such as front electrodes in selenium rectifier photocells, heated windshields/windows, and antistatic windows. In the 1960s, when display technology advanced from the cathode-ray tube to the first plasma display and the first liquid crystal display (LCD), the need for a transparent, conductive material became more important [14, 17].

Although the LCD industry now has the greatest market for TCEs, research on and demand for TCEs are also developing due to the rising need for renewable energy technologies (PVs and, flexible optoelectronic devices). The production of these electronic devices has recently increased, and it is expected that this increase will range from 5% to 30% annually [18]. As reported by Quince Market Insights in the 2020 report, the global transparent conductive film market is predicted to reach USD 10.2 billion by 2028, up from USD 4.5 billion in 2020 [19].

Since the 1960s, various TCEs, especially oxides such as tin oxide (SnO_2), zinc oxide (ZnO), and indium tin oxide (In_2O_3:Sn), commonly known as ITO, have been discovered [18]. In 1978, Bachmann used magnetron sputtering and ion beam deposition to produce amorphous and polycrystalline ITO films on several substrates for use in solar cells. Since then, TCEs made of ITO generated by magnetron sputtering have increasingly replaced other materials in a variety of applications due to their remarkable properties of wide bandgap semiconductors and high transparency and conductivity [20-23]. Despite having exceptional qualities as an electrode for optoelectronic devices, ITO still has several flaws that limit its usefulness in large-area solar applications. First, indium is a rare earth element whose cost has gone up over time, and second, the ITO's applicability in flexible electronics is constrained by its mechanical and chemical instability. Furthermore, the high energy requirements of ITO processing (such as magnetron sputtering, thermal evaporation, and pulsed laser deposition) result in higher processing costs [12, 14, 23, 24].

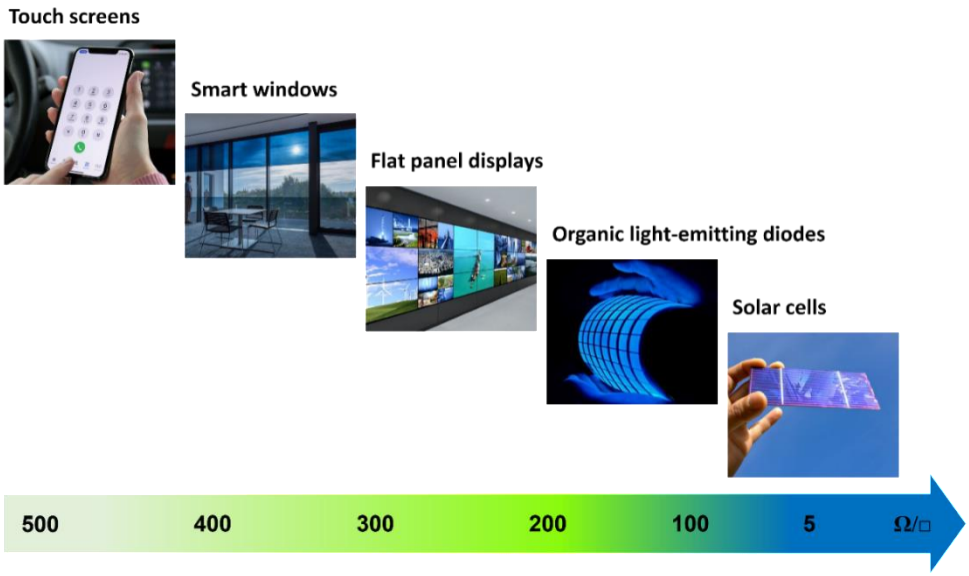

Figure 3: *TCE sheet resistance range in Ohm/square(Ω/□) for use in different optoelectronic devices. Adapted from [25, 26].*

Different optoelectronic devices have different requirements for transparency and conductivity (sheet resistance). For TCEs to be effectively implemented in solar cells, they must have high optical transmittance and low sheet resistance (Figure 3). However, these two important characteristics typically trade-off with one another. The cost of the electrodes is a crucial factor that must be taken into account in addition to their functional properties to achieve the objective of producing low-cost large-area solar cells. For the end customers, the cost per square meter of the final market price of solar cells matters a lot compared to that for other optoelectronic devices. A customer would be happy to buy a 1000 € television, but for solar cells, the cost should be $1/10^{th}$ of that amount (around 100 €). If we assume the power conversion efficiency (PCE) of the market-dominated silicon solar cells to be around 20%, then the 100 €/m^2 would correspond to a 0.5 €/Watt peak. Thus, for emerging PVs like organic photovoltaics (OPVs) to reach the same capacity, the end cost needs to be halved as well.

Moreover, to produce solar cells at this price, the overall material and processing costs should be significantly lower, which ITO cannot offer. Thus, to address these issues, several alternative transparent conductive materials have recently been discovered, such as conductive polymers poly(3,4-ethylenedioxythiophene) polystyrenesulfonate (PEDOT:PSS) and metal nanowires (NWs), which can easily be produced at low costs. Also, TCEs that can be fabricated using fully solution-processed techniques by employing printing and coating techniques such as screen printing, flexographic printing, gravure printing, slot die coating, and blade coating are currently being realized [27].

For solar cells to properly function, the best possible TCE must be selected. Apart from the standard TCEs such as ITO, many other TCEs have been discovered, making it difficult to select the best TCE for solar cells. This thesis addresses the issue of TCE rating, more precisely selecting the proper TCE for solar cells, by introducing a novel and exact figure of merit (FOM). The detailed balance limit was used to assess the power conversion efficiency limit functionality depending on the TCE properties. Additional physical characteristics, such as transition sheet resistance and target sheet resistance, have also been introduced, which can be used by researchers as a guide for optimizing TCEs for a certain PV material system. The second section of the thesis also contains work toward expanding the applicability of exact FOM for different geometrical solar module scenarios cases such as the addition of serial connections and metal grids.

Of the possible TCEs available, TCEs based on conductive polymers, particularly with PEDOT:PSS, have gained interest in the field of OPVs. This thesis also includes a thorough analysis of PEDOT:PSS processing to comprehend the change in characteristics of PEDOT:PSS films that can eventually affect the operation of the solar cells. Furthermore, the strategy to produce highly conductive semi-transparent PEDOT:PSS electrodes that could be integrated into solar cells is also discussed in this thesis.

Chapter 2

Fundamentals and Background

This section discusses the basic concepts of organic photovoltaics (OPVs), solar cell parameters, the functional properties of transparent conductive electrodes (TCEs), and different types of TCEs.

2.1 Organic photovoltaics

Due to their simplicity in production employing conjugated small molecules and polymers, low material cost, and significant benefits in process optimization, OPVs have gained favor among researchers and industries. Modern organic solar technology has achieved up to 18% PCE, which opens up numerous opportunities for the future application of OPV from lab to fab [28]. OPVs are ideal candidates for the low-cost fabrication of large-area devices because of their processing-based compatibility with flexible substrates and high-throughput roll-to-roll manufacturing procedures. Also, by making the appropriate structural alterations during synthesis, the electrical and optical characteristics of OPVs can be significantly modified, creating materials with specialized features for particular applications. Additionally, in comparison to inorganic PV technologies, life-cycle analysis has demonstrated that OPV modules are anticipated to have substantially lower energy payback times and improved environmental sustainability with lower greenhouse gas (CO_2) emissions [12, 29-33].

2.1.1 Working mechanism of organic photovoltaics

A typical standard structure of an OPV from top to bottom comprises a top electrode (generally TCEs), an interfacial layer (an electron transport layer (ETL) or a hole transport layer (HTL)), an active layer, a second interfacial layer (ETL or HTL) and a bottom electrode (metals). The active layer, which is responsible for the photovoltaic activity of the cell, is made up of an interconnected network of materials – donor (D) and acceptor (A). The active layer is sandwiched between ETL and HTL, each having different work functions to facilitate the selective transfer of electrons and holes. Depending on the structure of OPV, the electrodes (TCEs or metals) are placed on the top or bottom [32, 34].

Four essential processes take place in an OPV to transform solar energy into electrical power (Figure 4) [32]:

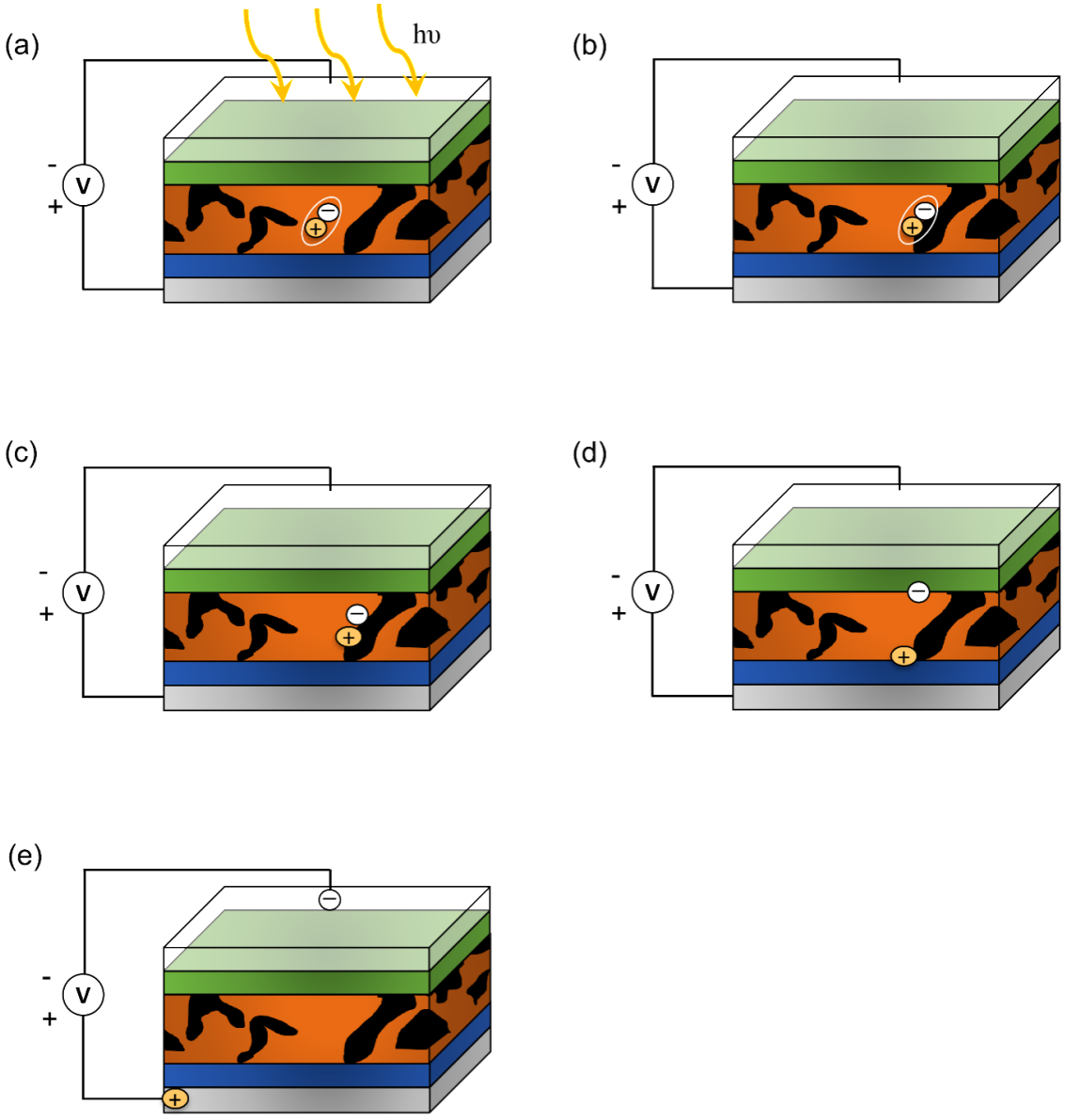

Figure 4: *Working mechanism of a conventional structured (top to bottom layer stack: transparent conductive electrode (transparent)/electron transport layer (green)/active layer (donor – orange, acceptor – black)/hole transport layer (blue)/back electrode(grey)) OPV (a) Photon absorption generating an electron-hole pair (exciton), (b) exciton diffusion to the donor–acceptor interface (or decay), (c) exciton dissociation, (d) charge transport, and (e) charge extraction.*

1) Incident light absorption resulting in exciton (electron–hole pair) generation: When light shines on the solar cell, the light is absorbed by the active material, which results

in the generation of excitons. Often, the light-absorbing material is the donor; however, recent research has also concentrated on light-absorbing acceptors.

2) Diffusion of the exciton to a donor-acceptor interface.
3) Exciton dissociation: The offset of energy levels at the donor–acceptor interface causes exciton dissociation, i.e., the separation of electrons and holes. The electrons are released from D→A or holes are released from A→D.
4) Charge transport: Enabled by the electric field across the photoactive layer, the electrons travel to the ETL, while the holes travel to the HTL.
5) Charge extraction: The charge carriers will be extracted by the interfacial layers and then collected by the corresponding electrodes. The charge carriers are collected by the electrodes and put to use in the cell's external circuit to generate a current.

Each step is essential to effectively generate electricity, and this process includes several loss mechanisms. The asymmetric ionization energy or work function of the electrodes ensures the free charge collection at the opposite electrodes.

2.2 Solar cell parameters

2.2.1 Equivalent circuit of a solar cell

As illustrated in Figure 5, a solar cell may be modeled as a current generator working in parallel with a diode.

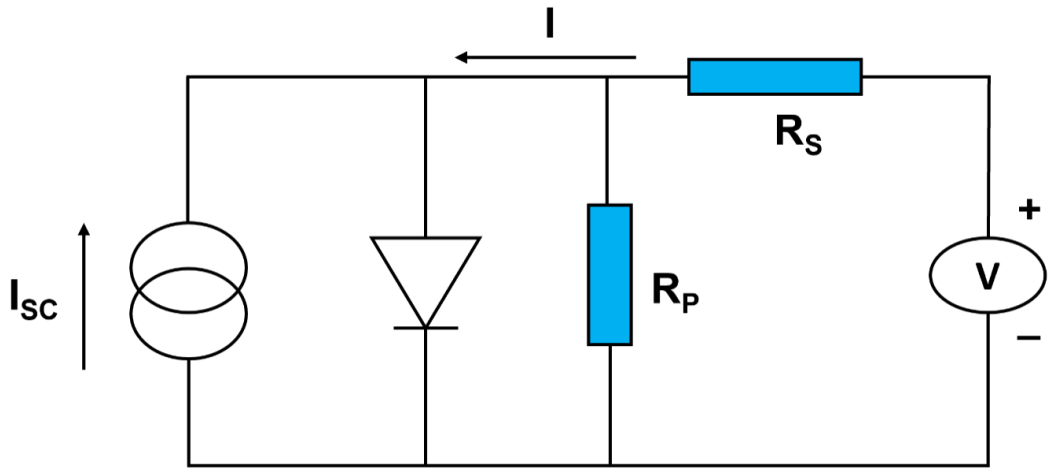

Figure 5: *Equivalent circuit for a solar cell based on the 1-diode model.*

It is clear from the equivalent circuit that the output current of the solar cell equals the sum of the current that flows through the diode and the current that flows through the shunt resistor, minus the current generated by the current source [35, 36].

$$I = I_D + I_{SH} - I_{SC} \quad (1)$$

where I is the output current, I_D is the diode current, I_{SH} is the shunt current, and I_{SC} is the short circuit current or the photo-generated current.

The voltage across these components that controls the current through them is given as follows:

$$V_j = V - IR_S \quad (2)$$

where V_j is the voltage across both the diode and resistor, V is the voltage across the output terminals and R_S is the series resistance.

By Ohm's law, the current diverted through the shunt resistor is as follows:

$$I_{SH} = \frac{V_j}{R_P} \quad (3)$$

where R_P is the shunt resistance.

The current that is transferred across the diode according to the Shockley diode equation is expressed by the following equation:

$$I_D = I_0 \{exp\,[\frac{qV_j}{nkT}] - 1\} \quad (4)$$

where I_0 is the reverse saturation current, q is the elementary charge, n is the diode ideality factor (1 for an ideal diode), k is Boltzmann's constant, and T is the absolute temperature.

The characteristic equation of a solar cell, which correlates solar cell parameters to the output current and voltage, is created by substituting equations 3 and 4 into equation 1:

$$I = I_o \cdot [exp\ \{\frac{q}{nkt}\ (V\ - IR_S)\} - 1] + \frac{V - IR_S}{R_P} - I_{SC} \quad (5)$$

2.2.2 Current-voltage curve of a solar cell

The current-voltage (IV) curve of an illuminated solar cell is the result of superimposing the dark IV curve of the solar cell with the light-generated current. The illumination has the

effect of shifting the IV curve into the fourth quadrant, wherein the solar cell delivers power [37] (Figure 6).

Short-circuit current: The current that flows through the solar cell when the voltage across the solar cell is zero (i.e., when the solar cell is short-circuited) is known as the short-circuit current (I_{SC}).

It depends on several factors, such as the area of the solar cell, the spectrum of the incident light, the number of photons, the optical properties such as the absorption and reflection of the solar cell, and the collection probability of the solar cell, which depends on the charge carrier lifetime and mobility, diffusion length, device electrodes, and morphology of the active layer.

Open-circuit voltage: The maximum voltage a solar cell can produce when there is no current flowing through it is known as the open-circuit voltage (V_{OC}).

The V_{OC} reflects the amount of forwarding bias on the solar cell caused by the junction's bias with the current produced by light. It is equivalent to the state of an open electrical circuit or system. For an ideal device, the V_{OC} derived from equation 5 is defined as follows:

$$V_{OC} = \frac{nkT}{q} ln\left(\frac{I_{SC}}{I_0} + 1\right) \tag{6}$$

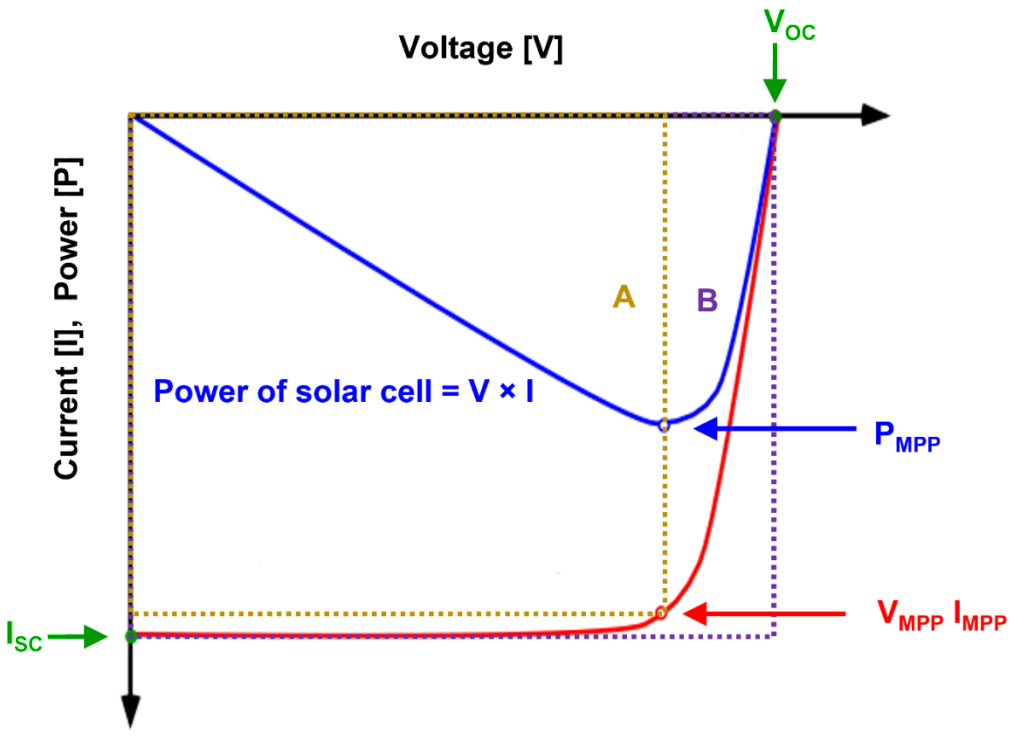

Figure 6: *IV curve of a solar cell. Adapted from [38].*

Fill factor: The fill factor (FF) determines the power fraction delivered by the solar cell compared to the $I_{SC}.V_{OC}$ (hypothetically the maximum current and voltage of the solar cell). Mathematically, FF is defined as follows:

$$FF = \frac{I_{MPP}V_{MPP}}{I_{SC}V_{OC}} \tag{7}$$

where I_{MPP} and V_{MPP} are the current and voltage at the maximum power point.

As seen in Figure 6, FF graphically represents a measurement of the "squareness" of the solar cell. It represents the area of the largest rectangle that can fit in the IV curve. Parasitic series resistance (R_S) and parallel resistance (R_P) have a considerable impact on FF. Good organic solar cells often provide FF values above 70%.

Power conversion efficiency: The PCE is the percentage of the incident power that is converted to electricity is the measure of a solar cell's efficiency and is defined as:

$$PCE = \frac{I_{SC} \cdot V_{OC} \cdot FF}{P_{in}} \tag{8}$$

where P_{in} is the input power. The testing procedures for solar cells were standardized to allow for a global comparison of PCE for various types of solar cells. With a solar cell temperature of 25 °C and an air mass (AM) of 1.5G solar spectrum, the illumination level is set at 100 mW/cm^2.

2.3 Transparent conductive electrodes for organic photovoltaics

Depending on where the TCE is located, which enables light to enter and exit the solar cells, the device architecture of an OPV can be divided into three categories (Figure 7).

i) The superstrate configuration of OPV is the first and most widely used OPV device architecture, in which light passes through the bottom TCEs and the substrate. In this configuration, the TCEs are coated or deposited on the substrates before coating the organic layers and reflecting electrodes.
ii) In the substrate-type OPV device, which is the second device architecture, light enters through the top electrodes. The use of opaque substrates is beneficial for this configuration.

iii) Transparent OPV is the third and presently the most researched device architecture. In this configuration, the top and bottom electrodes are both transparent (or semitransparent), allowing light to pass through from both sides [24].

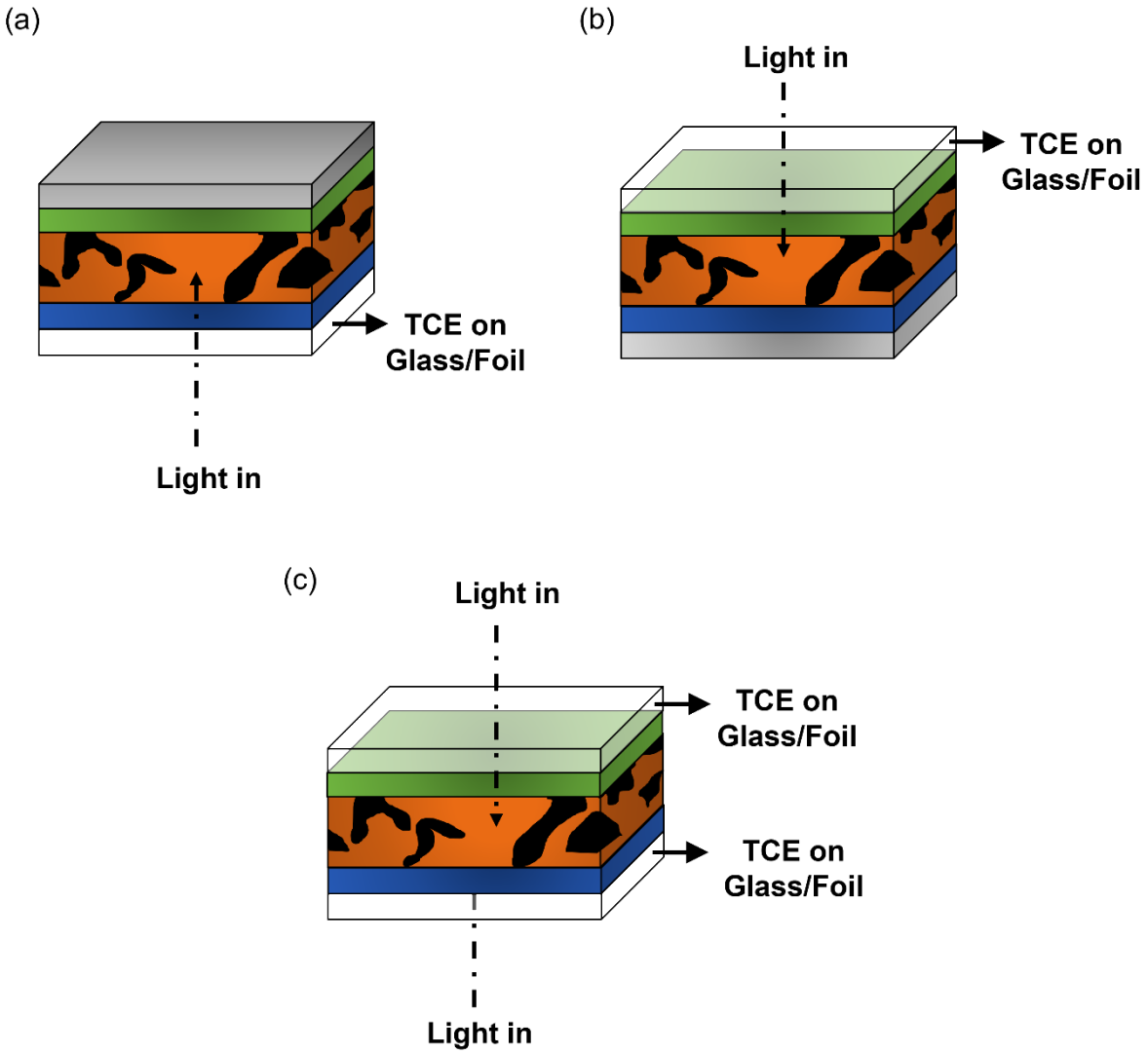

Figure 7: *Universal OPV designs: (a), Superstrate type OPV, (b) substrate type OPV, and (c) transparent OPV. (Color scheme: electron transport layer(green), active layer (black – donor, acceptor – orange), hole transport layer (blue), and back electrode (grey)).*

The performance of the devices is limited by the electrical conductivity and optical transparency of the TCEs. It can be challenging for TCEs to maintain good optical transparency and good electrical conductivity at the same time. The effect of transmittance on device performance is linear because if less light is incident on the device, less light will be absorbed by the photoactive layer, leading to reduced creation of charge carriers. The effect of the sheet resistance, however, is non-linear and more complex. Due to the electrodes' low

conductivity, series resistance losses may occur. However, it is preferable to compromise on a minor increase in sheet resistance, whereas it is preferable to prevent transmission losses [39, 40].

2.4 Transparent conductive electrodes properties

2.4.1 Optical properties

A good and efficient TCE should have excellent transparency, allowing the majority of sunlight to enter the devices. According to the Drude absorption term, the material's optical characteristics and electronic characteristics are inextricably linked [39, 41].

Usually, a TCE exhibits transparency in the UV–Vis–NIR spectral range because the plasma frequency (the resonance frequency of the electron density) is located in the infrared region of the electromagnetic spectrum. The Plasma frequency (ω_p) is defined by classical Drude's theory and is given by the following equation [14, 42]:

$$\omega_p{}^2 = \frac{ne^2}{\varepsilon_0 m^*} \quad (9)$$

where n is the charge carrier concentration, e is the elementary charge, ε_0 is the permittivity of free space, ε_r is the relative permittivity, and m* is the effective mass of the free carriers. One can think of it as the natural frequency (eigenfrequency) at which the electron density oscillates. If the material is irradiated with light having a frequency below ω_p the electron density will follow the motion of the field so that almost all light is getting reflected. For frequencies above ω_p, the electron gas can no longer follow the electric field fully and the material turns transparent. Since the plasma frequency is proportional to the carrier density, higher conductivity is frequently coupled with increased light absorption, resulting in reduced light transmission. However, it is theoretically feasible for a material to have a plasma frequency that is slightly below the visible frequency range, making it an excellent electrical conductor while being transparent in the visible frequency range [14, 39].

The carrier gas (electrons) creates a collective plasma excitation (a “plasmon”) in the electrical field of a light wave. The wavelength and the energy of the plasmon (E_p) are represented as follows:

$$E_p = \hbar \sqrt{\frac{ne^2}{m\varepsilon_0}} = \hbar\omega_p$$

(10)

$$\lambda_P = \frac{hc}{\hbar\omega_p} = \frac{2\pi c}{\omega_p}$$

(11)

where n is the charge carrier concentration, e is the elementary charge, ε_0 is the permittivity of free space, m is the electron mass, and ħ is the reduced Planck constant, ω_p is the plasma frequency, c is the speed of light, and h is the Planck constant.

The plasma wavelength of metals is in the deep UV range ($\lambda_P < 0.2$ µm), which makes them more reflective than transparent and thus mostly unusable as TCEs. Thus, alternative materials having plasma wavelengths in the near and mid-infrared range such as oxide semiconductors ($\lambda_P \approx 1$ µm) and carbon-based materials ($\lambda_P > 1$ µm) are often explored.

2.4.2 Electrical properties

The resistance of a typical three-dimensional conductor (Figure 8 (a)) is expressed as follows:

$$R = \rho \frac{L}{A} \tag{12}$$

where R is the resistance, ρ is the resistivity, L is the length of the material, and A is the cross-sectional area of the material. The resistance is directly proportional to the length of the conductor and inversely proportional to the cross-sectional area of the conductor.

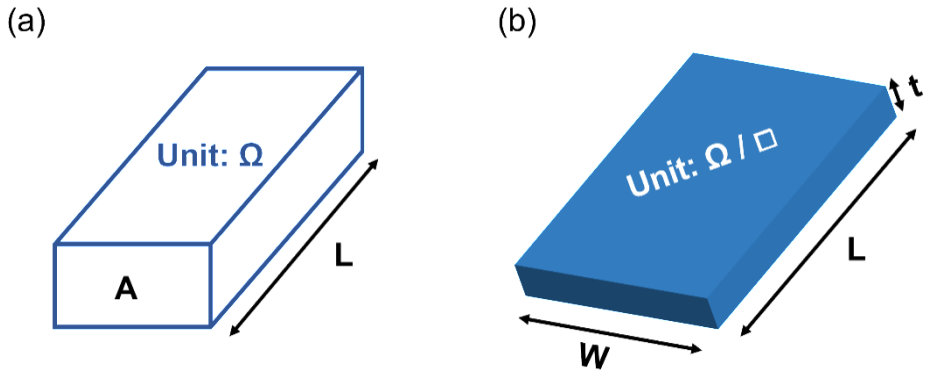

Figure 8: *Definition of geometrical quantities of (a) 3 – dimensional conductor, and (b) 2 – dimensional conducting thin film.*

The electrical property of TCEs (2-dimensional thin films (Figure 8 (b)), is generally described by sheet resistance ($R_{\square}$), which is defined as the resistance of one square-shaped tile of the electrode. The sheet resistance unit is Ohm/square (Ω/□), where □ denotes an electrode's square-shaped surface area with an arbitrary edge length and thus the size. The traditional formula for calculating the sheet resistance of a TCE only requires resistivity (ρ) and thickness (t) (equations 13 and 14) because the length (L) and width (W) of a square tile are equal [43].

$$R = \rho \cdot \frac{L}{A} = \rho \cdot \frac{L}{W \cdot t} = R_{\square} \frac{L}{W} \tag{13}$$

$$R_{\square} = \frac{\rho}{t} \tag{14}$$

When the conductivity of the film and its thickness is known, it is also possible to calculate the sheet resistance because conductivity (σ) is the inverse of resistivity (ρ). In that relationship, the sheet resistance can be defined as follows:

$$R_{\square} = \frac{1}{\sigma \cdot t} \quad \text{or} \quad \sigma = \frac{1}{R_{\square} \cdot t} \tag{15}$$

A material with a high electrical conductivity must, from a physical perspective, have a high carrier concentration (n) and a high charge carrier mobility ($\mu_{n,p}$).

$$\sigma = en\mu_{n,p} \tag{16}$$

Since electrons have a far lower effective mass than ions, they are much more mobile, and this causes electrons to act as charge carriers in excellent conductors. Since mobility and the number of charge carriers are directly proportional to conductivity, both could be maximized independently to enhance conductivity.

In summary, the series resistance depends more on the geometry of the region through which the current is transported than on its size. In terms of device functionality, the impact of sheet resistance is quite complicated and less straightforward. However, it strongly affects the device's performance [39, 40].

2.5 Assessment of transparent conductive electrodes

As previously described, the optical and electrical properties strongly govern the performance of electrodes. For a good performance of a TCE, high optical transmittance and low sheet resistance are the two major functional characteristics and prerequisites for this. [44].

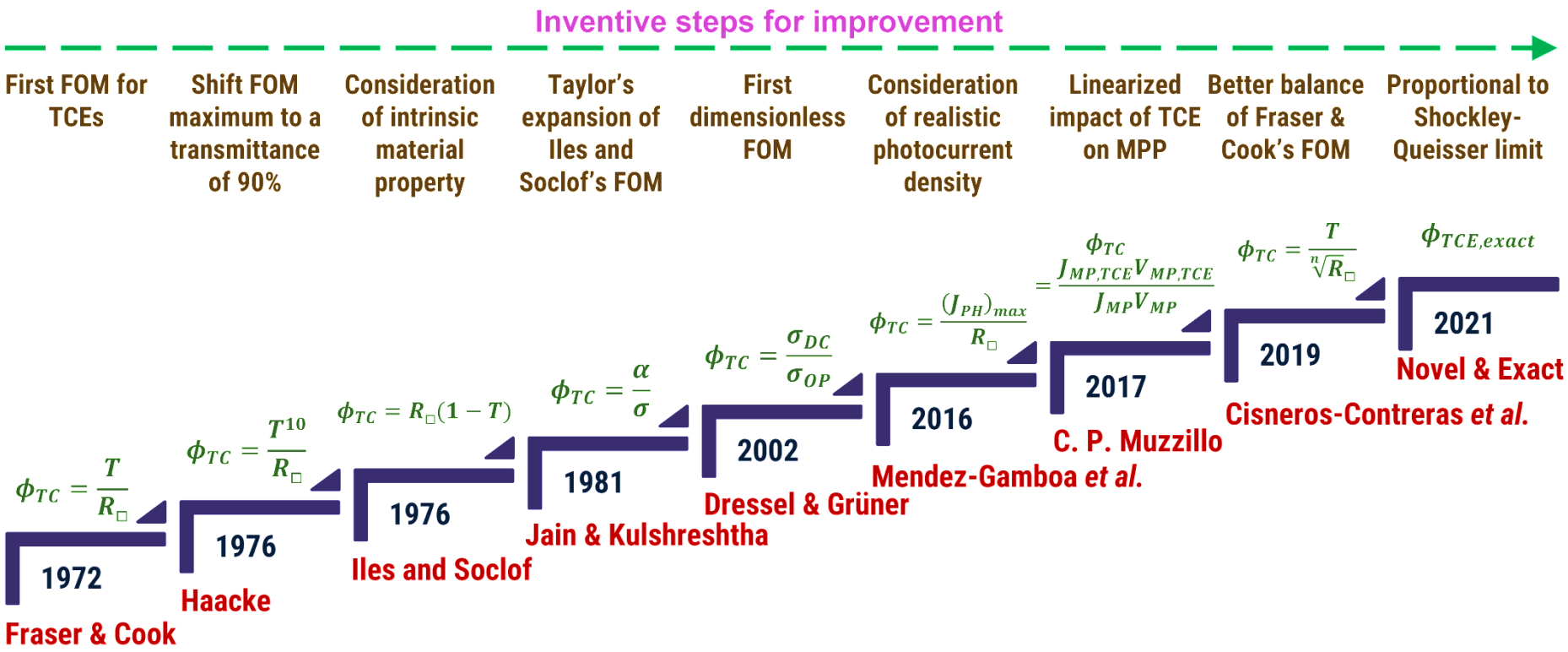

Figure 9: *Historical development of figures of merit. (T – Transmittance, $R_\square$ – Sheet resistance, α – Absorption co-efficient, σ – Conductivity, J_{PH} – Photon flux density, J – Current density, V – Voltage, MPP – Maximum powerpoint, E_G – Bandgap, l – Solar cell length).*

Maintaining the equilibrium between these two traits is a crucial effort that is frequently thwarted by the qualities of fundamental materials.

A figure of merit (FOM) is described as a suitable quantitative measure that may be used to assess an object's performance and how effective it is in comparison to other options for a certain application. Researchers have established several FOMs up to this point for evaluating the performance of TCEs. Figure 9 shows the historical development of FOMs from 1972 to the present, along with the inventive steps of improvement that were established for all FOMs. The description of each FOM in detail is as follows:

Fraser & Cook established the first FOM for transparent conductive electrodes in 1972, utilizing the fundamental relationship between transmittance and sheet resistance [45]:

$$\phi_{TC} = \frac{T}{R_{\square}},\ [\phi_{TC}] = \frac{1}{\Omega/\square} = \Omega^{-1} \tag{17}$$

with ϕ_{TC} being the FOM in units of Ω^{-1} where, according to the Lambert-Beer law, the transmittance T is a function of the layer thickness t and the absorption coefficient α:

$$T = \frac{I}{I_0} = e^{(-\alpha t)},\ [T] = 1 \tag{18}$$

where I is the transmitted intensity and I_0 is the incident intensity. The selection of Fraser & Cook was basic and easy, making it effective for rating TCEs. Due to the simple ratio between transmittance and sheet resistance, the FOM shows higher values for TCEs with i) higher transmittances and ii) lower sheet resistances.

In 1976, Haacke discovered that films with a transmittance of just 37%, which is extremely low for practical applications, provide the highest FOM for a given conductivity using the FOM (17) established by Fraser & Cook [46]. Haacke modified the FOM by giving the transmittance an exponent of ten to place greater emphasis on transparency:

$$\phi_{TC} = \frac{T^{10}}{R_{\square}},\ [\phi_{TC}] = \frac{1}{\Omega/\square} = \Omega^{-1} \tag{19}$$

with ϕ_{TC} being the FOM in units of Ohm^{-1}, where T is the transmittance at 550 nm, and $R_{\square}$ is the sheet resistance. The best FOM value for a given conductivity was obtained by this modification when the transmittance was more than 90%.

In 1976, Iles and Soclof defined the FOM as [47]:

$$\phi_{TC} = R_{\square}(1 - T) = (1 - e^{-\alpha t})/\sigma t,\quad [\phi_{TC}] = \Omega/\square \tag{20}$$

with ϕ_{TC} being the FOM in units of Ohm/square. For $\alpha t << 1$ (i.e., thin films with low optical absorption), the FOM becomes independent of the thickness, but for $\alpha t >> 1$, the FOM becomes dependent on the thickness of the films.

Jain and Kulshreshtha in 1981 defined the FOM as an indicator that is independent of film thickness and is characterized by the intrinsic material parameters only. The FOM is defined as the ratio of absorption coefficient (α) and conductivity (σ) [48].

$$\phi_{TC} = \rho \cdot \alpha = {}^{\alpha}/_{\sigma}, [\phi_{TC}] = \Omega \tag{21}$$

with ϕ_{TC} being the FOM in units of Ohm.

In 2002, Dressel & Grüner suggested a dimensionless FOM by dividing or comparing the conductivity in the zero-frequency (DC) domain with that in the optical regime. The relationship between optical conductivity and transmittance is as follows [49, 50]:

$$T = \left(1 + \frac{Z_o}{2}\sigma_{OP}t\right)^{-2} \tag{22}$$

where T is the transmittance, σ_{OP} is the optical conductivity, and Z_o is the impedance of the free space, which is 377 Ohm. The direct conductivity and the sheet resistance are related by the equation as follows:

$$\sigma_{DC} = \frac{1}{R_{\square} \cdot t} \tag{23}$$

where σ_{DC} is the direct conductivity, $R_{\square}$ is the sheet resistance, and t is the thickness of the film. Solving for t and putting in equation 22, the transmittance can be written as:

$$T = \left(1 + \frac{Z_o}{2R_{\square}}\frac{\sigma_{OP}}{\sigma_{DC}}\right)^{-2} \tag{24}$$

Therefore, FOM by Dressel & Grüner is defined as follows:

$$\phi_{TC} = \frac{\sigma_{DC}}{\sigma_{OP}} = \frac{188.5}{R_{\square}(T^{-\frac{1}{2}} - 1)}, [\phi_{TC}] = \frac{\sigma_{DC}}{\sigma_{OP}} = \frac{S/cm}{S/cm} = 1 \tag{25}$$

with ϕ_{TC} being dimensionless, and T and $R_{\square}$ as defined above. However, De *et al.* and Jacobs *et al.* demonstrated that the Dressel & Grüner FOM is limited in its applicability to thin uniform layers because it overvalues the importance of having a low sheet resistance while also having poor transmittance [49, 51].

By giving more weight to the transmittance against the sheet resistance, Contreras *et al.* were able to increase the resolution of the FOM by up to two orders of magnitude in 2019 [52]. They demonstrated in their work that Haacke's FOM was ineffective for TCEs with low transmittance. As a consequence, the "FOM Haacke High Resolution" FOM was established:

$$\phi_{TC} = \frac{T}{\sqrt[n]{R_{\square}}},\ [\phi_{TC}] = \frac{1}{(\Omega/\square)^{1/n}} = \Omega^{-1/n} \tag{26}$$

with ϕ_{TC} being the FOM in units of Ohm^{-1}, where T is the transmittance at 550 nm, and $R_{\square}$ is the sheet resistance.

One of the main issues with all of the FOMs discussed so far is the restriction of the value of transmittance to a single point (550 nm), which prevents the study of broad-range light transmission. Thus, the established FOMs are not ideal for rating TCEs which are used specifically for solar cells.

As a result, Gamboa *et al.* (2016) adopted a different methodology to determine the FOM for TCEs and simply took into account the maximum achievable photocurrent density by including the full spectral information of the transmittance of the TCEs and using the air mass 1.5 global photon flux spectrum. The photocurrent density was calculated for the energy range between the bandgaps of the absorber and TCE.

$$(J_{PH})_{max} = q \int_{E_G}^{E_{G,TCE}} PFD(h\nu) d(h\nu) \tag{27}$$

$$PFD(h\nu) = \frac{I_S(h\nu)\, T(h\nu)}{(h\nu)} \tag{28}$$

where J_{PH} is the photocurrent density, q is the elementary charge, $E_{G,\,TCE}$ is the bandgap of the TCE, E_G is the bandgap of the absorber, PFD(hν) is the photon flux density at energy hν, $I_S(h\nu)$ is the irradiance of the standard AM1.5G solar spectrum, including scattering, and T(hν) the transmittance spectrum of a particular TCE in the wavelength range from 300 to 1200 nm. Thus, the FOM by Gamboa *et al.* is defined as follows [53]:

$$\phi_{TC} = \frac{(J_{PH})_{max}}{R_{\square}},\ [\phi_{TC}] = \frac{mA/cm^2}{\Omega/\square} = mA/(cm^2 \cdot \Omega) \tag{29}$$

where $R_{\square}$ is the sheet resistance, and the FOM (ϕ_{TC}) has units of [$mAcm^{-2}\ Ohm^{-1}$].

In 2017, Muzzillo defined FOM as the ratio of power at the maximum powerpoint affected by the TCE to the power at the maximum powerpoint. For a solar cell operating at maximum powerpoint (MP) with current density (J_{MP}) and voltage (V_{MP}) with a uniform TCE, the J_{MP}

and V_{MP} would reduce to $J_{MP,TCE,}$ and $V_{MP,TCE}$ based on the assumption that $J_{MP,\ TCE}$ is only affected by $T_{TCE,avg}$, and $V_{MP,TCE}$ is only affected by $R_{\square}$.

$$J_{MP,TCE} = J_{MP} \cdot T_{TCE,avg} \tag{30}$$

$$V_{MP,TCE} = V_{MP} - R_{\square} \cdot A \cdot J_{MP} \tag{31}$$

Thus, the FOM (ϕ_{Muzzillo}) is defined as follows [54]:

$$\phi_{TC} = \frac{J_{MP,TCE} \cdot V_{MP,TCE}}{J_{Mp} \cdot V_{MP}} = T_{TCE,avg} \cdot \left(1 - \frac{R_{\square} \cdot L^2 \cdot J_{MP}}{3 \cdot V_{MP}}\right) \quad [\phi_{TC}] = \frac{A/m^2 \cdot V}{A/m^2 \cdot V} = 1 \tag{32}$$

Although Muzzillo's FOM is considered to be explicit, it depends on experimental maximum power point data and is relevant to functional electrodes of resistance up to 100 Ohm/square.

The exact FOM and its properties are discussed in Section 4.1.

2.5.1 Additional characteristics

Although FOM may help to pick up the best electrode for the devices, the choice and use of TCEs in solar cells are also greatly influenced by other characteristics, including the spectral range of the transparency window, processing techniques, work function, mechanical properties, and stability [44].

- **The spectral range of the transparency window**

As previously mentioned, the majority of FOMs are specified at a certain wavelength that may be utilized for general-purpose or display-oriented applications. However, for solar cells, the spectral range of the transparency window is very important and should be taken into account. Transmittance and sheet resistance should be balanced properly for a successful TCE. Thus, we saw the need to propose a new FOM to statistically assess TCE's appropriateness for PV applications, even though many factors have previously been adequately addressed by the current figures of merit [39].

- **Processing techniques**

Emerging PVs such as OPVs, perovskites, etc. are based on organic materials. Since organic materials are more sensitive to high temperatures, solvents, and ion/atom bombardment, it is more challenging to find processing methods for OPV that can prevent the loss of the underlying active layer [24]. To ensure large-area scalability, processing methods should be

compatible with substrates and the active layer, which facilitate easy patterning and are chemically resistant. Processing costs are an important element that must be taken into consideration, as one of the main objectives of the solar cell industry is to produce low-cost solar cells that have a good performance-to-cost ratio.

- **Ohmic contact**

To ensure that there is no energy barrier to the collection of holes and electrons, the electrodes for solar cells should be chosen carefully. To achieve barrier-free contacts for emerging PVs such as OPVs, perovskites, etc., the work function of the electrodes (anodes and cathodes) must match or be smaller or larger than the ionization potential of the donor and acceptor compounds, as most of the PVs are made of intrinsic semiconductors [44].

- **Mechanical properties**

The most common TCEs (like ITO) are brittle and prone to failure as a result of stress. Due to this, researchers are looking into alternative TCEs, including thin metals, conducting polymers, carbon nanotubes, and graphene, that can perform the same function as the standard TCE while also giving solar cells mechanical stability, which can enable the manufacturing of flexible solar cells. [24].

- **Stability**

Oxygen and moisture can damage the solar cells. Regarding the stability of the solar cells, the electrodes might potentially be a weak point. Through the anodes or cathodes, oxygen and water vapor may readily seep in. As a result, the selection of TCE materials and their subsequent engineering should include all potential outcomes to prevent or at the very least discover a strategy to suppress such behaviors [44].

2.6 State–of–the–art and different types of transparent conductive electrodes

TCEs can be divided into four main categories of materials that have been used as transparent electrodes in OPV devices (Figure 10): semiconductor-based TCEs (metal-doped oxides), metal-based TCEs (thin metal layers, dielectric/metal/dielectric (DMD), metal grids, and metal nanowires (NWs)), carbon-hydrate-based TCEs (conducting polymers), and carbon-based TCEs (graphene and carbon nanotubes).

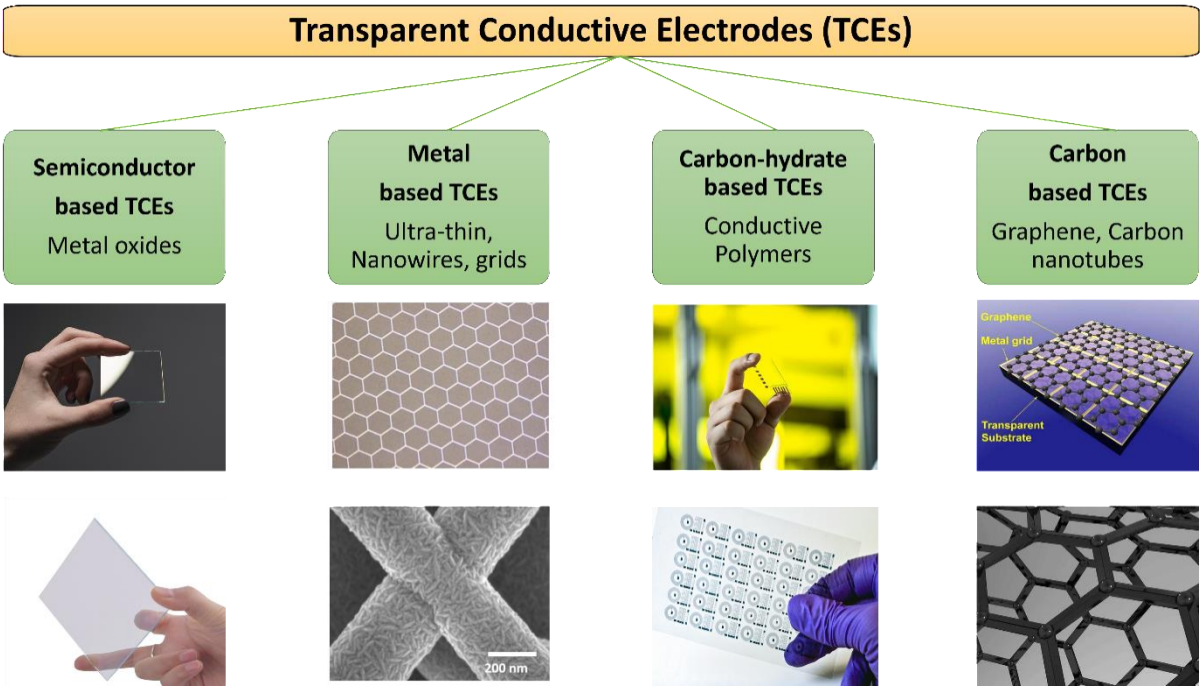

Figure 10: *Classification of TCEs* [55].

2.6.1 Semiconductor-based transparent conductive electrodes

Since the 1960s, various TCEs (especially oxides) such as tin oxide (SnO_2), zinc oxide (ZnO), and Indium tin oxide (In_2O_3:Sn) commonly known as ITO, have been discovered. Among all the discovered TCOs, Indium tin oxide (ITO) is a well-known TCE standard that is frequently utilized in the most effective solar cell technology [20, 24, 27]. Currently, it serves as a state-of-the-art TCE, to which new ideas are often compared. ITO has a very high concentration of charge carriers (~10^{21} cm^{-3}) and high conductivity of around 10^4 S/cm. ITO is the material of choice for the electrodes because of its large band gap (~3.75 eV), which results in a transmittance of more than 80% in the visible region. Despite having exceptional qualities as an electrode for optoelectronic devices, ITO still has several shortcomings that limit its usefulness in large-area applications [24]. First, indium is a rare earth element whose cost has gone up over time, and second, the ITO's applicability in flexible electronics is constrained by its mechanical and chemical instability. Additionally, the energy-intensive nature of ITO processing leads to higher processing costs.

Another state-of-the-art TCE is a fluorine-doped tin oxide (FTO). Since FTO is nontoxic and thermally more stable than ITO, it has historically been used as the bottom transparent electrode in dye-sensitized solar cells and more recently in metal-halide-based solar cells, producing power conversion efficiencies of more than 15% [56, 57]. Although using FTO

lowers material-related costs, the actual application of FTO is still constrained by processing costs.

Large bandgap semiconducting material like zinc oxide (ZnO) is also often utilized as TCEs. In comparison to the more popular ITO and FTO, ZnO has several benefits, including being relatively cheap, abundant material, and transparent in the visible and near-infrared region. For TCE applications, ZnO is often highly resistive in its pure state, requiring donor dopants like Al or Ga on Zn sites and/or F on O sites [58].

2.6.2 Metal-based transparent conductive electrodes

Ultra-thin metal films (ranging in thickness from 10 to 25 nm) such as gold (Au), aluminum (Al), silver (Ag), copper (Cu), and combinations of these metals have been extensively investigated as TCEs. These metal layers are semitransparent to visible light because of their very thin film thickness, which allows their integration as TCEs in solar cells. The main issue with ultra-thin metal films is the surface roughness; thus, a smooth morphology of the films must be maintained because it controls the films' conductivity even if thin metal films can transmit light [59]. To create smooth films with high conductivity and optical transparency, it is common practice to modify the surface of the metal films with surfactants or use another metal as a seed layer [60, 61].

A successful strategy to simultaneously boost the conductance and transmittance of the electrodes in comparison to bare thin metal films has been the combination of metals and dielectric materials. In DMD electrodes, the metal sandwiched between the two metal oxide layers improves the total transmittance of the electrode through optical interference effects with appropriately adjusted layer thicknesses [62]. The remarkable ductility of metals and the additional mechanical flexibility of DMD-structured electrodes make them suitable for use in flexible optoelectronic systems [63].

Other metal-based TCEs are metal NWs, which can be processed at low temperatures and can also be used for flexible substrates. NWs have also enabled the possibility of fabricating electrodes using fluid processing. The metal wires control strong lateral conductivity, and the random metal networks enable significant light transmission through the films. Metal NWs have a high aspect ratio and let light travel through uncovered areas, but they also have higher junction resistances between two wires that have an impact on the conductivity of the film. Metals such as Ag, Cu, Au, and others have been considered as possible NW electrode

materials. It has been demonstrated that these materials can increase film conductivity by reducing junction resistance [64-67].

Using metal networks, which are a bit bigger in all dimensions than metal NWs, is another way to boost the conductivity of TCEs without sacrificing their optical transparency. Using metal networks has the advantage that the metal inside the network provides lateral conductivity, and the gaps in the metal film can transmit light [68].

2.6.3 Carbon-hydrate-based transparent conductive electrodes

Due to their high transparency, easy solution processing, and excellent compatibility, conductive polymers such as polyaniline (PANI) and Poly(3,4-ethylenedioxythiophene) polystyrenesulfonate (PEDOT:PSS) have become quite popular in the optoelectronics industry [69].

It was realized that electrically conducting and optically transparent films could be fabricated by casting PANI and PANI-containing polyblends (inducing solubility with functionalized protonic acids). It was feasible to produce optically clear (i.e., do not scatter light) films with a surface resistance less than 100 Ω/□ and a transmittance of around 70% between 475 and 675 nm in the visible range, demonstrating the materials' potential. However, more research is needed to best balance the trade-off between transparency and conductivity. The PANI-based transparent conducting films have potential benefits for usage in a number of applications since they are flexible, mechanically stable, and simple to pattern [70, 71].

PEDOT:PSS is the most well-known and economically successful conductive polymer, which is widely utilized for antistatic coatings in traditional electronics and as transparent electrodes and charge transport layers in the area of PVs. PEDOT:PSS is in the form of a polyelectrolyte in aqueous dispersion, giving it strong film-forming capabilities on both rigid and flexible surfaces. In typical organic optoelectronic layer stacks, it is one of the most ecologically beneficially produced materials since it is processed from water. Its high work function (4.8 to 5.2 eV) values [72, 73], excellent visible range transparency [74], high conductivity with additional materials [75], and strong thermal, UV, and chemical durability [72, 76] make it the most successful commercial conductive polymer coating in the optoelectronics industry. Due to the numerous potential applications, PEDOT:PSS is currently commercially available in several formulations to satisfy the needs of various applications, including antistatic coatings, biosensors, conductive electrodes, OLEDs, organic

solar cells, thermoelectrics, health care monitoring devices, capacitors, and touch screens [77-89].

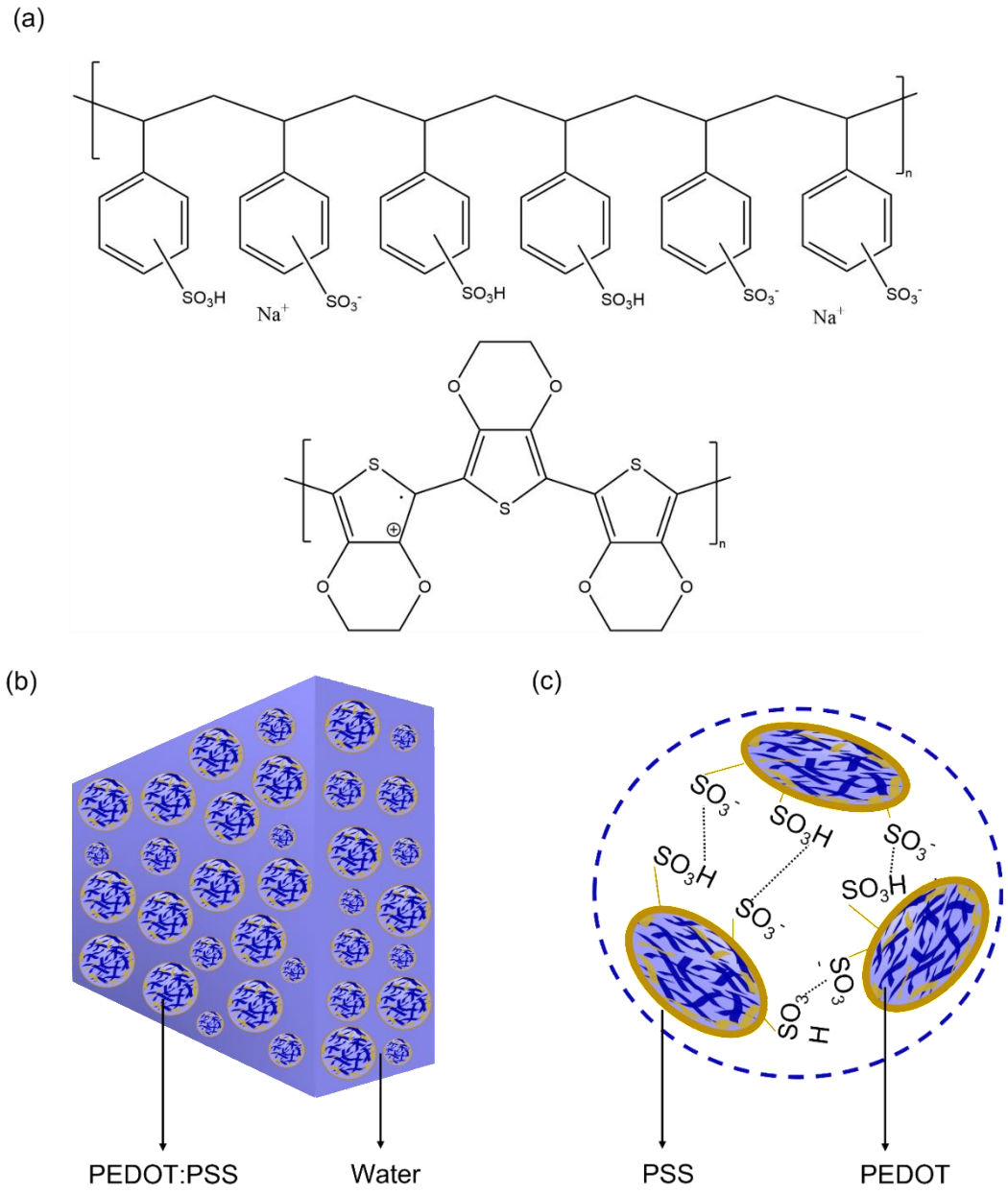

Figure 11: *(a) Schematic representation of the chemical structure of PEDOT:PSS, (b) schematic diagram of PEDOT:PSS in solution, and (c) schematic diagram of PEDOT:PSS as a solid film [90].*

As illustrated in Figure 11 (a), PEDOT:PSS is composed of a combination of positively charged conjugated PEDOT, negatively charged PSS, and positively charged counter-ions (mostly sodium and hydronium). The processing of aqueous dispersions is enabled by the polyelectrolyte PSS, which also permits doping. PEDOT:PSS is a phase-segregated structure

made up of conductive PEDOT polycationic spheres enclosed in PSS polyanionic shells (Figure 11 (b)). In contrast to hopping transport between neighboring PEDOT domains, charges are transported in band-like patterns inside PEDOT-rich phases and fibers [91-96].

Pristine PEDOT:PSS films have a conductivity of 0.1 S/cm, and thus different dopants [92, 97] such as ethylene glycol (EG) [98], polyethylene glycol (PEG) [99], dimethyl sulfoxide (DMSO) [100], different acids like HCl [101], H_2SO_4 [102], anionic surfactants [103, 104], ionic liquids [105], etc. have been employed to improve the conductivity of PEDOT:PSS to be used as TCE in solar cells.

2.6.4 Carbon-based transparent conductive electrodes

The most recent development in conductive materials is graphene [106]. Due to its two-dimensionality, it may be formed into thin, flat conductive films that have strong mechanical strength, inherent heat conductivity, and high visual transmittance [107, 108]. One of the main hurdles is still producing high-quality graphene sheets and ensuring effective deposition onto substrates [109]. Due to their distinctive electrical and mechanical characteristics, carbon nanotubes (CNTs) have also attracted significant interest for use as TCE. As a quasi-one-dimensional material with very high aspect ratios, CNT jackstraws can produce high lateral conductivity and high light transmittance at the same time. The potential for solution processibility, which can lead to cost-effective high-throughput processing of the electrodes, is one of the advantages of nanoscale materials. Despite having an electrical conductivity of 3×10^6 S/cm and 10^5 cm^2/Vs charge mobilities for each single-walled CNT, the practical use of CNTs is limited by their high contact resistance [109, 110].

Chapter 3

Experimental

3.1 Experimental details

The materials, their characteristics, solutions, and formulations that were investigated in this work are discussed in this chapter. To have a full understanding of all the experiments that were performed to accomplish this work, the detailed processes for fabricating films and devices and characterization methods are also explained.

3.1.1 Materials

Indium tin oxide (ITO) coated glasses with a sheet resistance of about 10 Ω/square were purchased from Xinyan Technology Limited (China). Glass substrates were purchased from Thermo Scientific, Gerhard Menzel GmbH (Germany). Different formulations of PEDOT:PSS (Clevios -P VP AI 4083, -PH, -PH1000, -HIL-E 100, -F HC Solar) bearing different properties (as described in Table 1) were purchased from Heraeus Epurio Clevios™ (Germany). PCDTBT (poly[N-9'-heptadecanyl-2,7-carbazole-alt-5,5-(4',7'-di-2-thienyl-2',1',3'-benzothiadiazole)]) and P3HT (poly(3-hexylthiophene) was used as donor material received from 1-material (Canada), $PC_{70}BM$ ([6,6]-phenyl-C_{70}-butyric acid methyl ester) and $PC_{60}BM$ (1-(3-methoxycarbonyl)propyl-1-phenyl[6,6]C61) with a purity of 99% was used as acceptor material received from Solenne B.V. (Netherlands). Dimethyl sulfoxide (DMSO) and chlorobenzene were bought from Sigma-Aldrich.

3.1.2 Solutions/Dispersions/Formulations

i. **Active layer solution:** PCDTBT and $PC_{70}BM$ were dissolved in a solvent combination of chlorobenzene (CB) and chloroform (CF), in a ratio of 1:1. The ratio of PCDTBT to $PC_{70}BM$ was 1:2, and the PCDTBT concentration was 5 mg/mL. For two weeks, the mixture was stirred at 50°C at 700 rpm. The concentration of the P3HT:$PC_{60}BM$ (composition weight ratio-3:2) solution was 12 mg⁄ml, dissolved in chlorobenzene.

ii. **PEDOT:PSS formulation:** Pristine PEDOT:PSS formulations (Table 1) were utilized in the majority of the experiments. The Clevios-PH1000 formulation was generally mixed with 5 vol% DMSO to fabricate conductive PEDOT:PSS films.

Table 1: *Information about different commercial formulations of PEDOT:PSS from Heraeus Epurio Clevios™ used in this study [90].*

Name	Work function [eV]	Resistivity [Ω·cm]	Conductivity [S/cm]	Viscosity [mPas]	PEDOT: PSS ratio [w:w]	Intended use
P VP AI 4083	5.0 – 5.2	500 – 5000	0.0002 – 0.002	5 – 12	1:6	Hole injection layers for OPVs and OLED displays and lighting
PH	4.8 – 5.2	0.0100 – 0.100	<10	20	1:2.5	Antistatic coatings on PET, PC, glass, papers, ESD
PH 1000	4.8 – 5.0	0.0012	850*	15 – 60	1:2.5	Transparent conductive electrodes, touch panels
HIL-E 100	5.0 – 5.2	0.0167	>60	15 – 60	1:7.5	Hole injection layers for OLED displays and lighting
F HC a Sol r	4.8 – 5.2	0.002	>500	8 – 70	1:2.5	Electrodes in OPVs printed sensors

*After the addition of 5% dimethyl sulfoxide. Measured on the dried coating.

3.1.3 Layer stack and solar cell devices

i. **Fabrication of PEDOT:PSS thin films:** Figure 12 depicts the precise steps involved in sample preparation and characterization. Glass substrates containing ITO coatings were washed with soap solution, rinsed, and soaked for 15 minutes in distilled water, toluene, acetone, and isopropanol. Commercially available PEDOT:PSS formulations with various characteristics, as shown in Table 1, were spin-coated on top of ITO at 3000 rpm for 45 seconds using a 0.45 µm Whatman™ puradisc polyethersulfone (PES) syringe filter to remove fine particles.

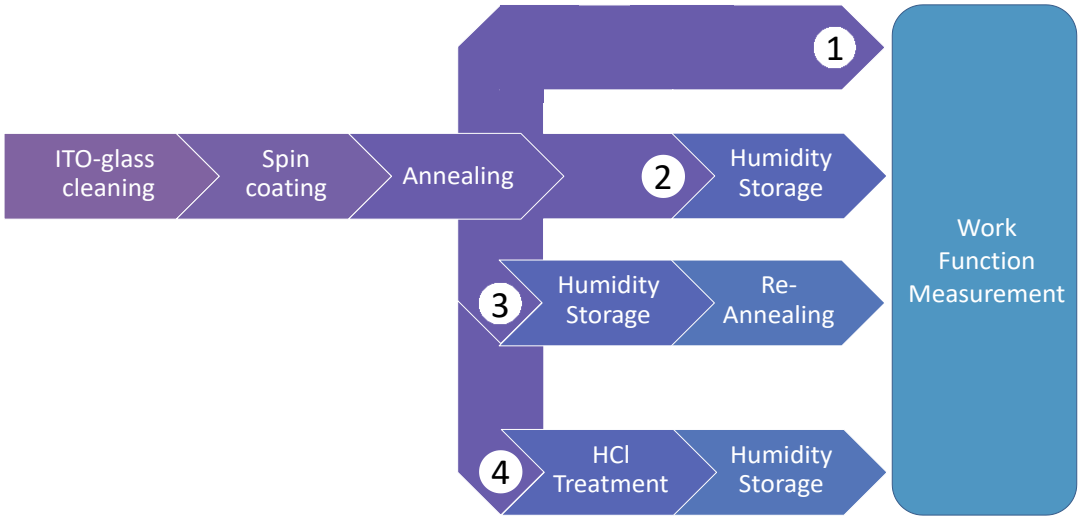

Figure 12: *Overview of the PEDOT:PSS sample preparation and characterization* [90].

a) *Thermal treatment:* PEDOT:PSS films (refer to Table 1) were thermally annealed for 15 minutes at various temperatures: 85, 100, 115, 130, 145, 160, 175, 190, 205, 220, 235, and 250°C, respectively, to investigate the impact of thermal treatment.

b) *Humidity exposure:* To evaluate the influence of relative humidity (RH), PEDOT:PSS films (refer to Table 1) were annealed at 178 °C for 15 minutes and the work function of PEDOT:PSS films were continually monitored in ambient air for two hours at 70 to 90% RH following the annealing procedure. For controlled investigations on the impact of humidity, PEDOT:PSS films (Clevios -P VP AI 4083, -PH1000, and -HIL-E 100) were annealed at 100, 130, 160, 190, 220, and 250 °C. Following annealing, PEDOT:PSS films were kept at room temperature for six hours in a BINDER climate chamber set to 20, 37, 50, 72, and 90% RH.

c) *Reversibility of surface properties:* PEDOT:PSS films (Clevios- P VP AI 4083) were thermally annealed at 178 °C for 15 minutes. Thereafter, PEDOT:PSS films were exposed at 0% or 90% RH for an hour or 12 hours following the annealing procedure. Following exposure, the PEDOT:PSS films were re-annealed for 15 minutes at 178 °C.

d) *Hydrochloric acid (HCl) treatment:* The compositional behavior of PEDOT:PSS films was studied by modifying PEDOT:PSS films with HCl. PEDOT:PSS films (Clevios-PH1000 + 5 Vol% DMSO) were spin-coated and annealed at 120°C for 15 minutes. 800 µL of a 32% HCl solution were drop-coated onto the films after annealing. The films were washed with distilled water and dried with nitrogen gas

after 10 minutes of reaction time. The films were once again annealed for 15 minutes at 120 °C, and the work function was measured. To study how humidity affected the films, the HCl-modified films were also kept at 0 or 90% RH for 1 hour.

ii. **Fabrication of solar cells using PEDOT:PSS films as the hole conducting layer:** to To examine the effects of PEDOT:PSS modification for thermal treatments and humidity treatments on devices, PCDTBT:$PC_{70}BM$ solar cells were fabricated following the layer stack: ITO/PEDOT:PSS/PCDTBT:$PC_{70}BM$/aluminum.

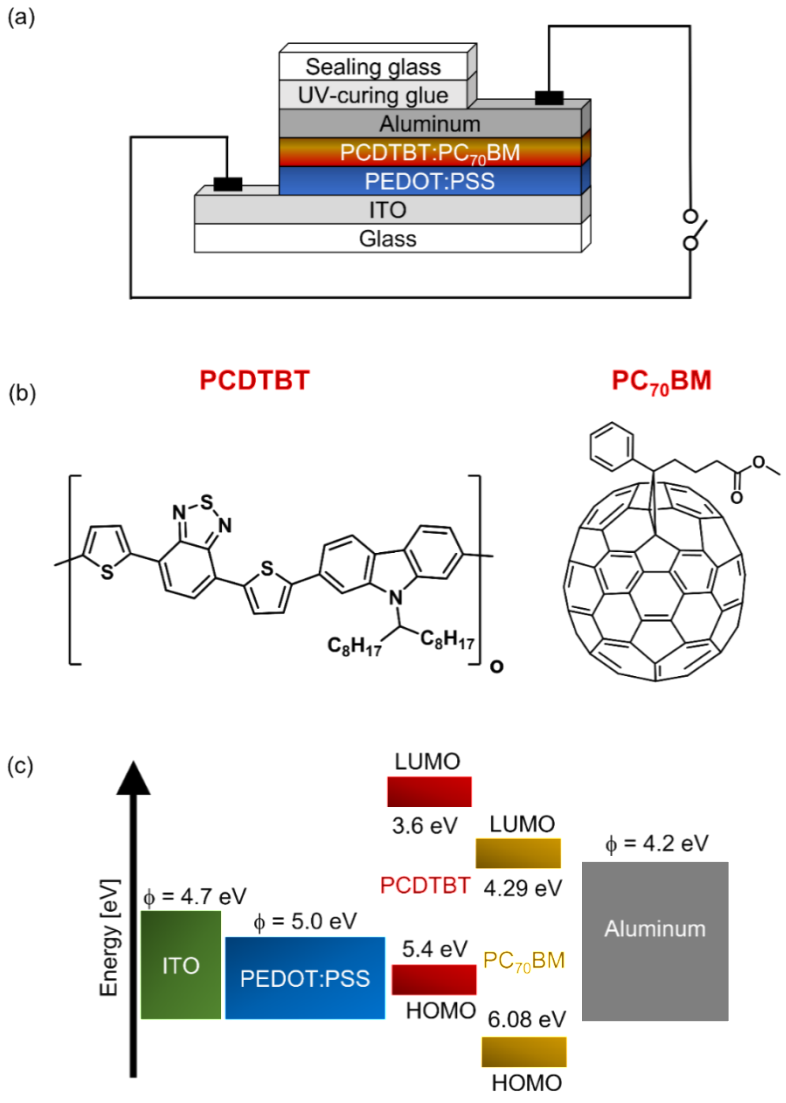

Figure 13: *(a) Schematic illustration of a PCDTBT:$PC_{70}BM$ solar cell (b) Chemical structure of the active layer: PCDTBT and $PC_{70}BM$ and (c) Energy diagram of a PCDTBT:$PC_{70}BM$ polymer solar cell (values taken from refs. [111, 112]) and ϕ being the work function [90].*

The PCDTBT:$PC_{70}BM$ polymer solar cell's energy diagram, active layer's molecular structure (PCDTBT, $PC_{70}BM$), and layer stack are all depicted schematically in Figure 13. After being cleaned with isopropanol (IPA) and toluene, ITO-coated glass substrates were sequentially ultrasonicated for 15 minutes in an IPA bath. After using nitrogen gas to dry the substrates, the substrates underwent a 5 minutes plasma treatment. On top of ITO, a layer of PEDOT:PSS was spin-coated using a Whatman™ PES 0.45 µm filter at 3000 rpm for 60 seconds, and then it was thermally annealed in an ambient atmosphere for 15 minutes at 178 °C. Samples were placed in the glove box after the PEDOT:PSS coating. At 1200 rpm for 45 seconds, 70 µl of PCDTBT:$PC_{70}BM$ solution was spun onto the PEDOT:PSS layer. The samples were thermally annealed at 80 °C for 10 minutes after the active layer coating. The PCDTBT:$PC_{70}BM$ layer was washed with methanol after it had been baked. Samples were put in a physical vapor deposition (PVD) chamber under a vacuum (2.4×10^{-7} mbar) following a methanol wash. Aluminum with a thickness of around 300 nm was deposited by physical vapor deposition (PVD). Glass slides were used to seal the devices using UV-curing adhesive glue. The area of solar cells was 0.42 cm^2.

3.2 Preparation techniques

3.2.1 Weighing

The analytical balance, a KERN ABT 120–5DM, is shown in Figure 14 and was used to weigh the ingredients of the active layer. The resolution of the balance is 0.1 mg, while the measurement range is 0.01 mg. The range of weights is 1 mg to 42 g/120 g.

Figure 14: *Picture of the KERN ABT 120–5DM analytical balance [113].*

3.2.2 Ultrasonic cleaning

The Bandelin Sonorex RK 255 H ultrasonic cleaner (Figure 15) was utilized to clean the glass substrates.

Figure 15: *Picture of the Bandelin Sonorex RK 255 H ultrasonic cleaner* [114].

The ultrasonic cleaner can operate continuously for 1 to 15 minutes and can operate at a temperature stabilized between 30 to 80 °C.

3.2.3 Plasma cleaning

Residues of hydrocarbons from fats, oils, or release agents are present on practically all surfaces. When the surface is subsequently treated, the adhesion of other materials is significantly reduced by these layers. This is why a routine plasma cleaning is done to remove the hydrocarbons and dirt particles through chemical reactions with ionized gases (Figure 16). A plasma system from Diener electronic was used to clean the glass substrates.

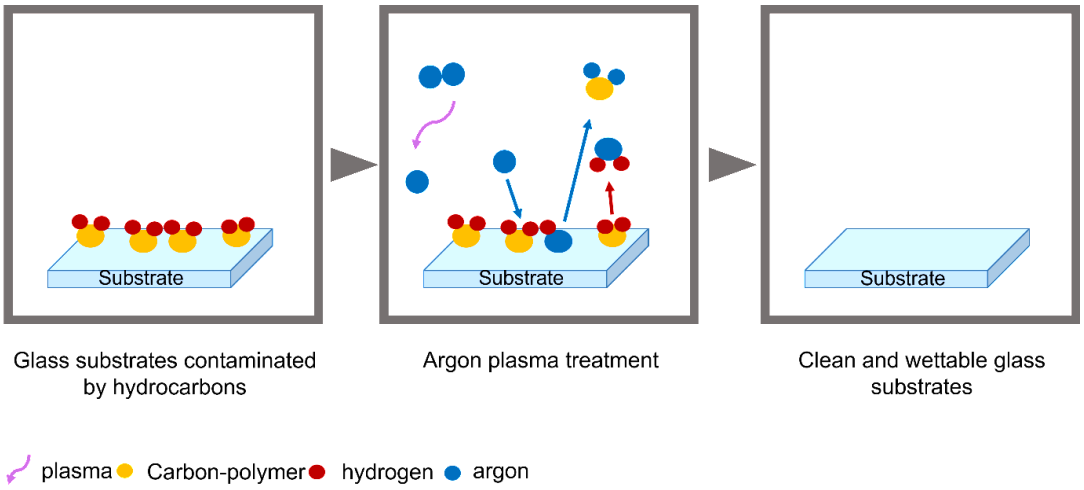

Figure 16: *Illustration of the plasma cleaning process. Adapted from* [115].

3.2.4 Spin coating

Spin coating is a quick and inexpensive method to create homogeneous layers. The substrate is covered with an excess of the dispersion or solution, which is subsequently dispersed by centrifugal force while rapidly rotating the substrate (Figure 17).

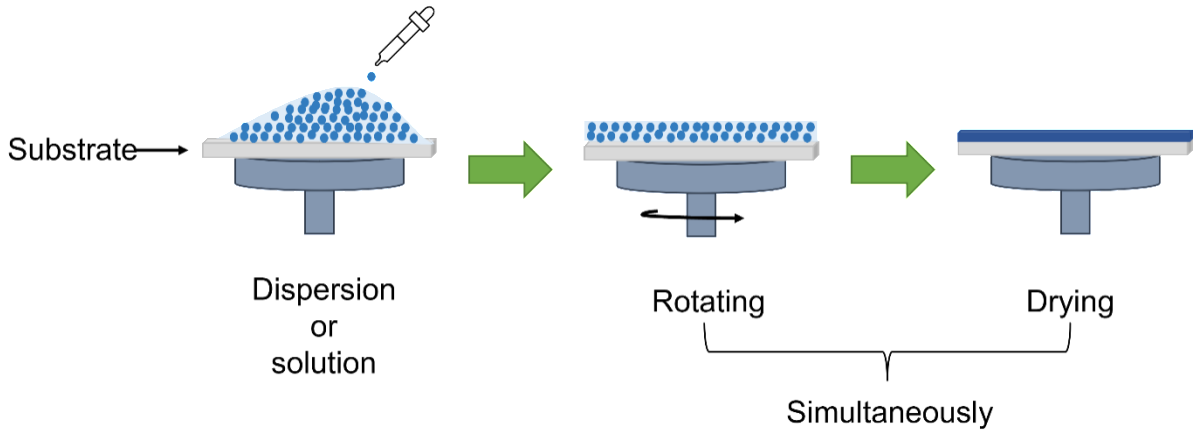

Figure 17: *Illustration of a spin coating process.*

The rotation duration, rotation speed, and solid concentration of the dispersion or solution can be changed to alter the film thickness. For the fabrication of PEDOT:PSS films, a Laurell WS–650MZ–23NPP Lite spin coater was used in the flow head, and for the fabrication of the active layer and ETL inside the glove box, an SÜSS MicroTec spin coater was used in the glove box.

3.2.5 Thermal annealing

For the thermal annealing of films, Praezitherm hot plate type PZ 2860-SR (Figure 18) was used. The temperature of the hot plate can be adjusted up to 350 °C.

Figure 18: *Picture of the Praezitherm hot plate type PZ 2860-SR* [116].

3.2.6 Physical vapor deposition

PVD is a technique for creating thin films of metals and coatings on a variety of substrates, such as metals, ceramics, glass, and polymers.

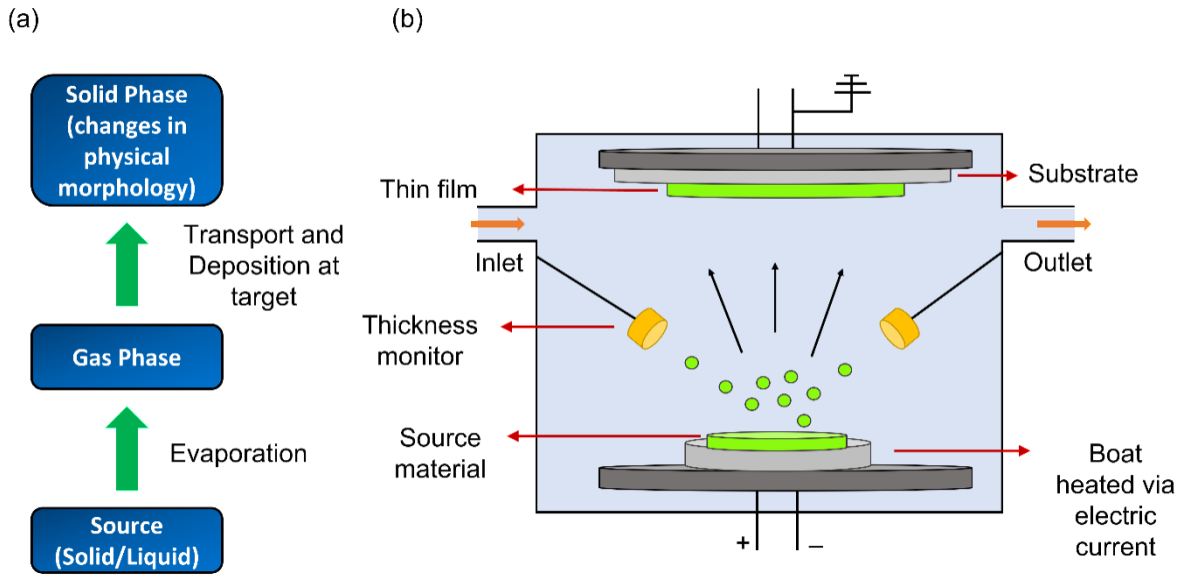

Figure 19: *(a) PVD process flow diagram, and (b) Illustration of the PVD process.*

The steps involved in the procedure can be outlined as follows (Figure 19): (1) The substance to be deposited is physically transformed into a vapor (high-temperature vacuum or gaseous plasma), (2) the vapor is transferred from its source to a low-pressure area, and (3) the vapor condenses on the substrate to produce a thin layer [117]. Films having thicknesses of between a few nanometers and thousands of nanometers are typically deposited using PVD techniques. For the work mentioned in this thesis, the Mini SPECTROS™ Kurt J. Lesker PVD machine was utilized to produce thin metal films. The working pressure for all depositions was about 1×10^{-6} mbar.

3.2.7 Sealing with UV curing

A customized JANOME JP 2200N mini GLT robot was utilized to encapsulate the solar cells (Figure 20). The dispenser, the sealing head, and the UV light are the three components of the robot. The dispenser is set up to dispense glue (DELOLP656) onto the stage-mounted solar cells. The sealing head is set up to pick up and position the sealing glass on the solar cells. The glue was cured with a UV light (Omnicure Series 1000). The exposure time to cure the glue on one substrate was 1 minute and 24 seconds.

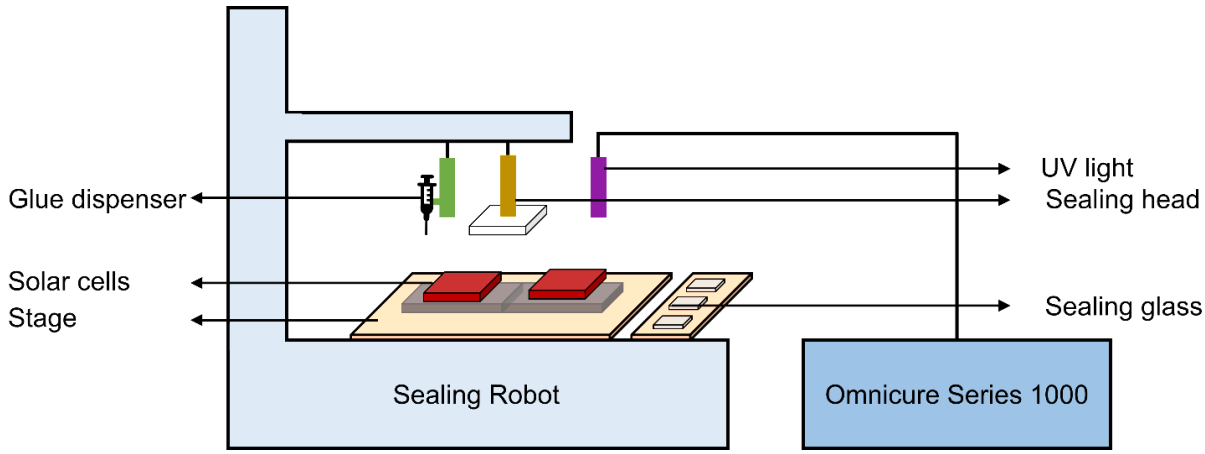

Figure 20: *Schematic of the Sealing robot.*

3.3 Characterization techniques

3.3.1 Simulation methods

The evaluation of the figure of merit (FOM) for all TCEs was carried out using a MATLAB program. The program calculated the PV power for a given solar cell length according to the Shockley-Queisser limit by using the photon flux descriptions of black body radiation at 300 K and the AM 1.5G solar spectrum, once for optimal values of sheet resistance $R_{\square}$ = 0.0001 Ohm/square and 100% light transmission, and once for the conditions specified by transmittance spectra, the sheet resistance, and the photovoltaically active spectral range. The transmittance data was extracted from each publication using an online tool called the web plot digitizer [118].

3.3.2 Kelvin probe

The photographic description of the KP calibration process and work function measurements of samples using KP is shown in Figure 21. The electronic work function is used to describe the difference between the fermi level and the vacuum level. A single-point Kelvin probe (KP) system from Anfatec Instruments AG (Germany) was used to measure the work function. All the measurements were conducted in ambient air. Highly oriented pyrolytic graphite (HOPG) was used to calibrate the Kelvin probe system with its known work function of 4.46 ± 0.04 eV. For every calibration of the Kelvin probe system, HOPG was freshly cleaved with the help of sticky tape, to expose a clean graphite surface.

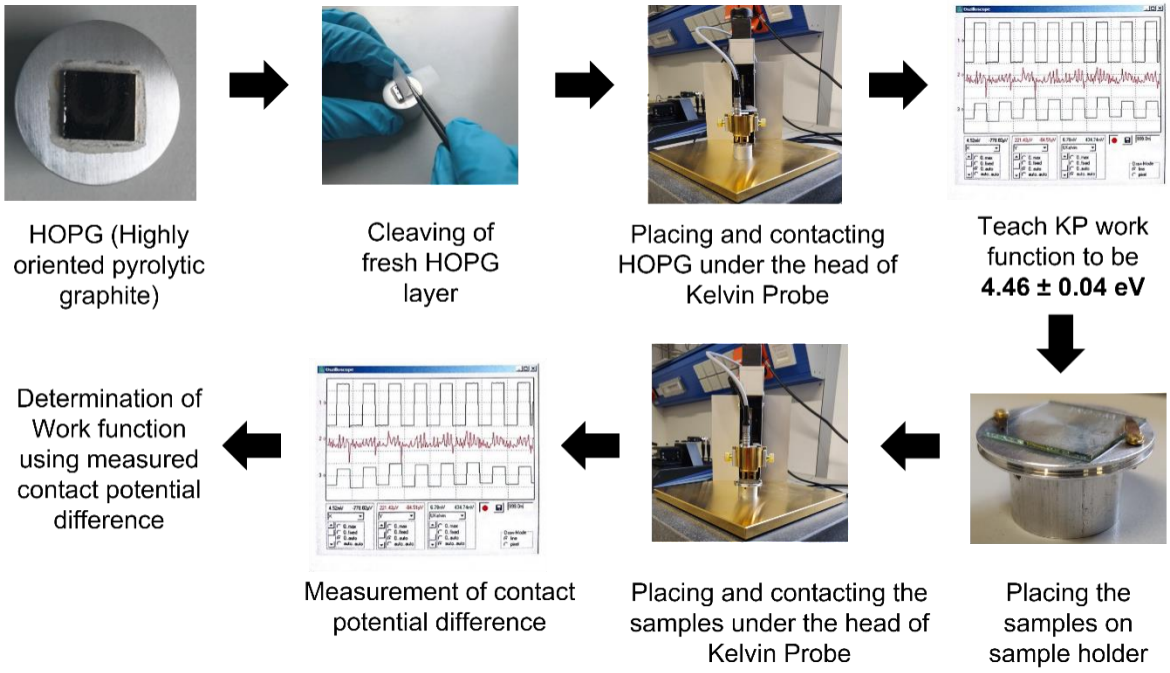

Figure 21: *A visual explanation of the calibration process for the Kelvin Probe and work function measurements of samples using the Kelvin Probe.*

Work function measurements for thermal treatment were carried out from 20 to 40% RH at room temperature. For the controlled humidity study, work functions were measured at an interval of one hour for each film, and the films were stored again inside a climate chamber.

3.3.3 Thermogravimetric analysis

Figure 22: *Picture of the TGA instrument (TG 209 F1 Iris by Netzsch)* [119].

Thermogravimetric analysis (TGA) is an analytical method that analyzes the weight change that takes place while a sample is heated at a constant pace to assess a material's thermal stability and the percentage of volatile components. This measurement sheds light on

chemical phenomena including chemisorptions, thermal breakdowns, and solid-gas interactions in addition to physical phenomena like phase transitions, absorption, adsorption, and desorption (e.g., oxidation or reduction) [120].

TGA was performed using TG 209 F1 Iris by Netzsch (Figure 22) in an ambient atmosphere ranging from 20 to 590 °C with a heating rate of 10 °C/min. Different formulations of PEDOT:PSS were poured into Teflon-lined Petri dishes and dried in a BINDER climate chamber at 20% RH and room temperature. After drying for 24 hours, free-standing PEDOT:PSS was crushed into a powder using a mortar and pestle and stored in airtight bottles.

3.3.4 Current-voltage measurements

Current-voltage (IV) curves were acquired under the illumination of one sun (AM 1.5) using a WaveLabs Sinus 70 LED-solar simulator and were recorded with a Keithley 2400 Source-Measure-Unit (SMU) (Figure 23). The intensity of the light source was calibrated by a pyranometer to confirm the AM 1.5 condition and an intensity of 100 mW/cm^2. The measurement range was between –2 to 2 V. The dark current-voltage curves of the solar cells were determined by repeating the measurement in the dark.

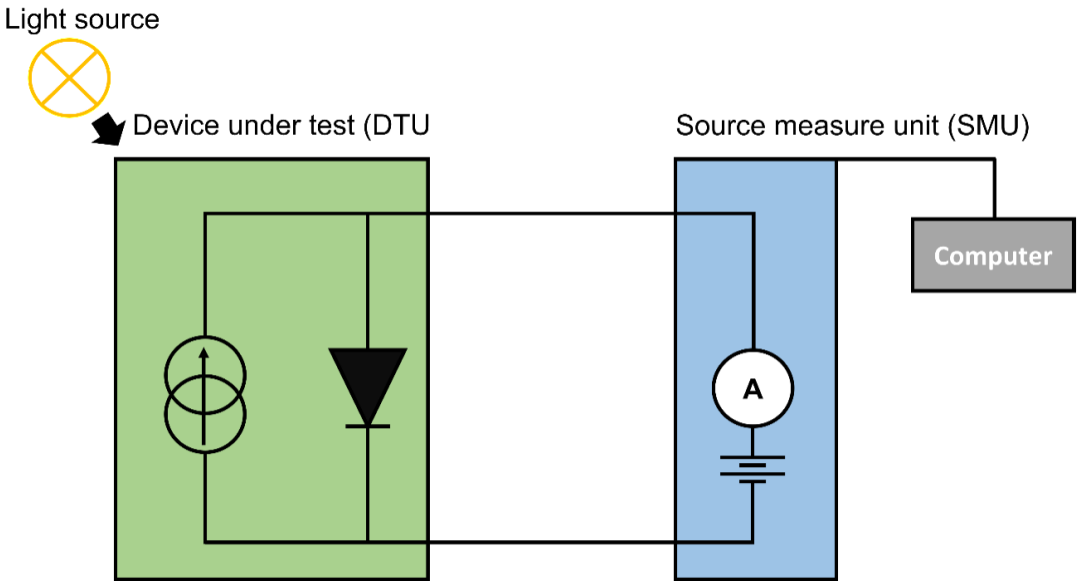

Figure 23: *Source measure unit and solar simulator for I-V measurement.*

3.3.5 External quantum efficiency measurements

External quantum efficiency (EQE) measurements were made on the solar cells to obtain the spectral response of the solar cells. EQE is defined as the ratio of the number of charge carriers collected by the solar cell to the number of photons of specific energy shining on the solar cell from the outside (incident photons).

$$EQE[\%] = \frac{electrons/sec}{photons/sec} = \frac{(current)/(charge\ of\ one\ electron)}{(total\ power\ of\ photons)/(energy\ of\ one\ photon)} \quad (33)$$

The EQE was measured with Bentham PVE300 under monochromatic light with an additional halogen bias light, providing an excitation intensity of about 1 sun. A silicon detector was used to calibrate the EQE system, and the wavelength was selected using a monochromator. Figure 24 depicts the measuring equipment's fundamental structure.

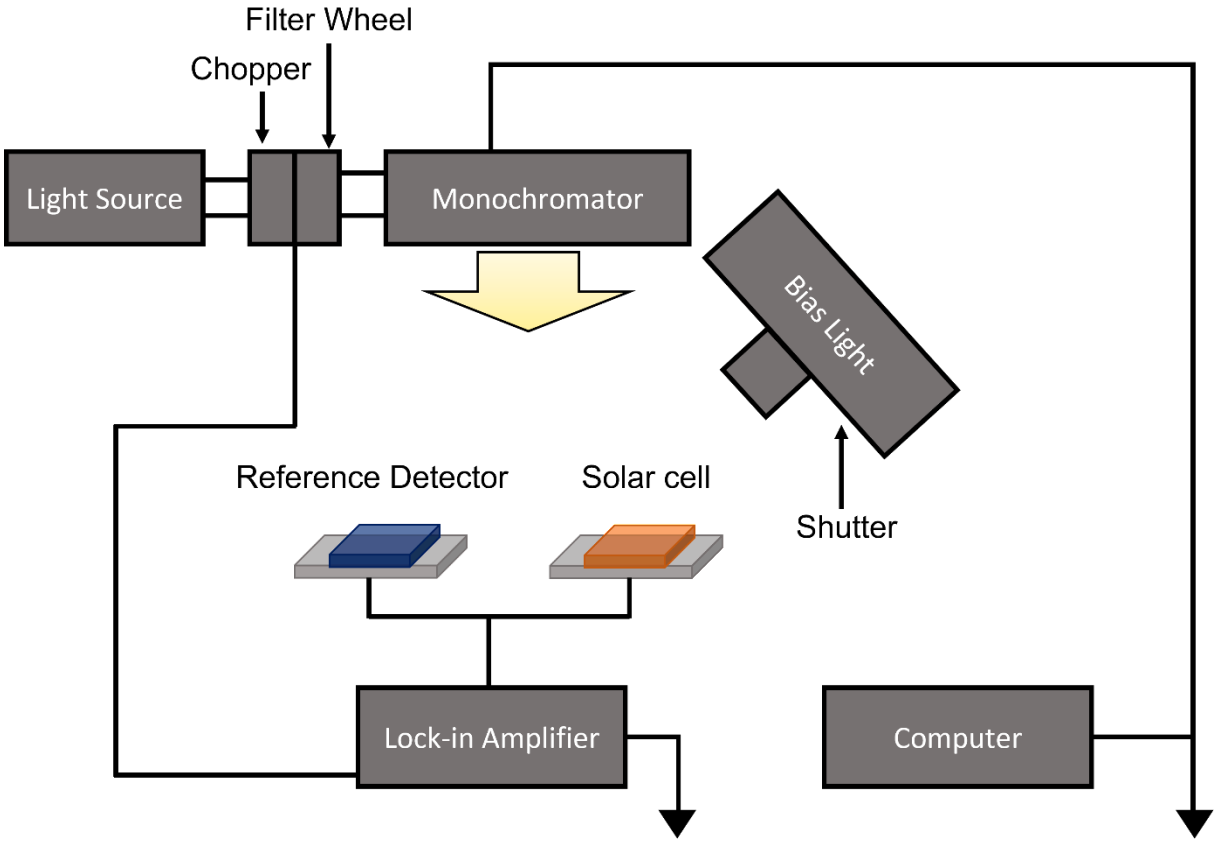

Figure 24: *Schematic of an EQE measurement setup.*

3.3.6 Reflectance, transmittance, and absorptance

The reflectance and transmittance of polymer films were measured using the Avantes AvaSpec-ULS3648-USB2-UA-25 fiber spectrometer (Figure 25). After measuring transmittance and reflectance, the absorptance was calculated using the formula:

$$A = 1 - (T + R) \tag{34}$$

where A is the absorptance, T is the transmittance, and R is the reflectance value at a particular wavelength. The majority of the films were measured at wavelengths between 300 and 1100 nm.

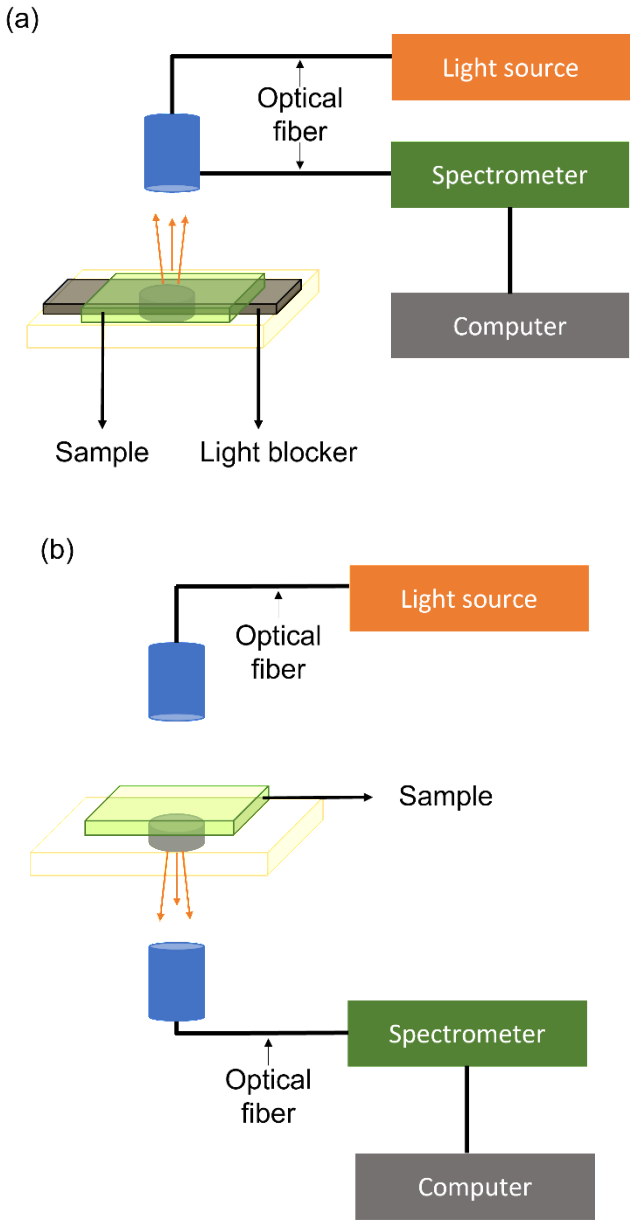

Figure 25: *Illustration of (a) reflectance, and (b) transmittance measurement setup.*

3.3.7 Four–point probe sheet resistance measurement

A four-point probe is one of the most common pieces of equipment used to measure the sheet resistance of a material. For this measurement, four identically spaced probes are arranged in a straight line. A direct current (DC) current (I) is applied between the outer two probes, and the voltage drop between the inner two probes is then measured (Figure 26 (a)).

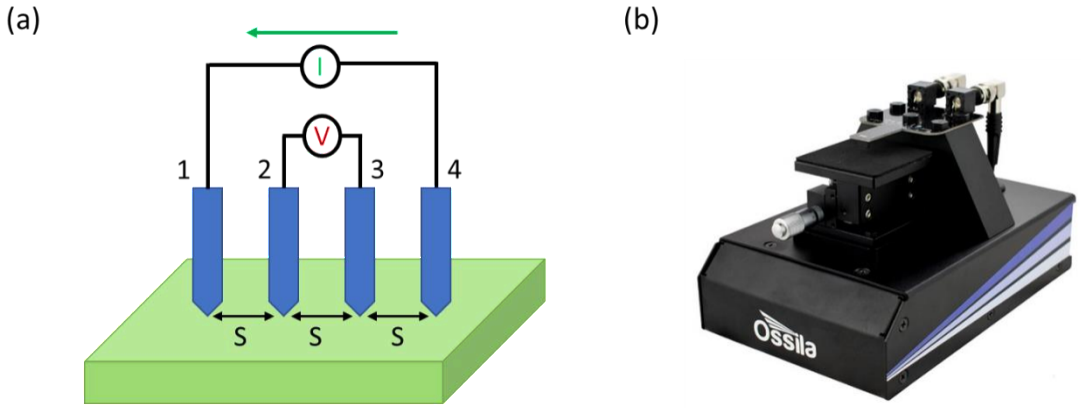

Figure 26: *(a) Illustration of the four-point probe operation mechanism, and (b) picture of the Ossila four-point probe measurement system* [121].

The sheet resistance can then be calculated using Valdes–Smits equation [122, 123] as described here:

$$R_{\square} = \frac{\pi}{ln(2)} \frac{\Delta V}{I} = 4.53236 \frac{\Delta V}{I} \quad (35)$$

where R□ is the sheet resistance, ΔV is the change in voltage measured between the inner probes, and I is the current applied between the outer probes. The sheet resistance of polymer films was measured using the Ossila four-point probe (T2001A3) (Figure 27 (b)). The measurement range of the Ossila four-point probe is from 100 mΩ/□ to 10 MΩ/□.

Note: This equation is only valid if the thickness of the substance being tested cannot exceed 40% of the distance between the probes and the sample has a suitably large lateral size. If not, geometric correction factors are required to take the sample's size, shape, and thickness into consideration.

3.3.8 Non–contact sheet resistance measurement

The non-contact sheet resistance testing equipment operates on the alternating current (AC) through the coil, creating a primary electromagnetic field that induces eddy currents in the sample (conductive materials). The induced current in the sample runs at the same frequency as the induction coils and results in a secondary field that opposes the primary field. The sheet resistance is defined as the total of both fields or the change in fields (Figure 27 (a)).

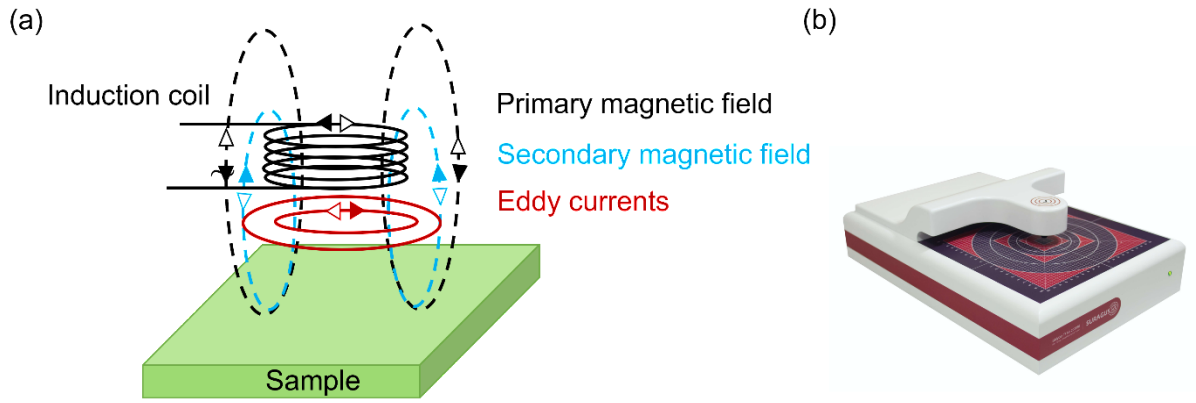

Figure 27: *(a) Illustration of Non-contact sheet resistance measurement mechanism, and (b) picture of SURAGUS EddyCus TF lab 2020SR Non-contact sheet resistance measurement setup* [124].

Using the SURAGUS sheet resistance tester-EddyCus TF lab 2020SR, the sheet resistance of polymer films was also measured (Figure 27 (b)). The measurement range of EddyCus TF lab 2020SR is from 0.1 mΩ/□ to 100 kΩ/□.

3.3.9 Atomic force microscopy

To obtain information about the morphology of PEDOT:PSS films, atomic force microscopy (AFM) was carried out using NanoWizard 4 from JPK-Bruker-Nano. An AFM picture is generated by recording the force changes when the probe (or sample) is scanned along the x and y axes. The sample is fixed to a piezoelectric scanner, which guarantees precise three-dimensional positioning with high resolution. The measurement was done in tapping mode. A flexible cantilever was used as a spring, and the force was measured by mounting the probe to it and measuring the cantilever's deflection (Figure 28) [125].

The AFM measurements were performed by Dipl.-Ing. Susanne Sandkuhl at Otto Schott Institute of Materials Research, Friedrich Schiller University Jena, Germany.

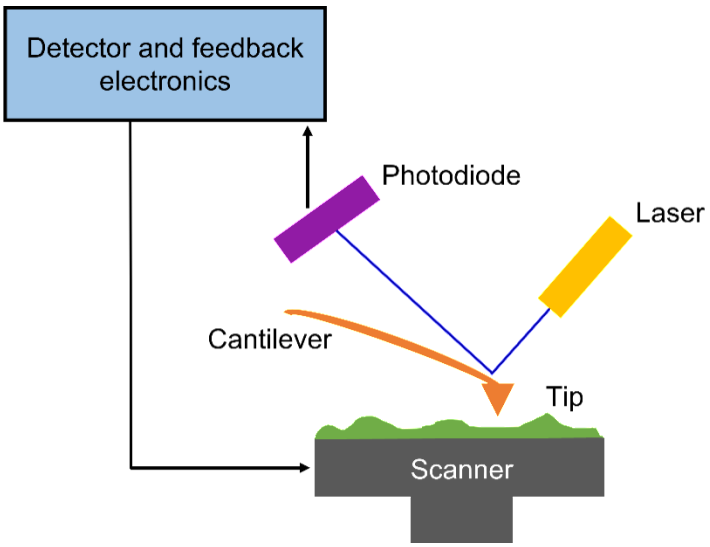

Figure 28: *Illustration of an AFM instrument.*

3.3.10 X-ray photoelectron spectroscopy

X-ray photoelectron spectroscopy (XPS) is an analytical method in which a material's surface is bombarded with X–rays and the kinetic energy of the electrons that are released are then measured. The surface sensitivity of this approach and its capacity to extract chemical state information from the components in the sample are two of the key qualities that make it effective as an analytical method [126].

XPS measurements were performed using monochromatized Al Kα excitation (SPECS Focus 500, $E_{excitation}$ = 1486.71 eV) under ultra-high vacuum conditions (10^{-10} mbar).

The XPS measurements were performed by the AG Fritz group at Friedrich Schiller University Jena, Germany.

3.3.11 Ultraviolet photoelectron spectroscopy

Ultraviolet photoelectron spectroscopy (UPS) is used to gather information on the bonding and valence electron levels of atoms. The sole difference between UPS and XPS is that in the former, photons with energies larger than 1 keV are utilized to cause the photoelectric effect, whereas, in the latter, ionizing radiation with energies of 10s of eV is employed.

UPS measurements were performed under ultra-high vacuum conditions (10^{-10} mbar) using monochromatized and p-polarized He Iα excitation (SPECS UVLS, Excitation = 21.22 eV). The photoelectrons were collected by a SPECS PHOIBOS 150 hemispherical electron

analyzer equipped with a 3D delay line detector (SPECS DLD4040-150). A bias of ~ –9 V was applied between the sample and the ground. Work functions were evaluated based on the secondary electron cut-off energy.

The UPS measurements were performed by the AG Fritz group at Friedrich Schiller University Jena, Germany.

Chapter 4

Results and Discussions

4.1 Figure of merit for transparent conductive electrodes

Even though the established figures of merit, as shown in the introduction section 2.5, can be used to rate the TCEs, it was found that they were mostly not designed specifically for TCEs used for photovoltaic (PV). Since those TCE options that might be ideal for other optoelectronic devices would not necessarily be best for PV applications, the need to introduce a novel figure of merit (FOM) was realized by us. In conclusion, for a for TCEs used in photovoltaics tailormade FOM a set of postulates has been elaborated: i) the FOM is proportional to the potential power output of PV devices so that it can be linked directly to the efficiency of the solar cell, ii) the FOM is normalized to the Shockley-Queisser limit (SQL) to quantify losses directly connected with properties of the TCE, and iii) as commonly used for ratings in general, the FOM should be a number, and thus dimensionless [39].

A FOM for evaluating the applicability of TCEs for PVs may be simply designed by rationalizing the impact of two crucial qualities: transmittance and conductance (respectively sheet resistance). However, the TCE performance limitations in PV applications are linked to solar cell geometry. Thus, information about the solar cell length (Figure 29) is necessary for an accurate assessment of the suitability of TCEs for PV applications [40, 127]. While the sheet resistance affects the overall series resistance of the solar cell depending on the length (in the direction of current transport) and width of the solar cell, the impact of the transmittance can be immediately quantified by losses in solar photon flux and consequently in charge carrier generation [53]. Typically, series resistance coming from TCE is avoided in lab-scale solar cells by miniature design. However, when scaling up to solar modules, power void areas cannot be avoided anymore, and it is important to comprehend how geometry affects solar cell performance [19, 21, 29, 30].

Because the impact of TCE on performance losses is being investigated solely, the solar cells were assumed to be ideal in terms of detailed balance theory, because real solar cells have numerous loss mechanisms associated with optical losses (reflection loss, parasitic absorption loss, transmission loss) and electrical losses (charge carrier recombination loss, junction loss)

[128]. Thus, additional series resistances (such as contact resistances) were not taken into account.

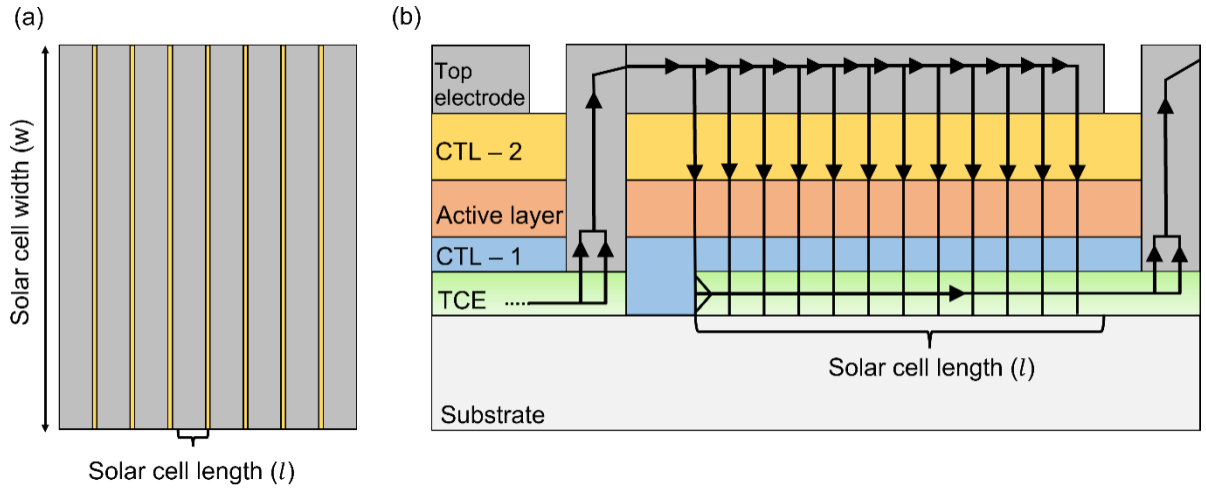

Figure 29: *Schematic of monolithic solar module with serial interconnection (a) top view and (b) cross-section showing the current flow direction within the device and geometric parameters (adapted from reference [40]).*

To calculate the power output, the geometry of the solar cell or module was defined. Since the effect of the sheet resistance entirely depends on the length of the solar cell, a decision must be taken to evaluate TCEs, and for most of the calculations, the solar cell length was taken to be 5 mm long [40, 129, 130]. Furthermore, the solar cell's width was arbitrarily chosen to be 100 mm, which has no bearing on the overall findings because any potential decrease in series resistance is compensated for by photocurrent scaling with the area. More specifically, an increase in width results in a proportionally higher photocurrent but a correspondingly lower series resistance, creating a zero-sum situation for overall power production (refer to the appendix - section 1).

4.1.1 Definition of the exact figure of merit

The established FOM is called exact FOM because it accurately determines the exact losses resulting from the TCE as well as the potential for power conversion efficiency provided by the TCE. The exact FOM is defined as the ratio of the power generated by an ideal solar cell having a bandgap E_G and length l for a particular TCE defined by its spectral transmittance and sheet resistance, to the power generated by the same ideal solar cell with an ideal TCE

(where $R_{\square}$ is for practical reasons set to be 0.0001 Ω/□ and the transmittance throughout the spectral range is 100%):

$$\phi_{TCE,exact} = \frac{P_{MPP}(E_G,T(\lambda),R_S(R_{\square}),l)}{P_{MPP}(E_G,T=100\%\forall\lambda,\, R_{\square}=0.0001\ \Omega/\square,l)},\ [\phi_{TCE,exact}] = \frac{W}{W} = 1 \tag{36}$$

The input parameters are transmittance (T), sheet resistance ($R_{\square}$), bandgap (E_G), and solar cell length (l). The T and $R_{\square}$ are TCE parameters, the E_G is a system-specific parameter, and the l is a free parameter i.e., it is a matter of choice.

4.1.2 Derivation of the exact figure of merit

The short circuit density (J_{sc}), is typically correlated with the number of photons that pass through the transparent conducting electrodes which are used as front contact in the solar cells. Thus, transmittance-induced deviation from the ideal box-shaped external quantum efficiency of the solar cell was considered. The short circuit density is therefore can be obtained by the following equation:

$$J_{SC} = q\int_0^{\lambda_G} T(\lambda)\cdot\phi_{Sun,AM1.5G}(\lambda)d\lambda \tag{37}$$

where q is the elementary charge, λ_G is the wavelength corresponding to the band gap of the solar cell, T is the transmittance spectrum, and $\Phi_{sun,\ AM1.5G}$ is the photon flux density at AM 1.5 global which was extracted using spectral irradiance from NREL ASTM G173-03 and dividing the irradiance at the given wavelength by the energy of the corresponding photon.

According to Planck's law of blackbody radiation, the spectral energy density as a function of wavelength (λ) and temperature (T_K) is given by:

$$B_\lambda(\lambda,T) = \frac{2\pi hc^2}{\lambda^5}\frac{1}{exp(\frac{hc}{\lambda n k_B T_K})-1} \tag{38}$$

where B_λ is the spectral irradiance, h is Planck's constant, c is the speed of light, T_K is the temperature, k_B is the Boltzmann constant, and λ is the wavelength.
Therefore, the blackbody radiation photon flux density can be calculated by dividing the blackbody radiation spectral energy density at the given wavelength by the energy of the corresponding photon.

$$\phi_{BB,300K}(\lambda,T=300K) = \frac{B_\lambda(300K)}{h\nu} = \frac{B_\lambda(300K)}{h\frac{c}{\lambda}} = \frac{B_\lambda(300K)\cdot\lambda}{hc} \tag{39}$$

And, the dark saturation current density (J_0) can be obtained by using the following equation:

$$J_O = q \int_0^{\lambda_G} T(\lambda) \cdot \phi_{BB,300K}(\lambda) d\lambda \quad (40)$$

where q is the elementary charge, λ_G is the wavelength corresponding to the band gap of the solar cell, T is the transmittance spectrum, and $\Phi_{BB,300K}$ is the blackbody radiation photon flux density at 300 K.

The short circuit current (I_{SC}) and the dark saturation current (I_0) can be calculated by using the short circuit density (J_{sc}) and dark saturation current density (J_0) and area (A).

$$I_{SC} = J_{SC} \cdot A \quad (41)$$

$$I_O = J_O \cdot A \quad (42)$$

$$A = l \cdot w \quad (43)$$

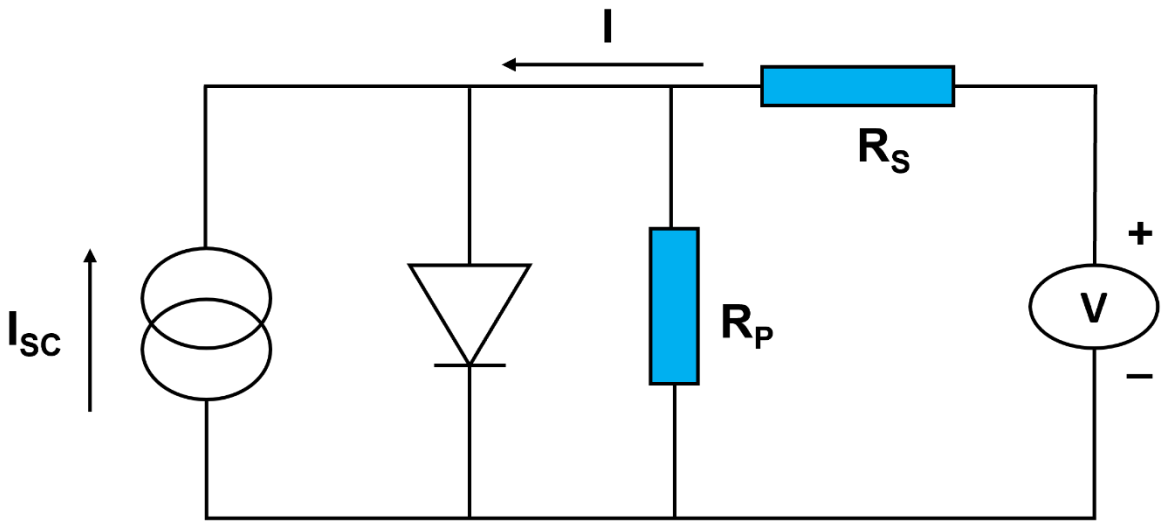

Figure 30: *Equivalent circuit for a solar cell based on the 1-diode model*

Using the self-consistent 1-diode equation based on the implicit Shockley equation the current can be calculated, which is defined as follows [40]:

$$I = I_o \cdot [exp\{\frac{q\,(V - IR_S)}{nk_B T_K} - 1\}] + \frac{V - R_s}{R_P} - I_{SC} \quad (44)$$

where I is the total current, I_{SC} is the short circuit current, I_0 is the dark saturation current, R_S is the series resistance, R_P is the parallel resistance, T_K is the temperature (300 K), k_B is the Boltzmann constant, q is the elementary charge and n is the diode ideality factor (n = 1 for ideal solar cell). The 1-diode equivalent circuit of a solar cell is shown in Figure 30.

Since the parallel resistance is not dependent on the sheet resistance of the electrodes but rather depends on the whole layer stack of the solar cell, the assumption of the ideal solar cell

results in a parallel resistance (R_P) of infinity. Thus, the implicit Shockley equation can be reduced to:

$$I = I_o \cdot [exp\{\frac{q\,(V-IR_S)}{k_B T_K} - 1\}] - I_{SC} \quad (45)$$

As shown by Hoppe *et al.*, the relationship between the series resistance (R_S) and the sheet resistance ($R_\square$) of electrodes can be described as [40]:

$$R_S = R_\square \cdot \frac{l}{3w} \quad (46)$$

where l is the length of the solar cell and w is the width of the solar cell. In this work, a 5 cm^2 cell area (length = 0.5 cm and width = 10 cm) was chosen for the simulation [40, 129, 130].

The power at the maximum power point (P_{MPP}) can be calculated by using voltage (V) and total current (I) and finding the maximum value of their product:

$$P_{MPP} = (V \cdot I)_{max} \quad (47)$$

The power loss within an ohmic resistance is proportional to the current squared passing through it [40]. Therefore, it is defined as follows:

$$P_{Loss} = I^2 \cdot R_S \quad (48)$$

The power conversion efficiency of the solar cells can be calculated using the power at the maximum power point (P_{MPP}) and the input power (P_{in} = 1000 W/cm^2):

$$\eta = \frac{P_{MPP}}{P_{in}} \times 100\% \quad (49)$$

4.1.3 Comparison between the Shockley-Queisser limit and the exact figure of merit efficiency

The maximum theoretical efficiency of solar cells is known as the Shockley-Queisser limit (SQL), often referred to as the detailed balance limit. It is one of the most significant theoretical contributions in the area of photovoltaics and was calculated by Shockley and Queisser in 1961 [131]. The SQ limit of a single-junction solar cell with a cell temperature of 300 K and a black body with a surface temperature of 6000 K was calculated. Five presumptions form the basis of the SQ limit: Only photons with energies greater than the bandgap energy will be absorbed, only radiative recombination occurs, only one electron-hole pair is produced by photons with energies greater than the bandgap energy, thermal

equilibration of the electron system with the environment, contacts are perfectly selective, and there are no ohmic losses inside the solar cell. [131, 132].

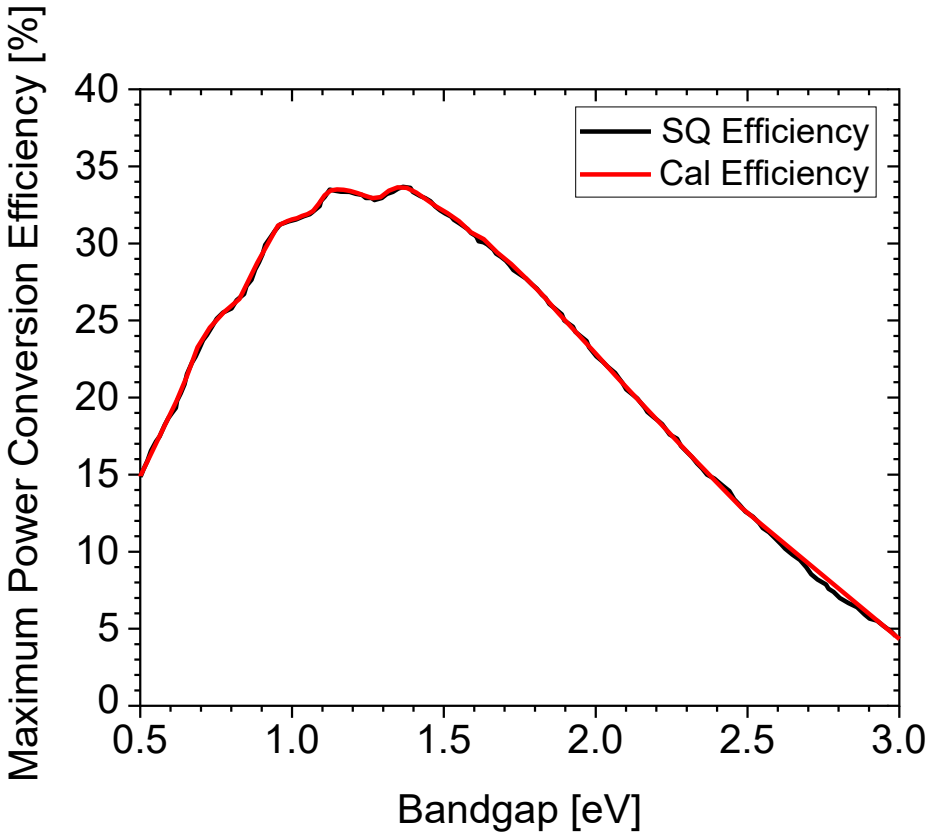

Figure 31: *Maximum PCE vs. bandgap graph [39, 133].*

Compared to SQL, which uses the blackbody spectrum for the calculation of the maximum power conversion efficiency limit, Rühle determined the maximum PCE using the standard AM 1.5 global solar spectrum, which considers scattered light from the atmosphere and is relevant to the majority of PV systems without light concentration. His calculation results in a maximum PCE of 33.7% for a bandgap of 1.34 eV (928 nm) if emission from the rear side of the cell is perfectly stopped by a perfect reflector [133]. Data from Rühle's PCE graph for AM 1.5G illumination was extracted [133] and compared with the calculated efficiency (equation 49) to verify the accuracy of the calculation for the exact FOM. As seen in Figure 31, the calculated efficiency curve overlaps well with the SQL power conversion efficiency as calculated by Rühle *et al.*, which indicates that the proposed calculation for the FOM was formulated correctly, normalized to the SQ Limit, and linear to the attainable photovoltaic power.

4.1.4 Assessment of different figures of merit

The exact FOM was compared with the different established FOMs as defined in the introduction section 2.5.

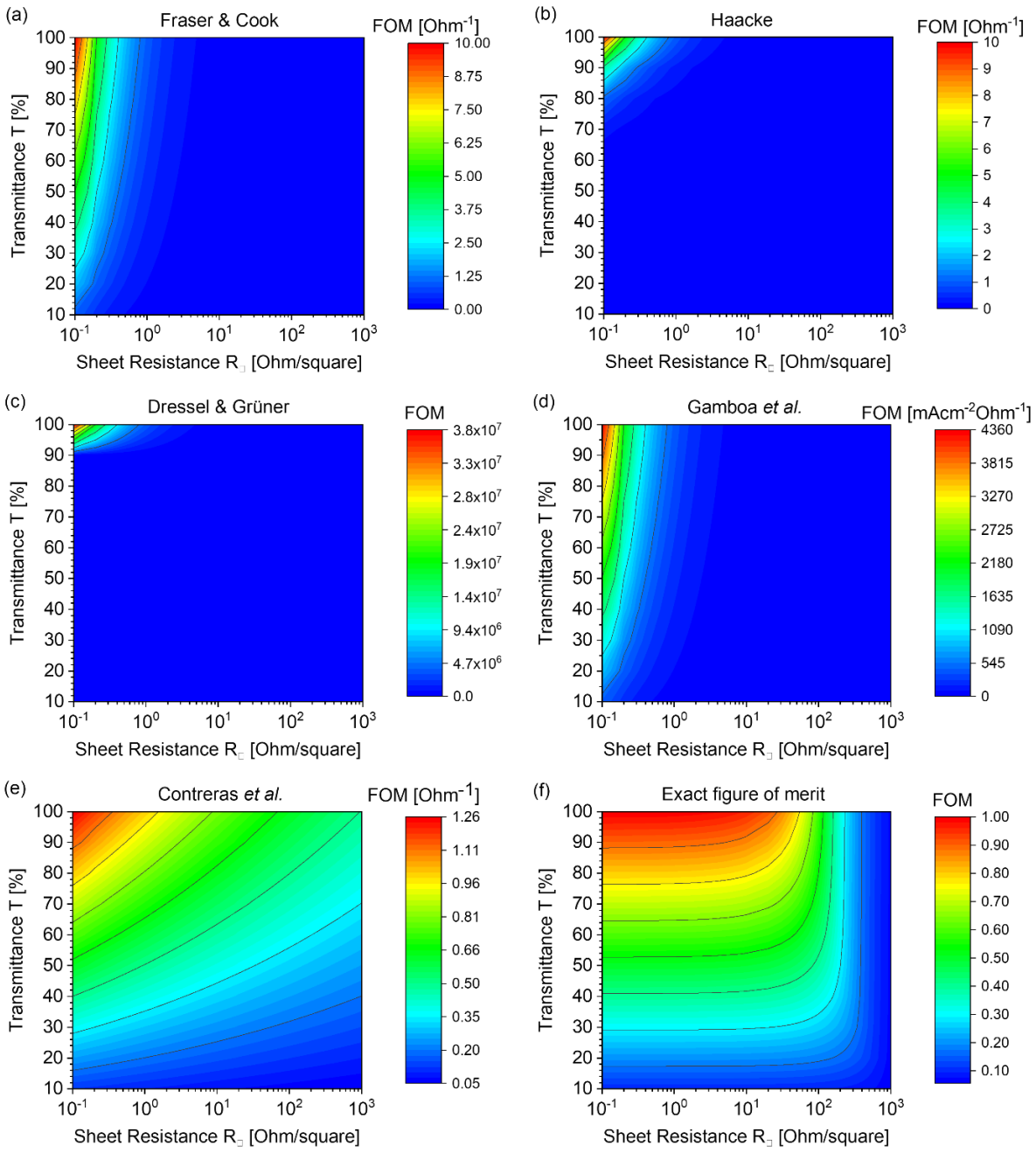

Figure 32: *Comparison of the exact calculation for the impact of transmittance and sheet resistance on PV performance for the spectral range from 280 to 1100 nm and a solar cell length of 5 mm, according to the following established figures of merit: (a) Fraser & Cook, (b) Haacke, (c) Dressel and Grüner, (d) Gamboa et al., (e) Contreras et al.(n = 10), and (f) exact FOM.*

A simulation was performed for hypothetical TCEs with transmittances ranging from 10 to 100% (over the spectral range from 280 to 1100 nm) and sheet resistances ranging from 0.1 to 1000 Ω/□. Figure 32 displays contour plots that allow a preliminary comparison of the various FOM proposed by (a) Fraser & Cook, (b) Haacke, (c) Dressel and Grüner, (d) Gamboa *et al.*, (e) Contreras *et al*. (n = 10), and (f) exact FOM. The contour plots clearly illustrate that FOMs (a) to (d) exhibit a strong dependence on the sheet resistance, but FOMs (e) and (f) show less dependence.

For FOM (a) to (d) (Fraser & Cook, Haacke, Dressel & Grüner, Gamboa *et al.*), the gap between "the standard values" for TCEs (transmittance - 90% and sheet resistance - 100 Ω/□) and the ideal value (transmittance - 100% and sheet resistance -0.0001 Ω/□) was huge whereas FOM (e) (Contreras *et al.*) demonstrated only a factor of two between the same. The exact FOM (f) captures the correct balance of effects between transmittance and sheet resistance of TCEs due to the complexity of the computation by design, which is also demonstrated by a linear dependence on transmittance over the majority of the $R_{\square}$ range. For convenience, a double logarithmic plot was also used to compare the figures of merit (Figure A1).

The different FOM values were replotted in a cross-section for transmittance of 90%, which is practically both a desirable and an (almost) feasible number, for an improved understanding of the dependencies of the various FOMs on the sheet resistance. Figure 33 shows the comparison of figures of merit on a double logarithmic plot. It should be noticed that the double logarithmic plot exhibits the same trend for FOMs (a) to (d) For an equal change in sheet resistance, they span a range of five orders of magnitude, although they are offset from one another by certain pre-factors. Since they are all proportional to $1/R_{\square}$ and only differ in their proportionality factor, this is not surprising.

The FOM (e) proposed by Contreras *et al.*, in contrast to these, has only very modest reliance on the sheet resistance and varies by less than one order of magnitude. A comparison with the exact FOM shows that for values of sheet resistance above 100 Ω/□, the functional dependency of the FOMs (a) - (d) is in good agreement, while for values below 100 Ω/□, the FOM (e) by Contreras *et al.* is exhibiting a great agreement even for the absolute value.

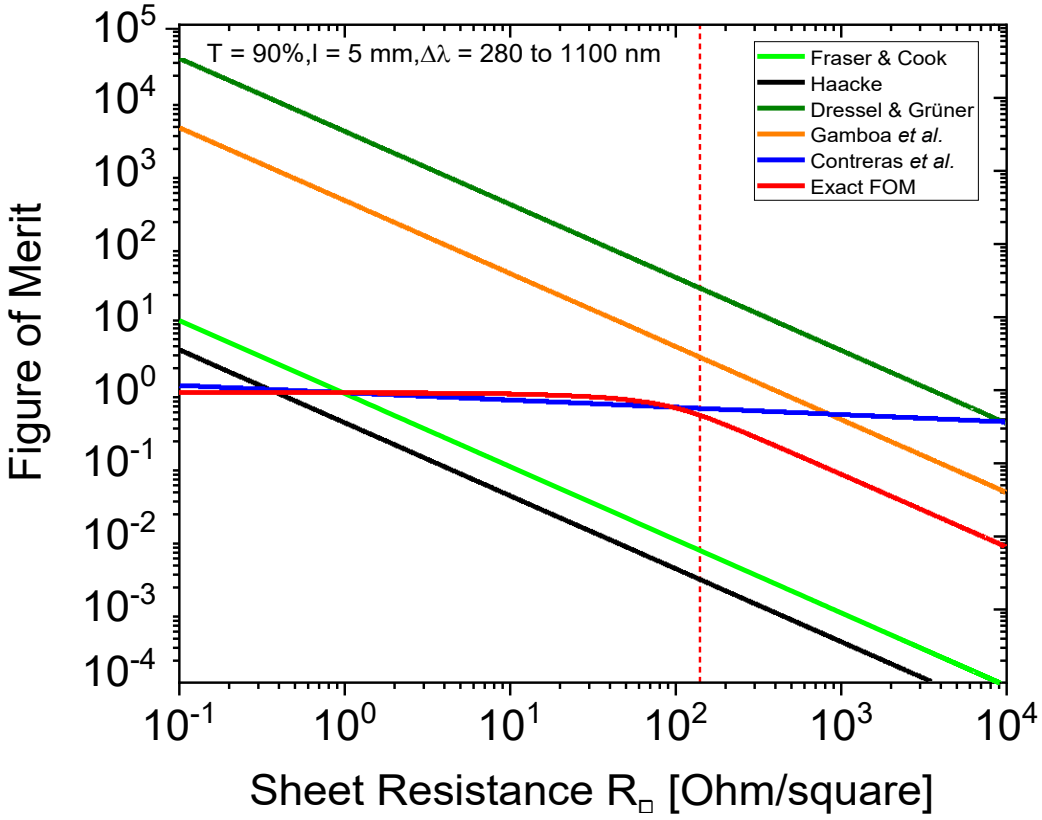

Figure 33: *Evaluation of established figures of merit against sheet resistance for a hypothetical TCE that considers the entire spectrum and has a transmittance of 90% (280 to 1100 nm).*

To characterize the abrupt change in the behavior of the exact FOM i.e., the exhibition of a deflection point, critical sheet resistance ($R_{□,c}$) was defined at which half the maximum value of the achievable performance may be achieved and where the function changes in curvature. Due to the simplicity of the formulas, none of the other FOMs accounted for this distinct change in behavior, which is located at 140 Ω/□ (Figure 34). The critical sheet resistance (R,c) can be crucial information for material scientists since it shows whether a material system is acceptable for a specific solar cell length (l) and whether the interesting region of conductivity is within easy reach. The comparison for additional hypothetical TCEs with varying transmittance values is shown in Figure A2 (a-j) of the appendix. The critical sheet resistance values for different transmittances are shown in Figure 35.

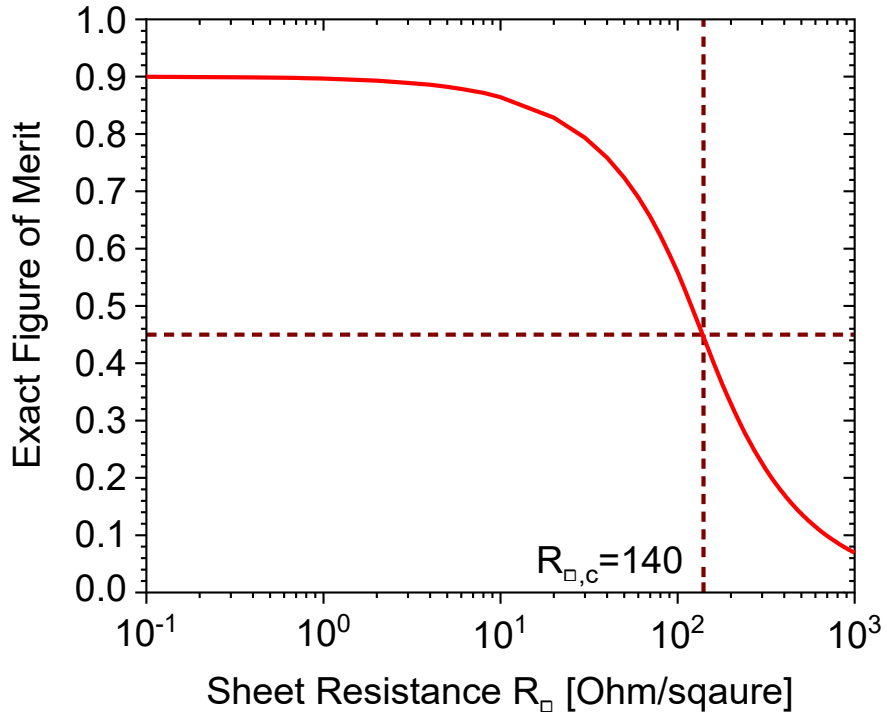

Figure 34: *Exact FOM vs. sheet resistance for TCE with a spectral transmittance of 90% from 280 to 1100 nm and a solar cell length of 5 mm.*

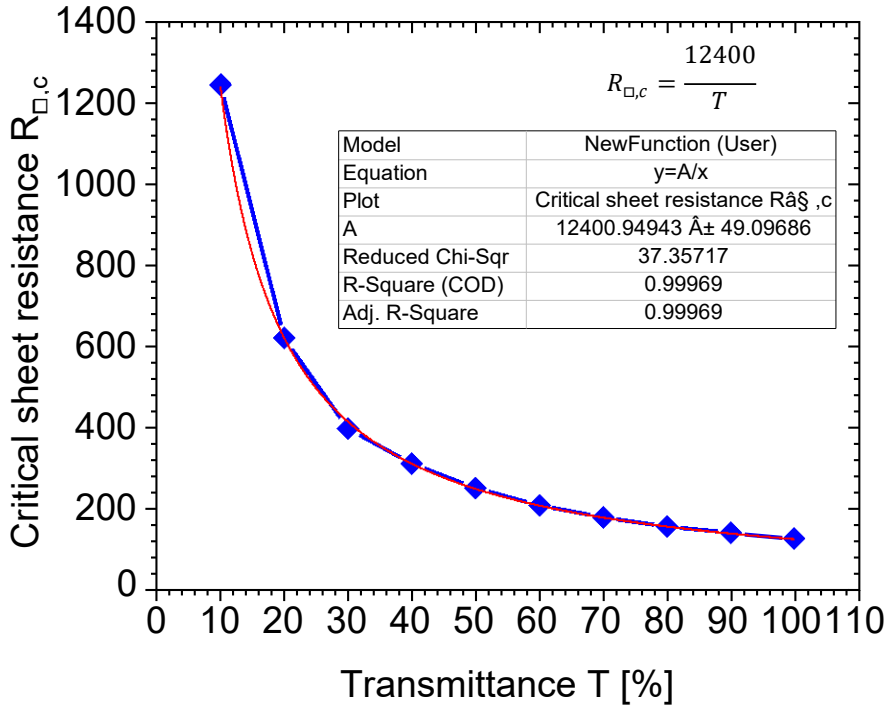

Figure 35: *Critical sheet resistance vs. transmittance for TCE for the spectral range of 280 to 1100 nm and a solar cell length of 5 mm.*

4.1.5 Transition and target sheet resistance

Intrigued by the FOM (e) proposed by Contreras *et al.* to closely follow the exact FOM calculation, a short optimization for an even better suitable parameter 'n' in the formula of Contreras *et al.* was carried out. It was found that n = 100 was sufficiently close to the ideal after a brief optimization process to match the actual computation (see Figure 36).

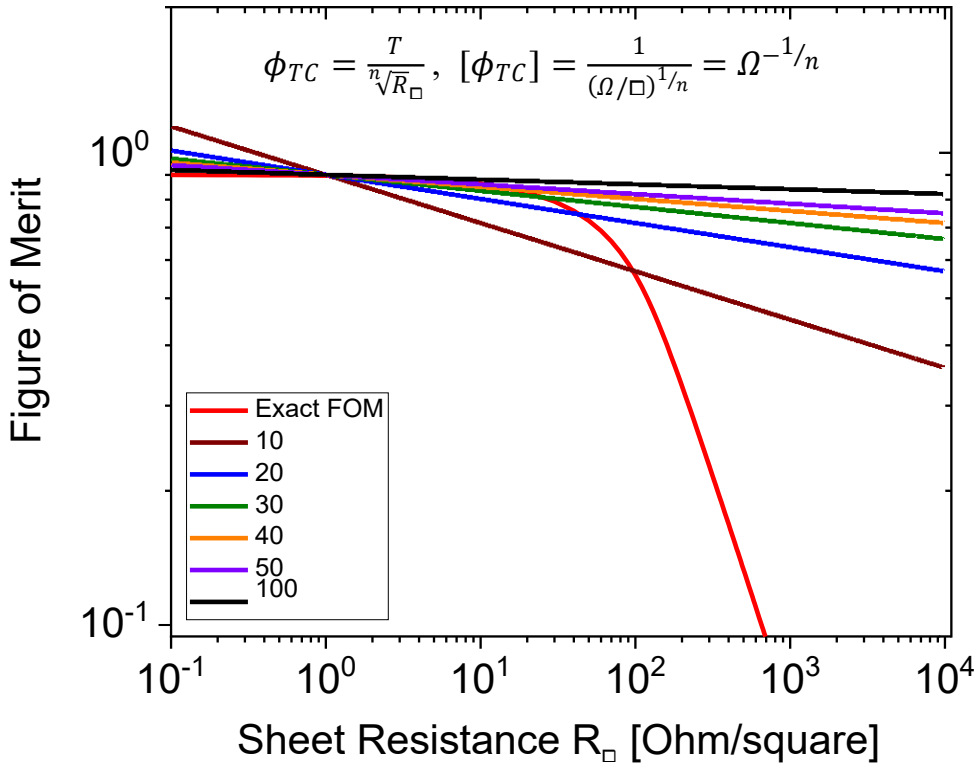

Figure 36: *FOM vs. sheet resistance for TCE with a transmittance of 90% over the spectral range of 280 to 1100 nm and a solar cell length of 5 mm. Contreras et al. FOM with various n values.*

It was possible to construct the established FOMs as tangents to the exact FOM using this modified FOM (Contreras *et al.*) and by renormalizing FOMs (Fraser & Cook, Haacke, Dressel & Grüner, Gamboa *et al.*) to the exact calculation. Another interesting transition region was identified, which is termed transition sheet resistance (θR□) which clearly distinguished the transmittance and sheet resistance limit regimes. As seen in Figure 37, it was observed that above the transition sheet resistance, the validity of FOM (Contreras *et al.*) was declining and all of the renormalized FOMs (Fraser & Cook, Haacke, Dressel & Grüner, Gamboa *et al.*) closely followed the exact calculation.

By taking the crossing point between renormalized FOMs (Fraser & Cook, Haacke, Dressel & Grüner, Gamboa *et al.*) and FOM by Contreras *et al.*, the transition sheet resistance ($\theta R_{\square}$) was determined to be 80 Ω/□ for the hypothetical situation of a solar cell with an absorption range of 280 to 1100 nm, a length of 5 mm, and TCE with a transmittance of 90% over the entire spectral range.

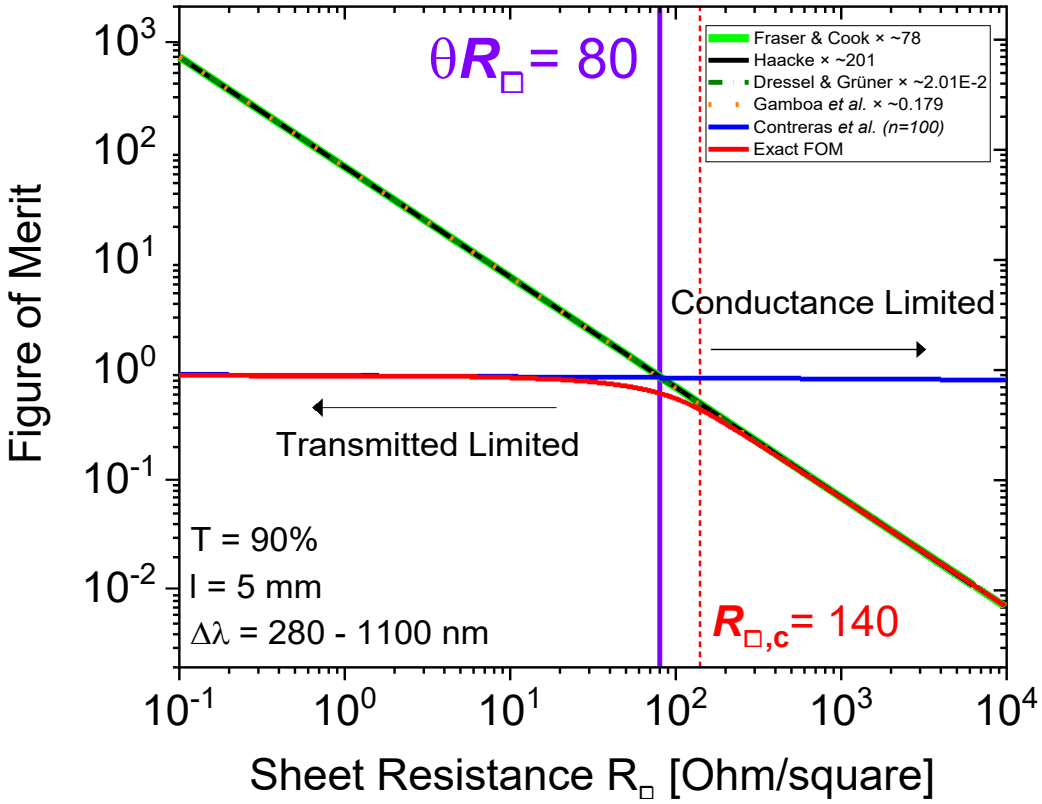

Figure 37: *Definition of the transition sheet resistance (θR□), which separates the regions: transmitted and conductance limit. The calculation was done for a hypothetical TCE having a transmittance of 90% throughout the spectrum considered (280 to 1100 nm) and a solar cell length of 5 mm.*

To show the critical dependency of solar cell geometry, the solar cell length varied between 2.5 and 20 mm, and the transition sheet resistance was assessed as previously said for a TCE with 90% transmittance over the spectral range from 280 to 1100 nm to learn more about the functional dependency of the transition sheet resistance. The findings are shown in the appendix (Figure A3 (a-d)), which already shows a strong dependence of θR□ on the length of the solar cell.

To find an analytical description of the FOM in the conductance limited regime, a solar cell which is entirely constrained by the series resistance was taken into account. A series resistance limited (SRL) condition is shown in Figure 38, where series resistance (R_S) determines the form of the IV characteristics in the fourth quadrant.

It is now easy to note down the power output of such a device. Since in general:

$$R_S = \frac{\Delta V}{\Delta I} \tag{50}$$

is true, in this case, this can be identified as follows:

$$R_S = \frac{V_{OC} - 0}{0 - (-I_{SC})} = \frac{V_{OC}}{I_{SC,SRL}} \tag{51}$$

where V_{OC} is the open circuit voltage, which is basically independent of the series resistance and only determined by the illumination intensity, and $I_{SC,SRL}$ is the short circuit current, which is fully limited by the series resistance.

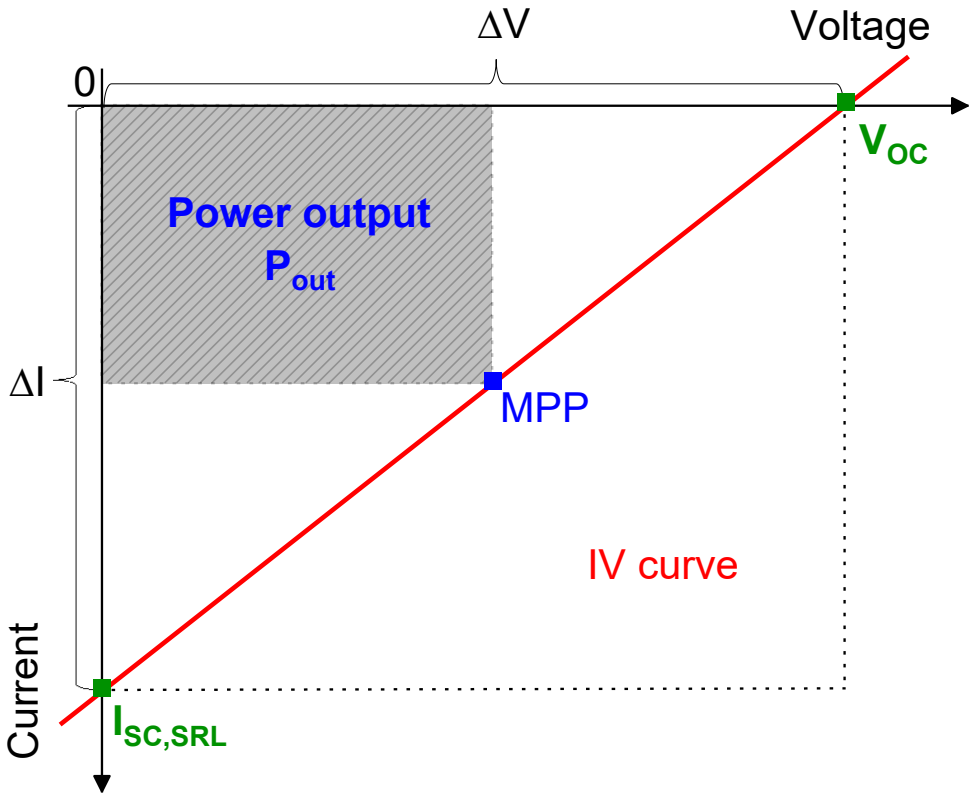

Figure 38: *Series resistance limited (SRL) current-voltage characteristics in the 4th quadrant are shown. In this case, the short circuit current $I_{SC,SRL}$ directly depends on the series resistance (as shown in the text), and the FF is strictly 25%.*

And since the series resistance is a function of the sheet resistance, it can be described as follows [40]:

$$R_S = R_{\square} \cdot \frac{l}{3w} \tag{52}$$

with l and w being the length and the width of the solar cell, the power output of the solar cell under SRL can be obtained as follows:

$$P_{MPP,SRL} = I_{SC} \cdot V_{OC} \cdot FF = \frac{V_{OC}}{R_{\square} \cdot \frac{l}{3w}} \cdot V_{OC} \cdot 25\% = \frac{3}{4} \cdot \frac{w}{l} \cdot \frac{{V_{OC}}^2}{R_{\square}} \tag{53}$$

The FF is strictly 25% in the particular situation with series resistance limited IV characteristics, also known as conductance limitation (compare with Figure 38). And hence it is possible to get the approximate FOM under the SRL regime:

$$\phi_{TCE,SRL} = \frac{P_{MPP,SRL}}{P_{MPP,SQL_{AM1.5}}} \tag{54}$$

whereas for the transmittance limited (TL) regime, the average transmittance over the PV active spectrum was merely selected as an estimate (due to the normalization of the precise FOM):

$$\phi_{TCE,TL} = T_{avg} \tag{55}$$

where Tavg is the average transmittance throughout the photovoltaic active spectrum.

The transition sheet resistance ($\theta R_{\square}$) may now be defined as the one point that is shared by the transmittance and conductance limited regimes using these definitions for an approximation of the FOM:

$$\phi_{TCE,TL} = T_{avg} \overset{!}{=} \phi_{TCE,SRL} = \frac{P_{MPP,SRL}(R_{\square}=\theta R_{\square})}{P_{MPP,SQL_{AM1.5}}} \tag{56}$$

$$\Leftrightarrow T_{avg} = \frac{3}{4} \cdot \frac{w}{l} \cdot \frac{{V_{OC}}^2}{\theta R_{\square}} \cdot \frac{1}{I_{SC,max} \cdot V_{OC} \cdot FF_{max}} \tag{57}$$

$$\Leftrightarrow \theta R_{\square} = \frac{3}{4} \cdot \frac{w}{l} \cdot \frac{1}{T_{avg}} \cdot \frac{V_{OC}}{I_{SC,max} \cdot FF_{max}} \tag{58}$$

$$\Leftrightarrow \theta R_{\square} = \frac{3}{4} \cdot \frac{w}{l} \cdot \frac{1}{T_{avg}} \cdot \frac{V_{OC}}{w \cdot l \cdot J_{SC,max} \cdot FF_{max}} \tag{59}$$

$$\Leftrightarrow \theta R_{\square} = \frac{3}{4} \cdot \frac{1}{l^2} \cdot \frac{1}{T_{avg}} \cdot \frac{V_{OC}}{J_{SC,max} \cdot FF_{max}} \tag{60}$$

where $J_{SC,max}$, $V_{OC,}$ and FF_{max} are to be taken from the calculation in the SQL for AM 1.5G for the corresponding bandgap of the solar cell considered.

Figure 39 shows the functional relationship between the transition sheet resistance and solar cell length (varying from 2.5 to 20 mm) with an average transmittance of 90%. Clearly, equation 60 shows that shorter solar cell lengths provide significantly larger transition sheet resistances. This conclusion underlines once again how crucial device geometry is, or in this case, how much the length of the solar cell affects the changeover between the conductance and transmittance limited regimes.

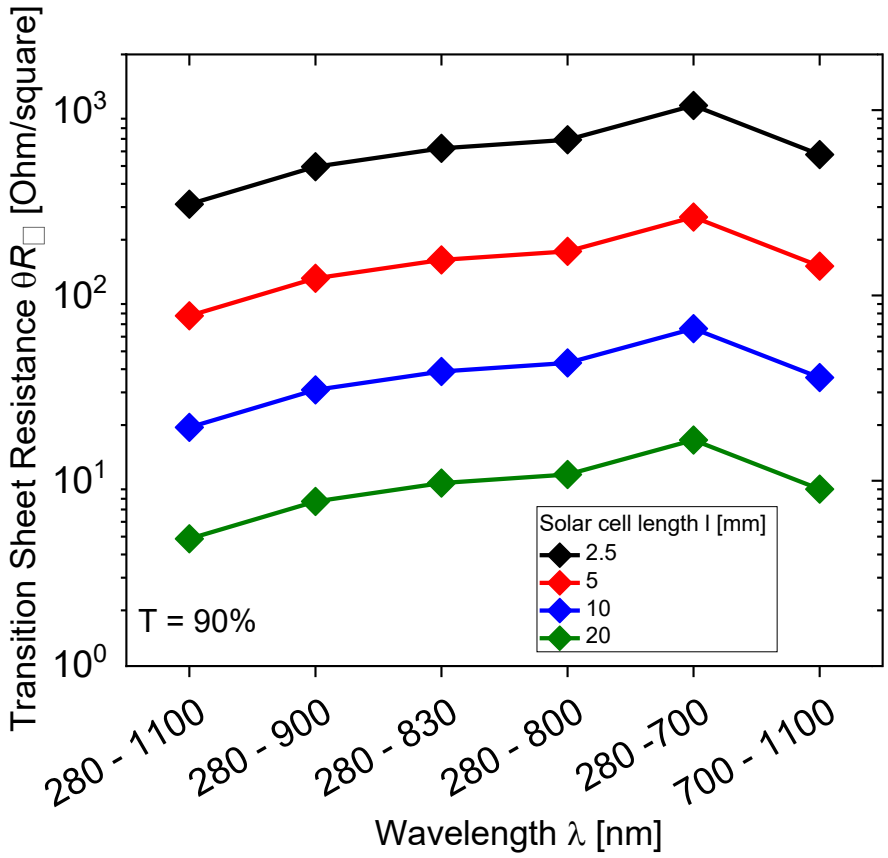

Figure 39: *Functional dependence of TCE's 90% overall spectral transmittance on the length of the solar cell for the transition sheet resistance ($\theta R_{\square}$).*

Since the transition sheet resistance yields only about two-thirds of the attainable FOM, a thumb rule was introduced for aiming the practical sheet resistance under a given set of PV-parameters (in this case $J_{SC,exp}$, FF_{exp}, $V_{OC,exp}$ are to be taken) for a given average transmittance T_{avg}, limiting additional losses due to a finite sheet resistance to about 5% and less. Thus, the target resistance was defined as:

$$R_{\square,target} < \frac{1}{6}\theta R_{\square} = \frac{1}{8} \cdot \frac{1}{l^2} \cdot \frac{1}{T_{avg}} \cdot \frac{V_{OC,exp}}{J_{SC,exp} \cdot FF_{exp}} \quad (61)$$

Target resistance ($R_{\square, target}$) can be thought of as a development objective. In other words, for a particular transmittance, the target sheet resistance designates the value below which relative TCE-related losses are within 5% of the ideal sheet resistance.

4.1.6 Approximate figure of merit

Based on the above calculations, a simplified version of the exact FOM (approximate FOM) may be readily derived. At the point of $\theta R_{\square}$ the descriptions of FOM for the two regimes coincide, and thus the FOM equals both the transmittance as well as a reciprocal function with regards to sheet resistance ($R_{\square}$):

$$T_{avg} = \phi_{TCE,TL}(\theta R_{\square}) \overset{!}{=} \phi_{TCE,SRL}(\theta R_{\square}) = \frac{A}{\theta R_{\square}} \quad (62)$$

$$\Leftrightarrow A = T_{avg} \cdot \theta R_{\square} \quad (63)$$

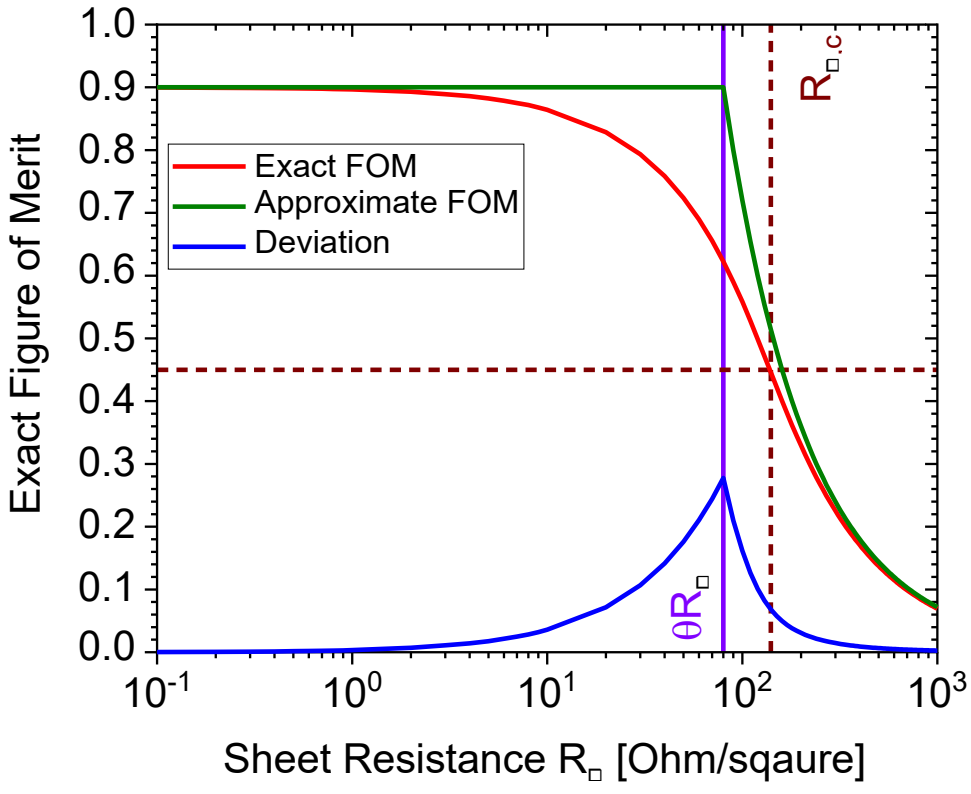

Figure 40: *Comparison of exact and approximate FOM and the deviation between them. The calculation was done for a hypothetical TCE having a transmittance of 90% throughout the spectrum considered (280 to 1100 nm) and a solar cell length of 5 mm.*

Thus, the simplified function of the exact FOM, i.e., the approximate FOM, can be defined as follows:

$$\phi_{TCE} = \begin{cases} T_{avg} & \forall\ R_{\square} < \theta R_{\square} \\ T_{avg} \cdot \frac{\theta R_{\square}}{R_{\square}} & \forall\ R_{\square} > \theta R_{\square} \end{cases} \quad (64)$$

where T_{avg} is the average transmittance, $\theta R_{\square}$ is the transition sheet resistance, and $R_{\square}$ is the sheet resistance.

Figure 40 shows the comparison of exact FOM and approximate FOM and the deviation between them. The appealing aspect of this straightforward method is that it simply needs the average transmittance and PV parameters that have been obtained by experiment, together with a choice of solar cell length, to compute $\theta R_{\square}$ in accordance with equation 60.

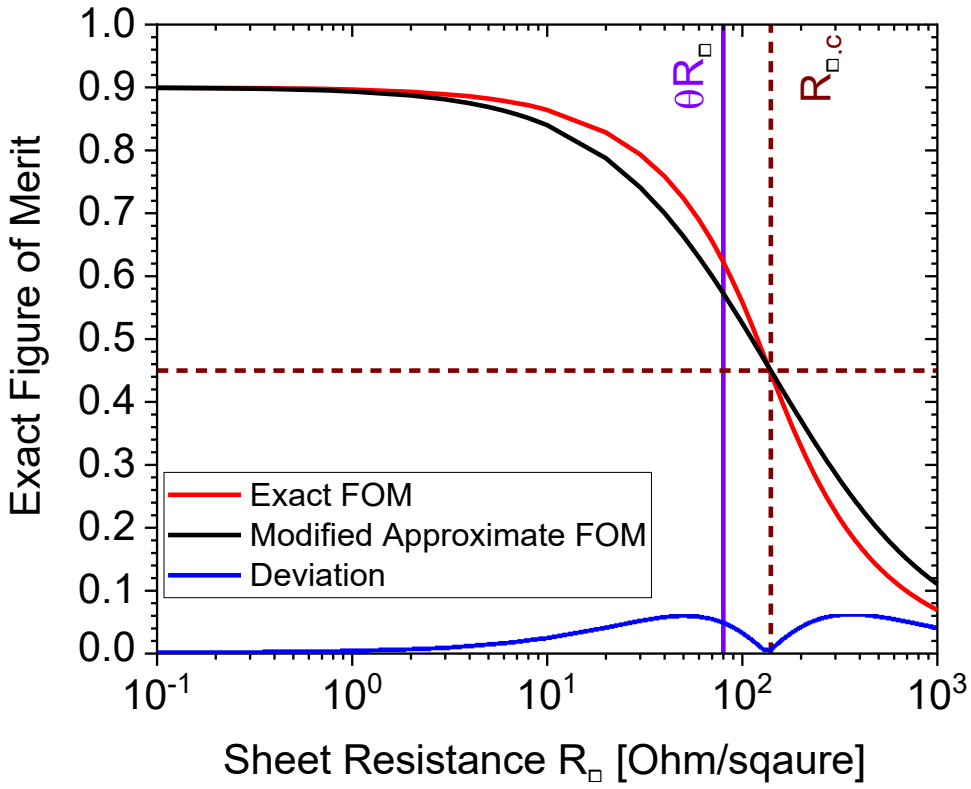

Figure 41: *Comparison of exact and modified approximate FOM and the deviation between them. The calculation was done for a hypothetical TCE having a transmittance of 90% throughout the spectrum considered (280 to 1100 nm) and a solar cell length of 5 mm.*

To ease the calculational effort by looking at the symmetry of the exact FOM curve. The approximate FOM was modified and compared with the exact FOM (Figure 41). A reduction

in the deviation from the exact FOM was observed. The work to reduce the deviation even more to the approximate form is still in process.

$$\phi_{m,TCE} = T\ [1 - \frac{1}{\frac{R_{\square,G}}{R\square}+1}] \quad (65)$$

4.1.7 Evaluation of the requirements for a photovoltaic material system

Various material systems were examined with regard to their maximum PV characteristics under AM1.5G in the Shockley-Queisser-Limit (SQL) since solar cells based on different PV material systems will exhibit different requirements regarding the TCEs. According to their electronic bandgap, maximal SQL AM1.5G performance, and range of absorption wavelengths, Table 2 summarizes the parameters of most PV material systems.

Table 2: *Different PV material systems and their characteristics.*

Photovoltaic material systems	**Wavelength range** $\Delta\lambda$ **[nm]**	**Bandgap [eV]**	**Efficiency SQL AM 1.5G [%]**
c-Si, m-Si, nc-Si, CIGS, CZTS	280 – 1100	1.13	33.4
GaAs, CdTe, InP, PbS QD	280 – 900	1.38	33.6
Dye/TiO2 (DSSC)	280 – 830	1.49	32.2
typical OPV, Perovskite	280 – 800	1.55	31.4
a-Si, GaInP	280 – 700	1.77	27.7
AgrOPV (OPV for Agrivoltaics)	700 – 1100	1.13	17.4

PV systems with spectral wavelengths ranging from 280 to 1100 nm include crystalline silicon (C-Si), monocrystalline solar cells (m-Si), copper zinc tin sulfide (CZTS), and copper indium gallium selenide solar cells (CI(G)S), which are among the reported high-efficiency solar cells [134, 135]. The spectral wavelength range from 280 to 900 nm includes thin-film semiconductors, multijunction solar cells such as gallium arsenide solar cells (GaAs), cadmium telluride solar cells (CdTe), as well as indium phosphide (InP), and lead sulfide

quantum dots (PbS QD) PV systems [135]. A Dye-sensitized solar cell (DSSC), a third-generation PV system, falls under the spectral wavelength range of 280 to 830 nm. The spectral wavelength range from 280 to 800 nm includes OPV and hybrid perovskites, which are emerging PV systems [21, 134]. The spectral wavelength range from 280 to 700 nm includes amorphous silicon solar cells (a-Si) and the gallium indium phosphide (GaInP) material system [135]. The material system that is specifically suited for agrivoltaics was named "AgrOPV" (OPV for agrivoltaics), since it may be possible to achieve it because organic semiconductors have the very distinctive ability to exhibit limited absorption bands. When the latter is tuned into the near-infrared (NIR) region (700 to 1100 nm), the light absorption of plants is unaffected [136].

All PV parameters were computed based on the SQL at AM1.5G conditions and are shown in Table 3 and Figure 42. These values can be used to determine the transition sheet resistance for the relevant TCE system.

Table 3: *Solar cell parameters for different spectral ranges.*

Wavelength range [nm]	**Short circuit current density J_{SC}** [mA/cm²]	**Open circuit voltage V_{OC}** [mV]	**Fill factor FF** [%]	**Maximum power point P_{MPP}** [mW]	**Dark saturation current density J_0** [mA/cm²]	**Power loss P_{loss}** [mW/cm²]
280 – 1100	43.52	883	87.04	33.45	6.4E-12	1.49E-05
280 – 900	33.74	1117	89.17	33.61	5.89E-16	9.05E-06
280 – 830	29.18	1225	89.93	32.15	7.73E-18	6.75E-06
280 – 800	27.27	1277	90.29	31.44	9.52E-19	5.92E-06
280 – 700	20.44	1484	91.38	27.71	2.37E-22	3.36E-06
700 – 1100	23.08	867	86.83	17.37	6.4E-12	4.14E-06

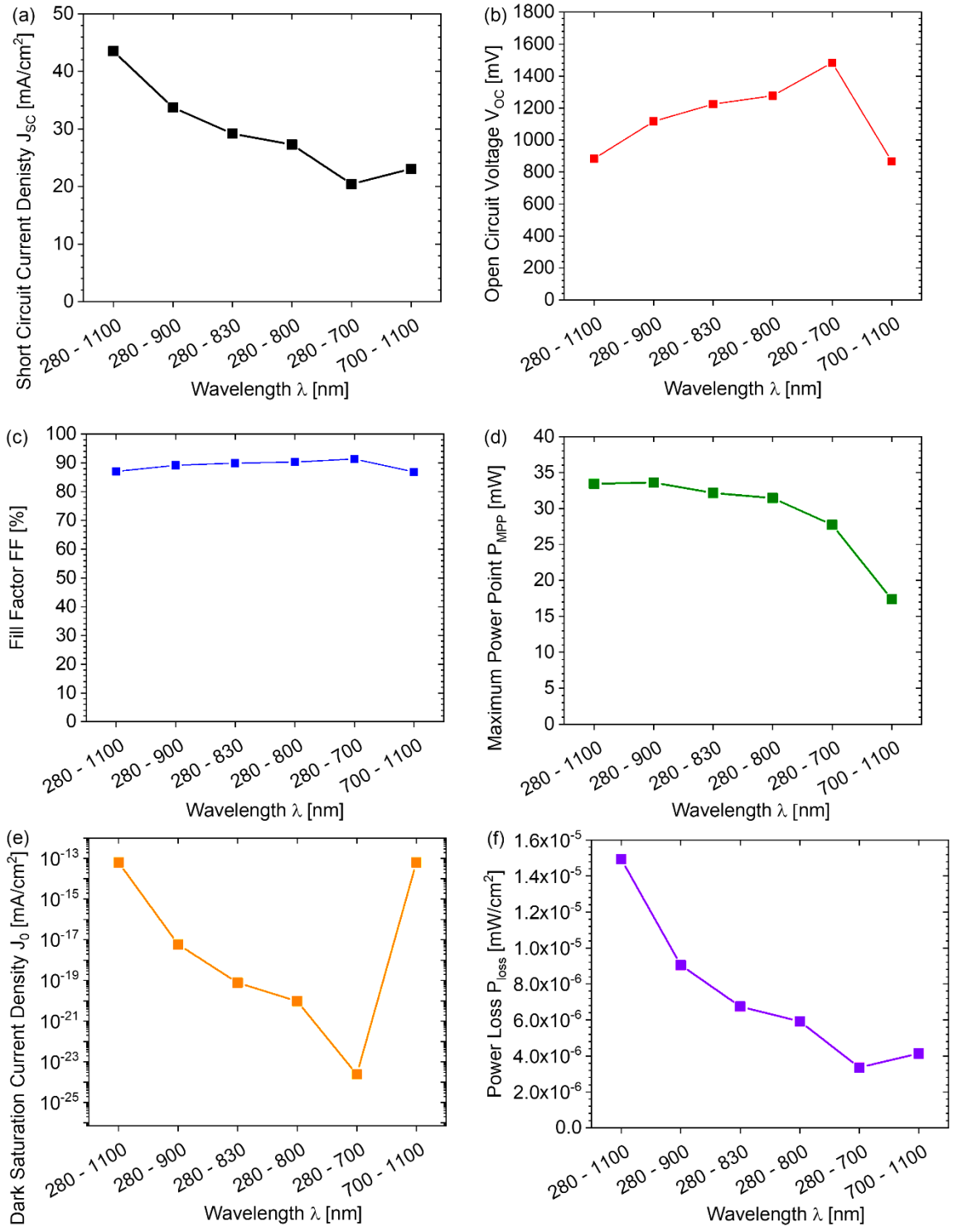

***Figure 42**: Different PV material systems' absorption wavelength range in relation to (a) short circuit current density, (b) open circuit voltage, (c) fill factor, (d) maximum power point, (e) dark saturation current density, and (f) power loss in the Shockley-Queisser limit (SQL) under AM 1.5G illumination.*

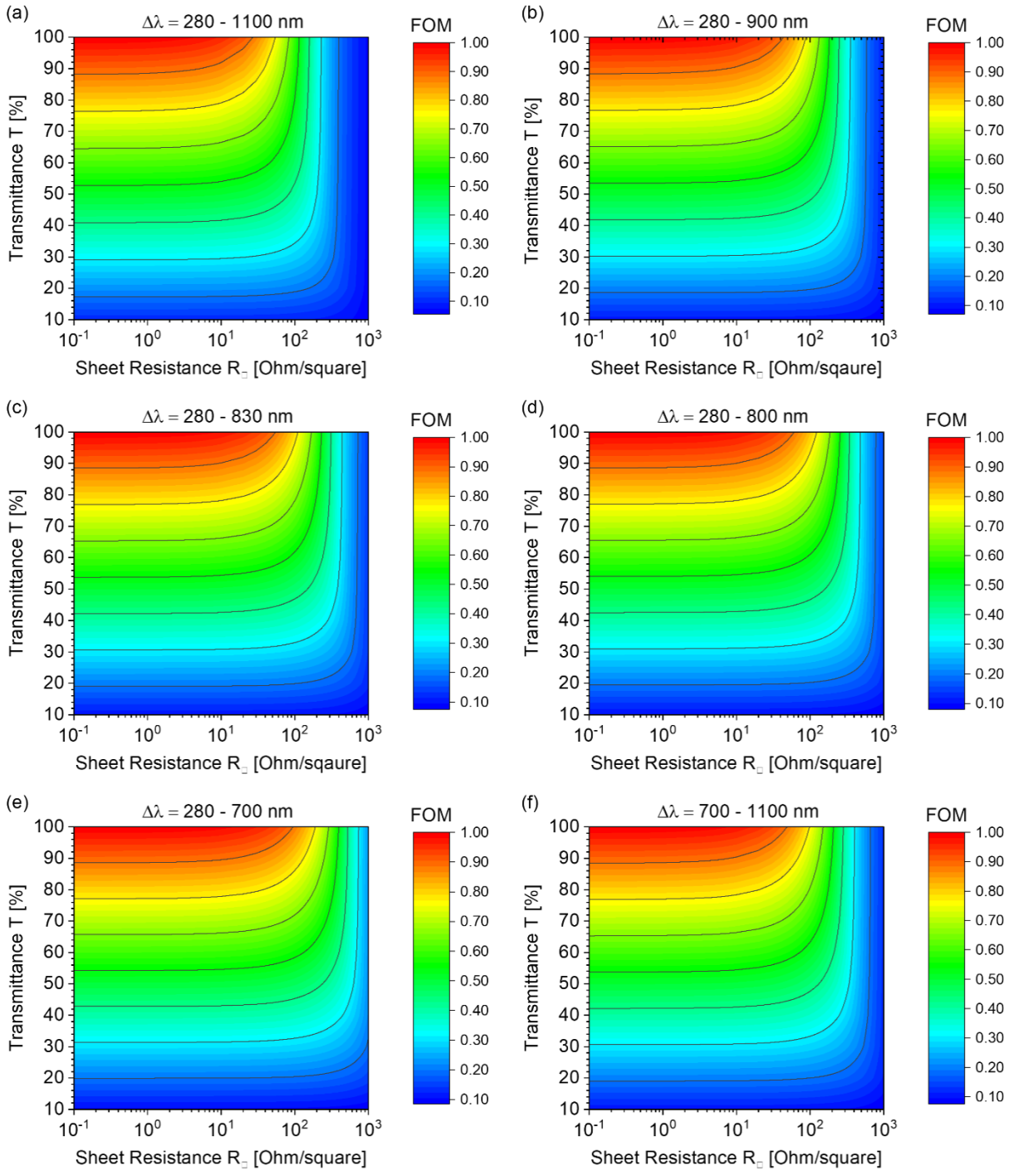

Figure 43: *Contour plot of the exact FOM for (a) C-Si, m-Si, nc-Si, CIGS, CZTS (280 to 1100 nm), (b) GaAS, CdTe, InP, PbS QD (280 to 900 nm), (c) Dye/TiO2 (DSSC) (280 to 830 nm), (d) OPV, Perovskite (280 to 800 nm), (e) a-Si, GaInP (280 to 700 nm), and (d) AgrOPV (OPV for Agrivoltaics) (700 to 1100 nm) solar cells for combinations of the transmittance and the sheet resistance.*

Figure 43 shows the contour plots for the exact FOM for combinations of transmittance and sheet resistance for various PV material systems. The exact FOM was plotted over the sheet resistance for several PV materials for a TCE with a transmittance of 90% across the spectral range in order to clearly comprehend the impact of the bandgap of different PV material systems (see Figure 44). Higher sheet resistances may be attainable because smaller absorption ranges lead to larger bandgaps, which in turn lead to smaller photocurrents and lower sheet resistance needs. Figure 44 also shows the critical sheet resistance, which is calculated at a transmittance value of half the average (0.45), as well as the threshold FOM for the target sheet resistance, which is 0.85 in the case of 90% transmittance.

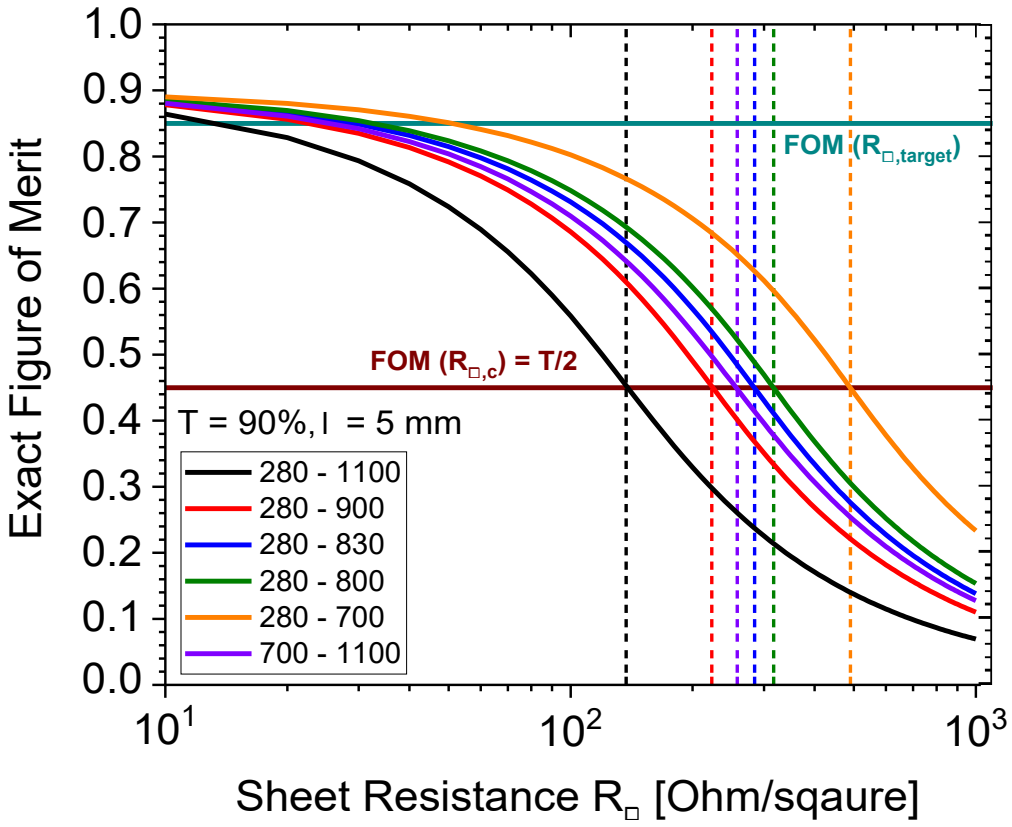

Figure 44: *Exact FOM vs. sheet resistance computed for different PV material systems, having a transmittance T = 90% throughout the spectral range and a solar cell length of 5 mm. Furthermore, the critical sheet resistance is evaluated, and the FOM for the target sheet resistance is depicted as well.*

Table 4 shows the critical sheet resistance ($R_{\square,c}$), transition sheet resistance ($\theta R_{\square}$), and target sheet resistance ($R_{\square}$, target) as determined by equations 60 and 61, respectively. The target sheet resistance is defined considerably more freely and serves a more useful function than the critical and transition sheet resistances, which were first introduced through useful mathematical formulations. It is intended to serve as guidance for researchers when designing TCEs for a certain PV material system. The calculational effort is significantly less than for the exact FOM because experimentally known PV characteristics can be used to predict sheet resistance requirements to reduce conductivity-related losses to less than 5%.

Table 4: *Critical, transition, and target sheet resistances are summarized for the different PV material systems defined according to their bandgap and spectral absorption range. The transmittance was assumed to be 90% throughout the spectral range, and the solar cell length was 5 mm.*

Photovoltaic material systems	**Wavelength range** [nm]	**Critical sheet resistance $R_{\square,c}$** [Ω/□]	**Transition sheet resistance $\theta R_{\square}$** [Ω/□]	**Target sheet resistance $R_{\square,Target}$** [Ω/□]
c-Si, m-Si, nc-Si, CIGS, CZTS	280 – 1100	138.6	77.7	13.0
GaAs, CdTe, InP, PbS QD	280 – 900	224.9	123.7	20.6
Dye/TiO2 (DSSC)	280 – 830	281.7	155.7	25.9
OPV, Perovskite	280 – 800	316.3	173.1	28.8
a-Si, GaInP	280 – 700	487.7	265.2	44.2
AgrOPV (OPV for Agrivoltaics)	700 – 1100	255.0	144.1	24.0

4.1.8 Evaluation of state-of-the-art transparent conductive electrodes by the exact figure of merit

As mentioned in Section 2.6, different TCEs have been recommended for use in solar cells. In order to evaluate the performance of various electrodes, recent novel TCE data were extracted from the literature, and their performances were rated based on existing FOMs and the exact FOM. Figure 45 shows the sheet resistance values of the various TCEs tested in this study, while Figure 46 shows the transmittance spectra of the TCEs divided into several subgroups, respectively.

Note: Transmittances beyond 90% should be regarded with care, however, as the already-bare glass substrate only provides a maximum transmittance of 92% owing to inescapable reflectance losses. Experimentally, anti-reflection coatings are to be used to produce greater transmittances. Transparency losses from glass were added in situations where transmittance was exceptionally high in order to allow for a comparison study between the various TCEs. Figure A4 shows the transmittance spectrum of bare glass.

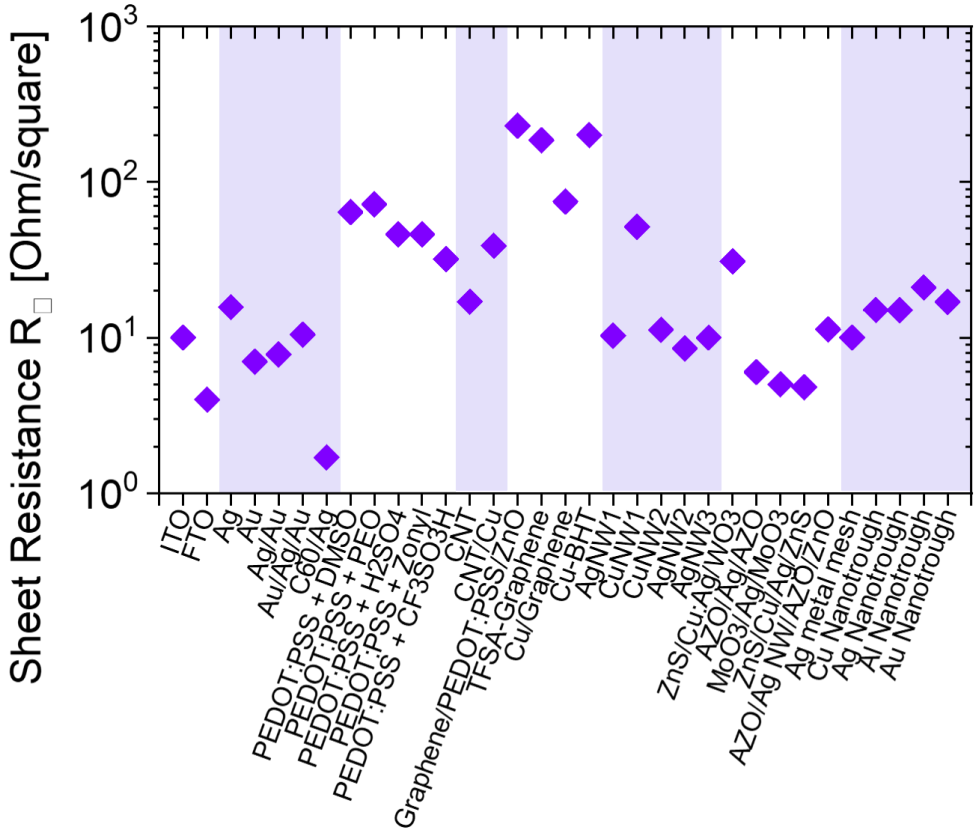

Figure 45: *Summary of sheet resistance values for different TCEs evaluated in this work.*

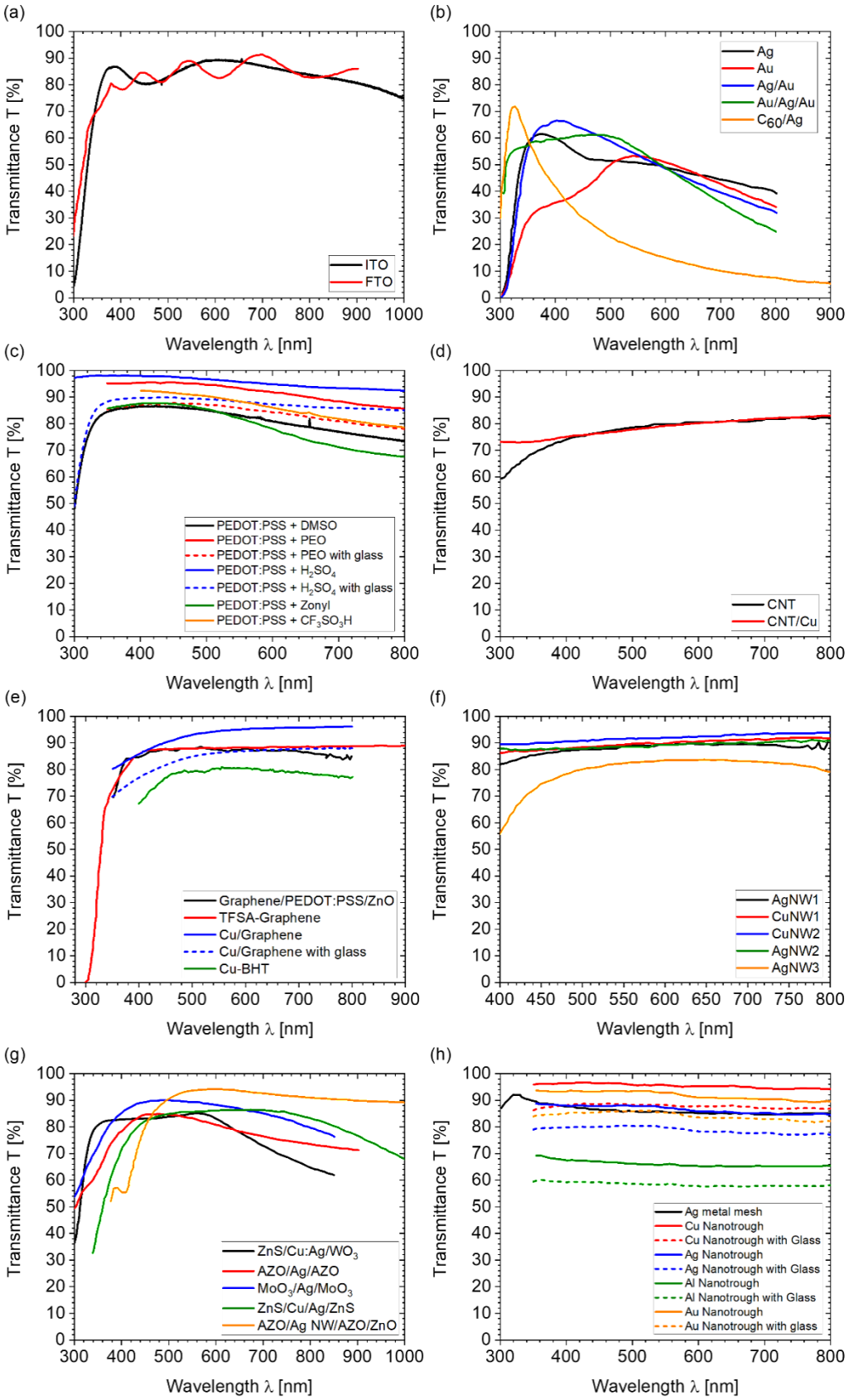
(a)
Transmittance T [%]
Wavelength λ [nm]
ITO
FTO
(b)
Transmittance T [%]
Wavelength λ [nm]
Ag
Au
Ag/Au
Au/Ag/Au
C60/Ag
(c)
Transmittance T [%]
Wavelength λ [nm]
PEDOT:PSS + DMSO
PEDOT:PSS + PEO
PEDOT:PSS + PEO with glass
PEDOT:PSS + H2SO4
PEDOT:PSS + H2SO4 with glass
PEDOT:PSS + Zonyl
PEDOT:PSS + CF3SO3H
(d)
Transmittance T [%]
Wavelength λ [nm]
CNT
CNT/Cu
(e)
Transmittance T [%]
Wavelength λ [nm]
Graphene/PEDOT:PSS/ZnO
TFSA-Graphene
Cu/Graphene
Cu/Graphene with glass
Cu-BHT
(f)
Transmittance T [%]
Wavlength λ [nm]
AgNW1
CuNW1
CuNW2
AgNW2
AgNW3
(g)
Transmittance T [%]
Wavelength λ [nm]
ZnS/Cu:Ag/WO3
AZO/Ag/AZO
MoO3/Ag/MoO3
ZnS/Cu/Ag/ZnS
AZO/Ag NW/AZO/ZnO
(h)
Transmittance T [%]
Wavelength λ [nm]
Ag metal mesh
Cu Nanotrough
Cu Nanotrough with Glass
Ag Nanotrough
Ag Nanotrough with Glass
Al Nanotrough
Al Nanotrough with Glass
Au Nanotrough
Au Nanotrough with glass

Figure 46: *Transmittance spectra of different groups of TCEs (a) metal oxides, (b) ultra-thin metals, (c) conductive polymers, (d) carbon nanotubes, (e) graphene, (f) metal NWs, (g) DMD, and (h) metal network groups. The transmittance data was extracted from literature using an online tool [118].*

In this study, the following TCEs were evaluated:

- Commercial ITO substrates from Xinyan Technology Limited (China)
- FTO fabricated by using horizontal ultrasonic spray pyrolysis deposition [56]
- Metal films based TCEs - Ag, Au, Ag/Au, Au/Ag/Au, and C60-surfactant/Ag [60, 61, 137]
- Lab-processed PEDOT:PSS (PH1000) modified by 5% v/v DMSO addition and various other PEDOT:PSS modifications obtained by polyethylene oxide (PEO), sulphuric acid (H_2SO_4), fluorosurfactant zonyl-FS300 and trifluoromethanesulfonic acid (CF_3SO_3H) [102, 138-140]
- Pristine CNT [64] and CNT/Cu composite nanofibers electrodes, which were fabricated using an electrospinning process to reduce the contact resistance [141]
- TCEs based on graphene, such as graphene electrodes coupled with PEDOT:PSS and zinc oxide (ZnO) nanoparticles [142], graphene doped with trifluoromethanesulfonyl-amide (TFSA) [143], and Cu/graphene hybrid electrodes [107]
- Another "graphene-like" hybrid 2D material – Cu-BHT (copper benzenehexathiol) [144, 145]
- Metal NWs-based TCEs – solution-processed Ag NW [66], Cu NW synthesized via a self-catalytic growth process [65], CuNW, Ag NW fabricated using a combination of electroless deposition and electrospinning technique [67] and solution-processed Ag NW [146]. To distinguish between them without confusion, the electrodes were listed with a number as AgNW1 [66], CuNW1 [65], CuNW2 [67], AgNW2 [67], and AgNW3 [146]
- DMD structure-based TCEs: ZnS/Cu:Ag/WO_3 [147], AZO/Ag/AZO [62], MoO_3/Ag/MoO_3 [148], ZnS/Cu/Ag/ZnS [149], and AZO/AgNW/AZO/ZnO [150]
- TCEs based on Ag metal networks based on a crackle lithography technique [151], and metal (Cu, Ag, Au, Al) nanotrough networks (based on templating ultralong polymer nanofibers fabricated using an electrospinning process) [152]

Figure 47 and Table 5 display the resulting exact FOM for the above-mentioned TCEs, which was assessed for the spectral range of 350 to 800 nm (if available) and a solar cell length of 5 mm. The copper nanowire-based electrode (CuNW2) was discovered to be the top-performing electrode, producing an outstanding FOM of 0.893. This was caused by the union of a high average optical transparency (90.88%) and low sheet resistance (11.2 Ω/□). The next-best electrodes were AZO/Ag NW/AZO/ZnO, which had a FOM of 0.883 and AgNW1 having FOM of 0.869.

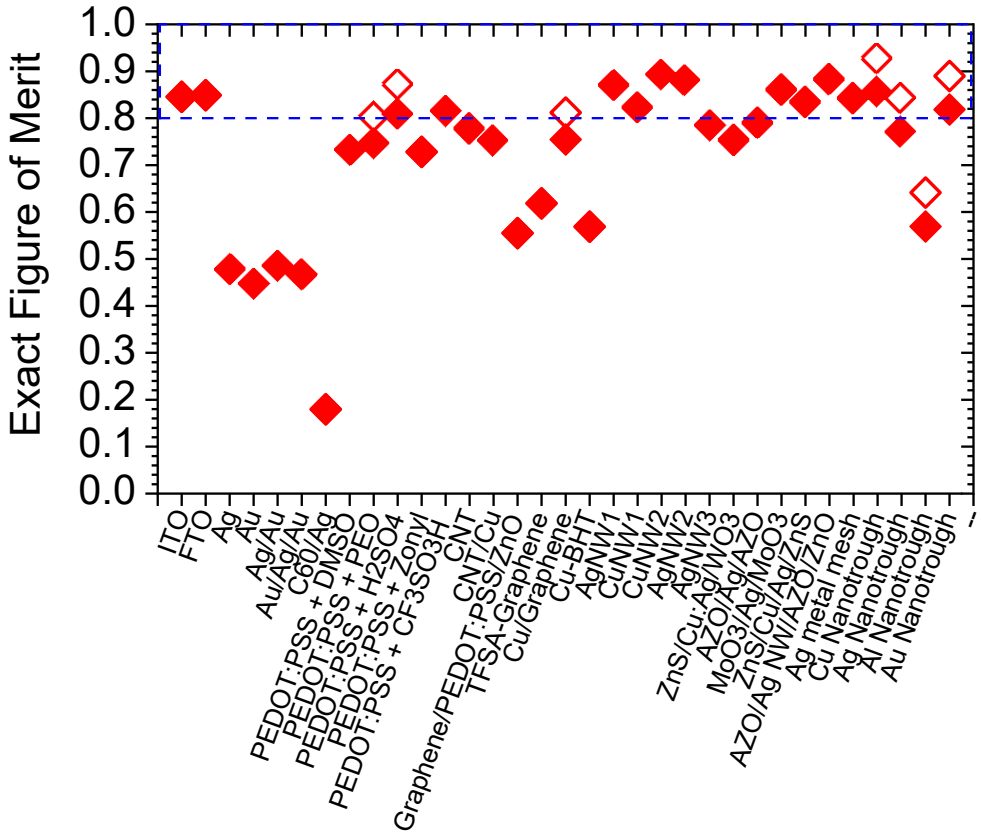

Figure 47: *Comparison of the exact FOM evaluated for different TCEs, done over a spectral range of 350 to 800 nm and for a solar cell length of 5 mm. [Note: The open red color symbol data points are FOM values of TCEs for which only film transmittance spectra data were available].*

To identify the most practical options, a randomly chosen criterion of 80% of the theoretically maximum attainable performance was created. Above this boundary, however, are the technical standards, ITO, and FTO. Fortunately, 12 alternative TCEs succeeded in crossing this line as well. Unfortunately, none of the ultra-thin metal layers were able to pass this barrier, while two of the highly conductive PEDOT:PSS formulations succeeded after receiving treatments above a FOM of 80%. The metal nanowire group displayed large FOMs

in general, exceeding the 80% limit in four out of five instances. When the glass was added, just one electrode in the graphene group produced yields close to 80%. The group of dielectric-metal-dielectric layer (DMD) layer stacks, of which three examples can be discovered above 80% and even the remaining ones are generally close to that, constitutes a very successful technique. Another effective approach was the group of "metal-nanotrough" layers, where two of the four materials performed above the cutoff. This method would produce the highest FOMs out of all those under consideration if only film transmittances were taken into account. Last but not least, the "metal-mesh" strategy based on silver outperformed the ITO performance for TCEs.

In the appendix, Figures A5 (a-f) and Tables A2 to A6 show the comparison between different TCEs evaluated by different FOMs.

***Table 5**: Comparison of the exact FOM evaluated for different TCEs, done over a spectral range of 350 to 800 nm and for a solar cell length of 5 mm.*

***Note:** TCEs with a * were evaluated for the spectral range of 400 to 800 nm due to insufficient data below 400 nm. The values inside brackets represent FOM values of TCEs for which only film transmittance spectra were taken into account for the analysis.*

***Abbreviation:** SR – Sheet resistance, T – Transmittance, Ref. – Reference, TW – This work.*

TCE	SR [Ω/□]	Average T [%]	Substrate	Exact figure of merit	Ref.
Metal oxides					
• ITO	10	85.53	Glass	0.846	TW
• FTO	4.0 ± 0.14	83.81	Glass	0.849	[56]
Ultra-thin metals					
• Ag	15.7	49.79	Glass	0.479	[61]
• Au	7	43.50	Glass	0.447	[61]
• Au/Ag	7.8	50.70	Glass	0.486	[61]
• Au/Ag/Au	10.42 ± 0.5	48.43	Glass	0.467	[137]
• C_{60}-surfactant/Ag	1.70	21.24	Glass	0.180	[60]

Conductive polymers					
• PEDOT:PSS + DMSO	64	81.37	Glass	0.730	TW
• PEDOT:PSS + PEO	72	91.84	Glass	0.745 (0.803)	[138]
• PEDOT:PSS + H_2SO_4	46.1	95.41	Glass	0.809 (0.873)	[102]
• PEDOT:PSS + Zonyl	46	79.09	Glass	0.728	[139]
• PEDOT:PSS + CF_3SO_3H*	32	85.99	PET	0.815	[140]
Carbon nanotubes					
• Pristine CNT	17	78.92	Glass	0.778	[64]
• CNT/Cu	39	79.14	Glass	0.752	[141]
Graphene					
• Graphene/PEDOT:PSS/ZnO	230	86.13	Glass	0.555	[142]
• TFSA-Graphene	185	87.29	PET	0.619	[143]
• Cu/Graphene	~75	90.63	Glass	0.755 (0.812)	[107]
• Cu-BHT*	200	78.29	Glass	0.569	[144]
Nanowires					
• AgNW1*	10.3	88.10	Glass	0.869	[66]
• CuNW1	51.5	89.35	PET	0.821	[65]
• CuNW2*	11.2	90.88	Glass	0.893	[67]
• AgNW2*	8.5	89.15	Glass	0.880	[67]
• AgNW3	~10	76.30	Glass	0.783	[146]
Dielectric/Metal/Dielectric					
• ZnS/Cu:Ag/WO_3	31	78.98	Glass	0.752	[147]
• AZO/Ag/AZO	6	79.04	Glass	0.789	[62]
• MoO_3/Ag/MoO_3	5	86.11	Glass	0.860	[148]

• ZnS/Cu/Ag/ZnS	4.8	81.54	Glass	0.833	[149]
• AZO/Ag NW/AZO/ZnO*	11.3	88.63	Glass	0.883	[150]
Metal network					
• Ag metal mesh	10	85.89	Glass	0.842	[151]
• Cu nanotrough	15	95.45	Glass	0.856 (0.928)	[152]
• Ag nanotrough	15	86.57	Glass	0.770 (0.842)	[152]
• Al nanotrough	21	66.16	Glass	0.569 (0.641)	[152]
• Au nanotrough	17	91.86	Glass	0.818 (0.890)	[152]

4.1.9 Summary and conclusions

To address the issue of TCE rating to assist in selecting the suitable TCE for solar cells, a novel and exact FOM was established that fulfilled the requirement of being linear to the achievable PV power, normalized with the Shockley-Queisser limit (SQL), dimensionless, and thus directly meaningful in general.

The exact FOM was presented in two forms: an exact form that was based on calculating the manner in which sheet resistance and transmittance spectra affect the maximum performance in accordance with the SQL, and an approximation form. The simplified approximate form may be used based on the researcher's experimental data, but the calculation effort for the exact form requires a numerical method. Furthermore, the input parameters are transmittance (T) and sheet resistance ($R_{\square}$), which are TCE parameters; bandgap (E_G), which is a system-specific parameter; and solar cell length (l) is free parameter i.e., it is a matter of choice. All these parameters have a significant impact on the sheet resistance of the TCE.

Using the transition sheet resistance, the approximate form helped to distinguish between the two regimes of TCE operation: transmittance and conductance limited. Assessing the

functional dependence of the exact FOM, a second approach for an approximate FOM bearing overall smaller deviations was presented.

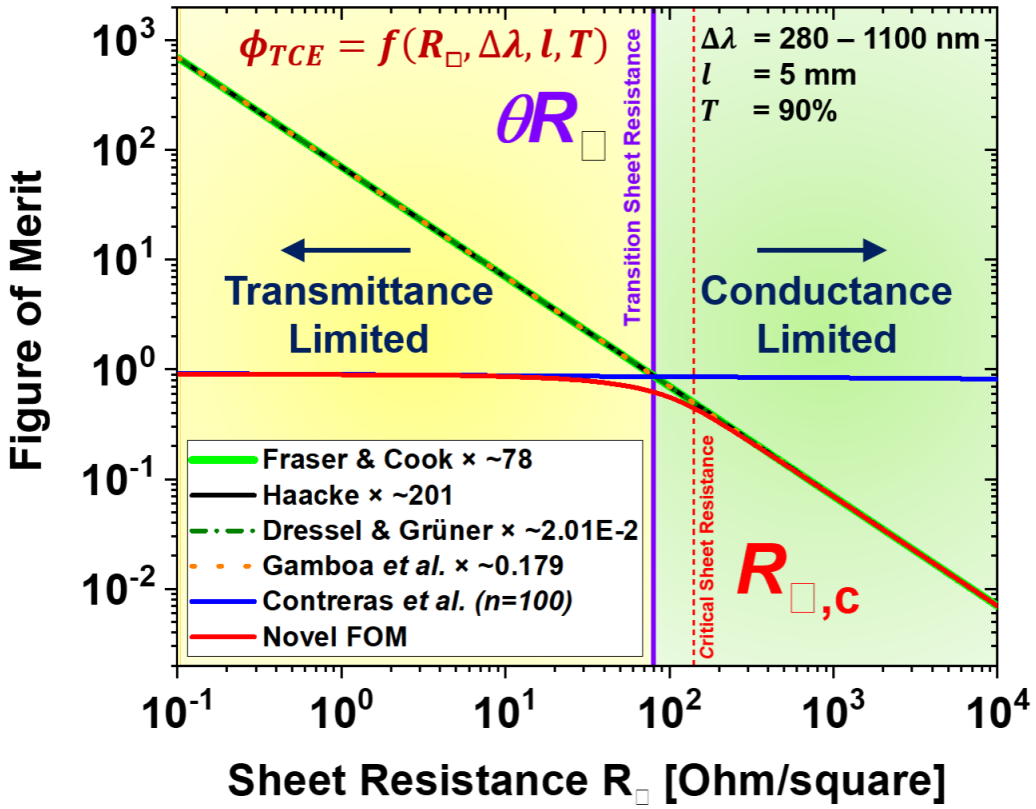

Figure 48: *Comparison between established figures of merit and the exact figure of merit.*

It was shown that the spectral range used is crucial in determining the actual needs for TCEs for different PV material classes. Based on the transition sheet resistance, an empirically derivable target sheet resistance has been established, which can serve as a roadmap for the development of certain electrode material systems. Finally, more than 30 TCE alternative materials were evaluated. While just 6 alternatives exceeded the exact FOM for standard ITO and FTO, the 12 already reported TCEs showed a promising trend of getting extremely close to the technical benchmark. It is envisaged that the exact FOM would help researchers stay focused on creating competitive solutions for high-performance TCEs for solar applications.

The results described in this section are published in *Advanced Energy Materials*, **2021**, *11*, *26*, 2100875, *DOI: https://doi.org/10.1002/aenm.202100875, Authors:* ***Aman Anand****, Md Moidul Islam, Rico Meitzner, Ulrich S. Schubert and Harald Hoppe.*

4.2 Extension of the exact figure of merit

Upon the publication of the novel and exact FOM (or FOM_{Anand}) [39], a comment was written by C.P. Muzzillo [54] in which he raised three points of criticism: i) the exact FOM is not exact and requires finite element modeling, ii) comparison to existing FOMs, the exact FOM is implicit, and iii) the calculation proposed is not suited for different solar module geometries (monolithic dead space, metal grids, etc.). This section discusses all the points raised by Muzzillo and addresses each of them.

Muzzillo's comment revealed that detailed evaluations have already been made for projecting the possible performance of solar cells as a function of the TCE features [51, 153], but Muzzillo's FOM was not noted before since the FOM was not explicitly mentioned and was not used to rate TCEs. The contribution from Muzzillo is appreciated for establishing a FOM that is dimensionless and proportional to the power output that may be achieved. However, the FOM is not normalized to the SQL limit and instead takes transmittance and conductance losses into account, which was the demand of the previous study [39]. The original goal of the previous study was to offer an absolute upper limit for possible PV performance, ignoring any influence of independent contributions, such as those caused by parallel or contact resistances. The focus was solely on those aspects that come about from TCE's limited transmittance and conductance.

Although the simulation is based on the one-diode model, the results are generally precise enough as long as the solar cell length is about 0.3 to 0.5 cm and the sheet resistance is up to 100 Ohm/square, as demonstrated by Seeland and Hoppe. The inaccuracy caused by lumping the series resistance in the one-diode model was found to be extremely small (<1%) [130]. As a result, under the limitations of having solar cell lengths that are close to ideal, the "exact FOM" can be extended for different solar module geometries (monolithic dead space, metal grids, etc.). It is agreed with Muzzillo that network simulations, rather than the one-diode model used here, are ultimately necessary for general calculations of any solar module geometry because they are capable of accurately accounting for the effect of distributed series resistances on power conversion efficiency [130]. However, such simulation falls outside the scope of this study and might be considered in future work.

4.2.1 Comparison between Muzzillo's figure of merit and the exact figure of merit

As described in Section 2.5, Muzzillo defined FOM as the ratio of power at the maximum powerpoint affected by the TCE to the power at the maximum powerpoint. For a solar cell operating at maximum powerpoint (MP) with current density (J_{MP}) and voltage (V_{MP}) with a uniform TCE, the J_{MP} and V_{MP} would reduce to $J_{MP,TCE,}$ and $V_{MP,TCE}$ based on the assumption that $J_{MP,\,TCE}$ is only affected by $T_{TCE,avg}$, and $V_{MP,TCE}$ is only affected by $R_{\square}$.

$$J_{MP,TCE} = J_{MP} \cdot T_{TCE,avg} \tag{66}$$

$$V_{MP,TCE} = V_{MP} - R_{\square} \cdot A \cdot J_{MP} \tag{67}$$

Thus, the FOM ($\phi_{Muzzillo}$) is [54]:

$$\phi_{TC} = \frac{J_{MP,TCE} \cdot V_{MP,TCE}}{J_{Mp} \cdot V_{MP}} = T_{TCE,avg} \cdot \left(1 - \frac{R_{\square} \cdot L^2 \cdot J_{MP}}{3 \cdot V_{MP}}\right), \ [\phi_{TC}] = \frac{A/m^2 \cdot V}{A/m^2 \cdot V} = 1 \tag{68}$$

Although Muzzillo's FOM (equation 68) is described as an explicit FOM, the very implicit equation that was used for the exact FOM—the Shockley equation—was solved in order to find the current density and voltage at the maximum power point for the comparison of the two FOMs. However, when considering real solar cells in practical situations, it is possible to calculate and evaluate the maximum power point parameters using the recorded IV characteristics, which appears to make the FOM proposed by Muzzillo appropriate in this situation, but still, it requires numerical efforts.

To make a less coarse approximation, the correction was made on the maximum power point voltage by simply taking into account the photocurrent's limitation by the TCE:

$$V_{MP,TCE} = V_{MP} - R_{TCE} \cdot A \cdot J_{MP} \cdot T_{TCE,avg} = V_{MP} - \frac{R_{sh,TCE} \cdot L \cdot J_{MP} \cdot T_{TCE,avg}}{3} \tag{69}$$

And thus, the modified Muzzillo FOM ($\phi_{Muzzillo,mod}$) was defined as follows:

$$\phi_{Muzzillo,mod} = \frac{J_{MP,TCE} \cdot V_{MP,TCE}}{J_{Mp} \cdot V_{MP}} = T_{TCE,avg} \cdot \left(1 - \frac{R_{sh,TCE} \cdot L^2 \, J_{MP} \cdot T_{TCE,avg}}{3 \cdot V_{MP}}\right) \tag{70}$$

Comparing between $\phi_{Muzzillo}$, $\phi_{Muzzillo,mod}$ and ϕ_{Anand} (the "exact FOM") (Figure 49), $\phi_{Muzzillo,mod}$ notably comes close to the exact FOM, bringing the gap to ϕ_{Anand} to less than 1% (Figure 49 subset). Both versions ($\phi_{Muzzillo}$, $\phi_{Muzzillo,mod}$) soon lose accuracy for sheet resistance above 100 Ohm/square, with an absolute inaccuracy rising above 10% with acceleration. For sheet resistances higher than 200 Ohm/square, both versions considerably diverge and even go the opposite way in the negative. Even if such a range of sheet resistances is not appropriate for any PV development, it highlights the aspiration associated with the exact FOM (ϕ_{Anand}) to cover all the regimes of sheet resistance properly [154].

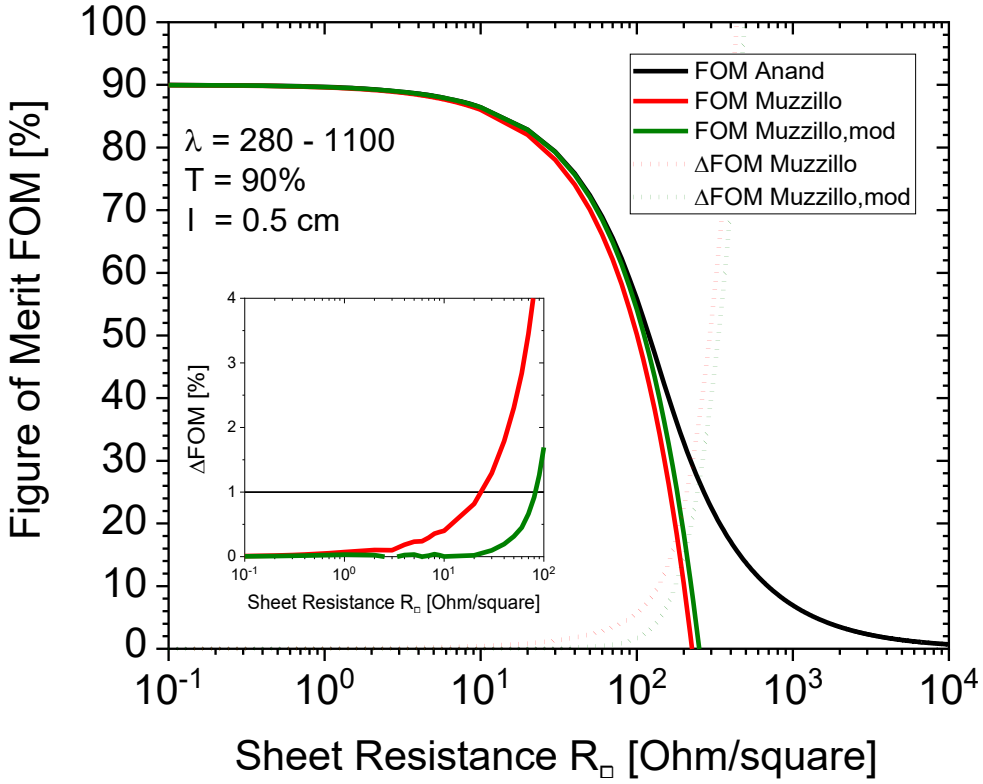

Figure 49: *Comparison of ϕ_{Anand} (the exact FOM), $\phi_{Muzzillo}$, and $\phi_{Muzzillo,mod}$ for TCE with a spectral transmittance of 90% from 280 to 1100 nm and a solar cell length of 5 mm. For the calculation of $\phi_{Muzzillo}$ and $\phi_{Muzzillo,mod}$ the $J_{MP,TCE}$ was 42.15 mA cm^{-2}, and $V_{MP,TCE}$ was 793.9 mV was taken from [54].*

Different FOMs were again re-evaluated in the same manner as in previous work since Muzzillo's FOM captured the interest and required a wider context. Previously overlooked FOM by Jain and Kulshreshtha reported in 1981 [48], was also included in the study.

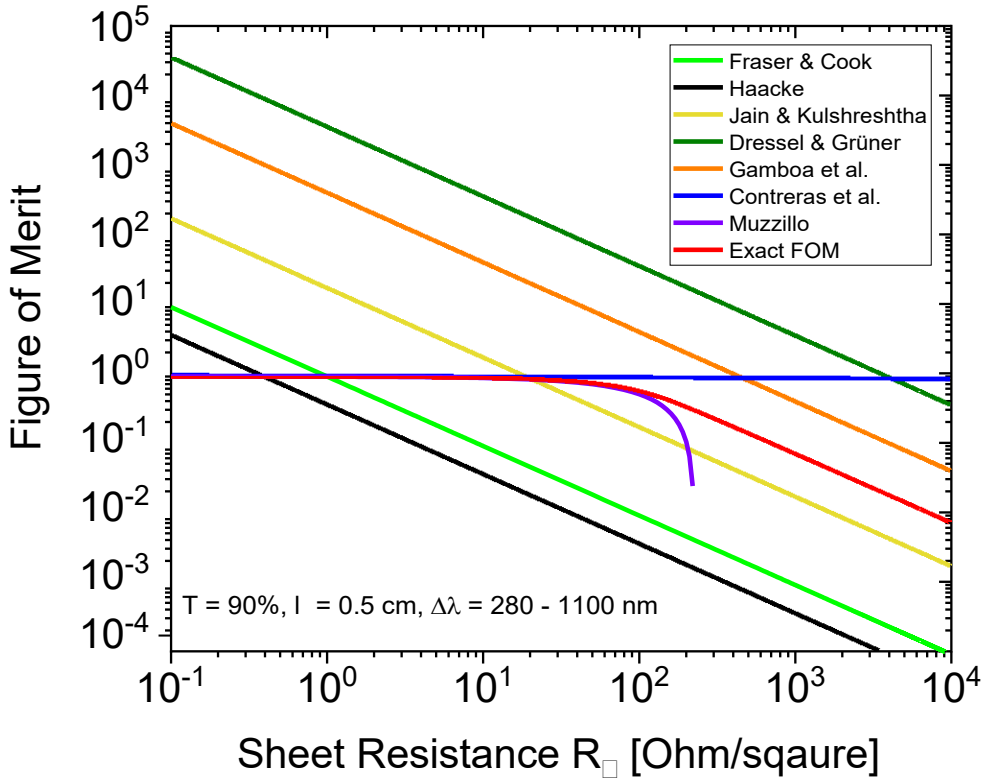

***Figure 50**: Comparison of different figures of merit for solar cells for TCE with a spectral transmittance of 90% from 280 to 1100 nm and a solar cell length of 5 mm.*

As seen in the double logarithmic plot (Figure 50), the FOMs by Fraser & Cook, Haacke, Jain & Kulshreshtha, Dressel & Grüner, and Gamboa *et al.* behave in the same way. They cover a five-order-of-magnitude range for an equivalent change in sheet resistance but are differentiated from one another by certain prefactors. Smaller sheet resistances always triumph over optical transmittance because they are not normalized, resulting in discrepancies in the achievable PV performance. The only FOMs that displayed exceptions to this norm were those by Muzzillo and Contreras *et al.* (n = 100). The FOM value in the regime for higher sheet resistances was, however, considerably divergent in both cases from the expected performance of a solar cell. The exact FOM, which is also represented by a hyperbolic dependence on sheet resistance for higher values of the same, captures the correct balance of influences between TCE transmittance and its sheet resistance.

4.2.2 Extension of the exact figure of merit model for different solar module geometries

In response to Muzzillo's comment, additional simulations were conducted for different solar module geometries to demonstrate the exact FOM model's applicability and to show that all of his specified cases can be matched.

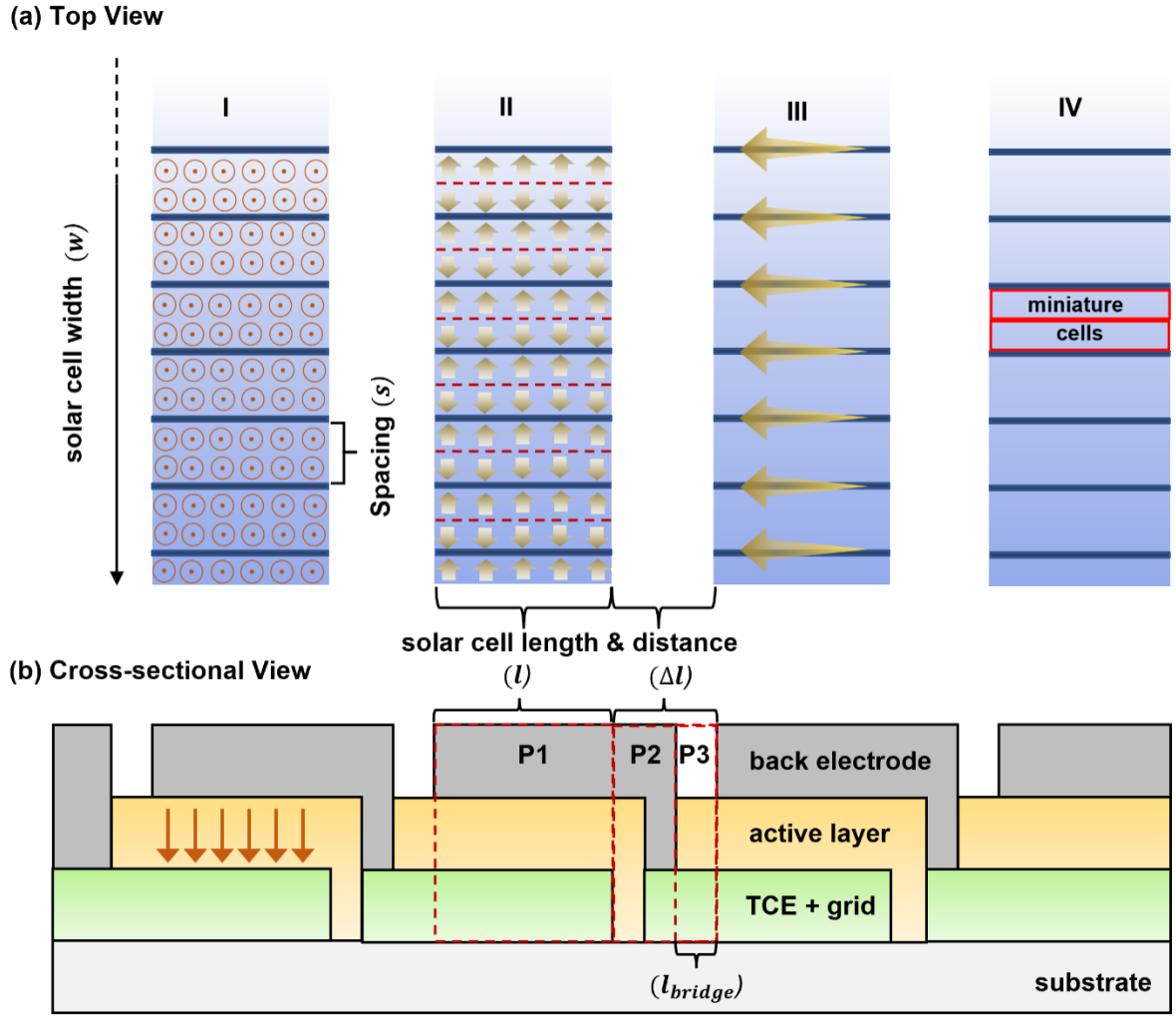

Figure 51: *Illustration showing the top and cross-sectional views of a monolithic solar module with serial connectivity. The arrows show the three ways in which the hierarchical current flows: I) vertically within, II) horizontally on top, and III) within the grid fingers, which is perpendicular to both of the latter two* [154].

(a) FOM for monolithic modules

The prefactor was simply added to the exact FOM considering the serial interconnection due to some finite solar cell length [40]. Thus, the exact FOM (ϕ_{Anand}) for monolithic solar modules is defined as follows:

$$\phi_{Anand,mono} = \frac{P_{MPP,TCE}}{P_{MPP,Ideal\,TCE}} \cdot \frac{l}{l+\Delta l} = \phi_{Anand} \cdot \frac{l}{l+\Delta l} \quad (71)$$

where l is the solar cell length and Δl is the solar cell distance (or "dead space") between adjacent cells within the module.

(b) FOM for monolithic modules considering the impact of the TCE bridge on the series resistance

To take into account a more plausible scenario, the impact of series resistance resulting from the serial connections caused by the TCE bridge (see Figure 51) was also taken into account.

For a tile of length L and width W with a constant current running over it becomes, the sheet resistance is described as follows:

$$R_{tile} = R_{\square} \cdot \frac{L}{W} \quad (72)$$

The relationship between the effective series resistance (R_S) and the sheet resistance ($R_{\square}$) of TCE due to the current transport direction can be given as [40]:

$$R_{TCE,eff} = R_{\square} \cdot \frac{l}{3w} \quad (73)$$

For a solar cell of length l and width w, assuming that the solar cell distance Δl can be sub-divided into three (P1-P3) equally wide laser trenches [155], the effective sheet resistance of the TCE bridge becomes [40]:

$$R_{TCE,bridge} = R_{\square} \cdot \frac{l_{bridge}}{w_{bridge}} = R_{\square} \cdot \frac{\Delta l}{3w} \quad (74)$$

where the bridge length l_{bridge} equates to one-third of the total solar cell distance. Thus, the total series resistance (R_s) due to the TCE for monoliths can be calculated as:

$$R_{S,mono,bridge} = R_{TCE,eff} + R_{TCE,bridge}$$

$$R_{S,mono,bridge} = R_{\square} \cdot \frac{l}{3w} + R_{\square} \cdot \frac{\Delta l}{3w}$$

$$R_{S,mono,bridge} = \frac{R_{\square}}{3w}(l + \Delta l\,) \tag{75}$$

$$\phi_{Anand,mono,bridge} = \phi'_{Anand} \cdot \frac{l}{l+\Delta l} \tag{76}$$

The ϕ'_{Anand} was calculated by solving the implicit Shockley equation using the series resistance as defined in equation 75.

Note: any potential effects of the contact resistance at the junction between the TCE and the back electrode were not taken into account. It would be necessary to conduct extra experimental measurements (or simulations) to include such an additional input parameter. But it was left on purpose since additional properties besides those of the TCE play a role here.

(c) FOM for monolithic modules considering the impact of grid lines on current collection and series resistance

The current collection can be divided into several stages by placing additional grid lines on top of the TCE or integrating them into a TCE (Figure 51).

When charges are generated, it flows toward the TCE (see Figure 51 (a) part I). Charges are attracted to the grid lines within the TCE because of the lower resistance causing potential gradients directed in their direction as depicted in Figure 51 (a) part II. The TCE toward the grid lines, the current collection inside an area of s/2 times l, can be expressed as:

$$R_{TCE,coll} = R_{\square} \cdot \frac{s}{2} \cdot \frac{1}{3l} \tag{77}$$

where $s/2$ corresponds to a miniature solar cell length and l is its width (see III in Figure 50 (a)). Since here only a fraction of a single cell was considered (see IV in Figure 51 (a)).

$$A_{cell,miniature} = A_{cell} \cdot \frac{s}{2w} \tag{78}$$

the impact of the whole current from the entire device surface must be considered by multiplying by the same factor, which effectively reduces the current under consideration to a fraction matching the tiny cell area:

$$R_{TCE,grid,eff} = R_{\square} \cdot \frac{s}{2} \cdot \frac{1}{3l} \cdot \frac{s}{2w} = R_{\square} \cdot \frac{s^2}{12lw} \tag{79}$$

After being collected by the grid, the current eventually flows within the grid lines in the direction of the solar cell length (see Figure 51 (a) part III), once more being subject to collecting a linearly increasing amount from the TCE along the way.

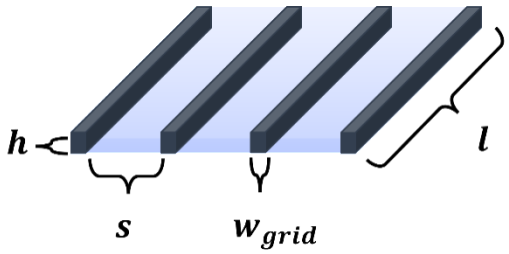

Figure 52: *Illustration showing the dimensions of the grid where h is the height of the grid, s is the spacing between two grid lines, w_{grid} is the width of the grid and l is the length of the grid [54].*

The effective sheet resistance of the grid ($R_{\square,grid}$) can be calculated by using the standard formula of sheet resistance using the grid metal resistivity (ρ_{grid}) and the thickness of the metal grid (t_{grid}):

$$R_{\square,grid} = \frac{\rho_{grid}}{t_{grid}} \tag{80}$$

where the hypothetical and the equivalent thickness can be calculated by considering the grid line volume over the area covered by the grid line for current collection (Figure 52):

$$t_{grid} = \frac{Volume}{Area} = \frac{w_{grid} \cdot h \cdot l}{l \cdot (s + w_{grid})} = \frac{w_{grid} \cdot h}{(s + w_{grid})} \tag{81}$$

where w_{grid} is the gridline width, h is the height of the metal grating, and t is the equivalent thickness for a homogeneous metal layer exhibiting the same volume as the grid lines. Thus, the series resistance due to the grid sheet resistance can be calculated as:

$$R_{grid,eff} = R_{\square,grid} \cdot \frac{l}{3w} \tag{82}$$

since the grid collects the current from a full cell area.

Thus, the total series resistance (R_s) becomes:

$$R_{S,grid} = R_{TCE,grid,eff} + R_{grid,eff}$$

$$R_{S,grid} = R_{\square} \cdot \frac{s^2}{12lw} + R_{\square,grid} \cdot \frac{l}{3w} \tag{83}$$

The overall transmittance due to metal grating would be reduced by the factor ($T_{grid} = \frac{s}{s+w}$) and thus the transmittance factor was multiplied to the final equation:

$$\phi_{Anand,grid} = \phi''_{Anand} \cdot T_{grid} \tag{84}$$

The ϕ''_{Anand} was calculated by solving the implicit Shockley equation using the series resistance as defined in equation 82.

(d) FOM for monolithic modules considering the impact of monolithic serial interconnection using grid lines

The prefactor was simply added to the equation 84 considering the serial interconnection due to some finite solar cell length. Thus, the FOM for monolithic solar modules using grid line is as follows:

$$\phi_{Anand,grid,mono} = \phi''_{Anand} \cdot T_{grid} \cdot \frac{l}{l+\Delta l} \tag{85}$$

Considering the additional effect of the TCE bridge on the series resistance:

$$R_{grid,bridge} = R_{\square,grid} \cdot \frac{\Delta l}{3w} \tag{86}$$

Thus, the total effective series resistance is defined as:

$$R_{S,grid,mono,bridge} = R_{TCE,grid,eff} + R_{grid,eff} + R_{grid,bridge}$$

$$R_{S,grid,mono,bridge} = R_{\square} \cdot \frac{s^2}{12lw} + R_{\square,grid} \cdot \frac{l}{3w} + R_{\square,grid} \cdot \frac{\Delta l}{3w}$$

$$R_{S,grid,mono,bridge} = R_{\square} \cdot \frac{s^2}{12lw} + R_{\square,grid} \cdot \frac{1}{3w} [l + \Delta l] \tag{87}$$

The following FOM results from adding together the effects of the solar cell's distance inside the serial interconnection and the impact of additional grid lines, the FOM can be defined as follows:

$$\phi_{Anand,grid,mono,bridge} = \phi'''_{Anand} \cdot T_{grid} \cdot \frac{l}{l+\Delta l} \tag{88}$$

The ϕ'''_{Anand} was calculated by solving the implicit Shockley equation using the series resistance as defined in equation 87.

Figure 53 shows the outcomes for each of the aforementioned scenarios (a-d) for various solar cell lengths. By using $\phi_{\text{Anand,mono}}$, the ideal solar cell length for monoliths was found to be 0.4 cm. It also shows how the grid affected the FOM along the whole length of the solar cell. The grid increases the range of solar cell lengths up to 1.3 cm that can be employed for construction when compared to solar cells with only transparent conducting electrodes. Additionally, the series resistance brought on by the transport inside the TCE or TCE-grid bridge is so negligible that it has no impact on the FOM's overall evaluation.

Thus, the exact FOM (or ϕ_{Anand}) can be applied to a wider range of solar module configurations, including those using additional metal grids, which addresses all the points raised by Muzzillo.

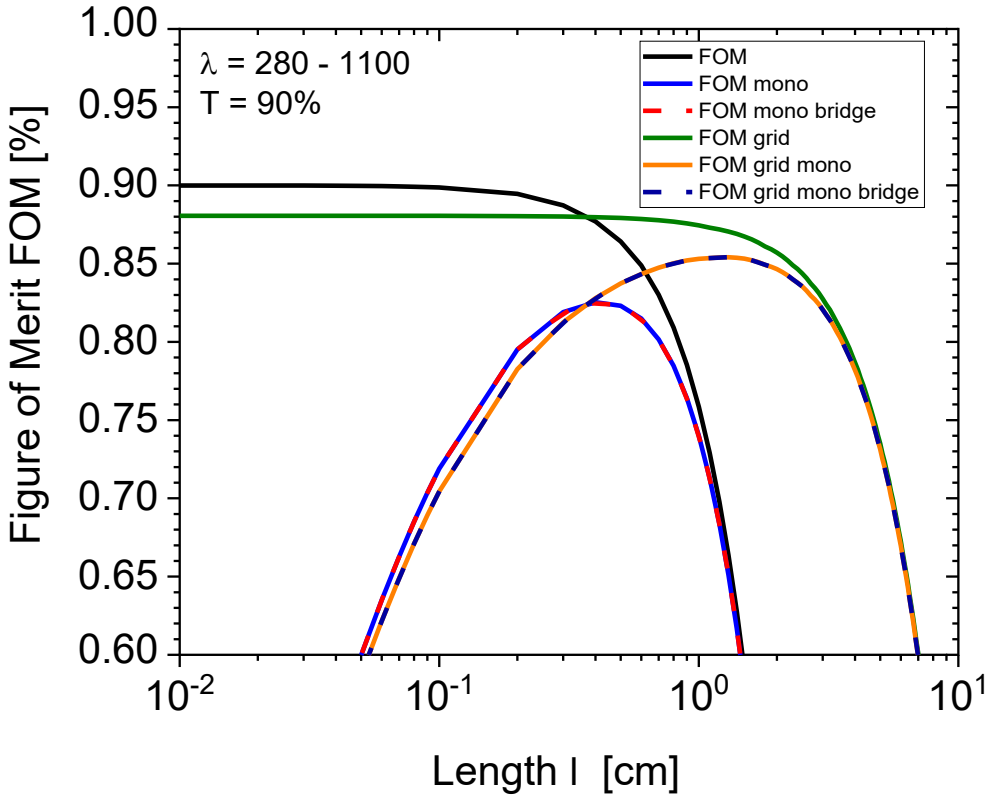

Figure 53: *FOMs versus cell length (l) for TCE with a spectral transmittance of 90% from 280 to 1100 nm and a solar cell length of 5 mm. Values used for calculation: sheet resistance ($R_{\square}$) = 10 Ω/□, monoliths deadspace (d) = 250 µm, width of grid metal strip (w_{grid}) = 56 µm, resistivity of grid metal (ρ_{metal}) =10^{-5} Ωcm, and height of grid metal (h_{metal})= 13 µm.*

4.2.3 Summary and conclusions

A comment was written by C.P. Muzzillo [54] in which he raised three points of criticism: i) the exact FOM is not exact and requires finite element modeling, ii) comparison to existing FOMs, the exact FOM is implicit, and iii) the calculation proposed is not suited for different solar module geometries (monolithic dead space, metal grids, etc.). The challenge to extend the exact FOM (or ϕ_{Anand}) applicability to different solar module scenarios was accepted and each point was addressed. It was observed that Muzzillo's FOM likewise requires the use of numerical methods to solve the implicit Shockley equation to determine the maximum power point values of an experimental IV-curve. Thus, Muzzillo's FOM can also be seen as implicit

to a great extent. Furthermore, Muzzillo's FOM can be preferred over the approximation FOM when using experimental maximum power point data, provided that the TCE's sheet resistance stays below the critical sheet resistance. However, once the critical sheet resistance is exceeded, Muzzillo's FOM first exhibits a large deviation before delivering unphysical values below zero. To make a less coarse approximation, the correction was made on the maximum power point voltage by simply taking into account the photocurrent's limitation by the TCE, and a modified version of Muzzillo's FOM was introduced. But for sheet resistances higher than 200 Ohm/square, both versions considerably diverge and even go the opposite way in the negative. Even if such a range of sheet resistances is not appropriate for any PV development, it highlights the aspiration associated with the exact FOM to cover all the regimes of sheet resistance properly

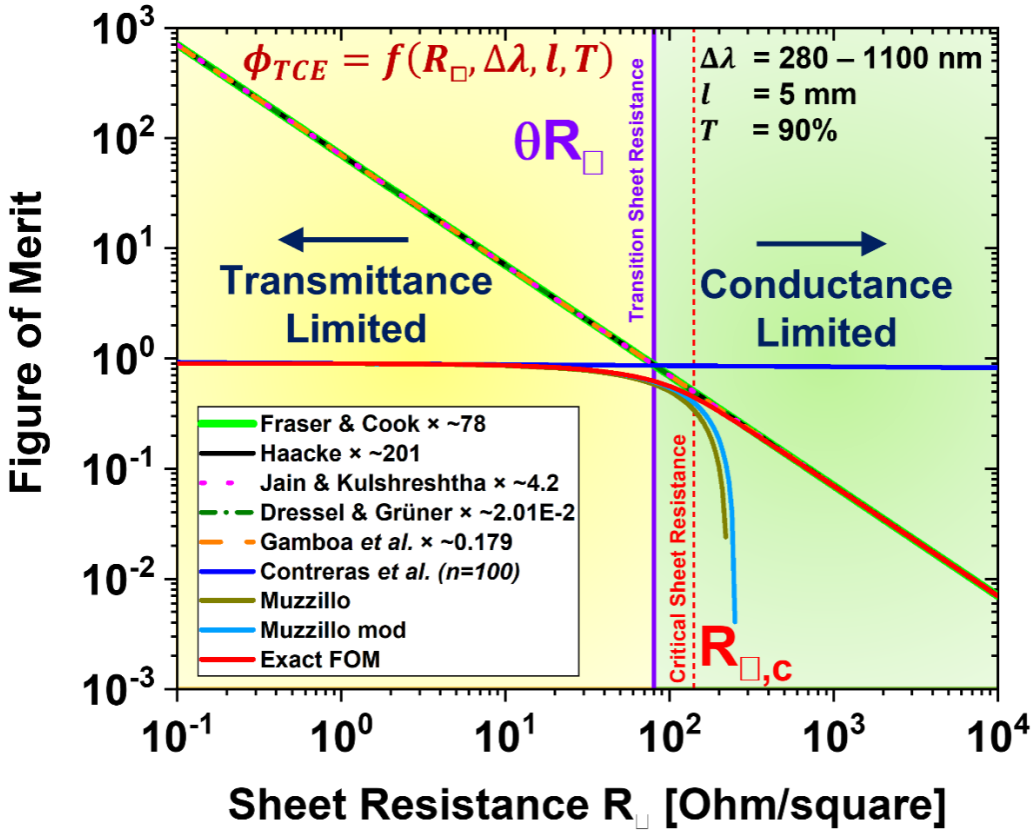

Figure 54: *Comparison between established figures of merit, Muzzillo figure of merit, modified Muzzillo figure of merit and the exact figure of merit.*

Ultimately, it was inferred that both perspectives (ϕ_{Anand} *(the exact FOM) and* $\phi_{Muzzillo}$) are still essential and can be applied to different scenarios based on the specific geometry of solar

cells and modules. Although numerical methods are needed to determine the exact FOM, the computational effort has been simplified over the years as a result of computerization and digitization. Thus, to support the further development of TCEs for PVs, it is planned to offer an online tool that will compute the exact FOM for their TCE and anticipate solar module geometry.

The results described in this section are published in *Advanced Energy Materials*, **2021**, *12*, *23*, 2200828, *DOI: https://doi.org/10.1002/aenm.202200828, Authors:* ***Aman Anand****, Md Moidul Islam, Rico Meitzner, Ulrich S. Schubert and Harald Hoppe.*

4.3 Understanding PEDOT:PSS films processing

This section discusses the impact of the processing conditions on the work function of PEDOT:PSS films. Various formulations were tested with regard to relative humidity levels, annealing temperatures, and solar cell performance.

It has been shown in earlier research that the different processing settings and circumstances under which PEDOT:PSS films are handled have a significant effect on the electrical, electronic, and physical properties of the films. Any change in the process could result in altered PEDOT:PSS films with distinct work functions. Koch *et al.* showed that, for increasing annealing temperatures, the enrichment of PSS at the surface of PEDOT:PSS films is followed by a considerable rise in the work function during thermal annealing in a vacuum [156]. Additionally, with humidity exposure, it was found that the surface composition was altered, resulting in a slightly higher concentration of PEDOT, which could indicate the possible reason for the work function being reduced. According to Yun *et al.*, higher annealing temperatures resulted in a weakening of the connection between PSS^- and sodium ions (Na^+) or protons (H^+), supporting the PSS^-groups at the film's surface that operate as a barrier to the extraction of electrons [157].

Huang *et al.* studied the conductivities that resulted after annealing operations on PEDOT:PSS films coated on ITO glass in the air and under nitrogen (N_2). After 10 to 20 minutes of annealing at 200 °C in the presence of N_2, the conductivity of PEDOT:PSS was maximized. In contrast to the films annealed in the air, the work function for films annealed in an N_2 atmosphere was not only higher but also marginally increased with higher temperatures [73, 76].

According to Nardes *et al.*, the conductivity of undoped PEDOT:PSS is a function of the annealing and cooling processes [94]. The in-situ conductivity of the PEDOT:PSS increases with temperature during the annealing process, but it decreases again at ever-lower temperatures during the subsequent cooling. The conductivity, however, stays higher after the annealing and cooling processes. After several hours of exposure to 49% RH, it was found that the PEDOT:PSS film that wasn't doped restored its previous weight, whereas the film that was doped with sorbitol consistently had less water absorption. Similarly, Bießmann *et al.* discovered that adding ethylene glycol and zonyl results in lower water absorption than pure PEDOT:PSS films [158].

Thus, it can be concluded that it is essential to keep a close eye on aspects of the processing conditions in order to produce PEDOT:PSS films that are conductive and stable.

4.3.1 Impact of thermal annealing on the work function of PEDOT:PSS films

PEDOT:PSS is often deposited from an aqueous dispersion into thin films using several techniques such as slot-die coating, spin coating, or doctor blading. These films are frequently thermally annealed since it is necessary to reduce the amount of water content that remains and to dry them.

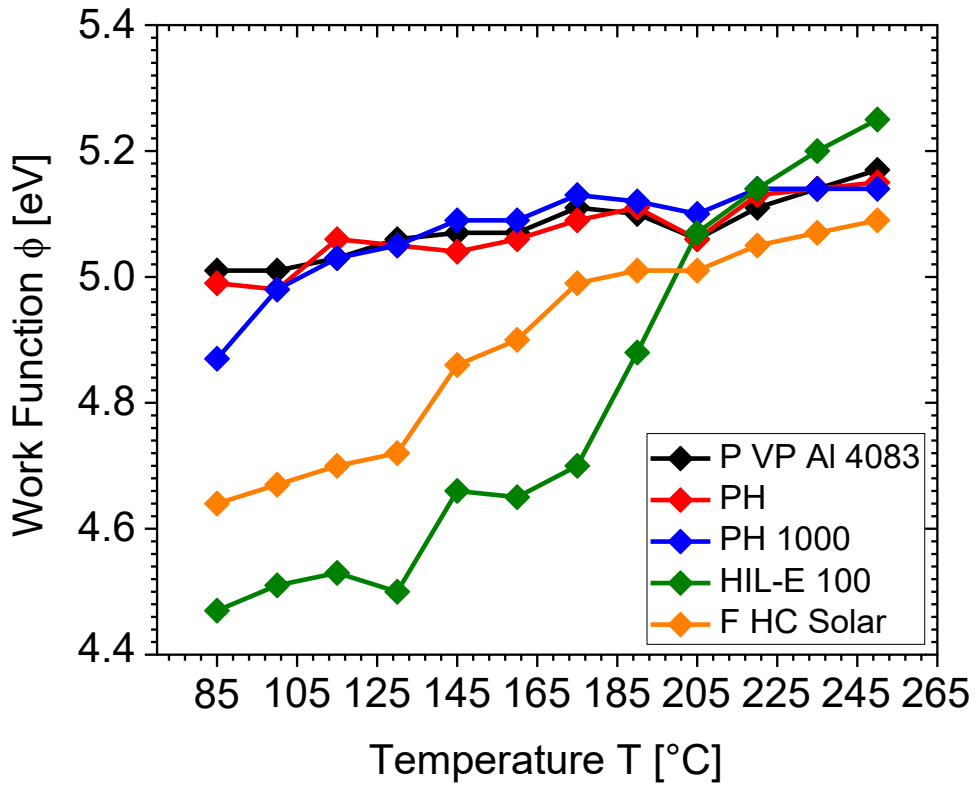

Figure 55: *The impact of annealing temperature on the work function of films made from several commercial PEDOT:PSS formulations.*

Thus, for the several commercial PEDOT:PSS formulations (Table 1), which were formed into films on top of ITO-glass substrates through spin coating, the impact of the annealing temperature on the resultant work function was initially examined. The thermal annealing was carried out at different temperatures as mentioned in experimental Section 3.1.3 (i). For the reason that higher annealing temperatures might potentially cause the disintegration of

PEDOT:PSS, the annealing temperature was kept below 250 °C [159]. The impact of annealing on the work functions of the PEDOT:PSS films is shown in Figure 55.

It is interesting to note that higher annealing temperatures often result in higher work functions, despite minor variations in the work function found for different formulations. In contrast to films cast from formulations HIL-E 100 and F HC Solar, which exhibited significant variations, films created from formulations P VP AI 4083, PH1000, and PH revealed a relatively similar trend in the work function throughout all the annealing temperatures. HIL-E 100 had the highest variation, with annealing temperatures ranging from 85 °C to 245 °C, covering a range of around 0.8 eV between 4.45 eV and 5.25 eV. The work function variation for F HC Solar was about halved, ranging from 4.65 eV to 5.10 eV. The overall increase in work function was not unexpected because similar patterns had already been noted by others [156, 157]. According to refs.[156, 157, 159-161], such an increase in the work function must be connected to the development of a PSS on the top layer, whose negative charge prevents electron extraction.

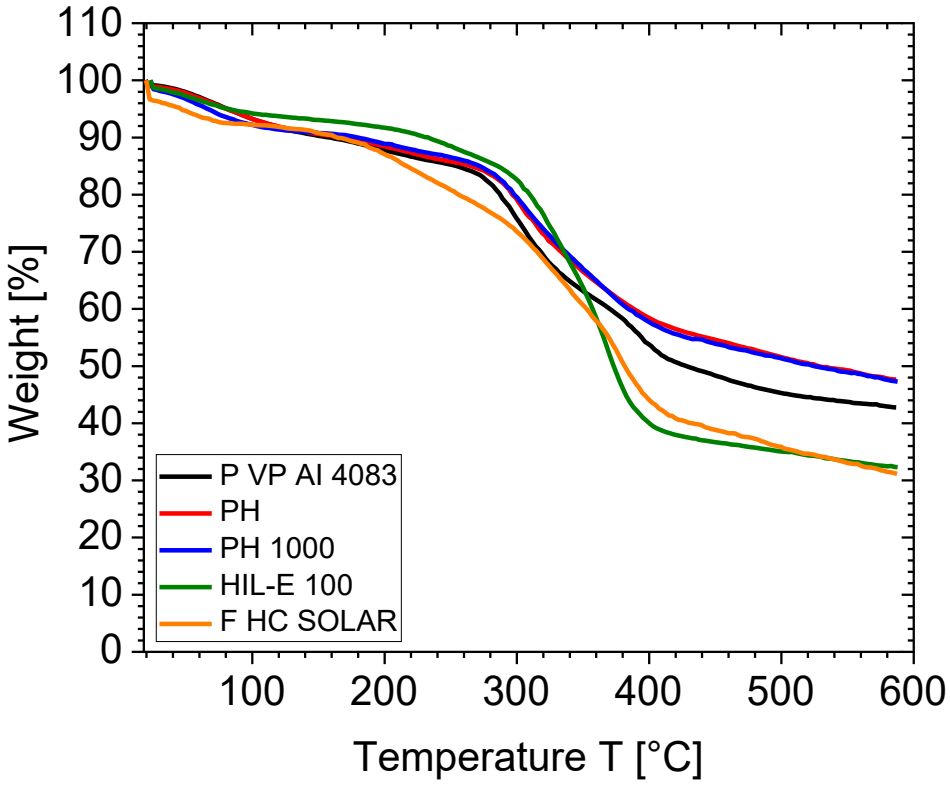

Figure 56: *TGA of various PEDOT:PSS commercial formulations.*

The dried film drop-cast from various PEDOT:PSS formulations was examined with thermo-gravimetric analysis (TGA) to learn more about the thermal stability of PEDOT:PSS, as shown in Figure 56. The PEDOT:PSS films were placed in a climate chamber overnight at room temperature for drying, and they were then brought right into the TGA measurement apparatus. Surprisingly, weight loss was already seen in every case when the temperature was below 100 °C. With increasing temperatures, a few percent progressive loss was observed, which changed to a rapid loss beyond 270 °C, indicating material breakdown.

At temperatures around and above 400 °C, this breakdown faded out, becoming a lower loss rate for all formulations with a residual weight of between 30 and 60% of the initial value. While pristine PEDOT decomposes as reported to undergo similar decomposition (as seen in Figure 56) eventually ending at about 70−75% of the initial weight [162], pristine PSS is said to be stable up to 400 °C and undergo a two-step thermal breakdown between 400 °C and 600 °C [163].

At such high temperatures, however, the weight fraction of PEDOT:PSS that was still present was typically larger for formulations with a low PSS component. The only formulation that seemed to defy this trend was Heraeus Clevios-F HC Solar. But between 180 °C and 280 °C, this formulation showed a significant extra loss of about 20%, which might be related to the elimination or breakdown of another ingredient. Without such a loss, the TGA curve beyond 400 °C would simply converge with the results reported for formulations PH and PH1000, which both include the same PEDOT:PSS component ratio. Clevios HIL-E 100, the formulation with the highest weight fraction of PSS (88% regarding PEDOT), demonstrated a distinct behavior. The final weight turns out to be surprisingly low, and it appears that this formulation follows a completely different pattern over the whole temperature range. In summary, it can be said that at this stage, mainly water, followed by additives with higher boiling points at higher temperatures, is what escapes from the PEDOT:PSS films during annealing up to roughly 120 °C. The PEDOT and PSS fractions decompose and partially overlap above 270 °C and 400 °C, respectively.

Conventional PCDTBT:$PC_{70}BM$ solar cells were fabricated as per the experimental section's (3.1.3 (ii)) guidelines to illustrate the impact of PEDOT:PSS thermal treatments on organic solar cells. The PEDOT:PSS formulations P VP AI 4083 and HIL-E 100 were selected as the hole transport layers since the first is regarded as a global laboratory standard and the second

may disclose stronger effects due to its demonstrated substantial fluctuation in work function with annealing temperature.

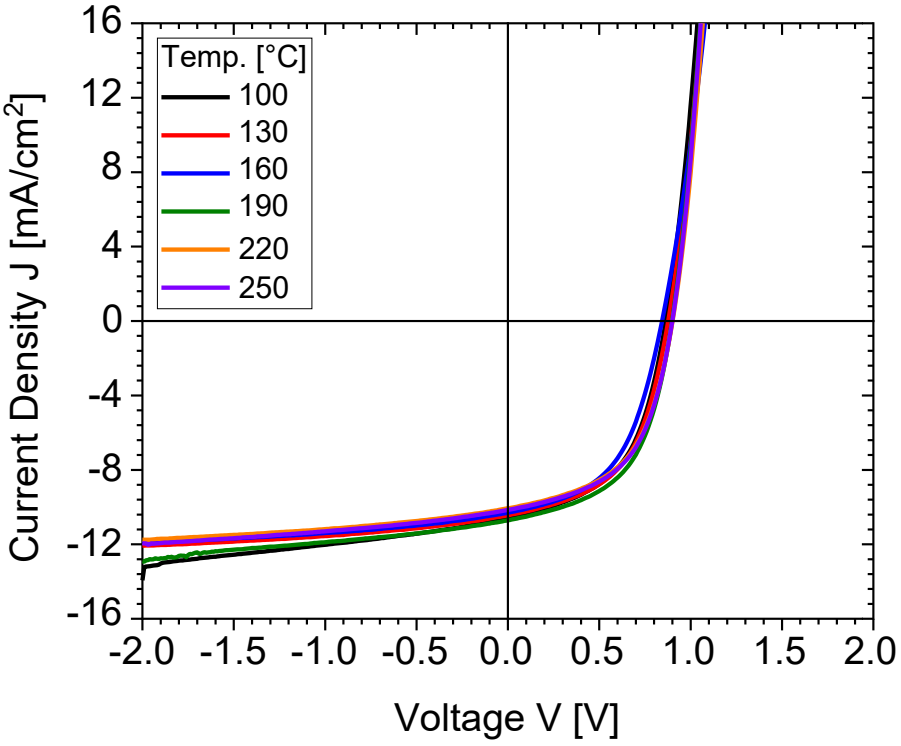

Figure 57: *Graph showing the relationship between current density and voltage for PCDTBT:$PC_{70}BM$ solar cells made from films of PEDOT:PSS (Clevios P VP AI 4083) that were annealed at various temperatures.*

Table 6: *Solar cell parameters of PCDTBT:$PC_{70}BM$ solar cells made from PEDOT:PSS (Clevios P VP AI 4083) films that were annealed at various annealing temperatures.*

Annealing Temperature of PEDOT:PSS (P VP AI 4083)	**J_{sc} [mA/cm²]**	**V_{oc} [mV]**	**FF [%]**	**PCE [%]**	**R_s [Ω]**	**R_p [Ω]**
100	9.10	855	53	4.13	8	1215
130	9.24	875	53	4.29	8	1264
160	9.85	842	51	4.22	10	1267
190	9.44	895	54	4.56	8	1279
220	9.19	898	53	4.38	8	1306
250	9.39	897	53	4.47	8	1289

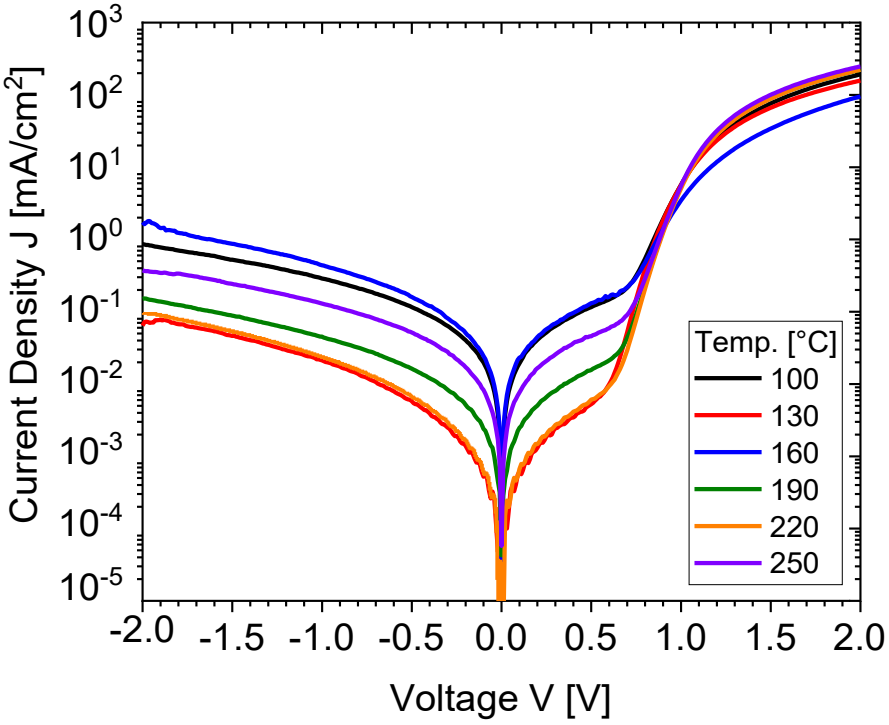

Figure 58: *Dark current density vs. voltage plot of PCDTBT:PC$_{70}$BM solar cells made from films of PEDOT:PSS (Clevios P VP AI 4083) that have been annealed at various temperatures.*

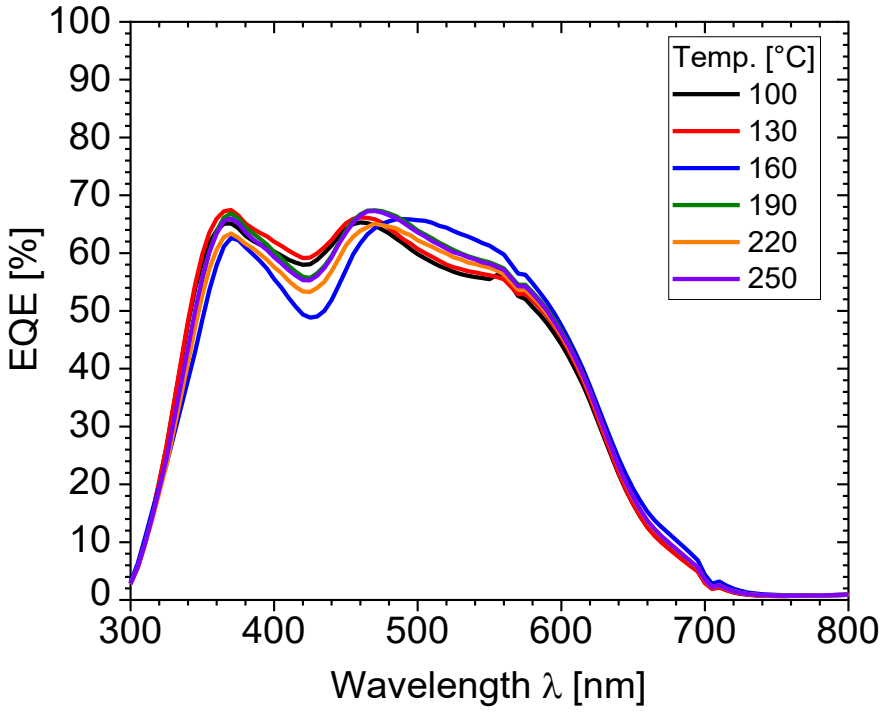

Figure 59: *EQE spectra of PCDTBT:PC$_{70}$BM solar cells made from films of PEDOT:PSS (Clevios P VP AI 4083) that have been annealed at various temperatures.*

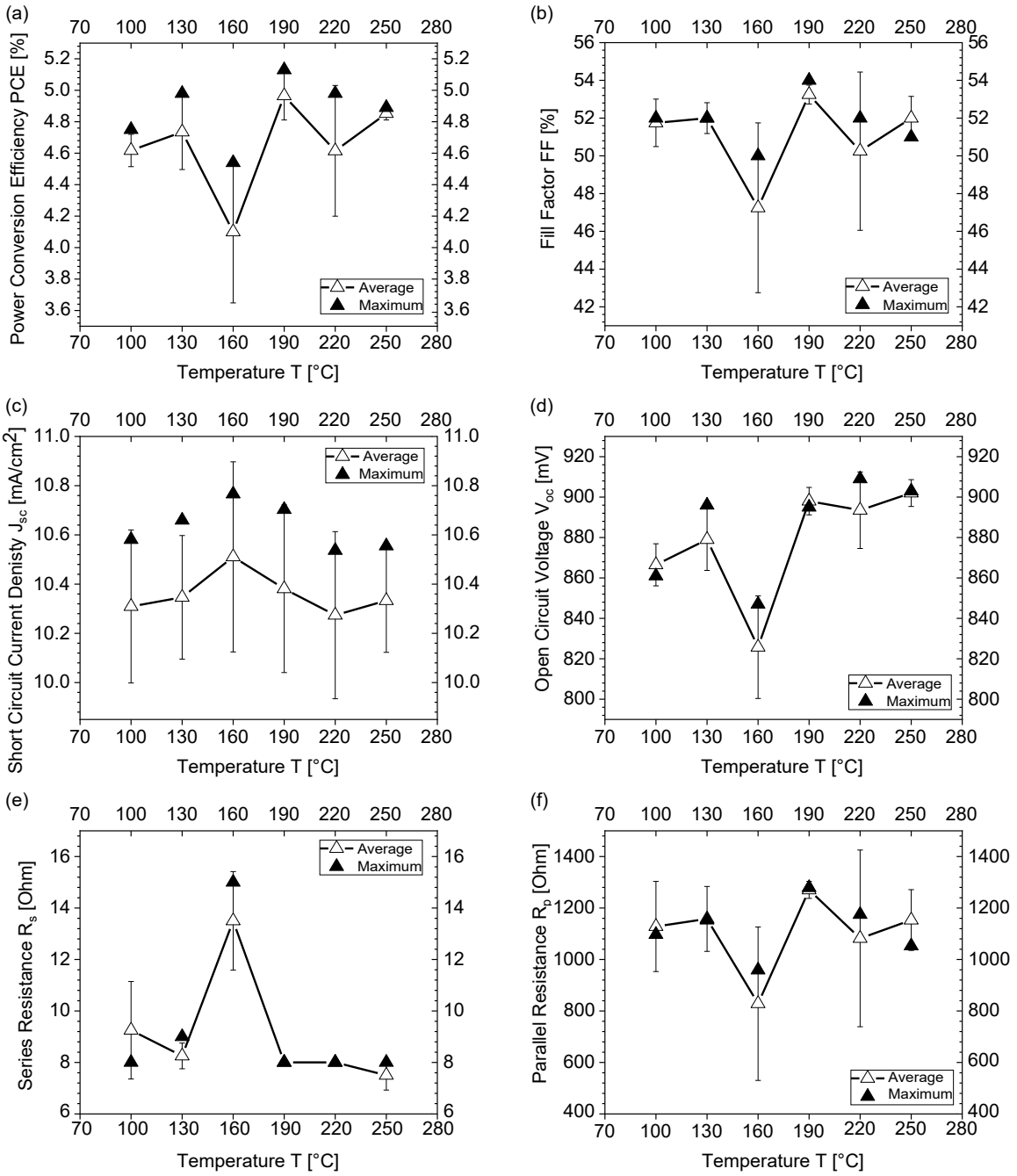

Figure 60: *Statistical analysis of (a) power conversion efficiency, (b) fill factor, (c) open circuit voltage, (d) short circuit current density, (e) series resistance, and (f) parallel resistance of PCDTBT:PC$_{70}$BM solar cells made from films of PEDOT:PSS (Clevios P VP AI 4083) that have been annealed at various temperatures.*

Figure 57 and Table 6 show the JV curves and solar cell parameters; Figure 58 and Figure 59 display the dark JV curves and EQE spectra; and Figure 60 depicts the statistical analysis of the PCDTBT:PC$_{70}$BM solar cells fabricated with PEDOT:PSS (Clevios P VP AI 4083).

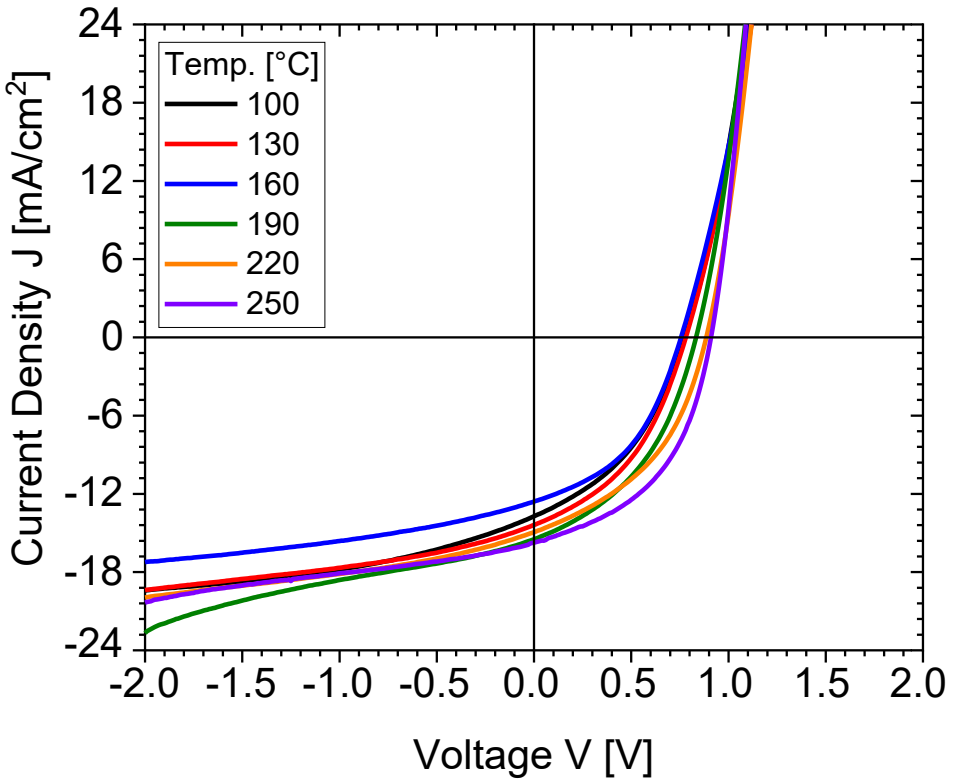

Figure 61: *Current density vs. voltage graph of PCDTBT:PC$_{70}$BM solar cells made from films of PEDOT:PSS (Clevios HIL-E 100) that were annealed at various temperatures.*

Table 7: *Solar cell parameters of PCDTBT:PC$_{70}$BM solar cells made from films of PEDOT:PSS (Clevios HIL-E 100) that were annealed at various temperatures.*

Annealing Temperature of PEDOT:PSS (HIL-E 100)	**J_{sc} [mA/cm²]**	**V_{oc} [mV]**	**FF [%]**	**PCE [%]**	**R_s [Ω]**	**R_p [Ω]**
100	8.96	772	40	2.77	12	360
130	8.92	780	41	2.86	12	400
160	8.85	756	44	2.95	12	488
190	8.86	831	42	3.10	8	425
220	8.32	884	43	3.17	9	437
250	8.95	907	47	3.82	8	545

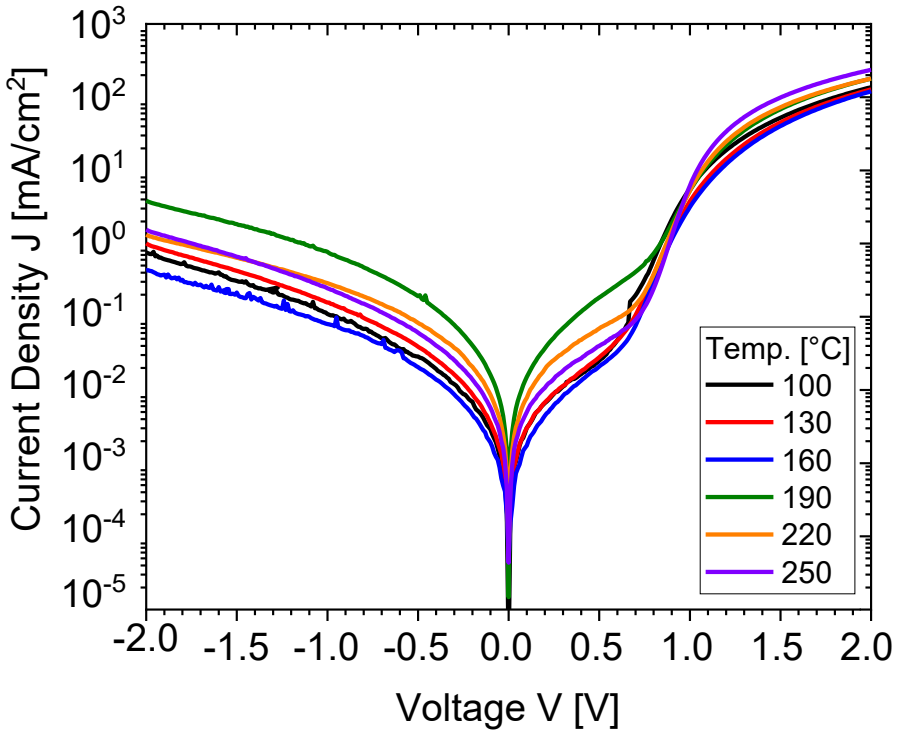

Figure 62: *Dark current density vs. voltage graph of PCDTBT:PC$_{70}$BM solar cells made from films of PEDOT:PSS (Clevios HIL-E 100) that were annealed at various temperatures.*

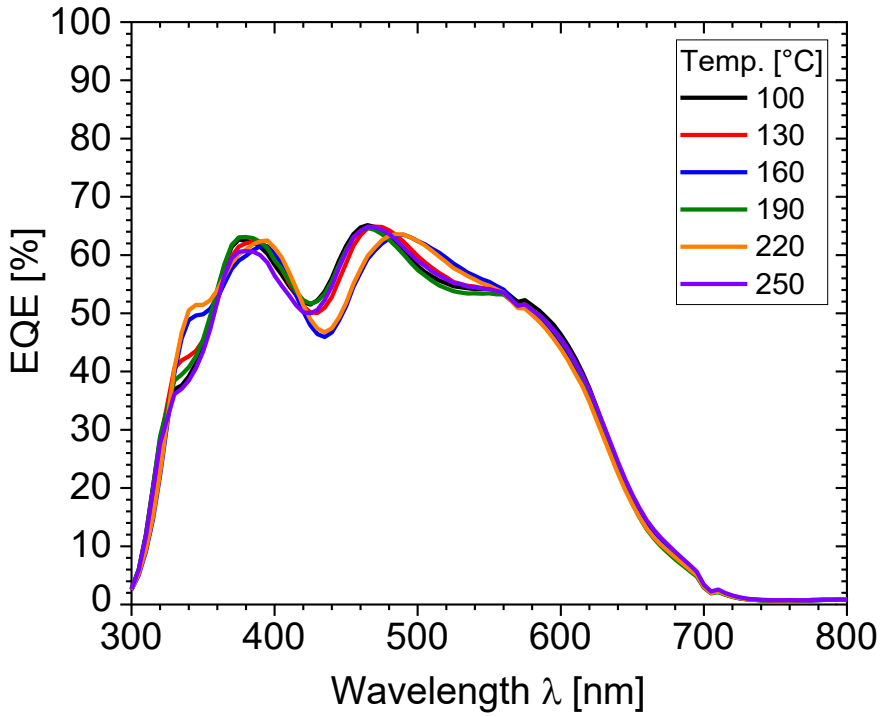

Figure 63: *EQE spectra of PCDTBT:PC$_{70}$BM solar cells made from films of PEDOT:PSS (Clevios HIL-E 100) that were annealed at various temperatures.*

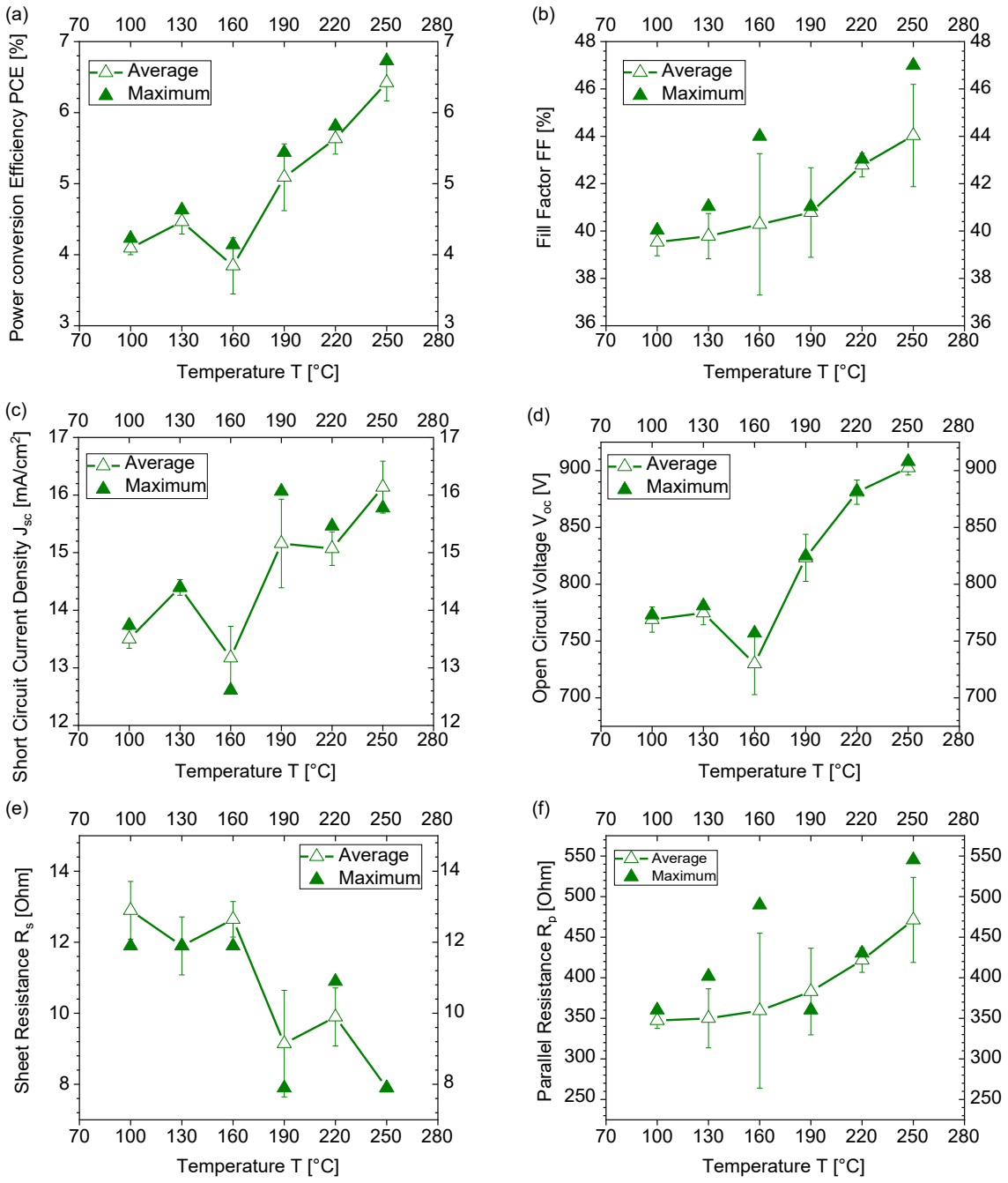

Figure 64: *Statistical analysis of (a) power conversion efficiency, (b) fill factor, (c) open circuit voltage, (d) short circuit current density, (e) series resistance, and (f) parallel resistance of PCDTBT:PC$_{70}$BM solar cells made from films of PEDOT:PSS (Clevios HIL-E 100) that were annealed at various temperatures.*

Figure 61 and Table 7 show the JV curves and solar cell parameters; Figure 62 and Figure 63 display the dark JV curves and EQE spectra; and Figure 64 depicts the statistical analysis of the PCDTBT:PC$_{70}$BM solar cells fabricated with PEDOT:PSS (Clevios HIL-E 100). To demonstrate the effect of PEDOT:PSS processing with different thermal treatments on a

standard system of organic solar cells, PEDOT:PSS (Clevios P VP AI 4083) films were also used as a hole transport layer in P3HT:$PC_{60}BM$ solar cells to test another system.

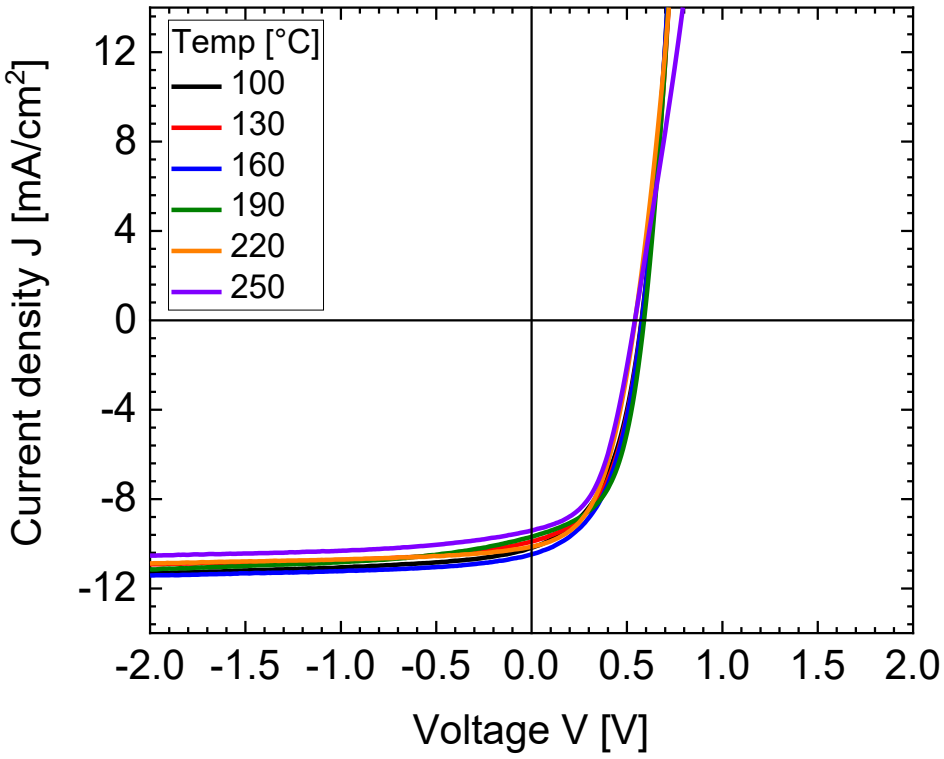

Figure 65: *Current density vs. voltage graph of P3HT:$PC_{60}BM$ solar cells made from films of PEDOT:PSS (Clevios P VP AI 4083) that were annealed at various temperatures.*

Table 8: *Solar cell parameters of P3HT:$PC_{60}BM$ solar cells made from films of PEDOT:PSS (Clevios P VP AI 4083) that were annealed at various temperatures.*

Annealing Temperature of PEDOT:PSS (PVP AI 4083)	**J_{sc} [mA/cm²]**	**V_{oc} [mV]**	**FF [%]**	**PCE [%]**	**R_s [Ω]**	**R_p [Ω]**
100	10.157	574	47	2.77	7	816
130	9.887	577	50	2.85	7	1036
160	10.455	576	49	2.94	7	966
190	9.675	587	53	3.02	7	982
220	10.112	541	49	2.66	8	1278
250	9.396	541	49	2.51	12	1139

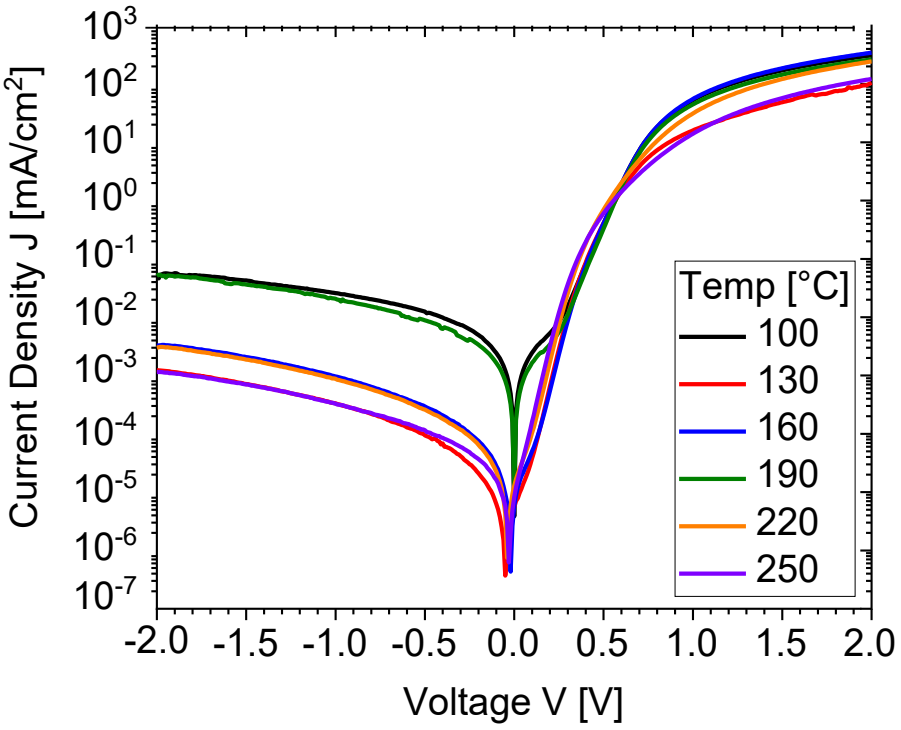

Figure 66: *Dark current density vs. voltage graph of P3HT:PC$_{60}$BM solar cells made from films of PEDOT:PSS (Clevios P VP AI 4083) that were annealed at various temperatures.*

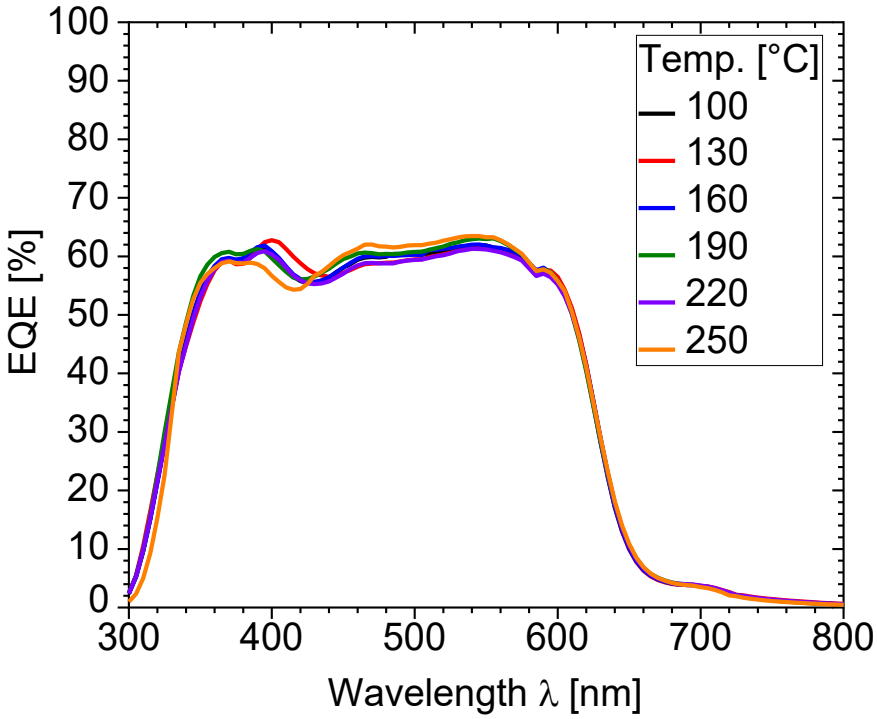

Figure 67: *EQE spectra of P3HT:PC$_{60}$BM solar cells made from films of PEDOT:PSS (Clevios P VP AI 4083) that were annealed at various temperatures.*

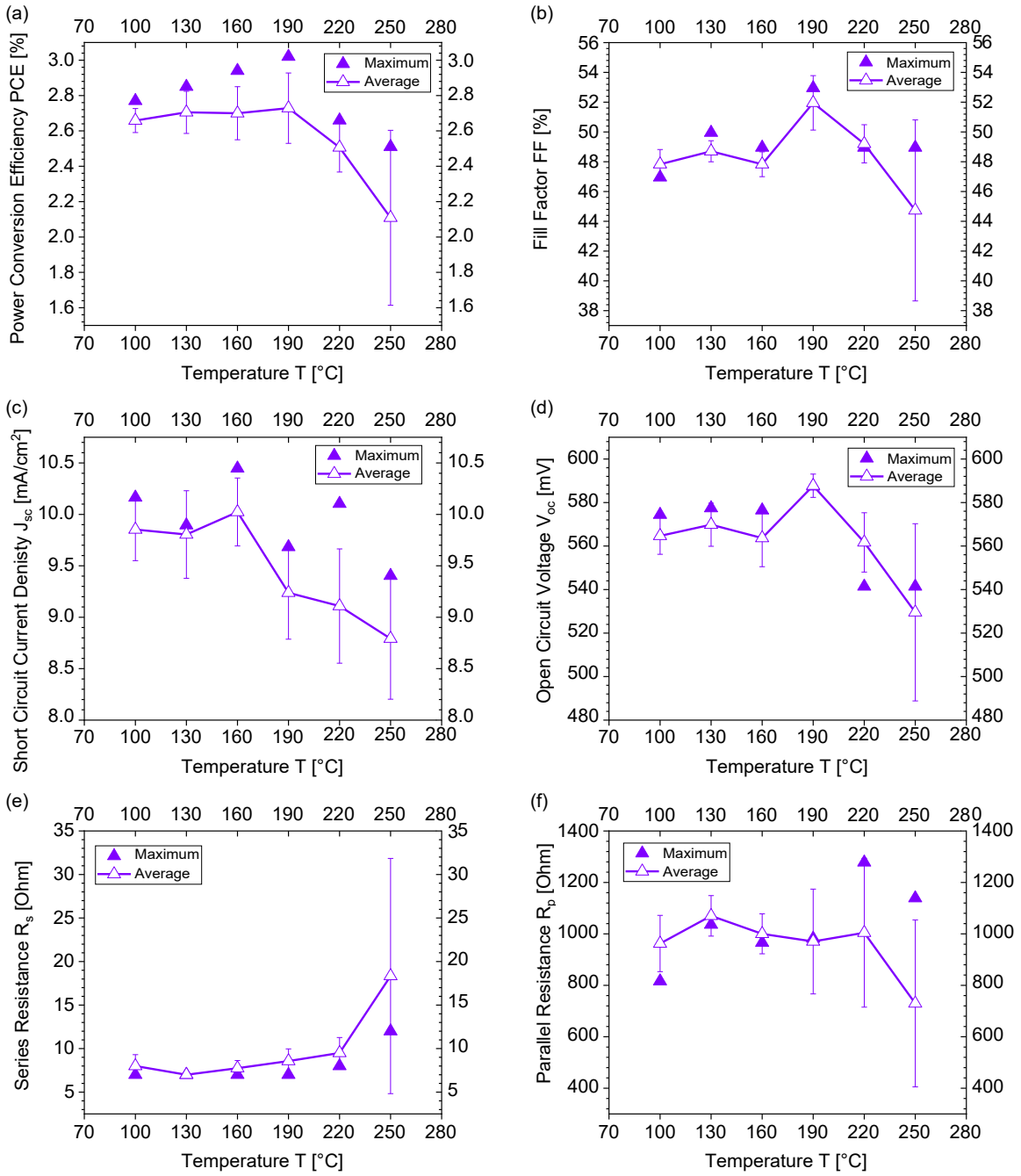

Figure 68: *Statistical analysis of (a) power conversion efficiency, (b) fill factor, (c) open circuit voltage, (d)s circuit current density, (e) series resistance, and (f) parallel resistance of P3HT:PC$_{60}$BM solar cells made from films of PEDOT:PSS (Clevios P VP AI 4083) that were annealed at various temperatures.*

Figure 65 and Table 8 show the JV curves and solar cell parameters; Figure 66 and Figure 67 display the dark JV curves and EQE spectra; and Figure 68 depicts the statistical analysis of the P3HT:PC$_{60}$BM solar cells fabricated with PEDOT:PSS (Clevios P VP AI 4083).

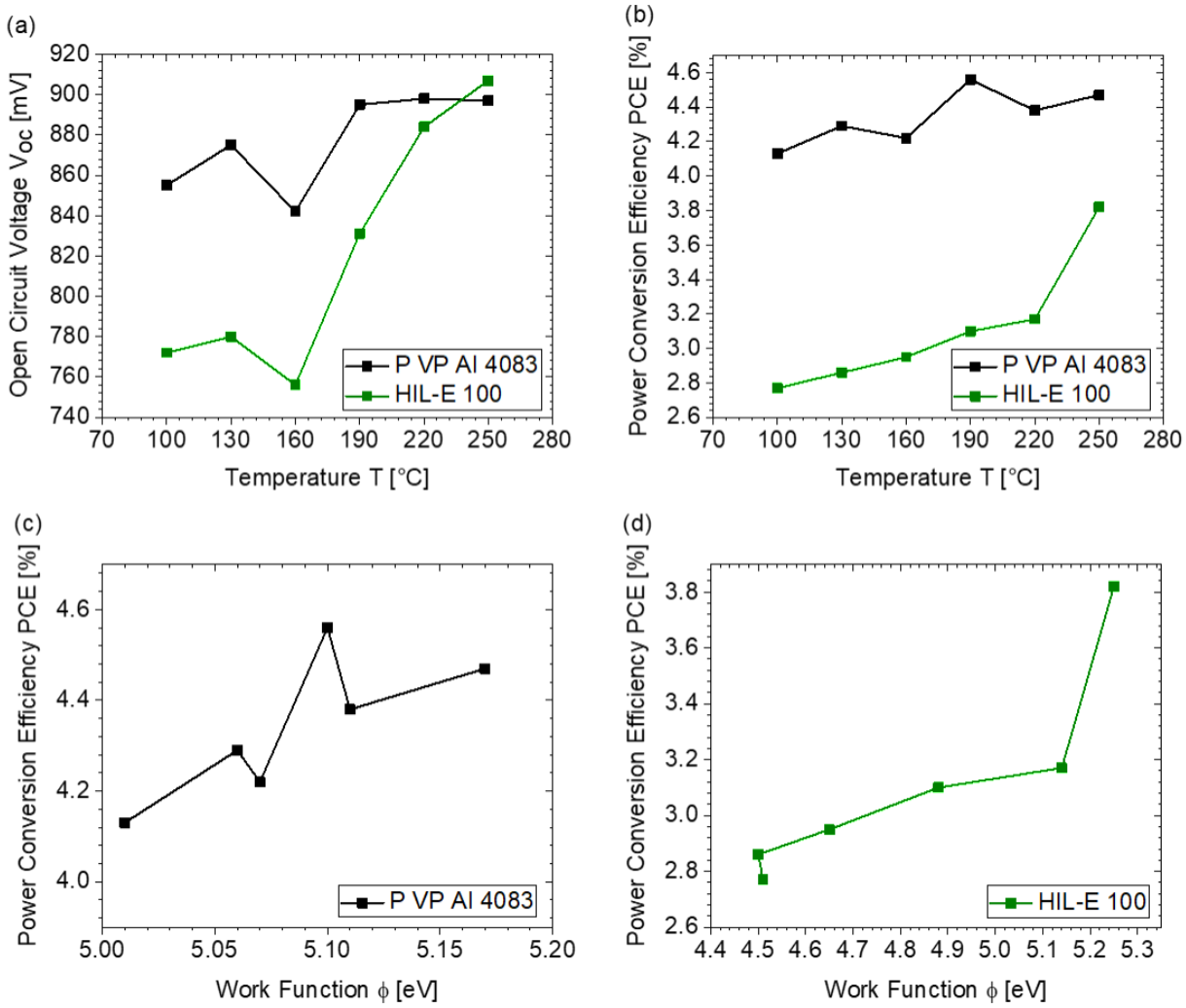

Figure 69: *(a) Open-circuit voltage vs. annealing temperature and (b) PCE vs. annealing temperature of PCDTBT:$PC_{70}BM$ solar cells made using Clevios P VP AI 4083 and HIL-E 100 formulations. Plots showing the power conversion efficiency of identical devices relative to the work function of PEDOT:PSS films manufactured from the Clevios P VP AI 4083 (c) and Clevios HIL-E 100 (d) formulations.*

The open-circuit voltage (V_{OC}) and PCE of typical PCDTBT:$PC_{70}BM$ solar cells show a clear trend, as shown in Figure 69 (a) and (b): with increasing annealing temperatures, the work function (Figure 55) and, consequently, also the PV parameters were raised. This would make sense given that more interfacial recombination is predicted to occur the closer the PEDOT:PSS work function is centered between the PCDTBT highest occupied molecular orbital (HOMO) (– 5.4 eV) and the $PC_{70}BM$ lowest unoccupied molecular orbital (LUMO) (– 4.3 eV). A work function of 4.85 eV would therefore be predicted to have the highest recombination probability. Furthermore, the performance of HIL-E 100 was generally worse,

resulting in a significant offset when compared to the other, more conventional PEDOT:PSS formulation. This illustrates clearly that the device performance is impacted by the PEDOT:PSS annealing and the consequent work function.

The lower performance (Figure 65, Figure 66, Table 8) variation in P3HT:$PC_{60}BM$ solar cells was attributed to the P3HT's higher HOMO level, which is positioned at about –5.1 eV The hole extraction barrier caused all PV parameters (Figure 68) to decrease as soon as the PEDOT:PSS work function exceeded the P3HT's HOMO threshold. These results furthermore demonstrate that other interfacial features, such as charge carrier selectivity, in addition to the work function, affect the device's performance.

4.3.2 Impact of humidity on the work function of PEDOT:PSS films

For the first trial, different PEDOT:PSS film formulations were coated on ITO-glass and annealed at 178 °C for 15 minutes as indicated in the experimental section's (3.1.3 (i)) to track changes in the work function for PEDOT:PSS. For the initial test (Figure 71), the shift in work function for P VP AI 4083 and PH1000 was observed, which was constantly observed at 70% RH for two hours. Different commercial PEDOT:PSS formulations showed an increase in work function over time, as seen in Figure 70. It was clear that when environmental conditions vary, PEDOT:PSS's work function alters, indicating that the film's surface has changed.

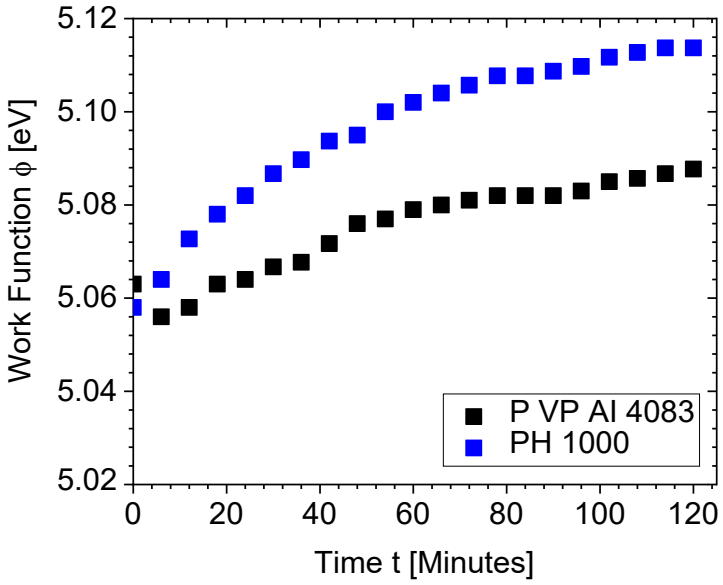

Figure 70: *Time-development of work functions of PEDOT:PSS formulation films (Clevios P VP AI 4083 and PH1000) at 70% RH.*

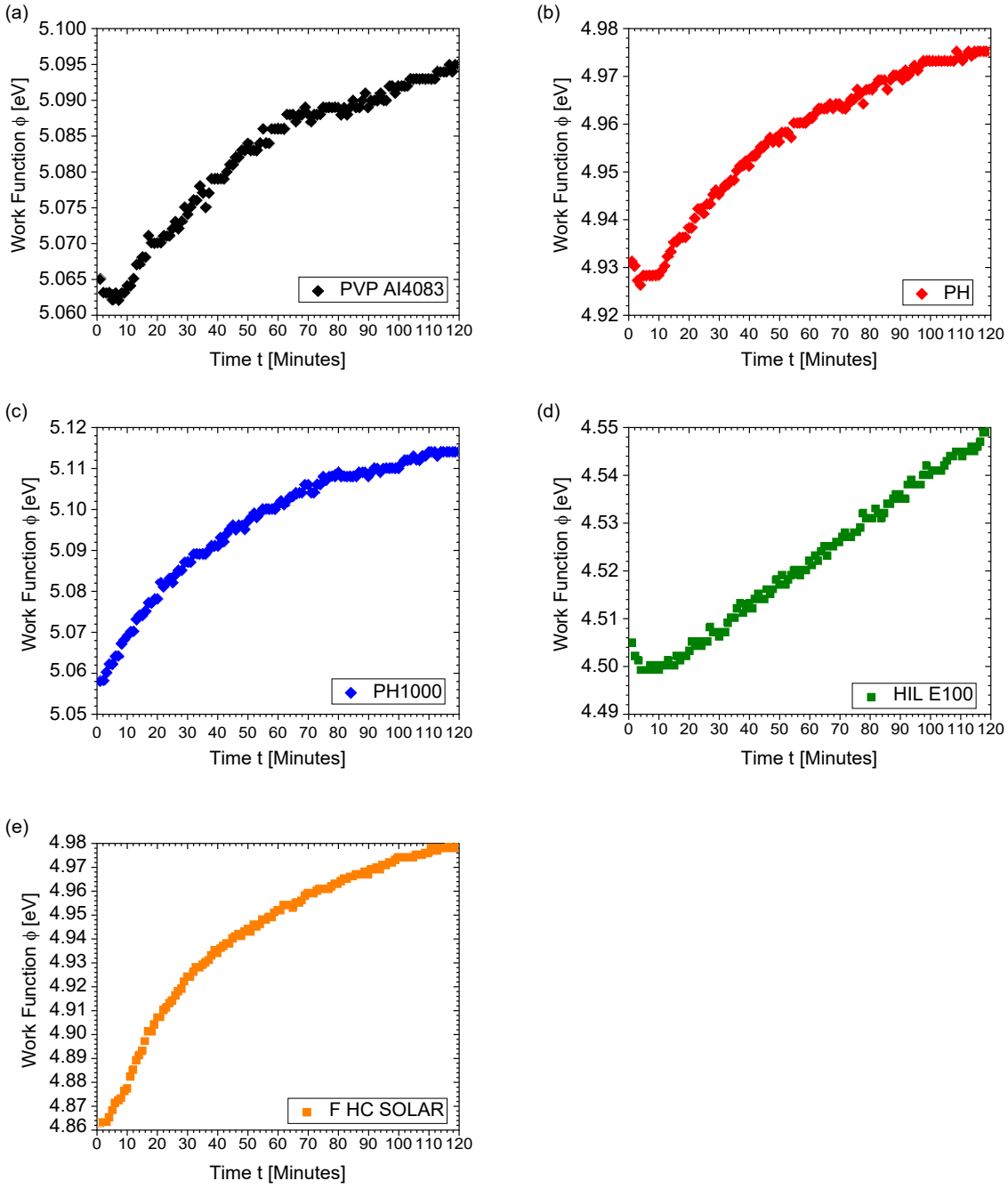

Figure 71: *Various PEDOT:PSS formulation films' work functions development with time in ambient air (a) P VP AI 4083 (70% RH), (b) PH (60% RH), (c) PH1000 (70% RH), (d) HIL-E 100 (94% RH), and (e) F HC Solar (93% RH) .*

For a controlled humidity investigation, three PEDOT:PSS formulations (P VP AI 4083, PH1000, and HIL-E 100) were chosen. On top of ITO-glass substrates, these PEDOT:PSS films were spin-coated at 3000 rpm and then thermally annealed at 100 °C, 130 °C, 160 °C, 190 °C, 220 °C, and 250 °C for 15 minutes each. PEDOT:PSS films were kept in a climate-controlled room with regulated humidity and temperature to analyze the influence of

humidity on the work function of PEDOT:PSS films. To track the change, the work function was assessed on a consistent hourly basis for a total of six hours. The results are shown in Figure 72, Figure 73, and Figure 74. A bifurcation in the relationship between the work function's development over time and the humidity level is seen, in addition to a minor reliance on the initial work function due to the various annealing temperatures. Selective water adsorption occurs at PSS sites at low RH (10-25%), as shown by Muckley *et al.*. At an RH of between 25% and 60%, water is absorbed and diffused throughout the film, whereas as the RH rises above 60%, the water in the film becomes saturated, causing a wetting layer to form on the top of the PEDOT:PSS [164].

Thus, it can be guessed that the selective water adsorption at PSS sites should be the cause of the work function's diverging long-term behavior at 20% RH. With a few exceptions, there was a general tendency toward somewhat higher work function values and rather consistent behavior of the same throughout storage time for RH levels up to 50% RH. The work function frequently decreased with time if the RH was set to be significantly greater than 50% RH, which is in excellent accord with the saturation mentioned above. For the films that were annealed at 250 °C, stabilization via a decreasing drop-in work function was seen at the end of the test.

PSS is a polyelectrolyte, composed of poly(styrenesulfonate) (PSS^+ Na^-) and poly(styrenesulfonic acid) (PSSH). The fact that PSS is hygroscopic, like many salts, means that it has a high capacity for absorbing water, which in turn causes the film to inflate and, as a result, increases the mobility of the polymers inside [156, 158, 164, 165]. Additionally, water is probably going to cause the PSSH groups to dissociate, releasing hydronium ions and lowering the pH level in the process [164]. Given that the equilibrium concentration of water in the PEDOT:PSS film should depend on the RH of the environment, it makes sense that at greater RH, the changes to the film composition and therefore the work function would be more pronounced.

It is interesting to note, nevertheless, that regardless of the precise humidity level, the PEDOT:PSS film over ITO-glass appears to have a common work function in the end, or at the very least a convergence of the work function values acquired at greater humidity. With extended storage durations, the work function drop for the films that were annealed at 250 °C began to weaken and eventually reached a limit of around 4.8 eV, which is about 0.3 eV lower than the normal high value for lower humidity.

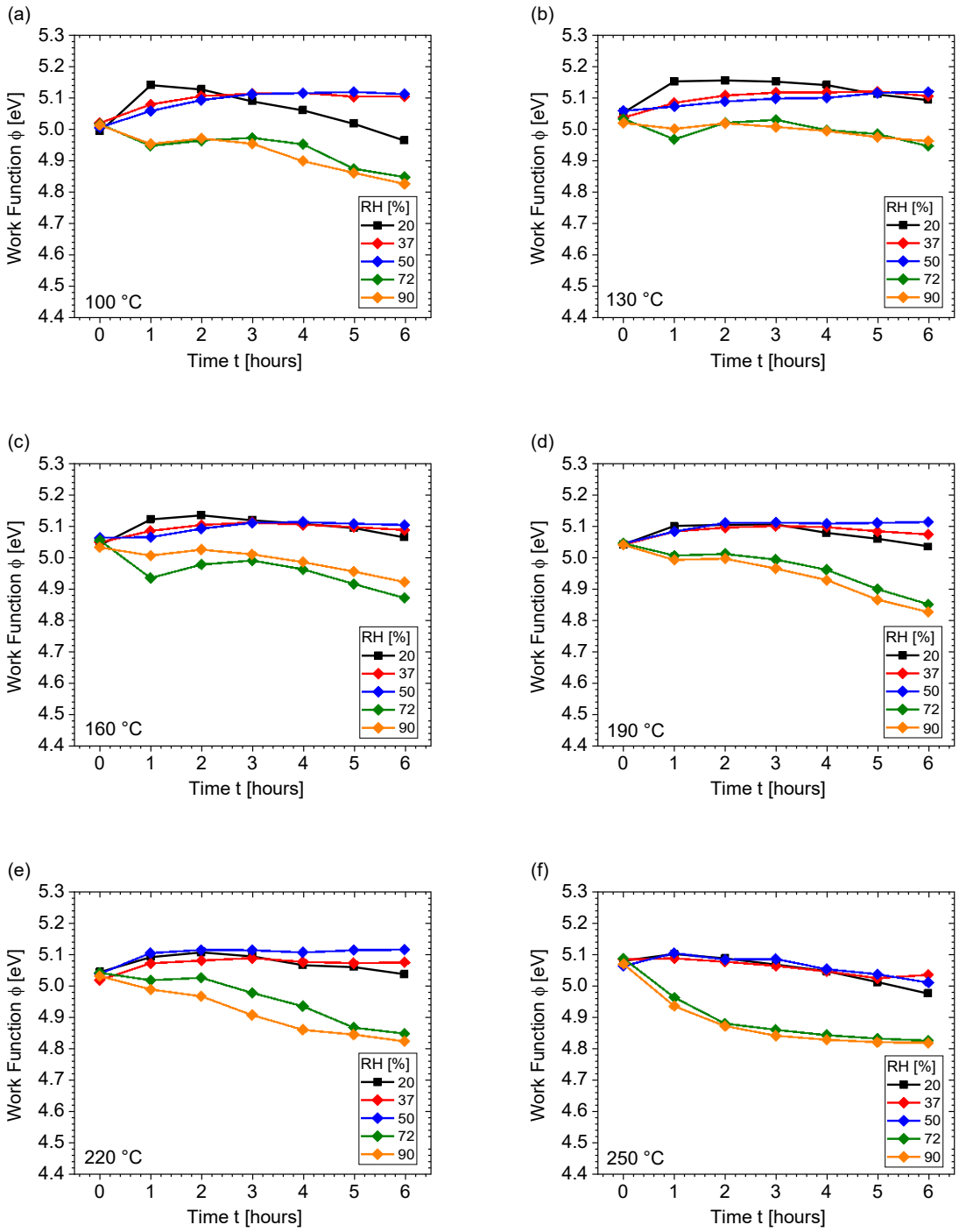

Figure 72: *Work function vs. storage duration of PEDOT:PSS (Clevios P VP AI 4083) films on ITO-glass for different annealing temperatures (a) 100 °C, (b) 130 °C, (c) 160 °C, (d) 190 °C, (e) 220 °C, and (f) 250 °C at different RH levels.*

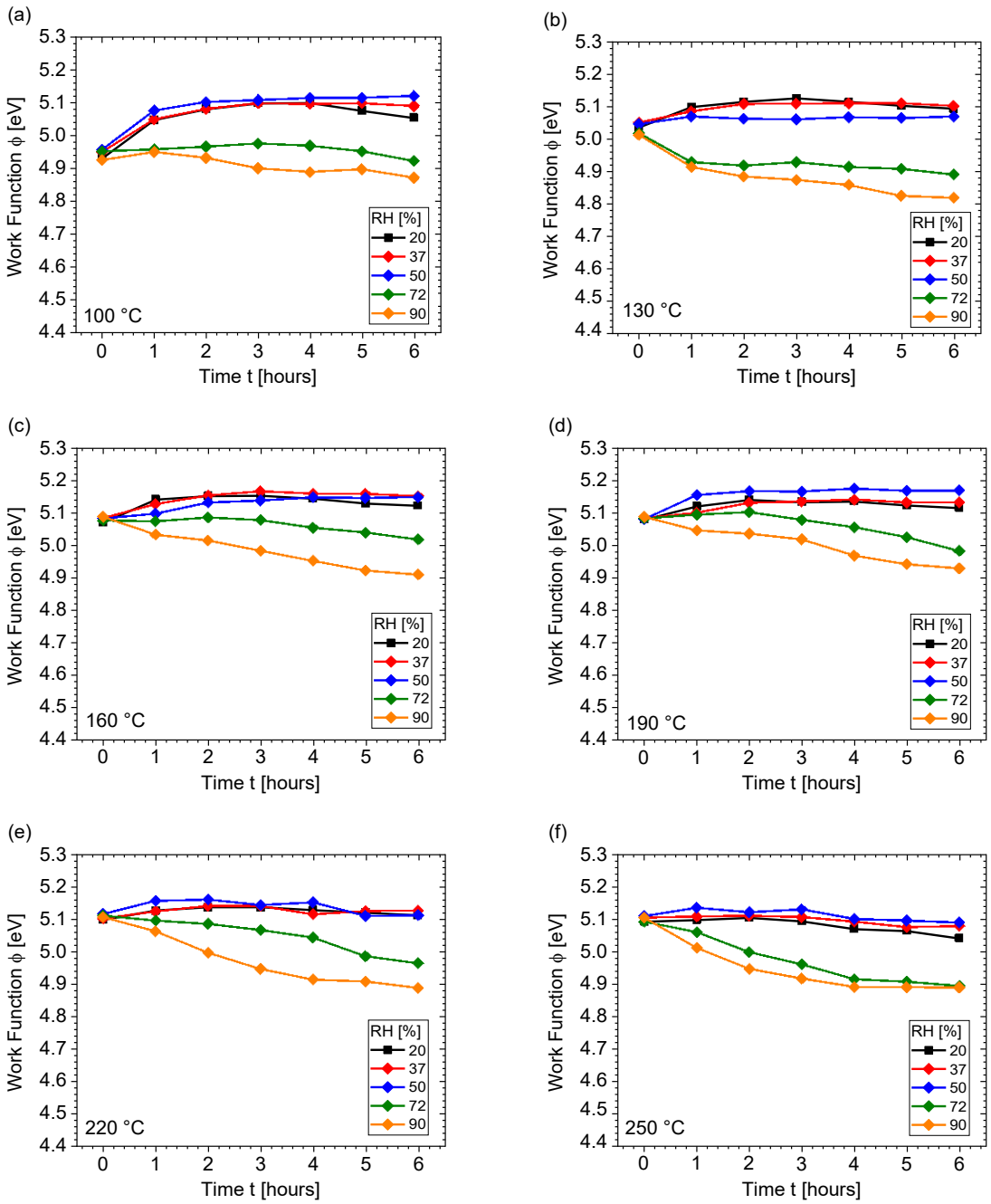

Figure 73: *Work function vs. storage duration of PEDOT:PSS (Clevios PH1000) films on ITO-glass for different annealing temperatures (a) 100 °C, (b) 130 °C, (c) 160 °C, (d) 190 °C, (e) 220 °C, and (f) 250 °C at different RH levels.*

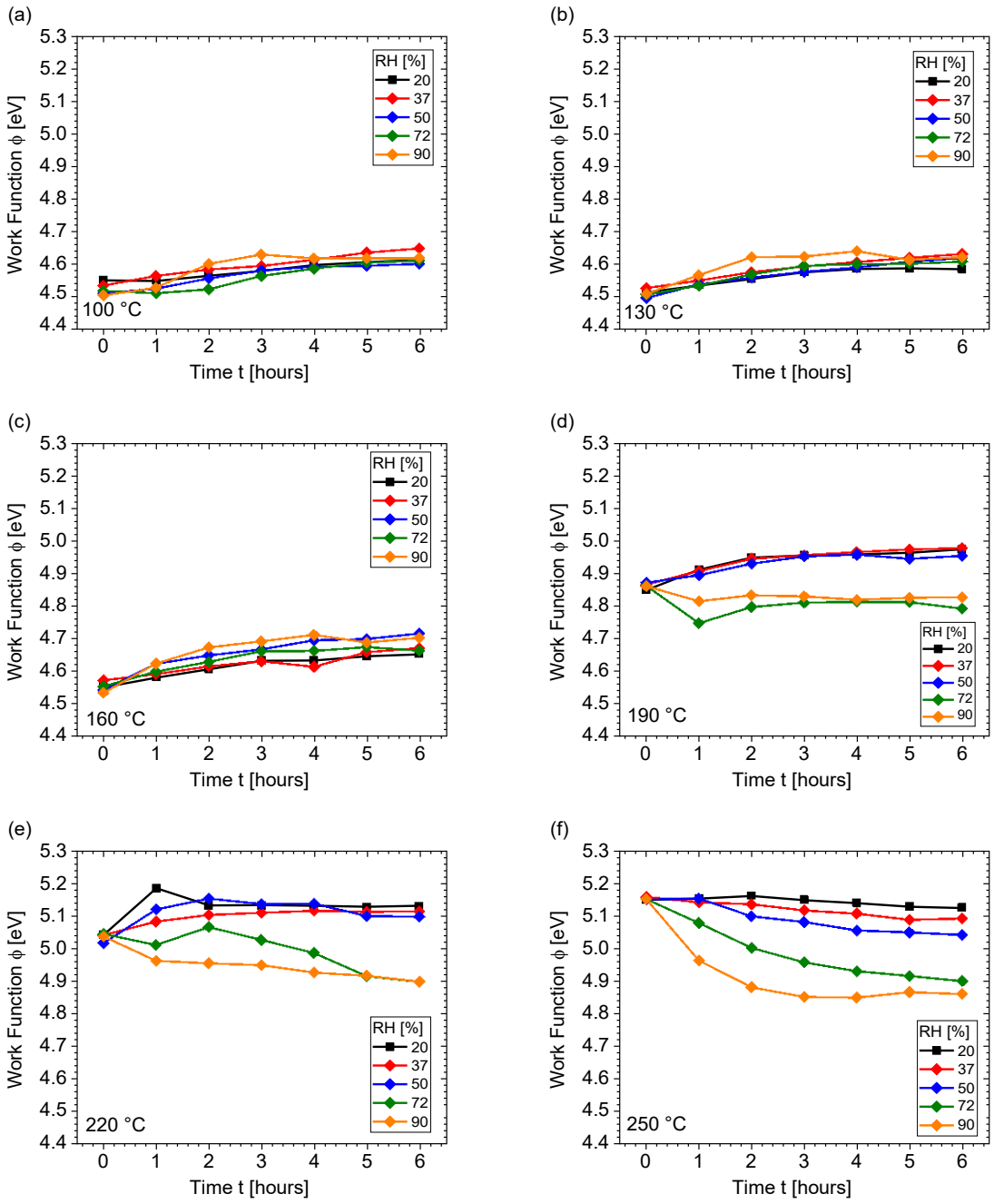

Figure 74: *Work function vs. storage duration of PEDOT:PSS (Clevios HIL-E 100) films on ITO-glass for different annealing temperatures (a) 100 °C, (b) 130 °C, (c) 160 °C, (d) 190 °C, (e) 220 °C, and (f) 250 °C at different RH levels.*

This experiment unequivocally demonstrates that extremely significant changes in the work function and, thus, in the prospective device performance are seen already during the first hour of storage, regardless of the precise chronological development.

For the moment, it is unclear if any vertical material rearrangement inside the PEDOT:PSS film, in addition to any potential rise in acidity caused by higher equilibrium concentrations of water, may affect the ensuing work function. Along with the work function, the PEDOT:PSS film's conductivity can also be negatively impacted by water-induced swelling because it may increase the average distance between conductive PEDOT chains [164, 166, 167]. This study demonstrates that there is a significant influence on the PEDOT:PSS films' ability to perform their intended function due to the (delayed) processing, or rather the storage environment.

4.3.3 PEDOT:PSS reversibility investigation

As it was previously mentioned, PEDOT:PSS films absorb water at greater relative humidity. That raises the question of whether this process is reversible. To investigate this, PEDOT:PSS films were applied to ITO-glass, annealed at 178 °C for 15 minutes, and then exposed in a climate room to 0 or 90% RH for an hour or 12 hours. The work function was then measured once again after removing the PEDOT:PSS films. After being exposed to humidity, PEDOT:PSS films were re-annealed under the same circumstances to recover their original characteristics.

The results are summarized in Figure 75 and Table 9 shows that storage for one hour at 0% RH had a very small influence on the work function and that re-annealing completely restored the initial value. Re-annealing even produced a little greater work function than during the first annealing in the case of a 12 hours storage period under identical RH conditions. For PEDOT:PSS films subjected to 90% RH, on the other hand, and as predicted from the humidity experiment above, there was a significant decline in the work function, which was even more obvious for the longer storage duration. Re-annealing resulted in a partial restoration of the work function in the event of a 1-hour storage period at high relative humidity. The lengthier exposure had no restoration after the second annealing, clearly demonstrating irreversibility under prolonged high RH conditions. According to the study, in order to preserve PEDOT:PSS's original qualities, exposure time to ambient air should be kept to a minimum.

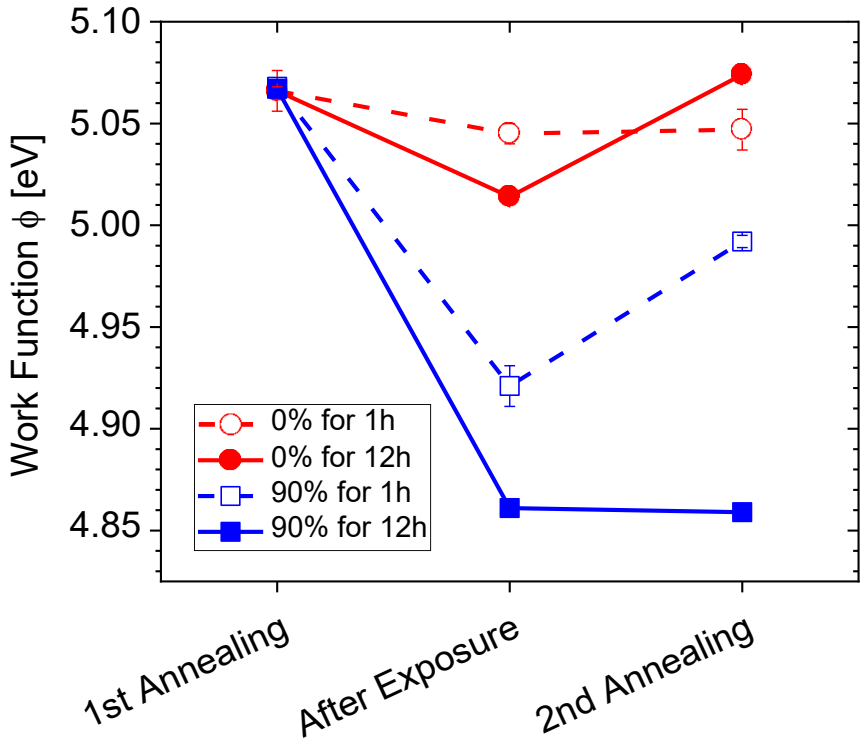

Figure 75: *Work function in relation to various processing settings for films made of PEDOT:PSS (Clevios P VP AI 4083) that were subjected to 0% or 90% RH for 1 hour or 12 hours, respectively.*

Table 9: *PEDOT:PSS (Clevios P VP AI 4083) film work function after exposure to 0% or 90% RH for an hour or 12 hours, respectively.*

Processing conditions of PEDOT:PSS films	**Work function [eV]**			
	0% RH for 1 h	**0% RH for 12 h**	**90% RH for 1 h**	**90% RH for 12 h**
1st Annealing	5.066 ± 0.010	5.066 ± 0.002	5.068 ± 0.003	5.067 ± 0.003
After Exposure	5.045 ± 0.005	5.014 ± 0.003	4.921 ± 0.010	4.861 ± 0.002
2nd Annealing	5.047 ± 0.010	5.074 ± 0.003	4.992 ± 0.003	4.859 ± 0.003

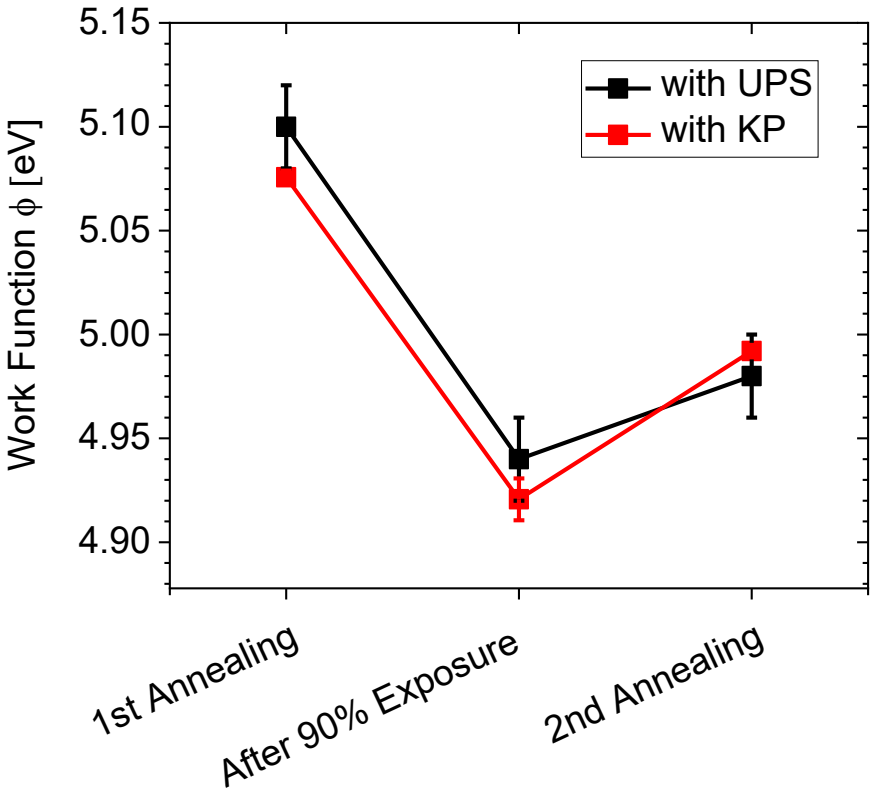

Figure 76: *Comparison between the results of the KP and UPS on films of PEDOT:PSS (Clevios P VP AI 4083) that had been re-annealed after being subjected to 90 percent RH for one hour.*

Table 10: *Comparison between the results of the KP and UPS work function values on films of PEDOT:PSS (Clevios P VP AI 4083) films exposed to 90% RH for one hour and then re-annealed.*

Processing conditions of PEDOT:PSS films	**Work function [eV]**	
	(KP)	**(UPS)**
1st Annealing	5.068 ± 0.003	5.10 ± 0.02
After 90% Exposure	4.921 ± 0.010	4.94 ± 0.02
2nd Annealing	4.992 ± 0.003	4.98 ± 0.02

The work functions of PEDOT:PSS films exposed at 90% RH for one hour were also obtained by UPS in order to confirm the Kelvin probe (KP) findings. Indeed, as shown in Figure 76 and Table 10, the work function values were acquired with astoundingly good agreement between the two measurement setups, with the largest divergence between the KP and UPS being just 32 meV. This verifies the KP system's accuracy.

For one hour, PEDOT:PSS films were subjected to 0% and 90% RH for one hour to show how exposure to varying humidity levels affected organic solar cells. Then, conventional PCDTBT:$PC_{70}BM$ solar cells were made according to standard procedure as explained in the experimental section (3.1.3 ii)). According to Figure 77, solar cells made with PEDOT:PSS (Clevios P VP AI 4083) films exposed to 0% RH performed similarly to solar cells made without any further processing other than the usual annealing at 178 °C for 15 minutes. The dark JV curves and the EQE spectra of solar cells which were fabricated with PEDOT:PSS films exposed at 0% or 90% RH for one hour are shown in Figure 78 and Figure 79 respectively. Figure 80 shows the statistical analysis of solar cells made with PEDOT:PSS exposed at 0% or 90% RH for one hour.

Was it possible for existing humidity-exposed PEDOT:PSS films to regain their original properties by an extra annealing step, this was particularly the specific interest of this study. Thus, after humidity exposure, PEDOT:PSS films were re-annealed PEDOT:PSS and then were used to fabricate solar cells.

Intriguingly, the performance of solar cells made using PEDOT:PSS films held at 0% RH for one hour as well as the same with an extra annealing step was almost the same, if not slightly enhanced. As shown in Table 11, solar cells made with PEDOT:PSS films exposed at 90% RH for one hour showed a decrease in V_{OC}, FF, and Rp, as well as an increase in Rs. Solar cells made with re-annealed PEDOT:PSS showed even more degradation after the same exposure. Once more, both deteriorations can be again linked to a decrease in the PEDOT:PSS work function, which encourages electron-hole recombination at this contact (compare with Figure 75). Organic solar cells using PEDOT:PSS layers had already been shown by Kawano *et al.* to exhibit a significant rise in series resistance when exposed to humid air, although this remained constant when just ITO was employed for hole extraction [168]. The same patterns were also seen in solar cells made with PEDOT:PSS films and subjected to 0% or 90% RH over 12 hours (Figure 81, Table 12).

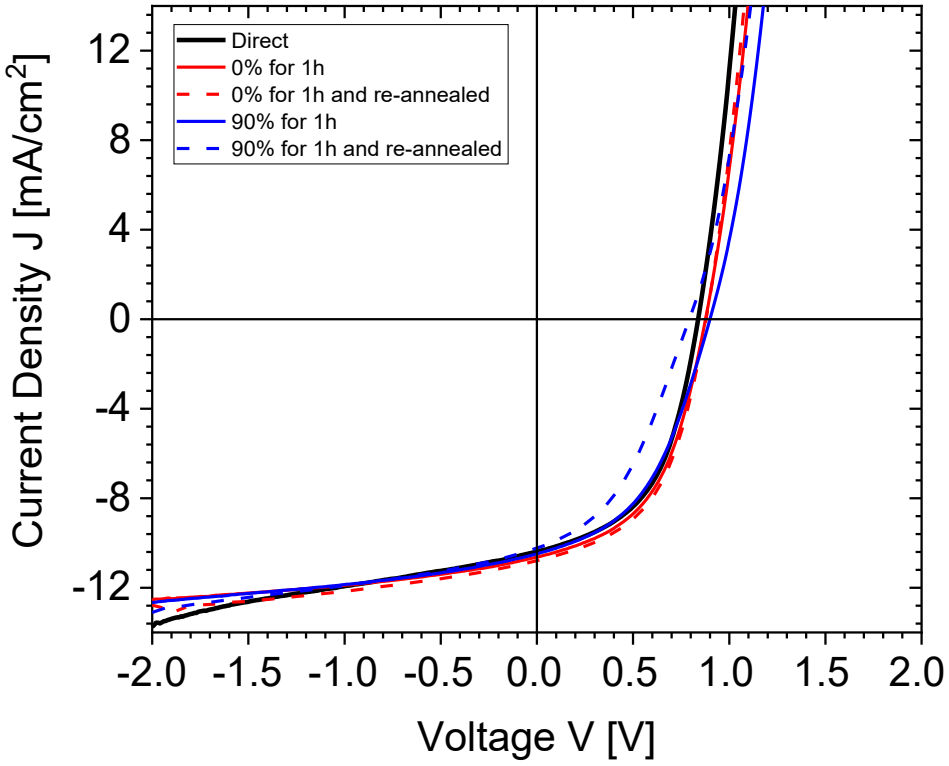

Figure 77: *Current density vs. voltage graph of PCDTBT:$PC_{70}BM$ solar cells made with PEDOT:PSS (Clevios P VP AI 4083) films that were subjected to 0% or 90% RH for one hour and re-annealed.*

Table 11: *Solar cell parameters of PCDTBT:$PC_{70}BM$ solar cells made with PEDOT:PSS (Clevios P VP AI 4083) films that were subjected to 0% or 90% RH for one hour and re-annealed.*

Processing conditions of PEDOT:PSS films	**J_{sc} [mA/cm²]**	**V_{oc} [mV]**	**FF [%]**	**PCE [%]**	**R_s [Ω]**	**R_p [Ω]**
As prepared	9.37	862	51	4.12	10	1158
0% RH for 1h	9.55	876	50	4.19	11	1140
0% RH for 1h and re-annealed	9.46	878	51	4.24	10	1113
90% RH for 1h	9.39	899	45	3.8	14	1020
90% RH for 1h and re-annealed	9.13	793	40	2.9	15	784

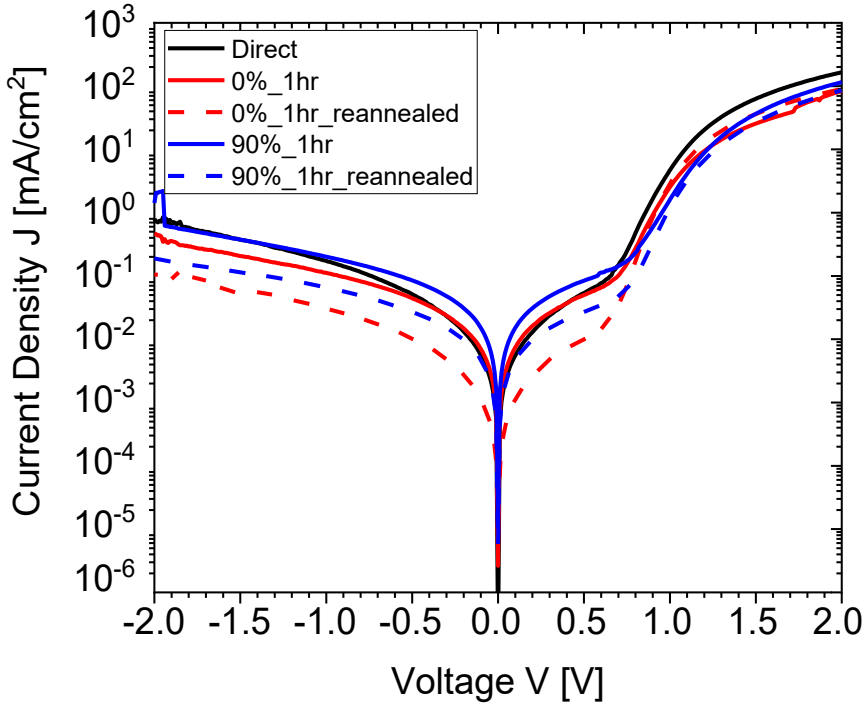

Figure 78: *Dark current density vs. voltage graph of PCDTBT:PC$_{70}$BM solar cells made with PEDOT:PSS (Clevios P VP AI 4083) films that were subjected to 0% or 90% RH for one hour and re-annealed.*

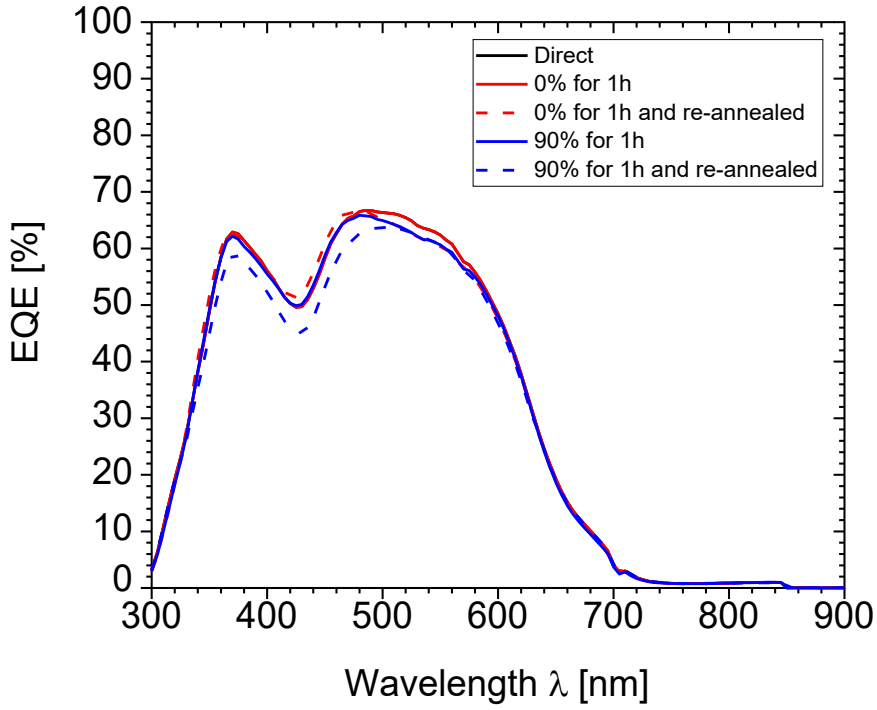

Figure 79: *EQE spectra of PCDTBT:PC$_{70}$BM solar cells made with PEDOT:PSS (Clevios P VP AI 4083) films that were subjected to 0% or 90% RH for one hour and re-annealed.*

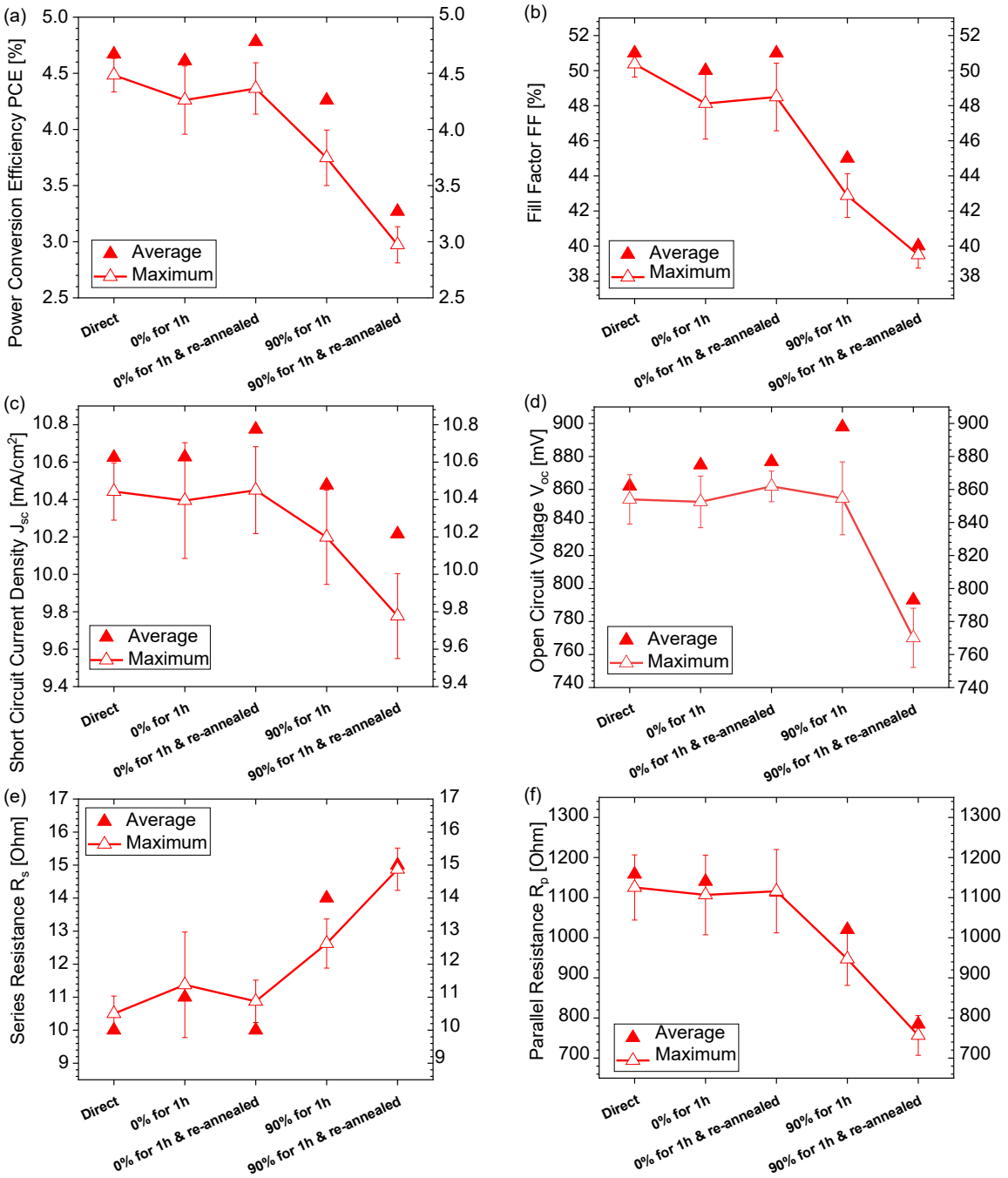

Figure 80: *Statistical analysis of (a) power conversion efficiency, (b) fill factor, (c) open circuit voltage, (d) short circuit current density, (e) series resistance, and (f) parallel resistance of PCDTBT:PC$_{70}$BM solar cells made with PEDOT:PSS (Clevios P VP AI 4083) films that were subjected to 0% or 90% RH for one hour and re-annealed.*

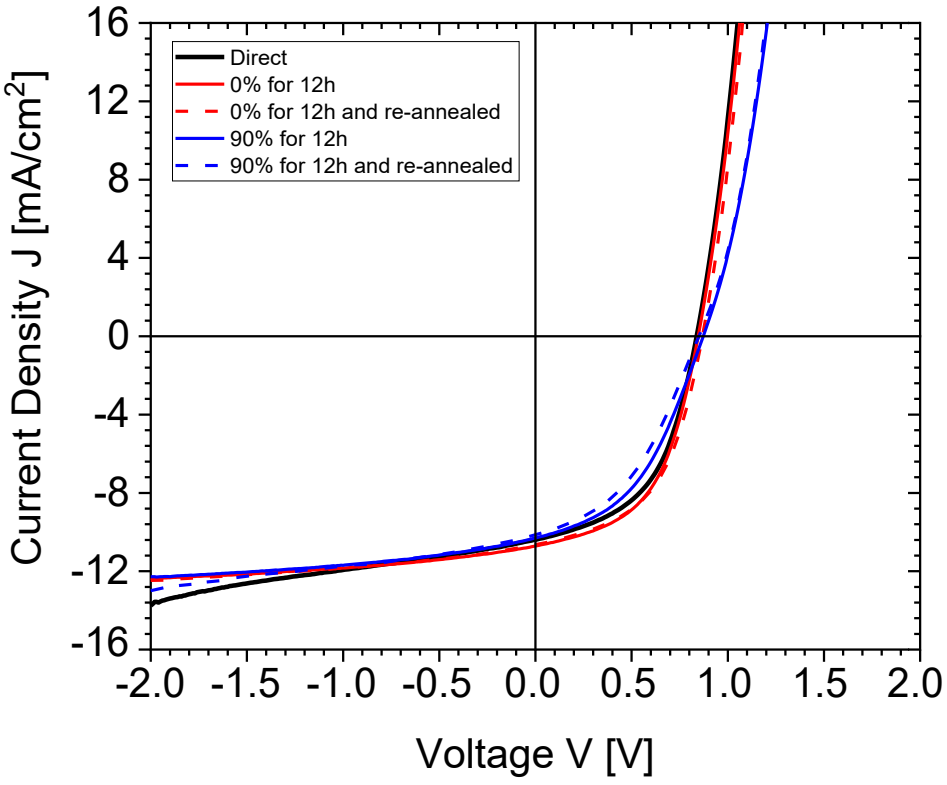

Figure 81: *Current density vs. voltage graph of PCDTBT:$PC_{70}BM$ solar cells made with PEDOT:PSS (Clevios P VP AI 4083) films that were subjected to 0% or 90% RH for 12 hours and re-annealed.*

Table 12: *Solar cell parameters of PCDTBT:$PC_{70}BM$ solar cells made with PEDOT:PSS (Clevios P VP AI 4083) films that were subjected to 0% or 90% RH for 12 hours and re-annealed.*

Processing conditions of PEDOT:PSS films	**J_{sc} [mA/cm²]**	**V_{oc} [mV]**	**FF [%]**	**PCE [%]**	**R_s [Ω]**	**R_p [Ω]**
As prepared	9.37	862	51	4.12	10	1158
0% RH for 12h	9.44	845	52	4.15	10	1235
0% RH for 12h and re-annealed	9.41	867	51	4.17	9	1198
90% RH for 12h	9.35	872	44	3.59	13	967
90% RH for 12h and re-annealed	9.25	850	42	3.31	13	840

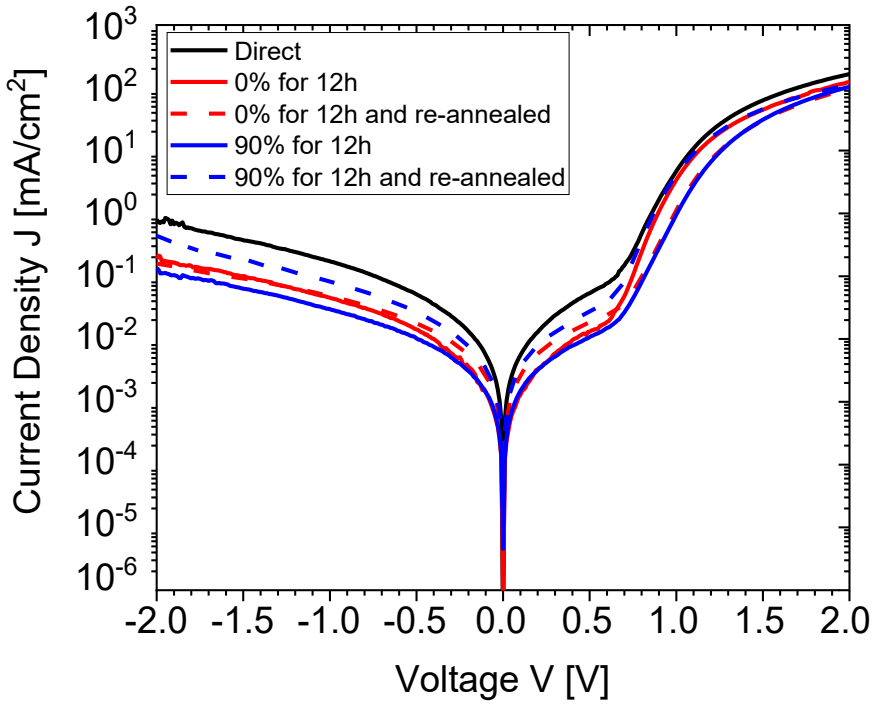

Figure 82: *Dark current density vs. voltage graph of PCDTBT:P$_{70}$CBM solar cells made with PEDOT:PSS (Clevios P VP AI 4083) films that were subjected to 0% or 90% RH for 12 hours and re-annealed.*

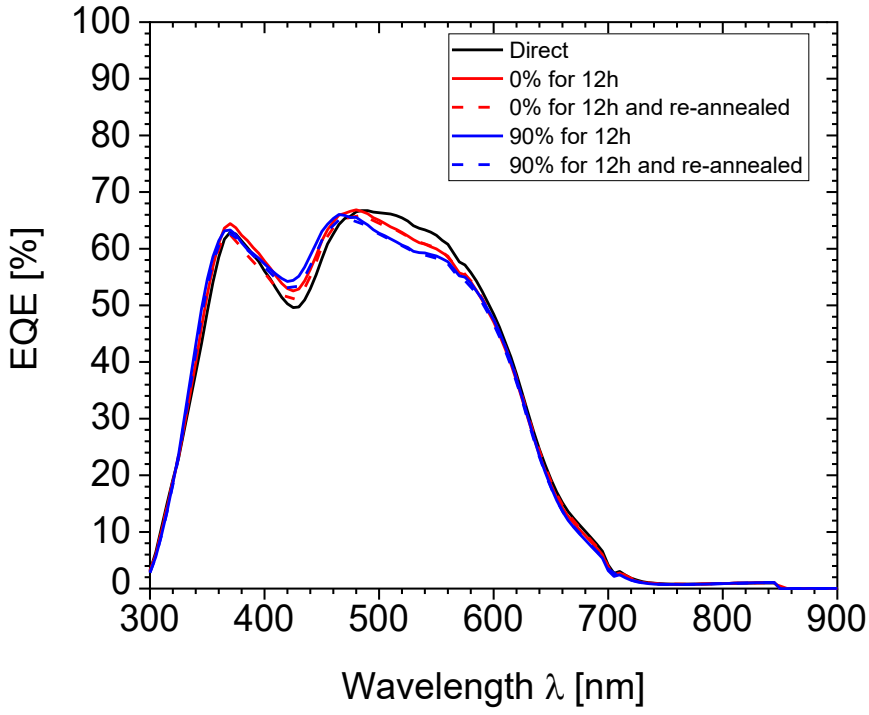

Figure 83: *EQE spectra of PCDTBT:P$_{70}$CBM solar cells made with PEDOT:PSS (Clevios P VP AI 4083) films that were subjected to 0% or 90% RH for 12 hours and re-annealed.*

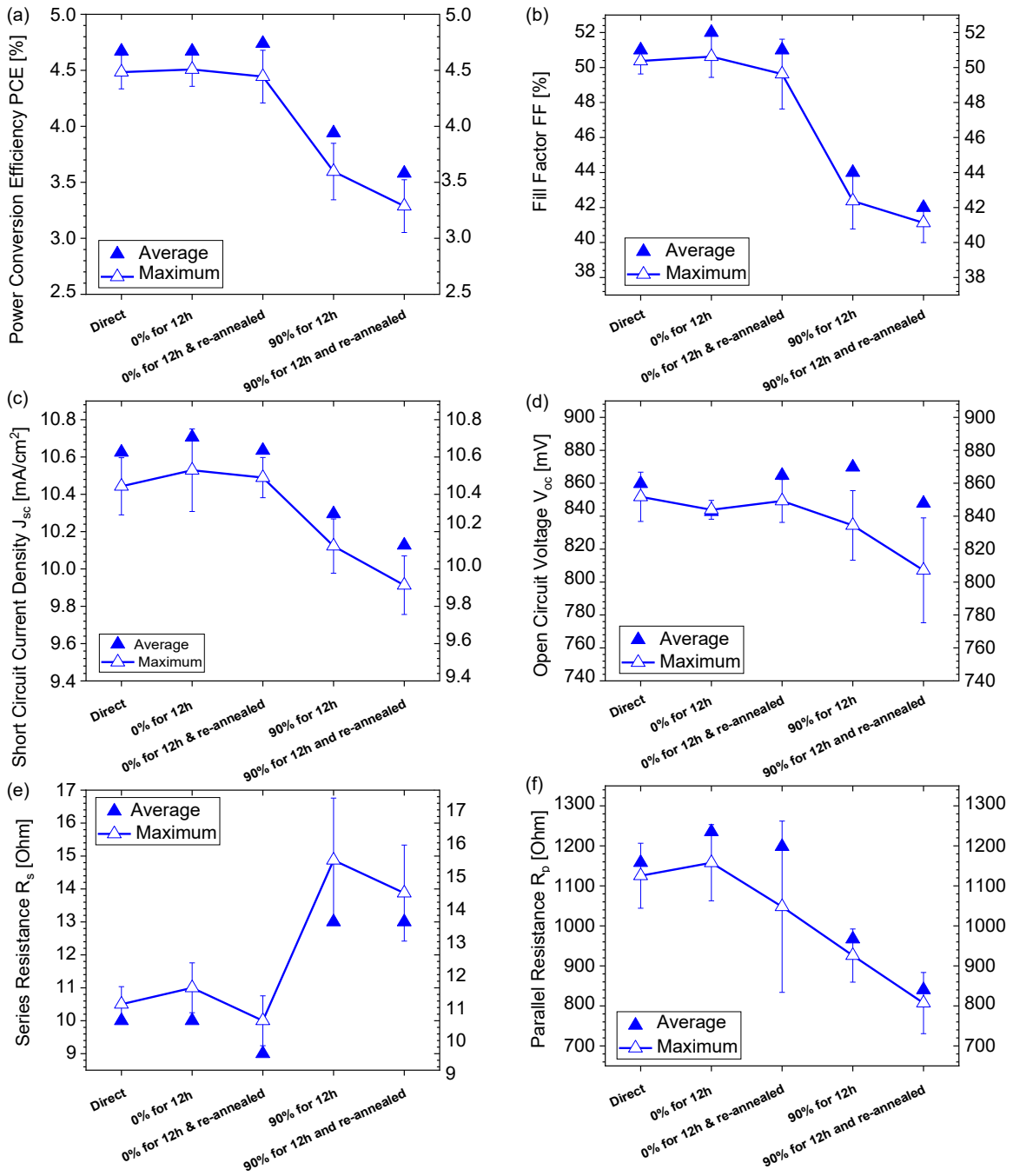

Figure 84: *Statistical analysis of (a) power conversion efficiency, (b) fill factor, (c) open circuit voltage, (d) short circuit current density, (e) series resistance, and (f) parallel resistance of PCDTBT:P$_{70}$CBM solar cells made with PEDOT:PSS (Clevios P VP AI 4083) films that were subjected to 0% or 90% RH for 12 hours and re-annealed.*

Figure 82 and Figure 83 show the dark JV curves and the EQE spectra of solar cells fabricated with PEDOT:PSS films exposed at 0% or 90% RH for 12 hours, respectively. Figure 84 shows the statistical analysis of solar cells made with PEDOT:PSS exposed at 0% or 90% RH for 12 hours.

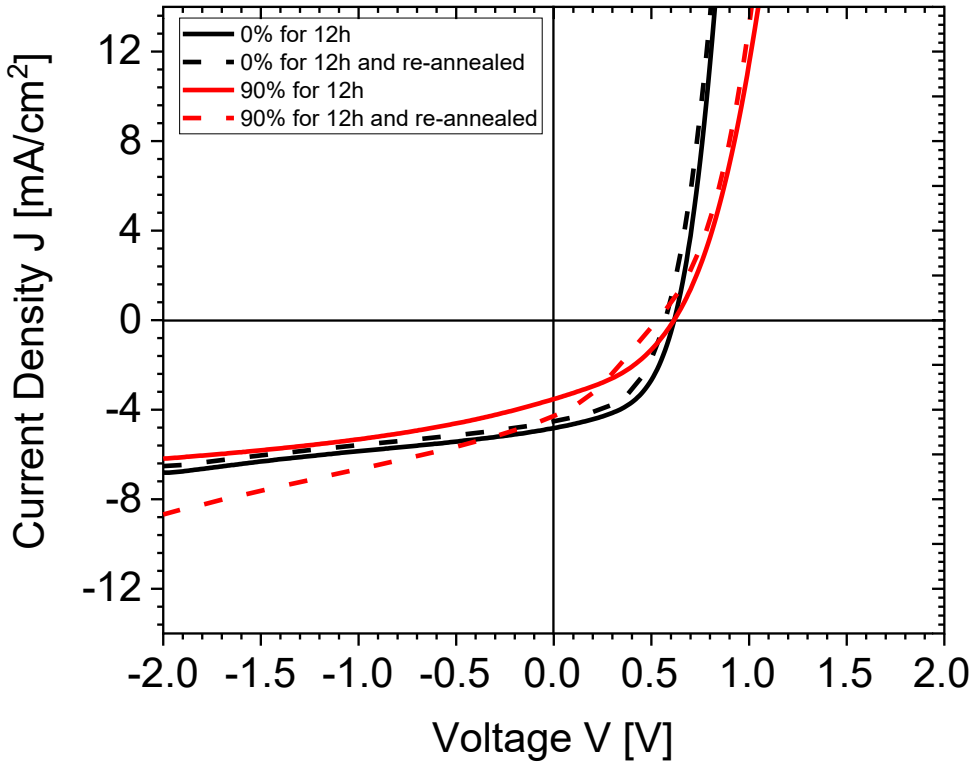

Figure 85: *Current density vs. voltage graph of P3HT:$PC_{60}BM$ solar cells made with PEDOT:PSS (Clevios P VP AI 4083) films that were subjected to 0% or 90% RH for 12 hours and re-annealed.*

Table 13: *Solar cell parameters of P3HT:$PC_{60}BM$ solar cells made with PEDOT:PSS (Clevios P VP AI 4083) films that were subjected to 0% or 90% RH for 12 hours and re-annealed.*

Processing conditions of PEDOT:PSS films	**J_{sc} [mA/cm²]**	**V_{oc} [mV]**	**FF [%]**	**PCE [%]**	**R_s [Ω]**	**R_p [Ω]**
0% RH for 12h	4.818	614	50	1.48	9	1450
0% RH for 12h and re-annealed	4.516	567	49	1.25	9	1376
90% RH for 12h	3.523	614	39	0.83	18	909
90% RH for 12h and re-annealed	4.269	530	32	0.72	12	631

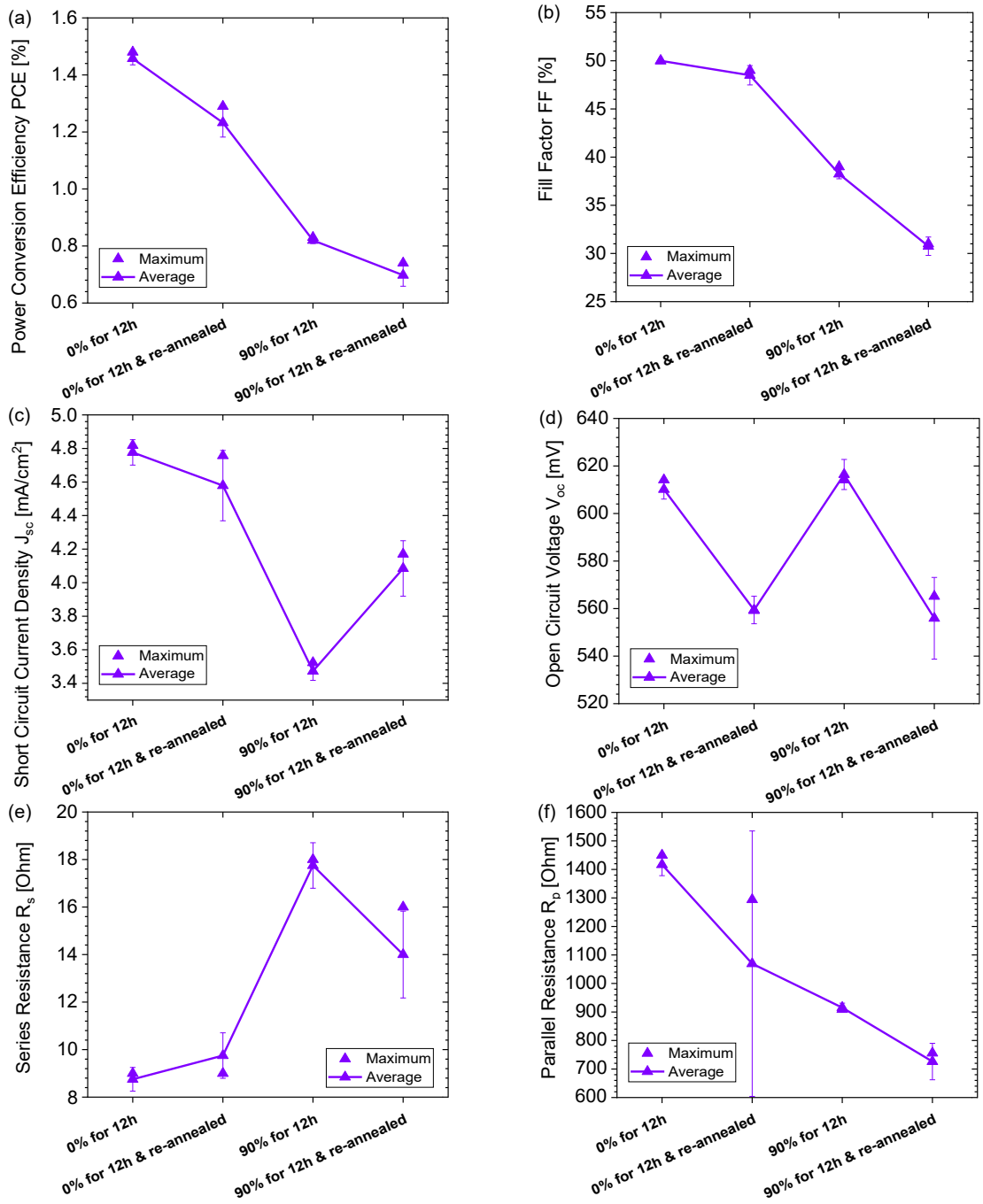

Figure 86: *Statistical analysis of (a) power conversion efficiency, (b) fill factor, (c) open circuit voltage, (d) short circuit current density, (e) series resistance, and (f) parallel resistance of P3HT:P$_{60}$CBM solar cells made with PEDOT:PSS (Clevios P VP AI 4083) films that were subjected to 0% or 90% RH for 12 hours and re-annealed.*

An identical experiment was also carried out with the P3HT:PC$_{60}$BM photoactive layer system. Indeed, as can be shown in Figure 85 and Table 13, the behavior of this second material system was very comparable to that of the organic solar cells based on PCDTBT:PC$_{70}$BM. Figure 86 shows the statistical analysis of solar cells made with

PEDOT:PSS exposed at 0% or 90% RH for 12 hours. The study, therefore, demonstrates that the device performance of the solar cells is affected by the exposure of PEDOT:PSS films to greater (relative) humidity, regardless of the photoactive system. Currently, it appears that the decline in device performance is only related to a decrease in work function after exposure to high relative humidity. But as of yet, it is unclear what led to this decline in work function. This question will be addressed in the next section.

4.3.4 Insights about the surface composition of PEDOT:PSS

The arrangement of the many layers and the interfaces between the layers in a semiconductor device is essential for the device's correct operation. PEDOT:PSS films were processed under various conditions on various substrates to determine whether a potential increase in acidity caused by higher equilibrium concentrations of water may affect the resulting work function or, in addition, whether any vertical material reorganization occurs inside the PEDOT:PSS film (ITO-glass, glass, and PET). XPS and UPS analysis were used to investigate the materials' chemical makeup and electrical characteristics.

The photoionization cross-sections estimated by Yeh *et al.* [169] were used to adjust the intensity of the XPS spectra. Additionally, the intensity was adjusted to be equal to the C 1s core level's maximum intensity. The element in the top left/right corner relates to an improvement in the intensity of the presented information. Additionally, the core levels' binding energies are adjusted such that the maximum of the C 1s level is located at 285 eV. For clarity, the corresponding XPS spectra were vertically shifted.

Films coated with PEDOT:PSS (Clevios P VP AI 4083) were exposed to 90% RH for an hour or six hours after being annealed at 190 °C for 15 minutes. Figure 87 (a) shows that for the PEDOT:PSS films that were subjected to 90% RH for either one hour or six hours, as predicted by the prior studies (compare with Figure 75), the work function was reduced. Interestingly, the indium content dramatically increased for the films that were subjected to increased humidity compared to the as-cast film, as observed in the XPS spectrum. Increased humidity for a longer period increased the concentration of indium and marginally the concentration of sodium on the surface of PEDOT:PSS films. The possibility of indium leakage arises from the fact that PEDOT:PSS is acidic and may etch ITO [165, 170].

However, the sodium content at the surface fluctuated very little, suggesting a small reservoir. By comparing the relative intensities of the S 2p peaks for the thiophene rings

(PEDOT, 162 to 166 eV) and the sulphonate group (PSS, 167 to 172 eV), the XPS spectra in Figure 87 (b) also show that the PSS is becoming slightly enriched at the surface as a result of the prolonged humidity treatment as seen in Figure 88. Overall, it was possible to see a definite anti-correlation between the indium concentration and the work function.

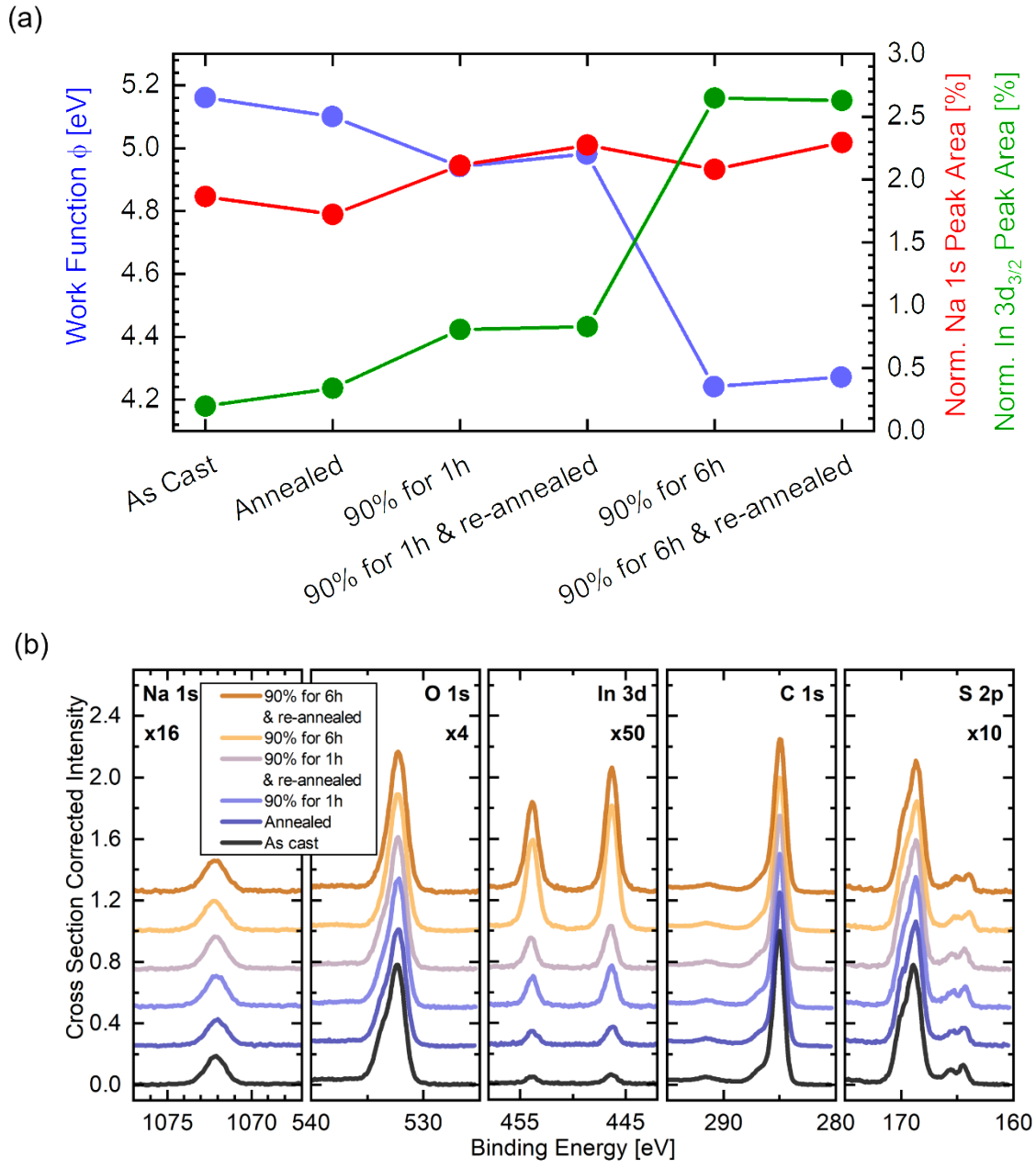

Figure 87: *(a) Relationship between work function and sodium and indium concentrations, and (b) XPS spectra of PEDOT:PSS (Clevios P VP AI 4083) films on ITO-glass substrates showing the change in surface composition after casting, 1st annealing, 90% RH exposure for one hour or six hours, and re-annealing after exposure. The peak areas of the Na 1s and In $3d_{5/2}$ core levels were normalized to the maximum intensity of the C 1s peak.*

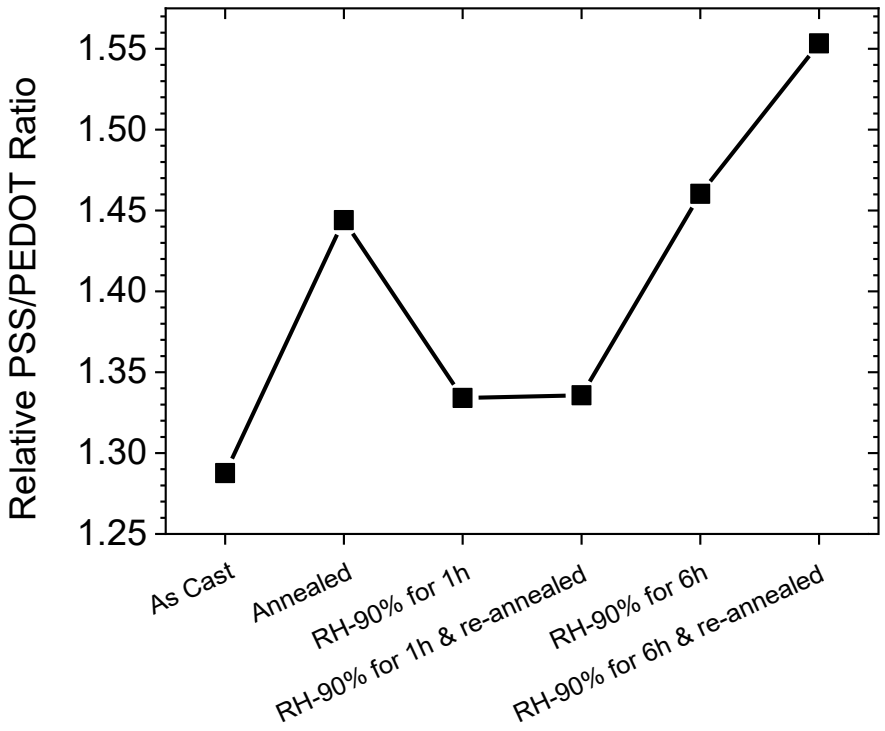

Figure 88: *Relative PSS/PEDOT ratio of PEDOT:PSS (Clevios P VP AI 4083) films on ITO-glass substrates showing the change in relative surface composition after casting, 1st annealing, 90% RH exposure for one hour or six hours, and re-annealing after exposure.*

Note: Each molecular repeat unit of PEDOT (140 Dalton (Da)) and PSS (182 Da) contains one Sulphur atom. Based on the PSS and PEDOT molecular weight ratio of 6:1 (refer to Table 1), the native S 2p ratio between PSS and PEDOT was calculated to be 4.6, based on the molecular weight of the corresponding repeating units. The relative PSS/PEDOT ratio was estimated by considering the maximum S 2p peak of the sulphonate group (PSS, 167 to 172 eV) and the thiophene ring (PEDOT, 162 to 166 eV) and dividing that by said 4.6.

On top of bare glass substrates, highly conductive PEDOT:PSS films (PH1000) were similarly prepared (annealing at 120 °C for 15 minutes) to investigate if the same result might occur from sodium alone (see Figure 89). While the indium peak was absent as anticipated, the layer stack produced significantly higher sodium concentrations. These concentrations grew significantly after the initial annealing step and only a little as a result of further processing steps, such as humidity exposure and re-annealing. An HCl-washing phase of the film, suggested by Greczynski *et al.*, may almost eliminate the sodium [77, 171]. This washing process caused the creation of NaCl, which was afterward eliminated from the film during the same phase by rinsing with DI water. The HCl-wash must result in the regeneration of PSSH,

which is the weaker acid relative to HCl, in the case of PSS- Na+, which is naturally present in the commercial PEDOT:PSS formulations [101, 172].

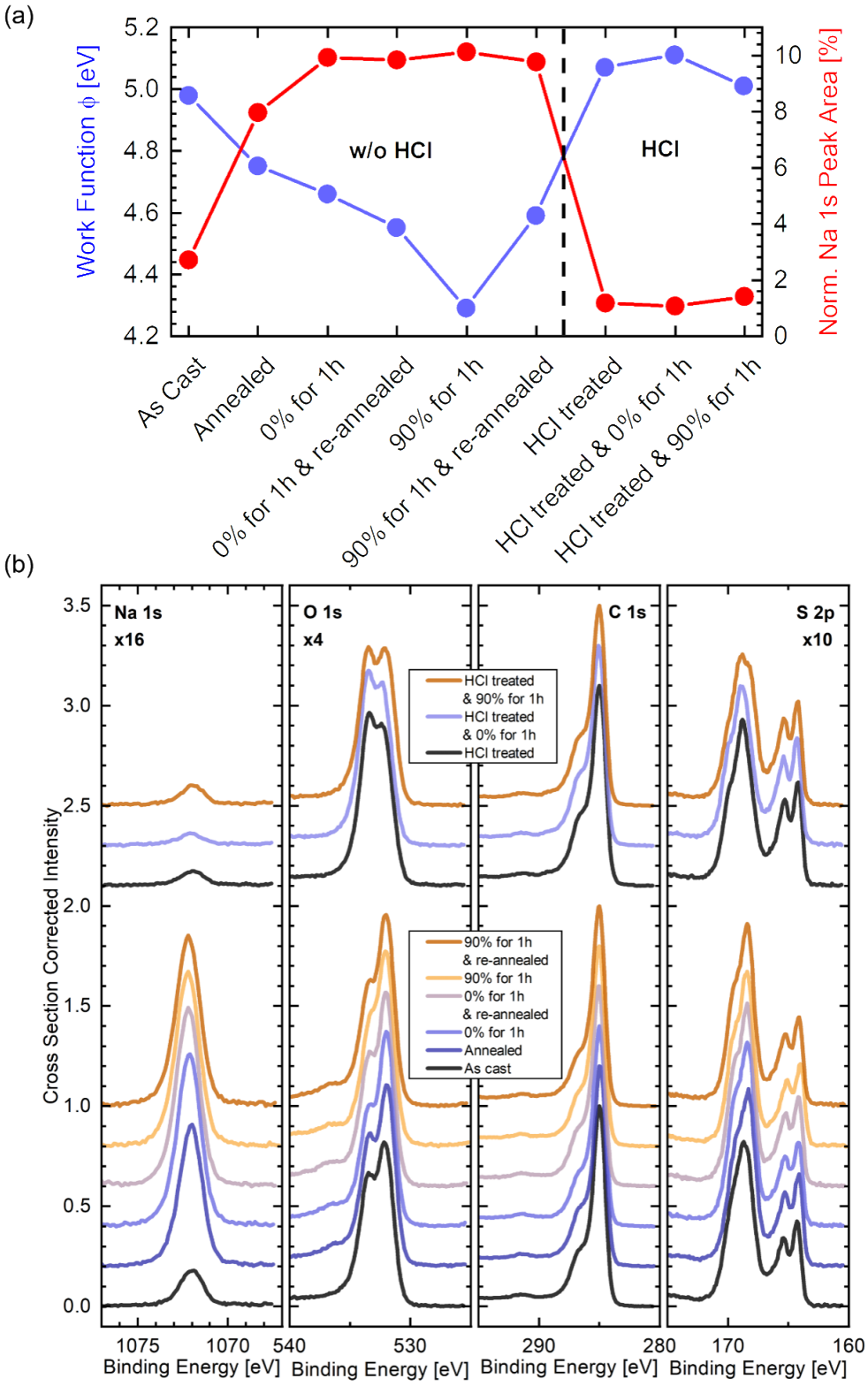

Figure 89: *(a) The relation between work function and sodium concentrations, and (b) XPS spectra of PEDOT:PSS (Clevios PH1000) films on glass substrates showing the change in*

surface composition after casting, 1st annealing, 0% and 90% RH exposure for one hour, re-annealing after exposure, HCl treated and 0% and 90% RH exposure for one hour after HCl treatment. The peak areas of the Na 1s core levels were normalized to the maximum intensity of the C 1s peak.

Phase separation between PEDOT and PSS is said to be encouraged by the HCl treatment, which increases the films' electrical conductivity. Finally, as seen in the XPS spectra (Figure 89 (b)), the sodium peak significantly diminishes with the acid wash. It was also noted that the PSS component of the S 2p state had somewhat decreased. The increase in the work function of the PEDOT:PSS films (Figure 89 (a)) is strongly correlated with this modification. This indicates that metal ions present in the PEDOT:PSS films serve as a physical restriction on the work functions. The work function and sodium surface concentration do not, however, have a clear inverse relationship because treatments with increased humidity caused the work function to further decline while the sodium surface concentration remained unchanged. We may thus surmise that the sodium bulk concentration may also affect how the work function is carried out. Finally, humidity treatment following the HCl wash resulted in a little augmentation of the sodium peak, which continues to denote sodium release from the glass substrate.

The same highly conductive PEDOT:PSS formulation (Clevios PH1000) was coated on PET (polyethylene terephthalate) substrates and annealed at 120 °C for 15 minutes to confirm that the acidity of the PEDOT:PSS is causing the migration of sodium from glass substrates into the PEDOT:PSS films. The presence of particular sodium content in the as-cast and annealed PEDOT:PSS (PH1000) films on PET, as shown in Figure 90 (a) and (b), indicates that some sodium is already present in the formulation in the form of a sulfonate-salt (PSS^-Na^+). However, compared to films made with PEDOT:PSS (PH1000) that were treated on glass, the measured concentrations are often an order of magnitude lower. In contrast to what happens on glass substrates, the sodium surface concentration decreases during annealing. With final concentrations around ten times lower than for the acid wash on the glass, the acid treatment again results in an almost total loss of the salt content in the PEDOT:PSS films. As was already mentioned, the sodium reduction was accompanied by a modest rise in the work function.

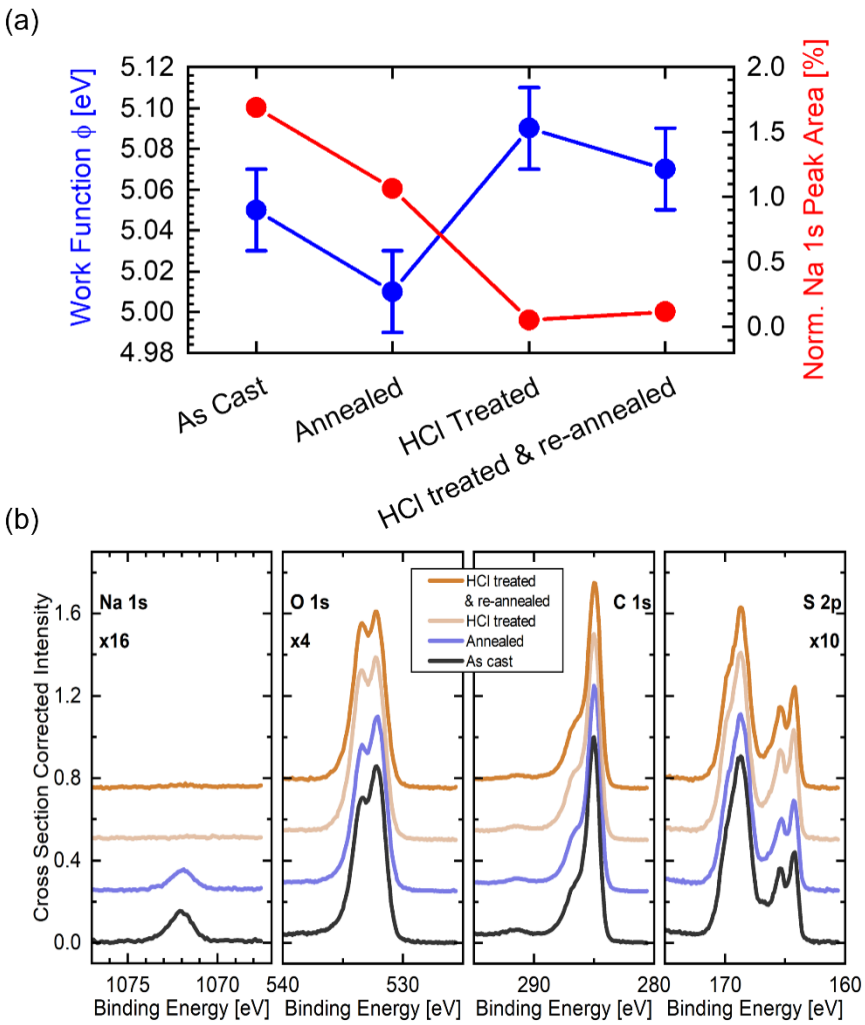

Figure 90: *(a) The relation between work function and sodium concentration, and (b) XPS spectra of PEDOT:PSS (Clevios PH1000) films on PET substrates showing the change in surface composition after casting, annealing, HCl treated, HCl treated and re-annealing. The peak areas of the Na 1s core levels were normalized to the maximum intensity of the C 1s peak.*

4.3.5 Summary and conclusions

To focus on the preparative and synthetic techniques that may be readily implemented for the large-scale manufacture of semi-TCEs for OPVs, the conductive polymer poly(3,4-ethylenedioxythiophene) polystyrene sulfonate (PEDOT: PSS) was thoroughly investigated. Based on the findings, it is advisable to keep the PEDOT:PSS films at the lowest possible RH if processing cannot be finished without a break, as it was noticed that the processing parameters have a strong influence on the PEDOT:PSS work function.

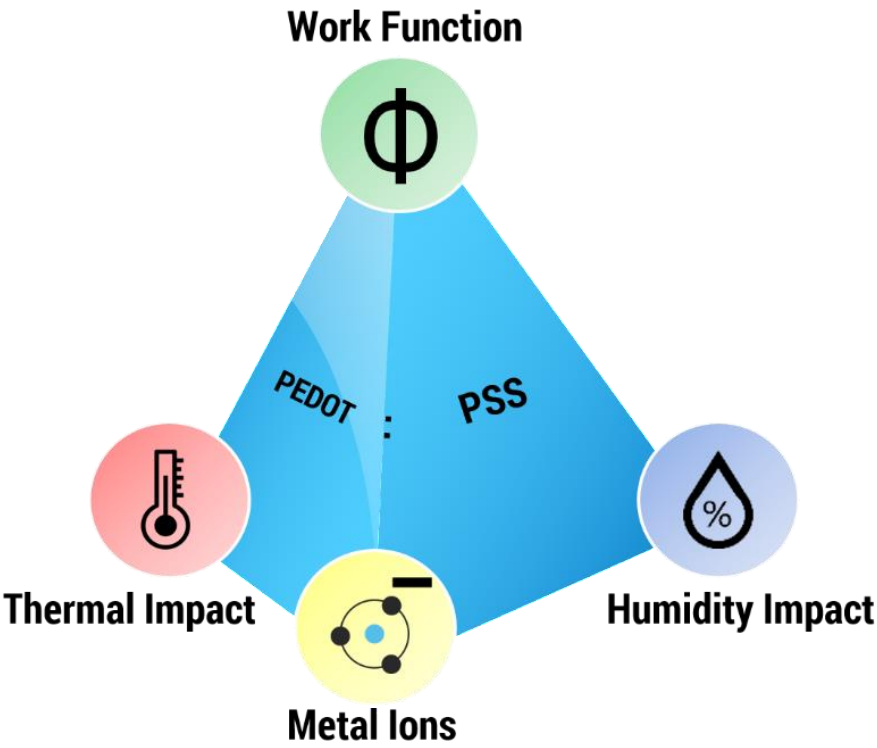

Figure 91: *Illustration demonstrating the relationship between the work function of PEDOT:PSS and its dependence on temperature, humidity, and metal ions.*

Other than the actual processing conditions, it has become evident that metal ion contaminants also influence the performance of the PEDOT:PSS films. It was observed that the release of metal ions from the substrate and enrichment within the film up to the surface is caused by the design of the processing conditions for the PEDOT:PSS films. Since it is challenging to reduce the acidity of PEDOT:PSS, stable organic optoelectronic devices that employ PEDOT:PSS would benefit from selecting substrates that are not quickly impacted by the PEDOT:PSS acidity.

The results described in this section are published in ACS Applied Electronic Materials, **2021**, *3*, 929–943, *DOI: https://doi.org/10.1021/acsaelm.0c01043, Authors:* ***Aman Anand****, Jose Prince Madalaimuthu, Maximilian Schaal, Felix Otto, Marco Gruenewald, Shahidul Alam, Torsten Fritz, Ulrich S Schubert, Harald Hoppe.*

4.4 Modification of PEDOT:PSS electrodes for organic photovoltaics

This section covers the earlier work done to create highly electrically conductive PEDOT:PSS electrodes as well as the strategy formed based on that research and experimental results.

A material with a high electrical conductivity must, from a physical perspective, have a high carrier concentration (n) and a high charge carrier mobility ($\mu_{n,p}$).

$$\sigma = en\mu_{n,p} \tag{89}$$

Since electrons have a far lower effective mass than ions, they are much more mobile, and this causes electrons to act as charge carriers in excellent conductors.

The morphology of the thin films has a significant impact on the charge carrier mobilities. The charge carrier mobilities and, thus, the conductivity is greatly influenced by the crystallinity and orientation of the crystalline domains within the films [173]. As illustrated in Figure 11 (a), PEDOT:PSS is composed of a combination of positively charged conjugated PEDOT, negatively charged PSS, and positively charged counter-ions (mostly sodium and hydronium). The processing of aqueous dispersions is enabled by the polyelectrolyte PSS, which also permits doping. Since PEDOT (p-doped conjugated polymer) and PSS are both ionic compounds and have hydrophobic and hydrophilic characteristics respectively, the electrostatic and hydrophobic forces present in the system are likely what regulate the local self-assembly and phase separation of this material. Therefore, PEDOT:PSS is a phase-segregated structure made up of conductive PEDOT polycationic spheres enclosed in PSS polyanionic shells (Figure 11 (b)). While the PSS facilitates the PEDOT's aqueous dispersion, its insulating nature restricts the usage of pristine PEDOT:PSS films as stand-alone PV electrodes [90].

The requirement for strong macroscopic electrical conductivity of PEDOT:PSS implies that the PEDOT:PSS blend system must provide a percolating channel of the PEDOT conjugated material with sufficient π-stacking while remaining close enough to PSS anions to allow doping. As electrostatic interactions constitute the main factor in these systems, phase segregation is a crucial requirement to create a pathway for the percolation of charge. For example, in bulk heterojunction (BHJ) solar cells, a percolating bicontinuous network is

instead created between the donor (D) and acceptor (A) components to transport excitons to the closest D–A interface and allow complementary charges to move through complementary percolating networks in the out-of-plane direction to reach their respective electrode [97, 173]. Therefore, the quantity of dopant and the process of doping must be tuned in a way that maintains a balance between charge carrier density and charge mobility for PEDOT:PSS to function as an electrode.

Different additives have been employed to improve the conductivity of PEDOT:PSS, including ethylene glycol (EG), polyethylene glycol (PEG), dimethyl sulfoxide (DMSO), methanol (MeOH), different acids like HCl, H_2SO_4, anionic surfactants, ionic liquids, salts, etc [92, 97, 174].

Lingstedt *et al.* achieved a conductivity of 2124 S/cm by using DMSO. The two-step modification process included mixing DMSO into the PEDOT:PSS formulation and then dipping the fabricated PEDOT:PSS films in a DMSO bath [175]. Vaagensmith *et al.* also used two-step modification processes using a blend of DMSO and EG and soaking in water:EG:ethanol blend, and they achieved a conductivity of 5012 S/cm [176]. Using a solution shearing deposition and MeOH postprocessing treatment to create PEDOT:PSS films, Worfolk *et al.* achieved a high conductivity of 4600 ± 100 S/cm [75]. As reported in most of the articles, the addition of solvents like DMSO causes the screening effect because of its high dielectric constant, and solvents like EG and PEG form hydrogen bonds with PSS^- and PSSH groups [97, 177]. Because of the screening effects, the electrostatic interaction between PEDOT and PSS gets reduced, which leads to phase separation between PEDOT and PSS. As a result, PEDOT can be stacked more efficiently in linear chains, which increases conductivity. [97, 173].

Out of all modifications, acid treatment has been reported to yield the highest conductivity values of PEDOT:PSS films. By exposing PEDOT:PSS films to 100% sulfuric acid (H_2SO_4) recently, Kim *et al.* achieved a high conductivity of 4380 S/cm [178]. They proposed a conductivity mechanism stating that the two ions of H_2SO_4 ($2H_2SO_4 \leftrightarrow H_3SO_4^- + HSO_4^-$) stabilize the positively charged PEDOT and PSS, leading to a stack of PEDOT networks. The uncoupled PSS is washed out by the water, and only a minimal amount is reorganized to act as a counterion. Shi *et al.* reached a conductivity of 6323.9 ± 364 S/cm. According to their research, a two-step post-treatment process yielded better PEDOT-phase alignment and tunable phase separation between PEDOT and PSS [179].

Recently, different ionic liquids (IL) such as 1-butyl-3-methylimidazolium tetrafluoroborate, 1-ethyl-3-methylimidazolium tetracyanoborate, 1-ethyl-3-methylimidazolium chloride, 1-ethyl-3-methylimidazolium tricyanomethanide, etc. have also been explored to modify the PEDOT:PSS [174]. The highest reported conductivity of 2103 S/cm for PEDOT:PSS with IL was achieved by Kee et al., where they used 1-ethyl-3-methylimidazolium tetracyanoborate [180]. With the introduction of the ionic liquid, counter-ion exchange occurs between the PEDOT:PSS and IL, which separates the PEDOT from the PSS, resulting in the higher-order molecular packing of PEDOT and PSS being replaced by smaller anions.

4.4.1 Strategy to yield conductive PEDOT:PSS films

As indicated earlier, unlike conjugated organic blends, PEDOT and PSS have additional electrostatic interactions, which promote their self-assembly into hierarchical structures and allow their segregation while locally retaining charge neutrality. By controlling these local constraints with additives, phase separation between PEDOT and PSS can be optimized.

Two stages of processing are necessary to produce highly conductive PEDOT:PSS films, as observed in the majority of the modifications made to PEDOT:PSS films in previous studies. The stages (Figure 92) are as follows:

i) Phase separation between PEDOT and PSS: The positively charged PEDOT must first be separated from the negatively charged PSS by the introduction of a secondary dopant (polar solvents or high-dielectric solvents). The separation of PEDOT from PSS can enable percolating channels in the PEDOT-conjugated material, facilitating high charge mobility.

ii) Removal of excess PSS: The vertical arrangement results in PSS on top of the films because of the interaction between PEDOT and PSS [90]. To lower the PSS concentration and increase the conductivity of the films, the extra PSS at the top must be removed or replaced by smaller anion molecules.

To understand the conductivity process and develop a good strategy for creating highly conductive PEDOT:PSS films, a systematic procedure of adding DMSO to the PEDOT:PSS formulation was carried out. The PEDOT:PSS formulation PH1000 was utilized to create PEDOT:PSS film, which was mixed with 5 Vol% of DMSO, as described in the experimental section, and electrical, optical, and surface characterization were performed on the films.

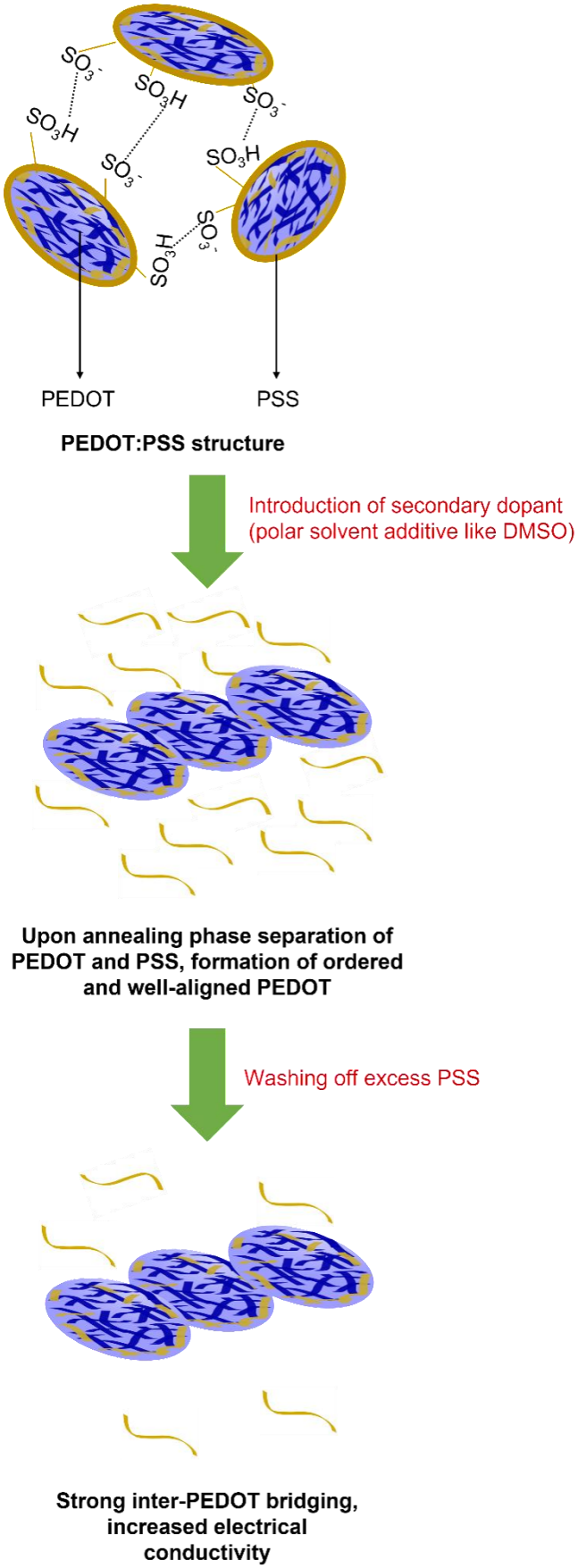

Figure 92: *Strategy stages for yielding conductive PEDOT:PSS films.*

4.4.1.1 Electrical properties of PEDOT:PSS

The electrical properties of as-cast and annealed PEDOT:PSS films were measured using non-contact sheet resistance measurement equipment. Figure 93 and Table 14 show the sheet resistance and conductivity values for as-cast and annealed PEDOT:PSS films. The conductivity is calculated using equation 15 for a PEDOT:PSS film having a thickness of 140 nm. As expected, the annealed PEDOT:PSS films, which were doped with DMSO, yielded the best sheet resistance values. When compared to the as-cast pristine PEDOT:PSS films, the conductivity of the annealed PEDOT:PSS + DMSO film increased by a factor of 10.

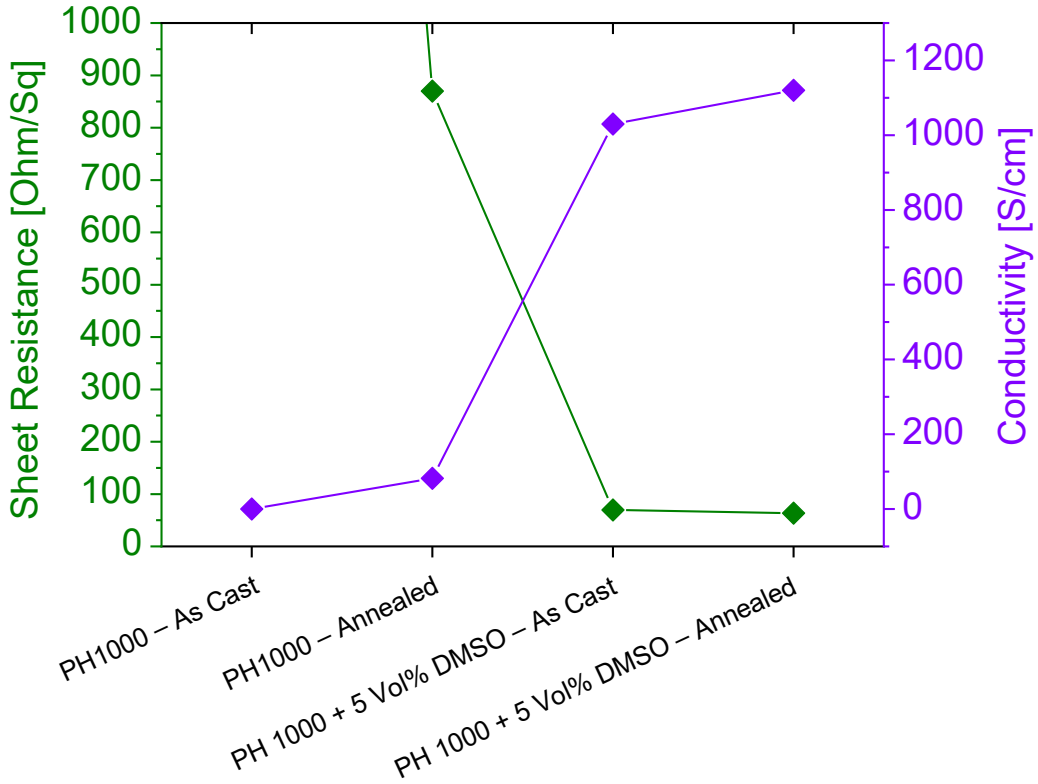

Figure 93: *Comparison of sheet resistance and conductivity for different PEDOT:PSS films.*

Table 14: *Sheet resistance of as-cast and annealed PEDOT:PSS films.*

Film	Sheet resistance [Ohm/sq]	Conductivity [S/cm]
PH 1000 – As Cast	>1000	>71.42
PH 1000 – Annealed	869.85 ± 5	82.15
PH 1000 + 5 Vol% DMSO – As Cast	69.49 ± 0.1	1030
PH 1000 + 5 Vol% DMSO – Annealed	63.53 ± 0.1	1120

4.4.1.2 Surface properties of PEDOT:PSS

To study the surface properties of PEDOT:PSS films, the AFM technique was chosen. Figure 94 shows the AFM images of annealed, pristine PEDOT:PSS and PEDOT:PSS doped with DMSO at different resolutions. The addition of DMSO promotes a densely packed fibril-like structure that is visible in the films produced from PEDOT:PSS mixed with DMSO as compared to the grain structure found in the pristine PEDOT:PSS films, indicating an effective separation of PEDOT from PSS and the formation of PEDOT chains inside the films.

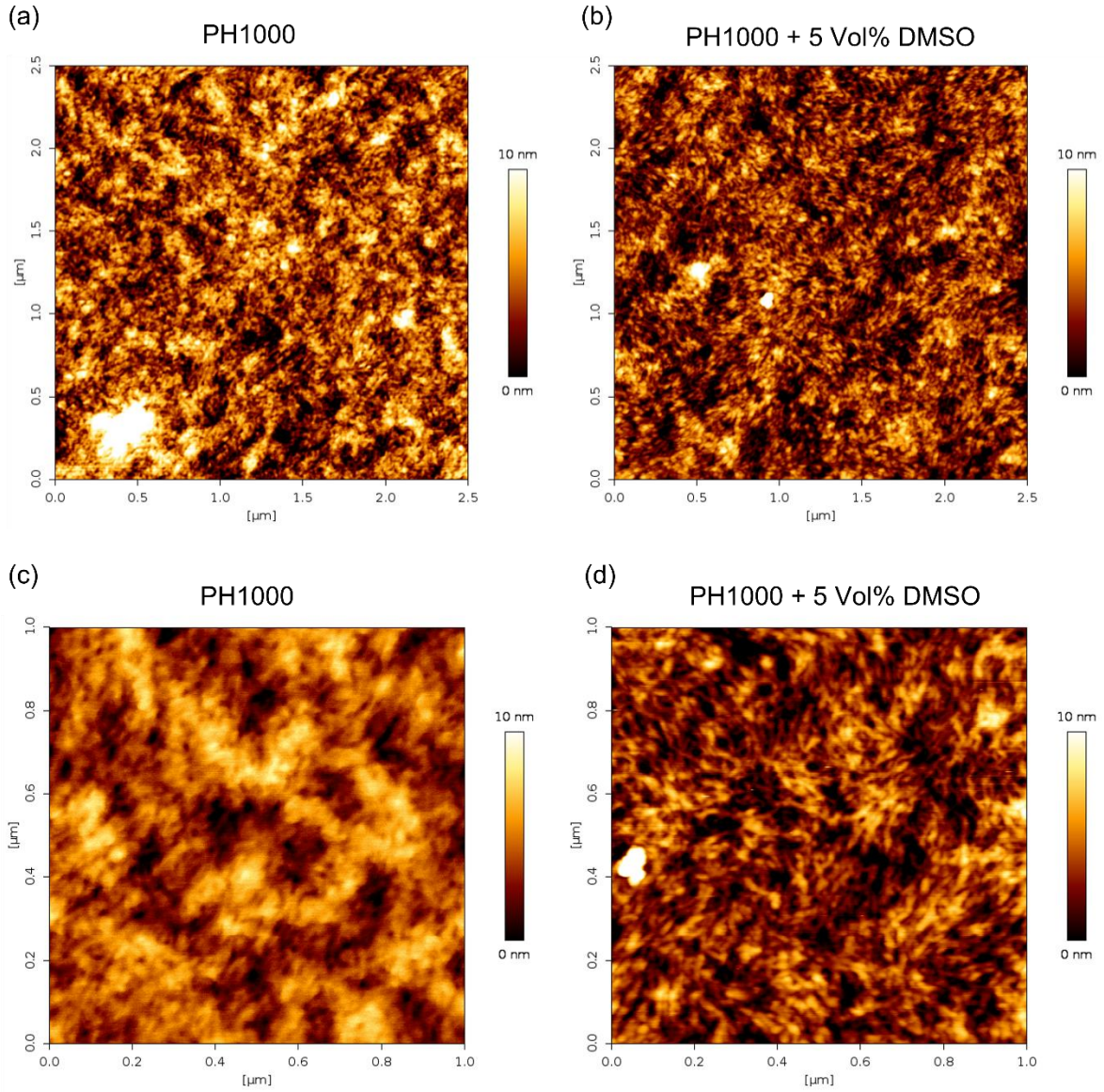

Figure 94: *Annealed PEDOT:PSS films AFM images (a,c) pristine PH 1000 (showing grains), and (b,d) PH 1000 + 5 Vol% DMSO (showing fibril structure). The resolution for (a,c) is 2.5 µm, and for (b,d) is 1 µm.*

4.4.1.3 Optical properties of PEDOT:PSS

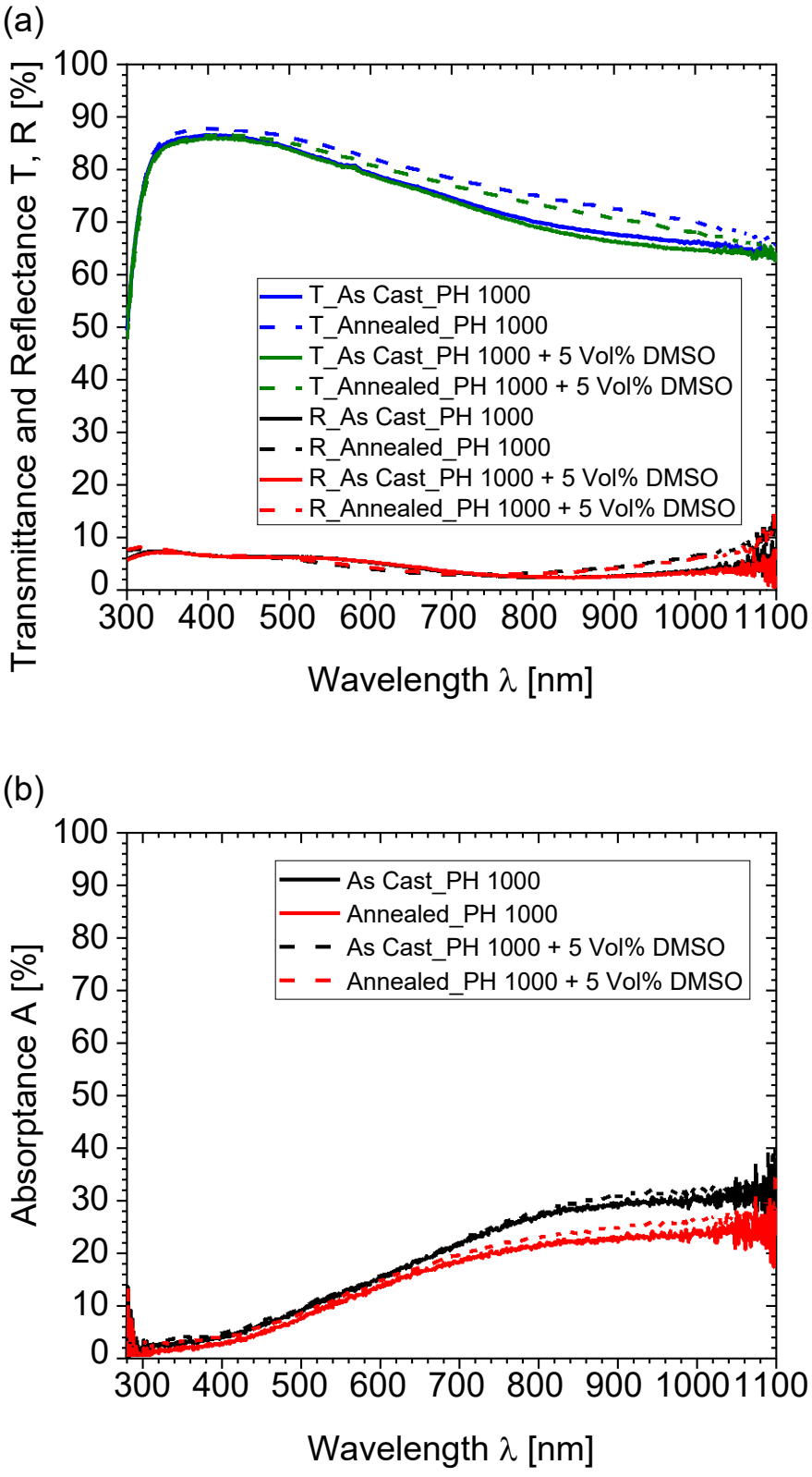

Figure 95: *Optical properties of as cast and annealed PEDOT:PSS films (a) transmittance and reflectance vs. wavelength, and (b) absorptance vs. wavelength.*

As shown in Figure 95 (a), the average transmittance of all PEDOT:PSS (with and without DMSO) films was around 74%, which makes it a potential candidate as a TCE. Metals show mirror-like reflectance below plasma frequency, whereas the reflectance goes to zero (ideally) at plasma frequency, and above plasma frequency, the transparency regime starts, which many include still one finite reflectance. As seen in the reflectance spectra, it can be inferred that for annealed PEDOT:PSS films, a shift in the plasma frequency happens. As per the Drude model (equation 90), the plasma frequency is directly proportional to the square root of static conductivity; thus, it is possible to increase the plasma frequency to increase the static conductivity.

$$\omega_p = \left(\frac{\sigma_0}{\varepsilon_0 \tau}\right)^{1/2} \tag{90}$$

where ω_p is the plasma frequency, σ_0 is the static conductivity, ε_0 is the permittivity of free space and τ is the relaxation time.

Figure 95 (b) shows the absorptance of the PEDOT:PSS films. It is interesting to see the change in the absorptance curve over the wavelength. Toward the IR region, an increase in absorptance was visible, which can be directly related to the plasma frequency and thus the number of charge carriers (Equation 9).

Compared to as-cast films, the annealed films showed lower absorptance. It can be inferred that upon annealing, the morphology of the films gets improved, as seen in Figure 94, which might improves the charge carrier mobility and decreases the number of charge carriers. Because conductivity depends on both the number and the mobility of the charge carriers, it is possible to increase one while lowering the other and still have high conductivity. Thus, the optimization process should be designed in such a way that it balances both factors. Adding DMSO as an additive to PEDOT:PSS already demonstrates a method for producing conductive PEDOT:PSS films.

4.4.2 Summary and conclusions

A strategy for enhancing PEDOT:PSS's electrical conductivity is proposed so that it can be used as TCE in solar cells. This strategy focuses on the phase separation of PEDOT and PSS by using a secondary dopant (like DMSO) to induce order and well-aligned PEDOT within the film for easy charge transport. To further improve morphology and conductivity, the next step involves washing the uncoupled PSS after the separation.

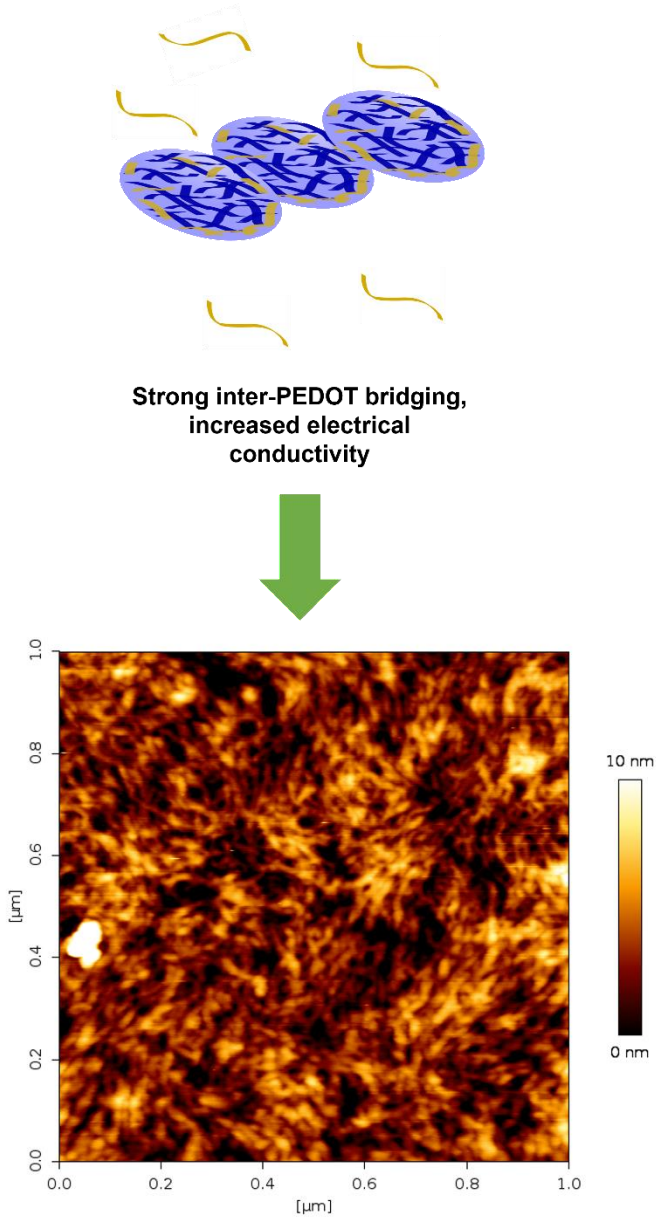

Figure 96: *An illustration and an AFM image demonstrating the inter-PEDOT bridging that results in the fibril structure.*

In the study, it was seen that the introduction of DMSO altered the PEDOT:PSS films' conductivity and morphology. A well-defined phase separation between PEDOT and PSS was observed, as the formation of a fibril-like structure was seen within the doped PEDOT:PSS films. The change in the morphology can be related to the electrical mobility, which is seen to be increased for the films modified with DMSO. A decrease in absorptance was also observed for doped PEDOT:PSS annealed films toward the IR region, which is directly proportional to the plasma frequency and, consequently, the number of charge carriers.

Chapter 5

Summary and Outlook

In short, this doctoral thesis is focused on developing a novel and exact figure of merit (FOM) to assess TCEs for use in photovoltaics. As postulated, the FOM is proportional to the potential power output of PV devices, which can be directly linked to the efficiency of the solar cell, it is normalized to the Shockley-Queisser limit (SQL) to quantify losses with respect to an ideal solar cell that are directly connected with properties of the TCE, and it is dimensionless as commonly used for ratings in general.

The novel FOM was presented in two forms: an exact form that required numerical calculations for solving the implicit Shockley-Equation, and an approximate form. The introduction of transition sheet resistance which separates the transmittance and conductance limited regimes makes the exact FOM of one its kind which is shown by no other FOMs. Assessing the functional dependence of the exact FOM, a second approach for an approximate FOM bearing overall smaller deviations was presented. A set of current state-of-the-art semi-transparent electrodes was comprehensively assessed using the exact FOM which shows that the exact FOM allows to assess different TCEs for photovoltaic applications.

Concerning Muzzillo’s comment, we found that Muzzillo's FOM also needs numerical methods. While his accusation is right for the exact FOM (being implicit), his model suffers from the same. As a result, Muzzillo's FOM can also be seen as implicit. The FOM of Muzzillo was further refined, better matching the exact FOM. It was also demonstrated that the exact FOM can be modified to consider solar module effects and grid TCE effects.

The work also includes a thorough study of the impact of processing conditions on the work function of PEDOT:PSS and on resulting solar cell performances. Various commercial PEDOT:PSS formulations were tested for storage under different annealing temperatures and relative humidity levels. The acidic and hygroscopic properties of PEDOT:PSS cause the release of metal ions from metallic substrates, which can compromise the functionality of the device. By removing such metal ions, the restoration of high work function could be demonstrated. In the final chapter of the thesis, the foundations and requirements for

achieving highly conductive PEDOT:PSS films were discussed. Optimizing charge carrier mobility first over charge carrier density is a beneficial strategy for the use of PEDOT:PSS in transparent conductive electrodes, as reducing the number of charge carriers would lower free carrier absorption.

For future work, an online page is under construction to allow scientists from all over the world to assess their TCE with the help of the exact FOM for a free choice of solar module geometry. It is also intended to continue with the development of highly conductive PEDOT:PSS transparent electrodes for organic solar cells, where the optimization of morphology and charge carrier mobility will be carried out utilizing various processing additives and refining steps.

Appendix

Section 1: Correlation between a solar cell power output and width of a solar cell

The power output of a solar cell is defined as:

$$P = V \cdot I \tag{91}$$

where V is the voltage and I is the current. The power loss within an ohmic resistance is proportional to the current squared passing through it [40]. Therefore, it is defined as:

$$P_{loss} = I^2 \cdot R_S \tag{92}$$

The current of a solar cell can be defined as:

$$I = J_{SC} \cdot l \cdot w \tag{93}$$

As shown by Hoppe *et al.*, the relationship between the series resistance (R_S) and the sheet resistance ($R_\square$) of electrodes can be described as [40]:

$$R_S = R_\square \cdot \frac{l}{3w} \tag{94}$$

If the width (w) of a solar cell is increased by a factor of n, the new width can be defined as:

$$w = n \,.\, w \tag{95}$$

Thus, the current and the series resistance can be redefined as:

$$I' = J_{SC} \cdot l \cdot w \cdot n = n \cdot I \tag{96}$$

$$R_S{}' = R_\square \cdot \frac{l}{3wn} = R_S \cdot \frac{1}{n} \tag{97}$$

So with the new current and the series resistance, the power output and power loss can be calculated:

$$P' = V \cdot I' = V \cdot n \cdot I = n \cdot P \tag{98}$$

$$P_{loss}{}' = (I')^2 \cdot R_S{}' = (n \cdot I)^2 \cdot R_S \cdot \frac{1}{n} = n \cdot P_{loss} \tag{99}$$

Thus, both the power output and the power loss are n times and thus the ratio of power output by power loss is constant.

$$\frac{P}{P_{loss}} = \frac{P'}{P_{loss}'} = Constant \tag{100}$$

Section 2: Figures and Tables

Figure A1 shows the comparison between established figures of merit on a double logarithmic plot.

Figure A2 (a–j) shows the FOM *vs.* sheet resistance graphs for different transmittance values (a) 100%, (b) 90%, (c) 80%, (d) 70%, (e) 60%, (f) 50%, (g) 40%, (h) 30%, (i) 20%, and (j) 10% throughout the spectral range of 280 to 1100 nm and a solar cell length of 5 mm.

With a solar cell length of 5 mm and a spectral range of 280 to 1100 nm, Table A1 displays the critical sheet resistance values for various transmittance values.

Figure A3 (a–d) shows he functional dependency of the transition sheet resistance on different solar cell lengths (a) 2.5 mm, (b) 5 mm, (c) 10 mm, and (d) 20 mm was assessed for TCE exhibiting 90% transmittance over the spectral range from 280 to 1100 nm

Figure A4 shows the optical properties of bare glass.

Figure A5 (a–f) shows the FOM (a) Fraser & Cook, (b) Haacke, (c) Dressel & Grüner, (d) Gamboa *et al.*, (e) Contreras *et al.,* and (f) exact FOM values for different transparent conductive electrodes, evaluated for the spectral range of 350 to 800 nm and a solar cell length of 5 mm. (*Note: The data points with open symbols are FOM values of TCEs for which only film transmittance spectra data were available*).

Tables A2 to A6 show the comparison between different TCEs evaluated by different FOMs.

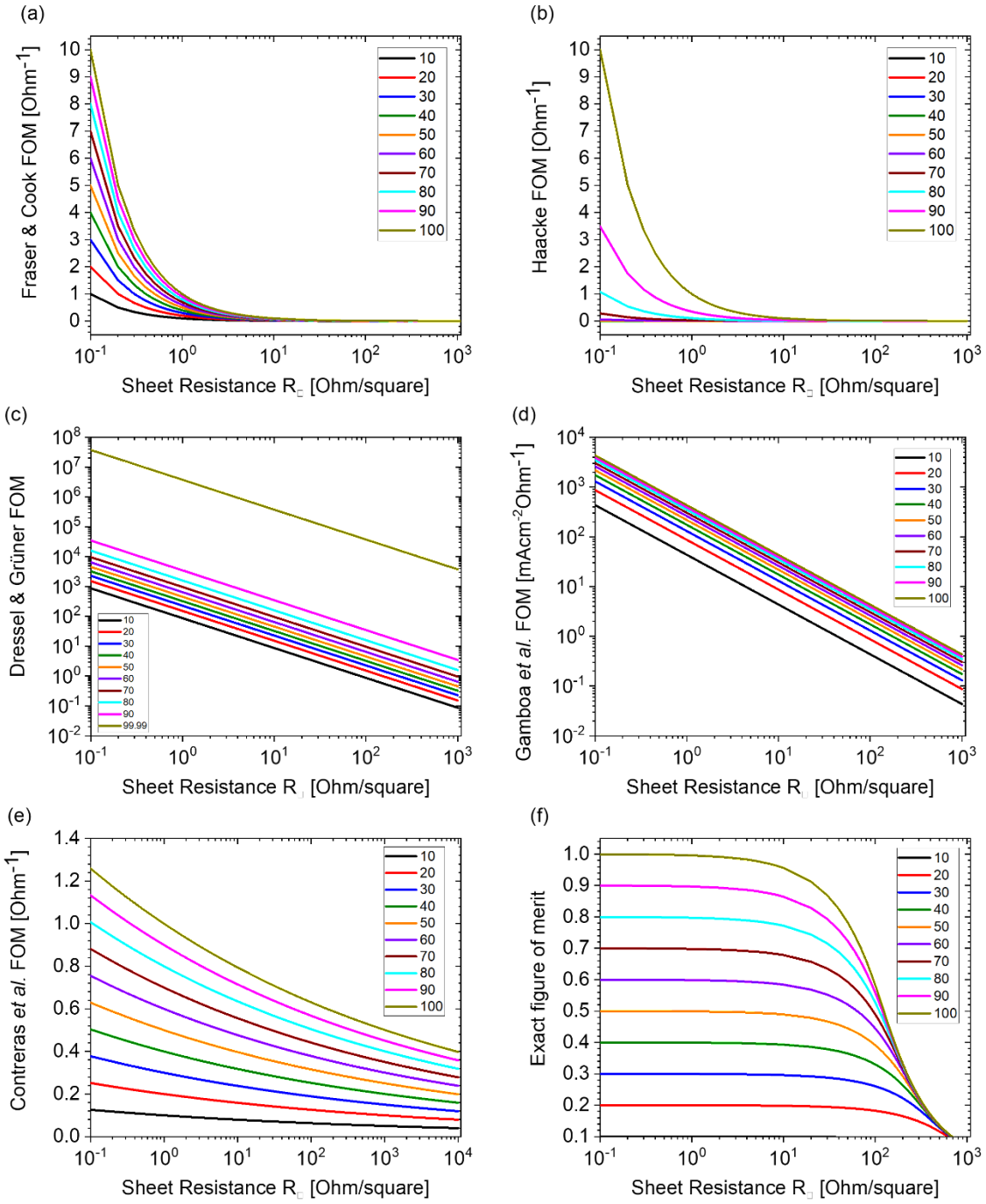

Figure A1: *Comparison of the exact calculation for the impact of transmittance and sheet resistance on PV performance for the spectral range from 280 to 1100 nm and a solar cell length of 5 on a double logarithmic plot, according to the following established figures of merit: (a) Fraser & Cook, (b) Haacke, (c) Dressel and Grüner, (d) Gamboa et al., (e) Contreras et al.(n = 10), and (f) exact FOM.*

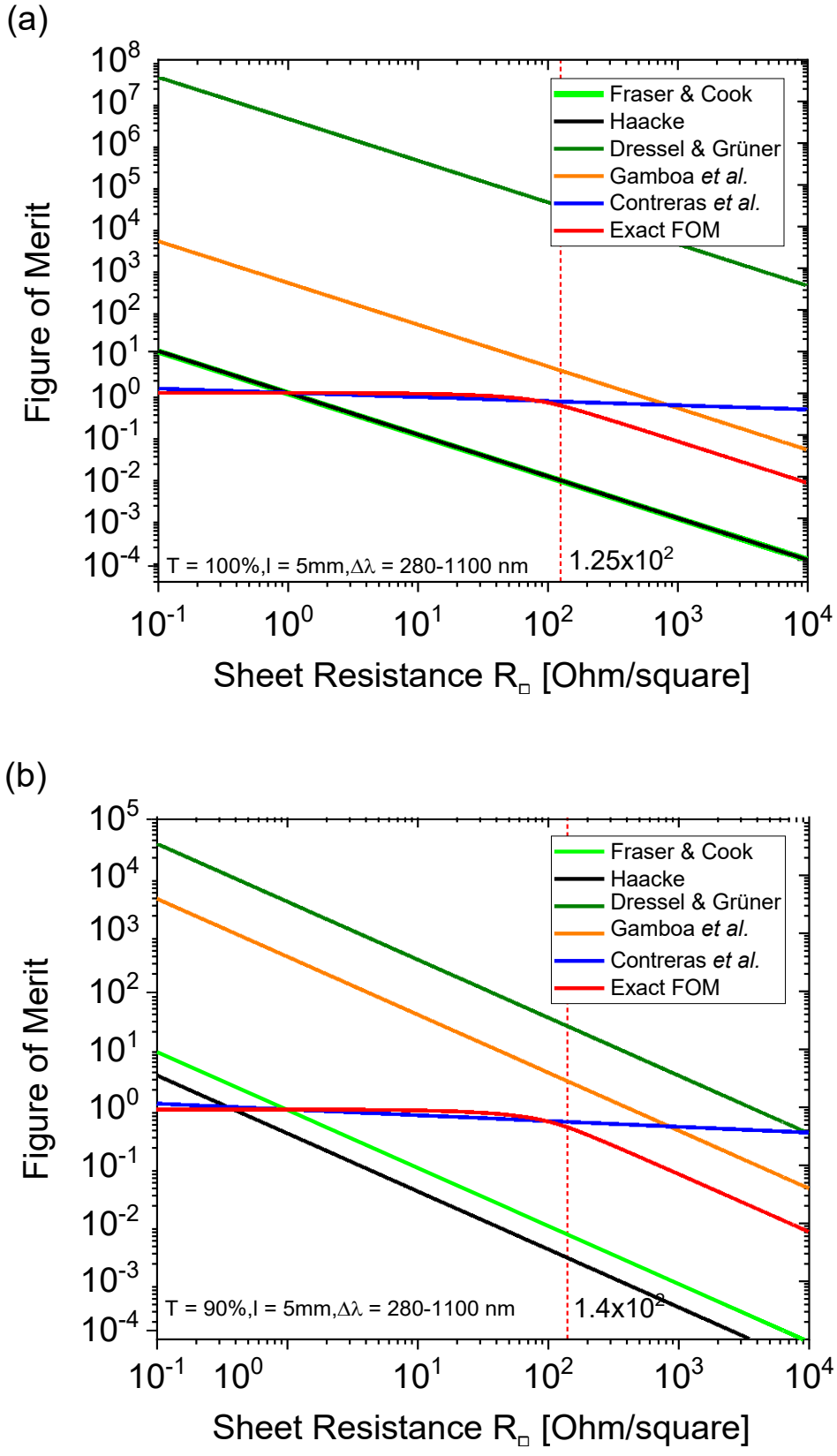

Figure A2ab: *FOM vs. R□ for spectral range (280 to 1100 nm), for (a) T=100% and (b) 90%.*

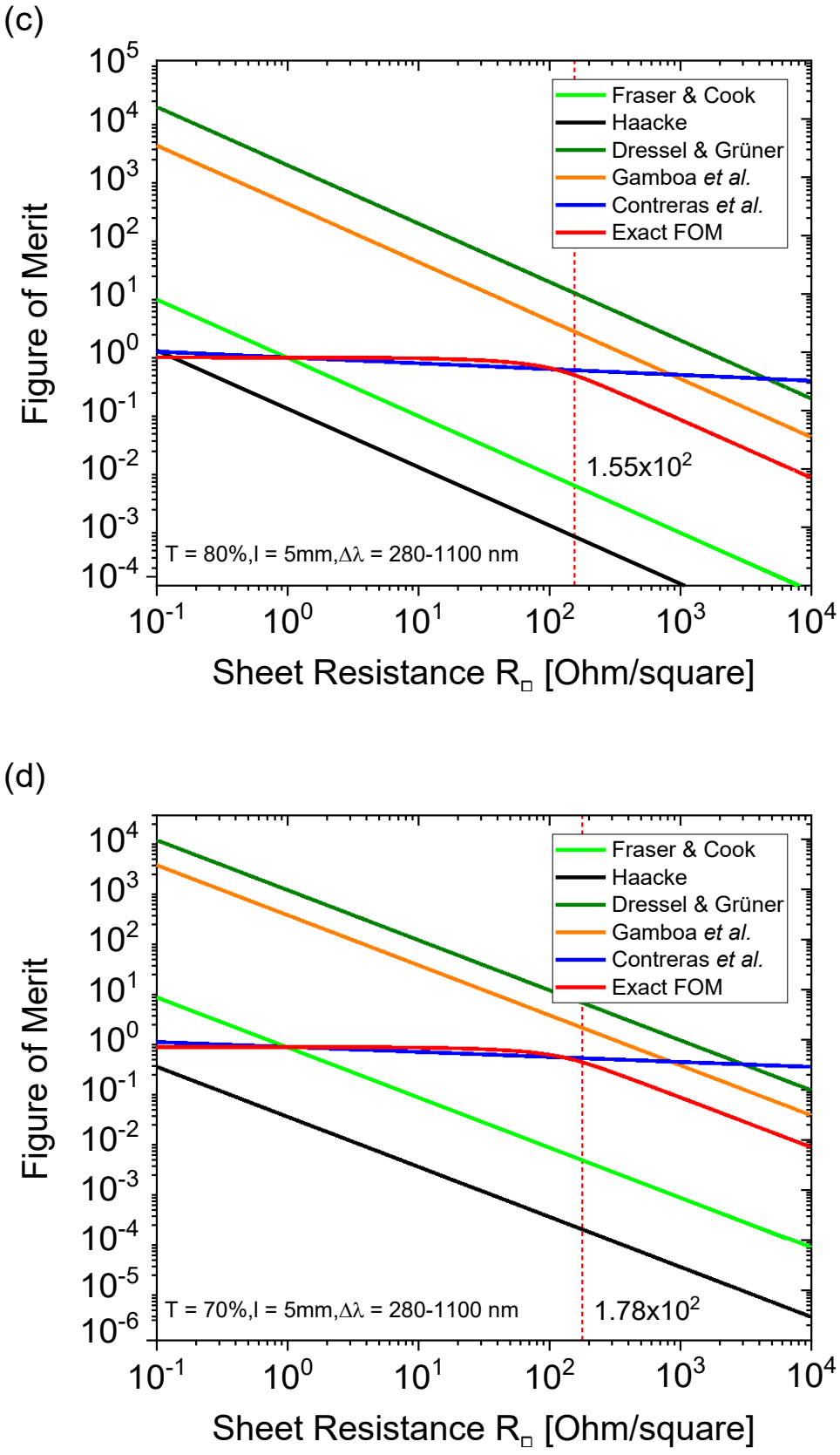

Figure A2cd: *FOM vs. R□ for spectral range (280 to 1100 nm), for (c) T=80% and (d) 70%.*

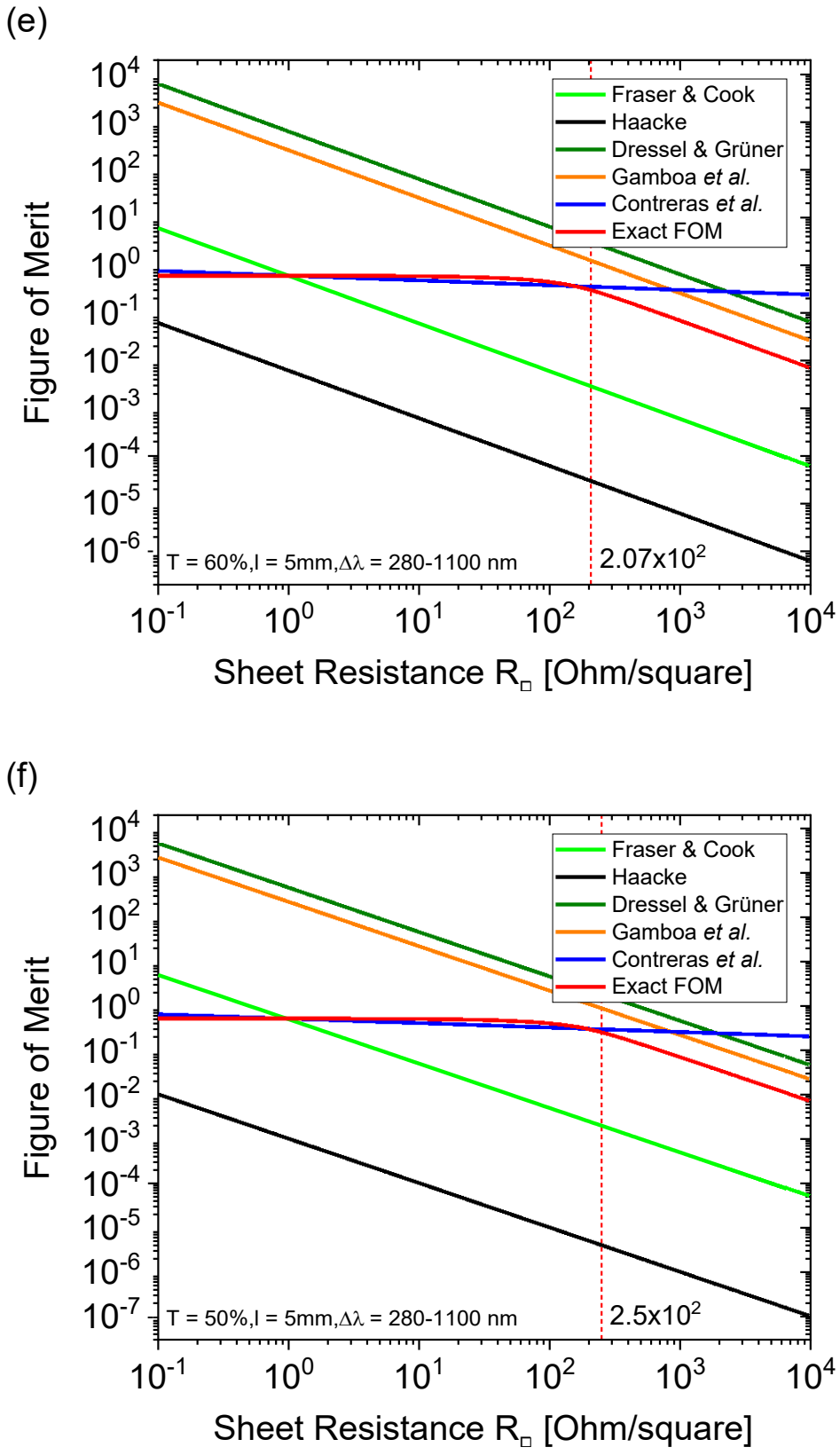

Figure A2ef: *FOM vs. R□ for spectral range (280 to 1100 nm), for (e) T=60% and (f) 50%.*

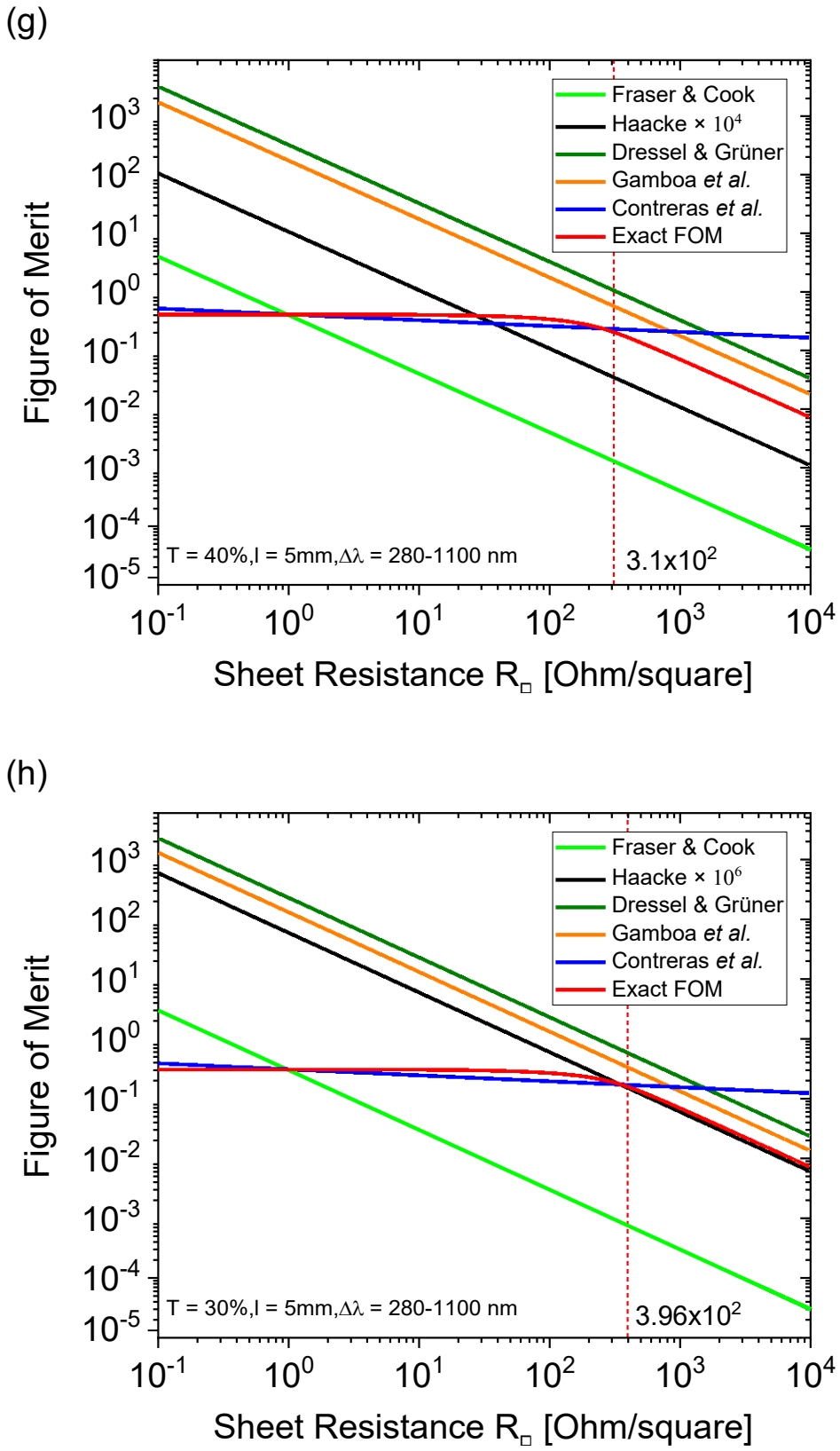

Figure A2gh: *FOM vs. R□ for spectral range (280 to 1100 nm), for (g) T=40% and (h) 30%.*

(i)

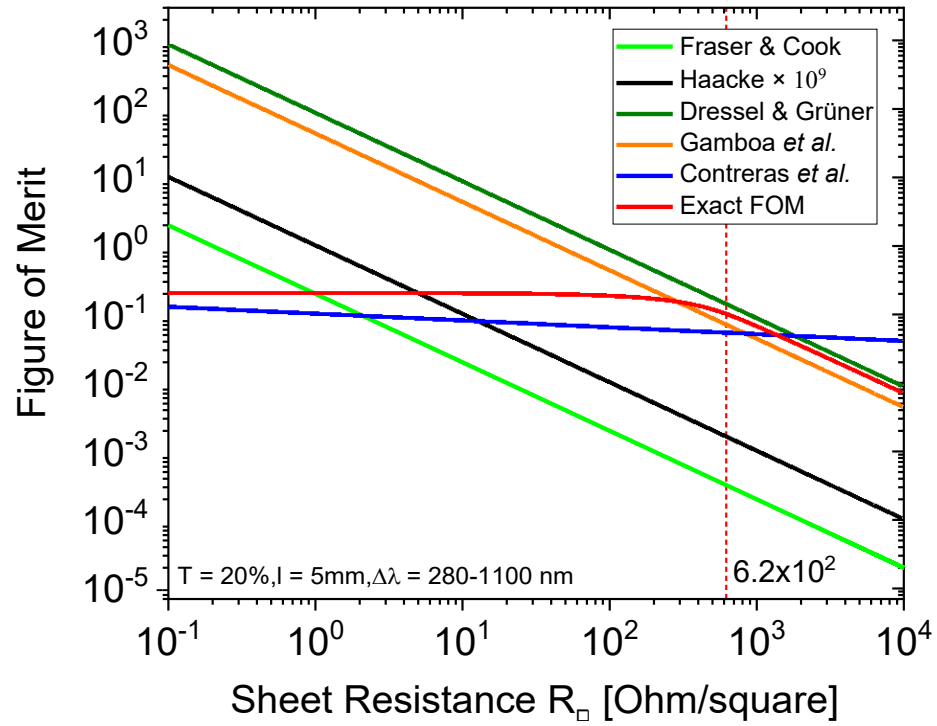

(j)

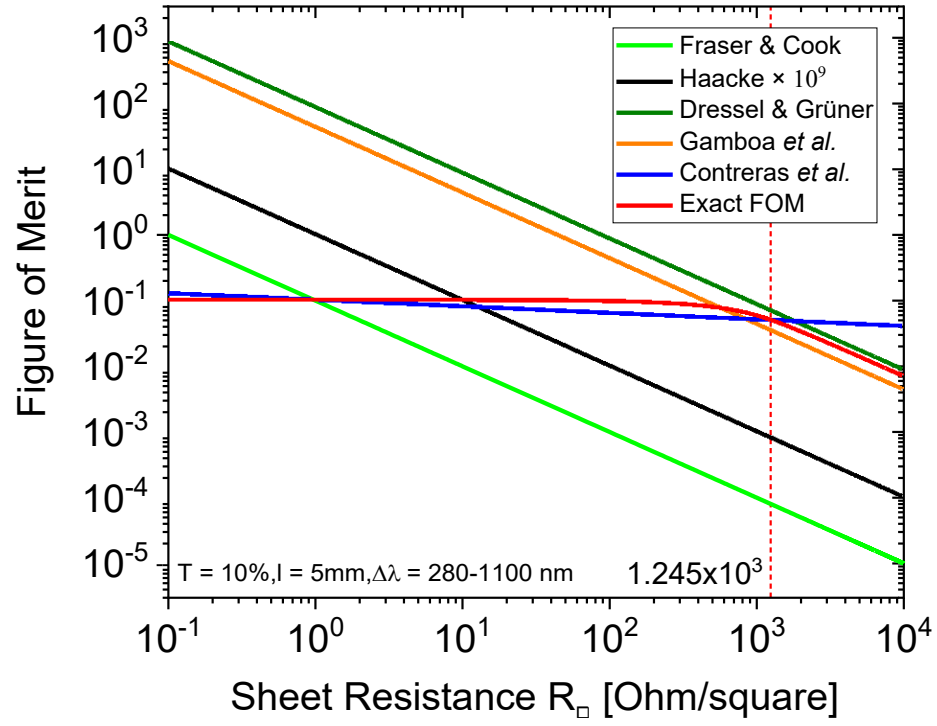

Figure A2ij: *FOM vs. R□ for spectral range (280 to 1100 nm), for (i) T=20% and (j) 10%.*

Table A1: *Critical sheet resistance for the exact FOM for various transmittance values in the 280-1100 nm spectral band with a 5 mm solar cell length.*

Transmittance Values for (280 – 1100 nm) [%]	**Critical sheet resistance $R_{\square,c}$ [Ω/□]**
100	125
90	140
80	155
70	178
60	207
50	250
40	310
30	396
20	620
10	1245

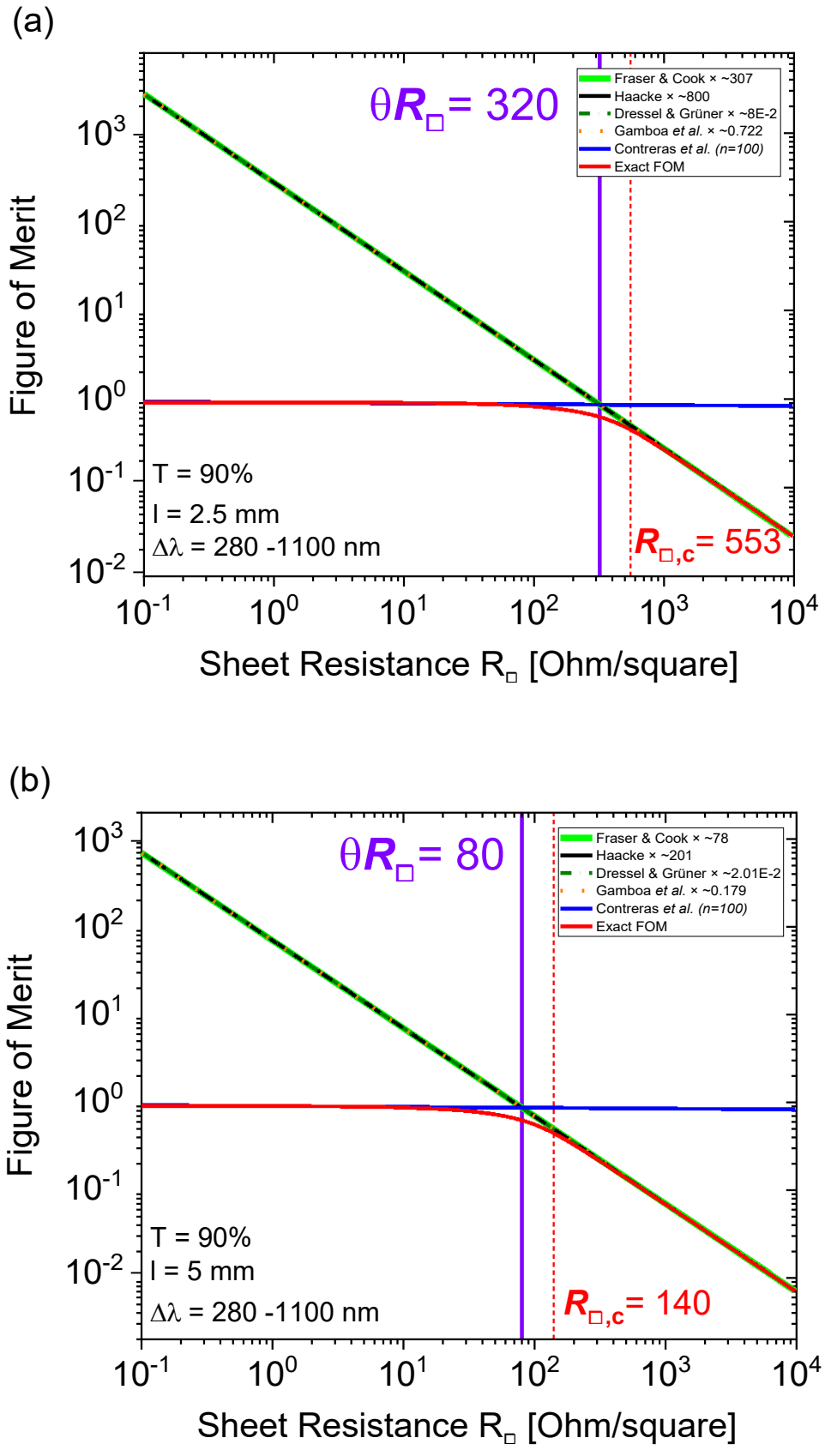

Figure A3ab: *FOM vs. R□ for different solar lengths, for (a) l = 2.5 mm and (b) l = 5mm.*

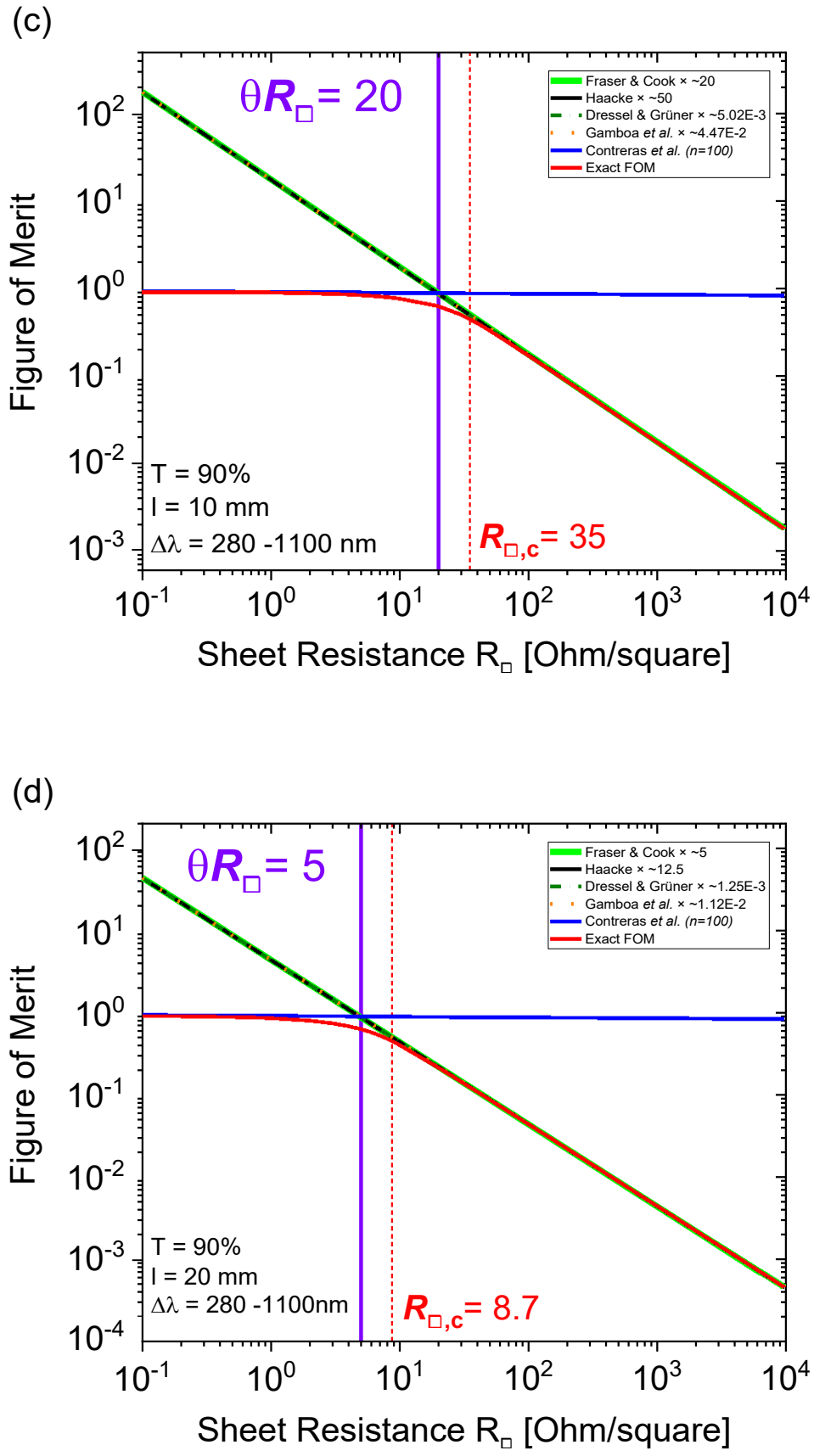

Figure A3cd: *FOM vs. R□ for different solar lengths, for (c) l = 10 mm and (d) l = 20 mm.*

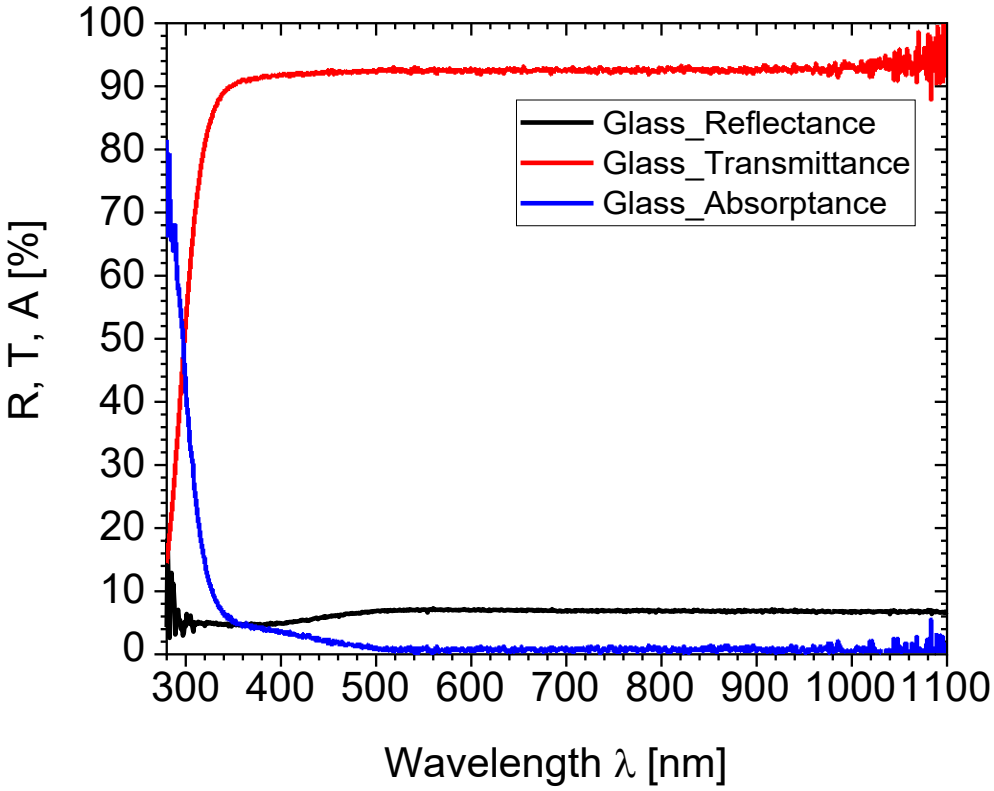

Figure A4: *Optical properties of a bare glass.*

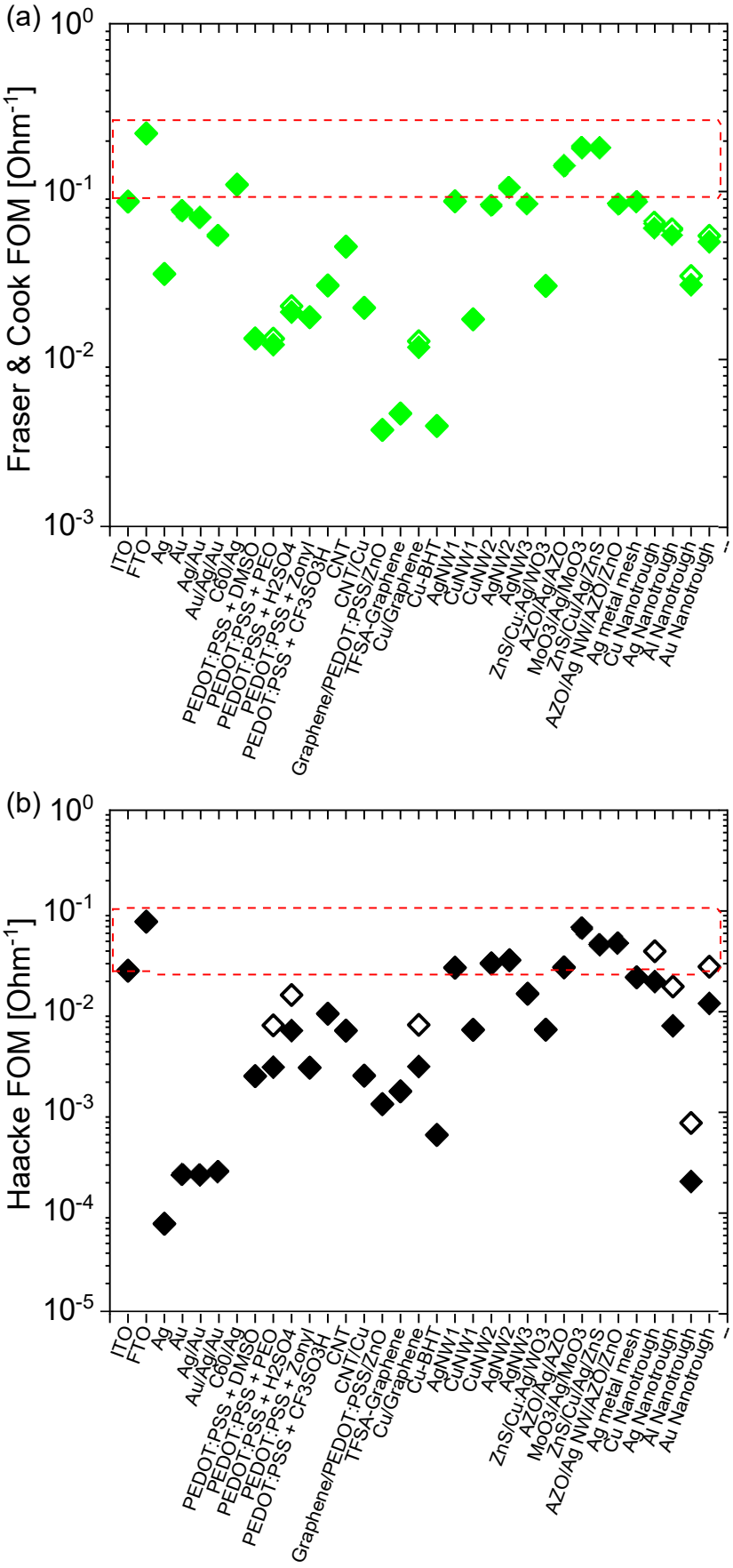

Figure A5ab: *(a) Fraser & Cook and (b) Haacke FOM for different TCEs.*

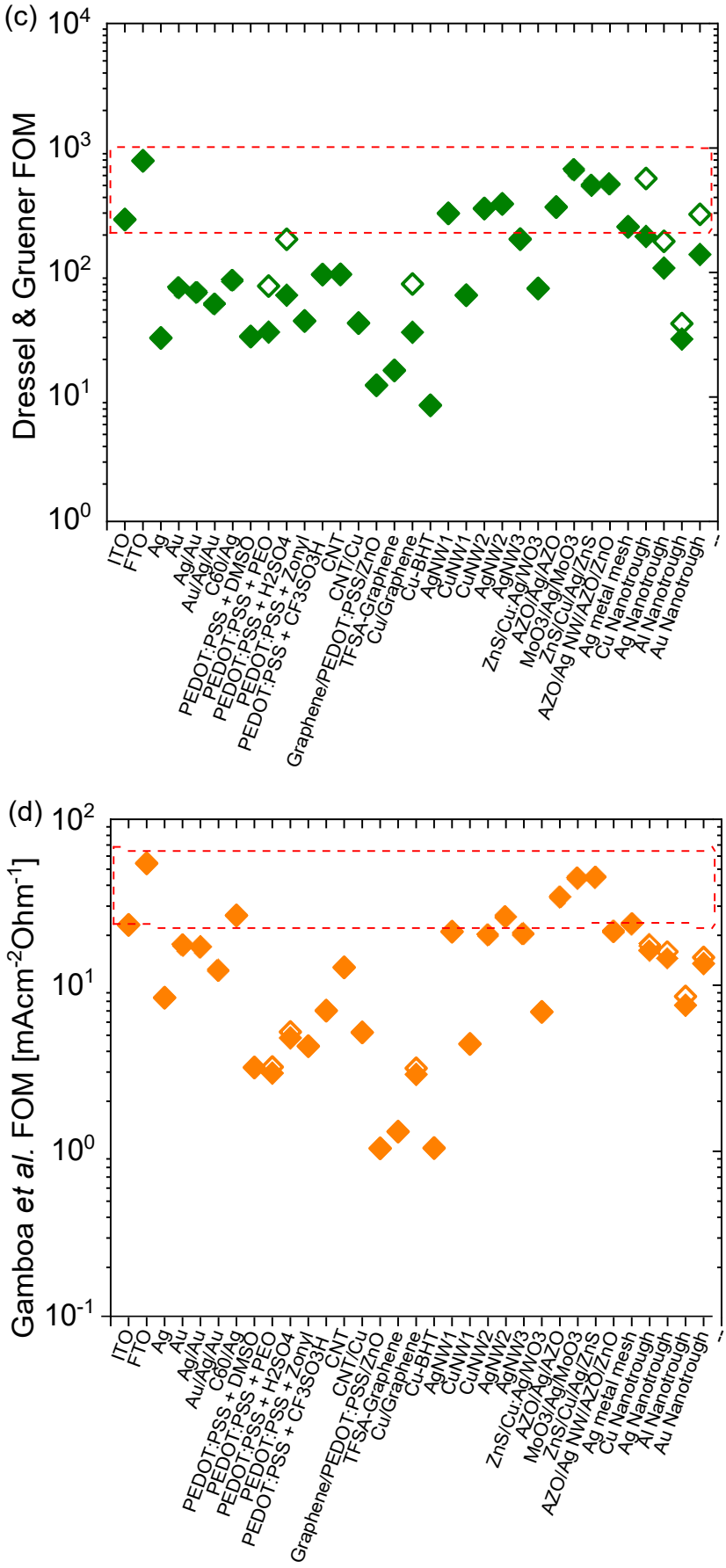

Figure A5cd: *(c) Dressel & Grüner and (d) Gamboa et al. FOM for different TCEs.*

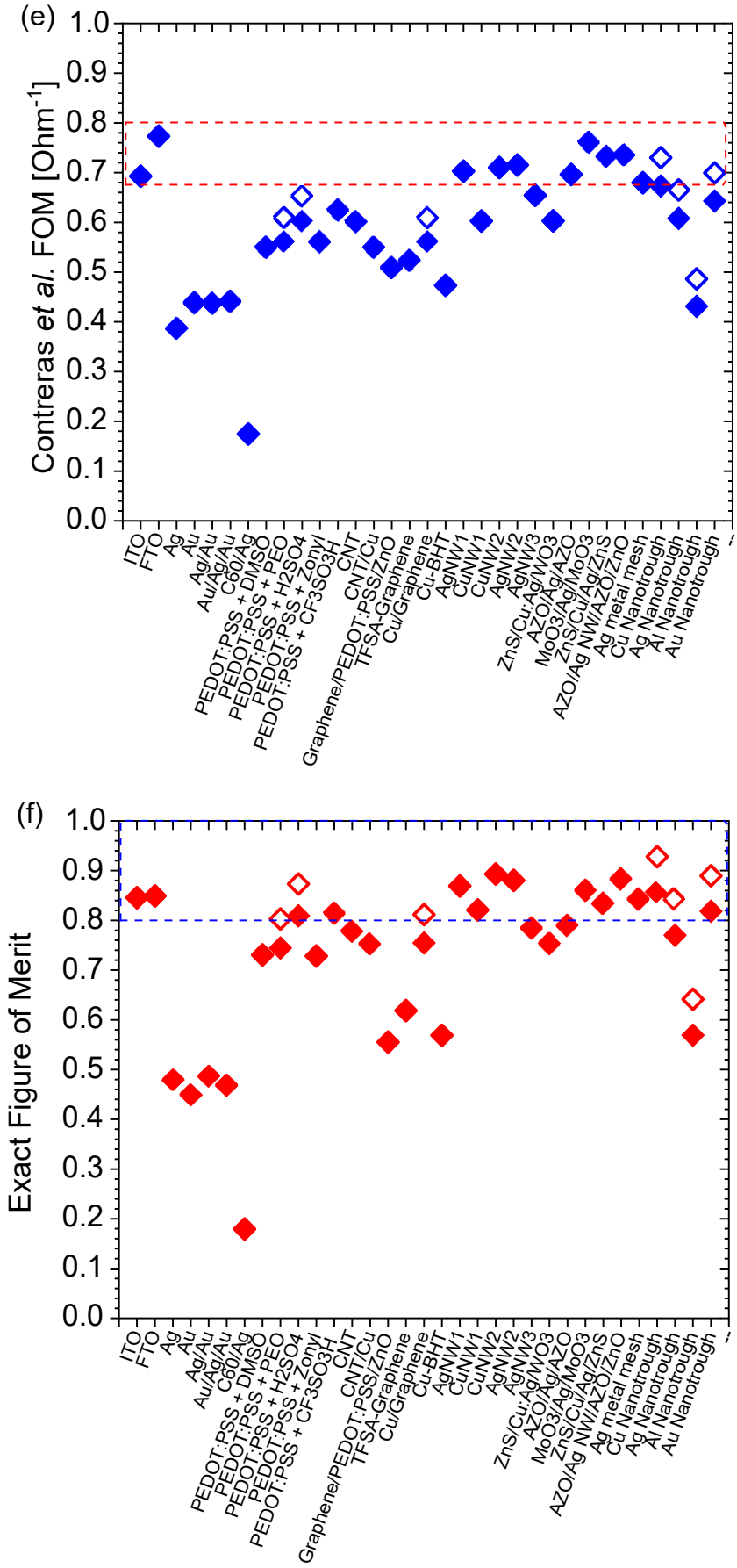

Figure A5ef: *(e) Contreras et al. and (f) exact FOM for different TCEs.*

Table A2: *Comparison of the FOM by Fraser and Cook evaluated for different TCEs for the spectral range of 350 to 800 nm and a solar cell length of 5 mm.*

Note: *TCEs with a * were evaluated for the spectral range of 400 to 800 nm due to insufficient data below 400 nm. The values with ǂ sign represent FOM values of TCEs for which only film transmittance spectra were taken into account for the analysis.*

Abbreviation: *SR – Sheet resistance, T – Transmittance, Ref. – Reference, TW – This work.*

TCE	SR [Ω/□]	Average T [%]	Substrate	Fraser & Cook [Ω^{-1}]	Ref.
Metal oxides					
• ITO	10	85.53	Glass	0.087	TW
• FTO	4.0 ± 0.14	83.81	Glass	0.222	[56]
Ultra-thin metals					
• Ag	15.7	49.79	Glass	0.032	[61]
• Au	7	43.50	Glass	0.076	[61]
• Au/Ag	7.8	50.70	Glass	0.069	[61]
• Au/Ag/Au	10.42 ± 0.5	48.43	Glass	0.053	[137]
• C_{60}-surfactant/Ag	1.70	21.24	Glass	0.108	[60]
Conductive polymers					
• PEDOT:PSS + DMSO	64	81.37	Glass	0.013	TW
• PEDOT:PSS + PEO	72	91.84	Glass	0.012	[138]
• PEDOT:PSS + H_2SO_4	46.1	95.41	Glass	0.013ǂ 0.019 0.021ǂ	[102]
• PEDOT:PSS + Zonyl	46	79.09	Glass	0.018	[139]
• PEDOT:PSS + CF_3SO_3H*	32	85.99	PET	0.028	[140]

Carbon nanotubes					
• Pristine CNT	17	78.92	Glass	0.047	[64]
• CNT/Cu	39	79.14	Glass	0.020	[141]
Graphene					
• Graphene/PEDOT:PSS/ZnO	230	86.13	Glass	0.004	[142]
• TFSA-Graphene	185	87.29	PET	0.005	[143]
• Cu/Graphene	~75	90.63	Glass	0.012 0.013‡	[107]
• Cu-BHT*	200	78.29	Glass	0.004	[144]
Nanowires					
• AgNW1*	10.3	88.10	Glass	0.0862	[66]
• CuNW1	51.5	89.35	PET	0.0174	[65]
• CuNW2*	11.2	90.88	Glass	0.081	[67]
• AgNW2*	8.5	89.15	Glass	0.104	[67]
• AgNW3	~10	76.30	Glass	0.0824	[146]
Dielectric/Metal/Dielectric					
• ZnS/Cu:Ag/WO_3	31	78.98	Glass	0.027	[147]
• AZO/Ag/AZO	6	79.04	Glass	0.139	[62]
• MoO_3/Ag/MoO_3	5	86.11	Glass	0.179	[148]
• ZnS/Cu/Ag/ZnS	4.8	81.54	Glass	0.178	[149]
• AZO/Ag NW/AZO/ZnO*	11.3	88.63	Glass	0.083	[150]
Metal network					
• Ag metal mesh	10	85.89	Glass	0.086	[151]
• Cu nanotrough	15	95.45	Glass	0.059 0.064‡	[152]
• Ag nanotrough	15	86.57	Glass	0.053	[152]

• Al nanotrough	21	66.16	Glass	0.058‡ 0.028 0.031‡	[152]
• Au nanotrough	17	91.86	Glass	0.050 0.055‡	[152]

Table A3: *Comparison of the FOM by Haacke evaluated for different TCEs for the spectral range of 350 to 800 nm and a solar cell length of 5 mm.*

Note: *TCEs with a * were evaluated for the spectral range of 400 to 800 nm due to insufficient data below 400 nm. The values with ǂ sign represent FOM values of TCEs for which only film transmittance spectra were taken into account for the analysis.*

Abbreviation: *SR – Sheet resistance, T – Transmittance, Ref. – Reference, TW – This work.*

TCE	SR [Ω/□]	Average T [%]	Substrate	Haacke [Ω^{-1}]	Ref.
Metal oxides					
• ITO	10	85.53	Glass	0.0255	TW
• FTO	4.0 ± 0.14	83.81	Glass	0.0764	[56]
Ultra-thin metals					
• Ag	15.7	49.79	Glass	0.0003	[61]
• Au	7	43.50	Glass	0.0001	[61]
• Au/Ag	7.8	50.70	Glass	0.0003	[61]
• Au/Ag/Au	10.42 ± 0.5	48.43	Glass	0.0003	[137]
• C_{60}-surfactant/Ag	1.70	21.24	Glass	0.0000	[60]
Conductive polymers					
• PEDOT:PSS + DMSO	64	81.37	Glass	0.0025	TW
• PEDOT:PSS + PEO	72	91.84	Glass	0.0030 0.0070ǂ	[138]
• PEDOT:PSS + H_2SO_4	46.1	95.41	Glass	0.0062 0.0140ǂ	[102]
• PEDOT:PSS + Zonyl	46	79.09	Glass	0.0030	[139]
• PEDOT:PSS + CF_3SO_3H*	32	85.99	PET	0.0091	[140]

Carbon nanotubes					
• Pristine CNT	17	78.92	Glass	0.0062	[64]
• CNT/Cu	39	79.14	Glass	0.0025	[141]
Graphene					
• Graphene/PEDOT:PSS/ZnO	230	86.13	Glass	0.0011	[142]
• TFSA-Graphene	185	87.29	PET	0.0015	[143]
• Cu/Graphene	~75	90.63	Glass	0.0031 0.0076‡	[107]
• Cu-BHT*	200	78.29	Glass	0.0006	[144]
Nanowires					
• AgNW1*	10.3	88.10	Glass	0.0295	[66]
• CuNW1	51.5	89.35	PET	0.0063	[65]
• CuNW2*	11.2	90.88	Glass	0.0326	[67]
• AgNW2*	8.5	89.15	Glass	0.0351	[67]
• AgNW3	~10	76.30	Glass	0.0144	[146]
Dielectric/Metal/Dielectric					
• ZnS/Cu:Ag/WO_3	31	78.98	Glass	0.0064	[147]
• AZO/Ag/AZO	6	79.04	Glass	0.0268	[62]
• MoO_3/Ag/MoO_3	5	86.11	Glass	0.0655	[148]
• ZnS/Cu/Ag/ZnS	4.8	81.54	Glass	0.0442	[149]
• AZO/Ag NW/AZO/ZnO*	11.3	88.63	Glass	0.0459	[150]
Metal network					
• Ag metal mesh	10	85.89	Glass	0.0210	[151]
• Cu nanotrough	15	95.45	Glass	0.0191 0.0430‡	[152]
• Ag nanotrough	15	86.57	Glass	0.0069	[152]

• Al nanotrough	21	66.16	Glass	0.0170‡ 0.0002 0.0007‡	[152]
• Au nanotrough	17	91.86	Glass	0.0121 0.0280‡	[152]

Table A4: *Comparison of the FOM by Dressel and Grüner evaluated for different TCEs for the spectral range of 350 to 800 nm and a solar cell length of 5 mm.*

Note: *TCEs with a * were evaluated for the spectral range of 400 to 800 nm due to insufficient data below 400 nm. The values with ǂ sign represent FOM values of TCEs for which only film transmittance spectra were taken into account for the analysis.*

Abbreviation: *SR – Sheet resistance, T – Transmittance, Ref. – Reference, TW – This work.*

TCE	SR [Ω/□]	Average T [%]	Substrate	Dressel & Grüner	Ref.
Metal oxides					
• ITO	10	85.53	Glass	266.350	TW
• FTO	4.0 ± 0.14	83.81	Glass	771.778	[56]
Ultra-thin metals					
• Ag	15.7	49.79	Glass	72.473	[61]
• Au	7	43.50	Glass	29.764	[61]
• Au/Ag	7.8	50.70	Glass	66.214	[61]
• Au/Ag/Au	10.42 ± 0.5	48.43	Glass	53.223	[137]
• C_{60}-surfactant/Ag	1.70	21.24	Glass	83.396	[60]
Conductive polymers					
• PEDOT:PSS + DMSO	64	81.37	Glass	30.514	TW
• PEDOT:PSS + PEO	72	91.84	Glass	33.167 75.155ǂ	[138]
• PEDOT:PSS + H_2SO_4	46.1	95.41	Glass	63.346 184.840ǂ	[102]
• PEDOT:PSS + Zonyl	46	79.09	Glass	39.425	[139]
• PEDOT:PSS + CF_3SO_3H*	32	85.99	PET	92.893	[140]

Carbon nanotubes					
• Pristine CNT	17	78.92	Glass	93.187	[64]
• CNT/Cu	39	79.14	Glass	39.199	[141]
Graphene					
• Graphene/PEDOT:PSS/ZnO	230	86.13	Glass	11.834	[142]
• TFSA-Graphene	185	87.29	PET	15.569	[143]
• Cu/Graphene	~75	90.63	Glass	33.095 88.787‡	[107]
• Cu-BHT*	200	78.29	Glass	8.172	[144]
Nanowires					
• AgNW1*	10.3	88.10	Glass	289.281	[66]
• CuNW1	51.5	89.35	PET	63.497	[65]
• CuNW2*	11.2	90.88	Glass	326.139	[67]
• AgNW2*	8.5	89.15	Glass	355.550	[67]
• AgNW3	~10	76.30	Glass	185.420	[146]
Dielectric/Metal/Dielectric					
• ZnS/Cu:Ag/WO_3	31	78.98	Glass	71.873	[147]
• AZO/Ag/AZO	6	79.04	Glass	328.383	[62]
• MoO_3/Ag/MoO_3	5	86.11	Glass	656.624	[148]
• ZnS/Cu/Ag/ZnS	4.8	81.54	Glass	487.495	[149]
• AZO/Ag NW/AZO/ZnO*	11.3	88.63	Glass	500.064	[150]
Metal network					
• Ag metal mesh	10	85.89	Glass	232.583	[151]
• Cu nanotrough	15	95.45	Glass	194.682 568.066‡	[152]
• Ag nanotrough	15	86.57	Glass	104.871	[152]

• Al nanotrough	21	66.16	Glass	177.616‡ 29.164 38.790‡	[152]
• Au nanotrough	17	91.86	Glass	134.576 292.681‡	[152]

Table A5: *Comparison of the FOM by Gamboa et al. evaluated for different TCEs for the spectral range of 350 to 800 nm and a solar cell length of 5 mm.*

Note: *TCEs with a * were evaluated for $\Delta\lambda$ = 400 – 800 nm due to insufficient data below 400 nm. The values with ǂ sign represent FOM values of TCEs for which only film transmittance spectra were taken into account for the analysis.*

Abbreviation: *SR – Sheet resistance, T – Transmittance, Ref. – Reference, TW – This work.*

TCE	SR [Ω/□]	Average T [%]	Substrate	Gambo-a *et al.* [mA/cm^{2}Ω]	Ref.
Metal oxides					
• ITO	10	85.53	Glass	23.108	TW
• FTO	4.0 ± 0.14	83.81	Glass	57.432	[56]
Ultra-thin metals					
• Ag	15.7	49.79	Glass	8.288	[61]
• Au	7	43.50	Glass	17.199	[61]
• Au/Ag	7.8	50.70	Glass	16.750	[61]
• Au/Ag/Au	10.42 ± 0.5	48.43	Glass	12.023	[137]
• C_{60}-surfactant/Ag	1.70	21.24	Glass	27.921	[60]
Conductive polymers					
• PEDOT:PSS + DMSO	64	81.37	Glass	3.388	TW
• PEDOT:PSS + PEO	72	91.84	Glass	3.127 3.410ǂ	[138]
• PEDOT:PSS + H_2SO_4	46.1	95.41	Glass	5.101 5.543ǂ	[102]
• PEDOT:PSS + Zonyl	46	79.09	Glass	4.547	[139]
• PEDOT:PSS + CF_3SO_3H*	32	85.99	PET	6.928	[140]

Carbon nanotubes					
• Pristine CNT	17	78.92	Glass	12.630	[64]
• CNT/Cu	39	79.14	Glass	5.507	[141]
Graphene					
• Graphene/PEDOT:PSS/ZnO	230	86.13	Glass	1.014	[142]
• TFSA-Graphene	185	87.29	PET	1.279	[143]
• Cu/Graphene	~75	90.63	Glass	3.075 3.370‡	[107]
• Cu-BHT*	200	78.29	Glass	1.019	[144]
Nanowires					
• AgNW1*	10.3	88.10	Glass	22.237	[66]
• CuNW1	51.5	89.35	PET	4.692	[65]
• CuNW2*	11.2	90.88	Glass	21.062	[67]
• AgNW2*	8.5	89.15	Glass	27.222	[67]
• AgNW3	~10	76.30	Glass	21.393	[146]
Dielectric/Metal/Dielectric					
• ZnS/Cu:Ag/WO_3	31	78.98	Glass	6.803	[147]
• AZO/Ag/AZO	6	79.04	Glass	35.626	[62]
• MoO_3/Ag/MoO_3	5	86.11	Glass	46.566	[148]
• ZnS/Cu/Ag/ZnS	4.8	81.54	Glass	47.051	[149]
• AZO/Ag NW/AZO/ZnO*	11.3	88.63	Glass	20.641	[150]
Metal network					
• Ag metal mesh	10	85.89	Glass	23.017	[151]
• Cu nanotrough	15	95.45	Glass	15.735 17.093‡	[152]
• Ag nanotrough	15	86.57	Glass	14.117	[152]

• Al nanotrough	21	66.16	Glass	15.474‡ 7.459 8.429‡	[152]
• Au nanotrough	17	91.86	Glass	13.297 14.494‡	[152]

Table A6: *Comparison of the FOM by Contreras et al. evaluated for different TCEs for the spectral range of 350 to 800 nm and a solar cell length of 5 mm.*

Note: *TCEs with a * were evaluated for the spectral range of 400 to 800 nm due to insufficient data below 400 nm. The values with ǂ sign represent FOM values of TCEs for which only film transmittance spectra were taken into account for the analysis.*

Abbreviation: *SR – Sheet resistance, T – Transmittance, Ref. – Reference, TW – This work.*

TCE	SR [Ω/□]	Average T [%]	Substrate	Contreras *et al.* [Ω^{-1}]	Ref.
Metal oxides					
• ITO	10	85.53	Glass	0.693	TW
• FTO	4.0 ± 0.14	83.81	Glass	0.773	[56]
Ultra-thin metals					
• Ag	15.7	49.79	Glass	0.386	[61]
• Au	7	43.50	Glass	0.438	[61]
• Au/Ag	7.8	50.70	Glass	0.437	[61]
• Au/Ag/Au	10.42 ± 0.5	48.43	Glass	0.441	[137]
• C_{60}-surfactant/Ag	1.70	21.24	Glass	0.175	[60]
Conductive polymers					
• PEDOT:PSS + DMSO	64	81.37	Glass	0.549	TW
• PEDOT:PSS + PEO	72	91.84	Glass	0.560 0.609ǂ	[138]
• PEDOT:PSS + H_2SO_4	46.1	95.41	Glass	0.602 0.653ǂ	[102]
• PEDOT:PSS + Zonyl	46	79.09	Glass	0.560	[139]
• PEDOT:PSS + CF_3SO_3H*	32	85.99	PET	0.625	[140]

Carbon nanotubes					
• Pristine CNT	17	78.92	Glass	0.602	[64]
• CNT/Cu	39	79.14	Glass	0.549	[141]
Graphene					
• Graphene/PEDOT:PSS/ZnO	230	86.13	Glass	0.508	[142]
• TFSA-Graphene	185	87.29	PET	0.523	[143]
• Cu/Graphene	~75	90.63	Glass	0.560 0.614‡	[107]
• Cu-BHT*	200	78.29	Glass	0.473	[144]
Nanowires					
• AgNW1*	10.3	88.10	Glass	0.703	[66]
• CuNW1	51.5	89.35	PET	0.603	[65]
• CuNW2*	11.2	90.88	Glass	0.710	[67]
• AgNW2*	8.5	89.15	Glass	0.715	[67]
• AgNW3	~10	76.30	Glass	0.654	[146]
Dielectric/Metal/Dielectric					
• ZnS/Cu:Ag/WO_3	31	78.98	Glass	0.603	[147]
• AZO/Ag/AZO	6	79.04	Glass	0.696	[62]
• MoO_3/Ag/MoO_3	5	86.11	Glass	0.761	[148]
• ZnS/Cu/Ag/ZnS	4.8	81.54	Glass	0.732	[149]
• AZO/Ag NW/AZO/ZnO*	11.3	88.63	Glass	0.735	[150]
Metal network					
• Ag metal mesh	10	85.89	Glass	0.680	[151]
• Cu nanotrough	15	95.45	Glass	0.673 0.730‡	[152]
• Ag nanotrough	15	86.57	Glass	0.608	[152]

• Al nanotrough	21	66.16	Glass	0.665‡ 0.431 0.486‡	[152]
• Au nanotrough	17	91.86	Glass	0.643 0.699‡	[152]

Reference

[1] T. D. Lee, A. U. Ebong, *Renewable and Sustainable Energy Reviews* **2017**, *70*, 1286-1297.

[2] T. Ahmad, D. D. Zhang, *Energy Reports* **2020**, *6*, 1973-1991.

[3] D. Gielen, F. Boshell, D. Saygin, M. D. Bazilian, N. Wagner, R. Gorini, *Energy Strategy Reviews* **2019**, *24*, 38-50.

[4] M. R. a. P. R. Hannah Ritchie, *Published online at OurWorldInData.org* **2020**.

[5] Grantham Research Institute, https://climate-laws.org/legislation_and_policies.

[6] F. Manzano-Agugliaro, A. Alcayde, F. G. Montoya, A. Zapata-Sierra, C. Gil, *Renewable and Sustainable Energy Reviews* **2013**, *18*, 134-143.

[7] International Renewable Energy Agency (IRENA), Renewable Capacity Statistics 2022,

[8] K. K. J. S Sharma, A Sharma, *Materials Sciences and Applications* **2015** *6*, 1145-1155.

[9] P. K. Nayak, S. Mahesh, H. J. Snaith, D. Cahen, *Nature Reviews Materials* **2019**, *4*, 269-285.

[10] S. Philipps, *Photovoltaics Report,* **2022**.

[11] Best Research-Cell Efficiency Chart, National Renewable Energy Laboratory.,

[12] W. R. Cao, J. G. Xue, *Energy & Environmental Science* **2014**, *7*, 2123-2144.

[13] R. G. Gordon, *MRS Bull.* **2000**, *25*, 52-57.

[14] K. Ellmer, *Nat. Photonics* **2012**, *6*, 808-816.

[15] M. Grundmann, *Physica Status Solidi a-Applications and Materials Science* **2015**, *212*, 1409-1426.

[16] K. Bädeker, *Annalen der Physik* **1907**, *327*, 749-766.

[17] L. Kinner, *Flexible transparent electrodes for optoelectronic devices*, Humboldt University of Berlin **2021**.

[18] K. Kawajiri, K. Tahara, S. Uemiya, *Resources, Environment and Sustainability* **2022**, *7*, 100047.

[19] Q. M. Insights, **2020**.

[20] C. J. M. Emmott, A. Urbina, J. Nelson, *Sol. Energy Mater. Sol. Cells* **2012**, *97*, 14-21.

[21] Q. S. Liu, Y. F. Jiang, K. Jin, J. Q. Qin, J. G. Xu, W. T. Li, J. Xiong, J. F. Liu, Z. Xiao, K. Sun, S. F. Yang, X. T. Zhang, L. M. Ding, *Sci. Bull.* **2020**, *65*, 272-275.

[22] B. G. Lewis, D. C. Paine, *MRS Bull.* **2000**, *25*, 22-27.

[23] L. H. Qin, Y. Q. Yan, G. Yu, Z. Y. Zhang, T. Zhama, H. Sun, *Materials (Basel, Switzerland)* **2021**, *14*.

[24] W. R. Cao, J. Li, H. Z. Chen, J. G. Xue, *Journal of Photonics for Energy* **2014**, *4*.

[25] R. Ramarajan, D. Paul Joseph, K. Thangaraju, M. Kovendhan, in *Metal and Metal Oxides for Energy and Electronics* (Eds.: S. Rajendran, J. Qin, F. Gracia, E. Lichtfouse), Springer International Publishing, Cham, **2021**, pp. 149-183.

[26] TCE application pictures, https://www.sciencemag.org/news/2019/04/marrying-two-types-solar-cells-draws-more-power-sun,

https://sites.google.com/site/theoledsupersite30/,
https://www.sageglass.com/en/article/what-electrochromic-glass,
https://www.viewsonic.com/my/products/lcd/professional-vp.php,
https://9to5mac.com/2018/12/12/thinner-iphones/

[27] F. C. Krebs, *Sol. Energy Mater. Sol. Cells* **2009**, *93*, 394-412.

[28] M. Zhang, L. Zhu, G. Zhou, T. Hao, C. Qiu, Z. Zhao, Q. Hu, B. W. Larson, H. Zhu, Z. Ma, Z. Tang, W. Feng, Y. Zhang, T. P. Russell, F. Liu, *Nat. Commun.* **2021**, *12*, 309.

[29] L. X. Chen, *ACS Energy Letters* **2019**, *4*, 2537-2539.

[30] L. Hong, H. F. Yao, Y. Cui, Z. Y. Ge, J. H. Hou, *Apl Materials* **2020**, *8*.

[31] H. Hoppe, N. S. Sariciftci, in *Photoresponsive Polymers Ii, Vol. 214* (Eds.: S. R. Marder, K. S. Lee), Springer-Verlag Berlin, Berlin, **2008**, pp. 1-86.

[32] H. Hoppe, N. S. Sariciftci, *J. Mater. Res.* **2004**, *19*, 1924-1945.

[33] R. O. Kesinro, A. O. Boyo, M. L. Akinyemi, M. E. Emetere, A. P. Aizebeokhai, *IOP Conference Series: Earth and Environmental Science* **2021**, *665*, 012036.

[34] J. D. Servaites, M. A. Ratner, T. J. Marks, *Energy & Environmental Science* **2011**, *4*, 4410-4422.

[35] J. Bisquert, *The Physics of Solar Cells*, CRC Press, Taylor & Francis Group, LLC, **2018**.

[36] A. L. a. S. Hegedus, *Handbook of Photovoltaic Science and Engineering*, John Wiley & Sons, Ltd., **2003**.

[37] F. A. Lindholm, J. G. Fossum, E. L. Burgess, *IEEE Transactions on Electron Devices* **1979**, *26*.

[38] C. B. H. a. S.G.Bowden, **2019**.

[39] A. Anand, M. M. Islam, R. Meitzner, U. S. Schubert, H. Hoppe, *Adv. Energy Mater.* **2021**, *11*.

[40] H. Hoppe, M. Seeland, B. Muhsin, *Sol. Energy Mater. Sol. Cells* **2012**, *97*, 119-126.

[41] L. Luo, *Solution-processed Transparent Electrodes from Metal Oxide Nanocrystals for Thin Film Optoelectronics*, ETH Zurich **2013**.

[42] T. Zinchenko, E. Pecherskaya, D. Artamonov, *Aims Materials Science* **2019**, *6*, 276-287.

[43] P. V. Zant, *Microchip fabrication : a practical guide to semiconductor processing*, New York : McGraw-Hill, **2000**.

[44] H. R. Barry P. Rand, *Organic Solar Cells, Fundamentals, Devices, and Upscaling*, Jenny Stanford Publishing, **2014**.

[45] D. B. Fraser, H. D. Cook, *J. Electrochem. Soc.* **1972**, *119*, 1368.

[46] G. Haacke, *J. Appl. Phys.* **1976**, *47*, 4086-4089.

[47] P. A. l. a. S. I. Soclof, in *Proc. IEEE 12th Photovoltaic Conf.*, **1976**, p. 978.

[48] V. K. Jain, A. P. Kulshreshtha, *Solar Energy Materials* **1981**, *4*, 151-158.

[49] S. De, P. J. King, P. E. Lyons, U. Khan, J. N. Coleman, *ACS Nano* **2010**, *4*, 7064-7072.

[50] M. Dressel, G. Grüner, *Electrodynamics of Solids: Optical Properties of Electrons in Matter*, Cambridge University Press, Cambridge, **2002**.

[51] D. A. Jacobs, K. R. Catchpole, F. J. Beck, T. P. White, *J. Mater. Chem. A* **2016**, *4*, 4490-4496.
[52] I. R. Cisneros-Contreras, A. L. Munoz-Rosas, A. Rodriguez-Gomez, *Results Phys.* **2019**, *15*, 8.
[53] J. A. Mendez-Gamboa, R. Castro-Rodriguez, I. V. Perez-Quintana, R. A. Medina-Esquivel, A. Martel-Arbelo, *Thin Solid Films* **2016**, *599*, 14-18.
[54] C. P. Muzzillo, *Adv. Energy Mater.* **2022**, *12*.
[55] Different class of TCE pictures, https://phys.org/news/2011-08-transparent-electronics-graphene-based-electrodes-video.html, https://www.medgadget.com/2020/04/3d-printed-brain-implants-using-conductive-polymer-ink.html, https://www.helmholtz-berlin.de/pubbin/news_seite?nid=14269&sprache=en&seitenid=74699, http://www.graphenesq.com/whatis/app.asp, https://www.exp-tech.de/en/accessories/other/5232/ito-indium-tin-oxide-coated-glass-50mm-x-50mm, http://www.perc-sinano.com/en/yjcg.asp?id=25&tit=6, https://www.vritratech.com/store/product/fluorine-doped-tin-oxide-coated-glass-fto-50mm-x-50mm-sr-10-ohm-sq-2/, http://www.businesskorea.co.kr/news/articleView.html?idxno=37079
[56] B. R. Koo, D. H. Oh, D. H. Riu, H. J. Ahn, *Acs Applied Materials & Interfaces* **2017**, *9*, 44584-44592.
[57] A. Mashreghi, H. Zare, *Journal of Solid State Electrochemistry* **2016**, *20*, 2693-2698.
[58] S. D. Ponja, S. Sathasivam, I. P. Parkin, C. J. Carmalt, *Sci Rep* **2020**, *10*, 638.
[59] E. H. E. Wu, S. H. Li, C. W. Chen, G. Li, Z. Xu, Y. Yang, *J. Disp. Technol.* **2005**, *1*, 105-111.
[60] C. C. Chueh, S. C. Chien, H. L. Yip, J. F. Salinas, C. Z. Li, K. S. Chen, F. C. Chen, W. C. Chen, A. K. Y. Jen, *Adv. Energy Mater.* **2013**, *3*, 417-423.
[61] G. Y. Xu, L. Shen, C. H. Cui, S. P. Wen, R. M. Xue, W. J. Chen, H. Y. Chen, J. W. Zhang, H. K. Li, Y. W. Li, Y. F. Li, *Adv. Funct. Mater.* **2017**, *27*, 10.
[62] M. Acosta, J. Mendez-Gamboa, I. Riech, C. Acosta, M. Zambrano, *Superlattices Microstruct.* **2019**, *127*, 49-53.
[63] S. H. Choa, C. K. Cho, W. J. Hwang, K. T. Eun, H. K. Kim, *Sol. Energy Mater. Sol. Cells* **2011**, *95*, 3442-3449.
[64] I. Jeon, C. Delacou, H. Okada, G. E. Morse, T. H. Han, Y. Sato, A. Anisimov, K. Suenaga, E. I. Kauppinen, S. Maruyama, Y. Matsuo, *J. Mater. Chem. A* **2018**, *6*, 14553-14559.
[65] H. Z. Guo, N. Lin, Y. Z. Chen, Z. W. Wang, Q. S. Xie, T. C. Zheng, N. Gao, S. P. Li, J. Y. Kang, D. J. Cai, D. L. Peng, *Sci Rep* **2013**, *3*, 8.
[66] J. Y. Lee, S. T. Connor, Y. Cui, P. Peumans, *Nano Lett.* **2008**, *8*, 689-692.
[67] P.-C. Hsu, D. Kong, S. Wang, H. Wang, A. J. Welch, H. Wu, Y. Cui, *J. Am. Chem. Soc.* **2014**, *136*, 10593-10596.
[68] Y. Galagan, J. Rubingh, R. Andriessen, C. C. Fan, P. W. M. Blom, S. C. Veenstra, J. M. Kroon, *Sol. Energy Mater. Sol. Cells* **2011**, *95*, 1339-1343.

[69] S. K. Andreas Elschner, Wilfried Lovenich, Udo Merker, Knud Reuter, *PEDOT Principles and Applications of an Intrinsically Conductive Polymer*, CRC Press, **2010**.
[70] Y. Cao, G. M. Treacy, P. Smith, A. J. Heeger, *Applied Physics Letters* **1992**, *60*, 2711-2713.
[71] S. Sharma, S. Shriwastava, S. Kumar, K. Bhatt, C. C. Tripathi, *Opto-Electronics Review* **2018**, *26*, 223-235.
[72] K. Sun, S. P. Zhang, P. C. Li, Y. J. Xia, X. Zhang, D. H. Du, F. H. Isikgor, J. Y. Ouyang, *J. Mater. Sci.-Mater. Electron.* **2015**, *26*, 4438-4462.
[73] J. S. Huang, P. F. Miller, J. S. Wilson, A. J. de Mello, J. C. de Mello, D. D. C. Bradley, *Adv. Funct. Mater.* **2005**, *15*, 290-296.
[74] D. A. Mengistie, M. A. Ibrahem, P. C. Wang, C. W. Chu, *Acs Applied Materials & Interfaces* **2014**, *6*, 2292-2299.
[75] B. J. Worfolk, S. C. Andrews, S. Park, J. Reinspach, N. Liu, M. F. Toney, S. C. B. Mannsfeld, Z. Bao, *Proceedings of the National Academy of Sciences* **2015**, *112*, 14138-14143.
[76] J. Huang, P. F. Miller, J. C. de Mello, A. J. de Mello, D. D. C. Bradley, *Synth. Met.* **2003**, *139*, 569-572.
[77] G. Greczynski, T. Kugler, M. Keil, W. Osikowicz, M. Fahlman, W. R. Salaneck, *J. Electron Spectrosc. Relat. Phenom.* **2001**, *121*, 1-17.
[78] Z. Fan, J. Y. Ouyang, *Adv. Electron. Mater.* **2019**, *5*, 23.
[79] Y. W. Han, J. Y. Choi, Y. J. Lee, E. J. Ko, M. H. Choi, I. S. Suh, D. K. Moon, *Adv. Mater. Interfaces* **2019**, *6*, 15.
[80] Y. Hu, C. Wenzhen, *Recent Patents on Materials Science* **2013**, *6*, 68-74.
[81] Y. H. Kim, C. Sachse, M. L. Machala, C. May, L. Muller-Meskamp, K. Leo, *Adv. Funct. Mater.* **2011**, *21*, 1076-1081.
[82] T. Mochizuki, Y. Takigami, T. Kondo, H. Okuzaki, *J. Appl. Polym. Sci.* **2018**, *135*, 6.
[83] K. L. Mulfort, J. Ryu, Q. Y. Zhou, *Polymer* **2003**, *44*, 3185-3192.
[84] M. Nikolou, G. G. Malliaras, *Chem. Rec.* **2008**, *8*, 13-22.
[85] A. M. Pappa, V. F. Curto, M. Braendlein, X. Strakosas, M. J. Donahue, M. Fiocchi, G. G. Malliaras, R. M. Owens, *Adv. Healthc. Mater.* **2016**, *5*, 2295-2302.
[86] C. Peng, G. A. Snook, D. J. Fray, M. S. P. Shaffer, G. Z. Chen, *Chem. Commun.* **2006**, 4629-4631.
[87] N. K. Sidhu, A. C. Rastogi, *Mater. Chem. Phys.* **2016**, *176*, 75-86.
[88] O. Synooka, F. Kretschmer, M. D. Hager, M. Himmerlich, S. Krischok, D. Gehrig, F. Laquai, U. S. Schubert, G. Gobsch, H. Hoppe, *Acs Applied Materials & Interfaces* **2014**, *6*, 11068-11081.
[89] S. D. Xu, M. Hong, X. L. Shi, Y. Wang, L. Ge, Y. Bai, L. Z. Wang, M. Dargusch, J. Zou, Z. G. Chen, *Chem. Mat.* **2019**, *31*, 5238-5244.
[90] A. Anand, J. P. Madalaimuthu, M. Schaal, F. Otto, M. Gruenewald, S. Alam, T. Fritz, U. S. Schubert, H. Hoppe, *ACS Applied Electronic Materials* **2021**, *3*, 929-943.
[91] S. R. Dupont, F. Novoa, E. Voroshazi, R. H. Dauskardt, *Adv. Funct. Mater.* **2014**, *24*, 1325-1332.

[92] X. Fan, W. Y. Nie, S. H. Tsai, N. X. Wang, H. H. Huang, Y. J. Cheng, R. J. Wen, L. J. Ma, F. Yan, Y. G. Xia, *Adv. Sci.* **2019**, *6*, 41.
[93] U. Lang, E. Muller, N. Naujoks, J. Dual, *Adv. Funct. Mater.* **2009**, *19*, 1215-1220.
[94] A. M. Nardes, M. Kemerink, M. M. de Kok, E. Vinken, K. Maturova, R. A. J. Janssen, *Org. Electron.* **2008**, *9*, 727-734.
[95] C. S. S. Sangeeth, M. Jaiswal, R. Menon, *J. Phys.-Condes. Matter* **2009**, *21*, 6.
[96] R. Colucci, G. C. Faria, L. F. Santos, G. Gozzi, *Journal of Materials Science: Materials in Electronics* **2019**, *30*, 16864-16872.
[97] N. A. Shahrim, Z. Ahmad, A. W. Azman, Y. F. Buys, N. Sarifuddin, *Materials Advances* **2021**, *2*, 7118-7138.
[98] S. H. Chang, C. H. Chiang, F. S. Kao, C. L. Tien, C. G. Wu, *IEEE Photonics J.* **2014**, *6*, 7.
[99] D. Alemu Mengistie, P.-C. Wang, C.-W. Chu, *J. Mater. Chem. A* **2013**, *1*, 9907-9915.
[100] L. V. Lingstedt, M. Ghittorelli, H. Lu, D. A. Koutsouras, T. Marszalek, F. Torricelli, N. I. Craciun, P. Gkoupidenis, P. W. M. Blom, *Adv. Electron. Mater.* **2019**, *5*.
[101] L. Biessmann, N. Saxena, N. Hohn, M. A. Hossain, J. G. C. Veinot, P. Muller-Buschbaum, *Adv. Electron. Mater.* **2019**, *5*, 10.
[102] N. Kim, S. Kee, S. H. Lee, B. H. Lee, Y. H. Kahng, Y. R. Jo, B. J. Kim, K. Lee, *Adv. Mater.* **2014**, *26*, 2268-2272.
[103] S. Mahato, L. G. Gerling, C. Voz, R. Alcubilla, J. Puigdollers, *IEEE J. Photovolt.* **2016**, *6*, 934-939.
[104] W. F. Zhang, B. F. Zhao, Z. C. He, X. M. Zhao, H. T. Wang, S. F. Yang, H. B. Wu, Y. Cao, *Energy & Environmental Science* **2013**, *6*, 1956-1964.
[105] S. Q. Xiao, C. Liu, L. Chen, L. C. Tan, Y. Chen, *J. Mater. Chem. A* **2015**, *3*, 22316-22324.
[106] K. S. Novoselov, A. K. Geim, S. V. Morozov, D. Jiang, Y. Zhang, S. V. Dubonos, I. V. Grigorieva, A. A. Firsov, *Science* **2004**, *306*, 666-669.
[107] J. H. Kang, S. Choi, Y. J. Park, J. S. Park, N. S. Cho, S. Cho, B. Walker, D. S. Choi, J. W. Shin, J. H. Seo, *Carbon* **2021**, *171*, 341-349.
[108] Z. Y. Yin, J. X. Zhu, Q. Y. He, X. H. Cao, C. L. Tan, H. Y. Chen, Q. Y. Yan, H. Zhang, *Adv. Energy Mater.* **2014**, *4*, 19.
[109] D. S. Hecht, L. B. Hu, G. Irvin, *Adv. Mater.* **2011**, *23*, 1482-1513.
[110] J. L. Bahr, E. T. Mickelson, M. J. Bronikowski, R. E. Smalley, J. M. Tour, *Chem. Commun.* **2001**, 193-194.
[111] O. Synooka, K. R. Eberhardt, J. Balko, T. Thurn-Albrecht, G. Gobsch, W. Mitchell, S. Berny, M. Carrasco-Orozco, H. Hoppe, *Nanotechnology* **2016**, *27*, 254001-254001.
[112] N. Blouin, A. Michaud, M. Leclerc, *Adv. Mater.* **2007**, *19*, 2295.
[113] Sigmaaldrich, KERN ABT 120–5DM analytical balance, https://www.sigmaaldrich.com/DE/de/product/aldrich/z757292.
[114] Bandelin Sonorex RK 255 H ultrasonic cleaner, https://bandelin.com/shop/sonorex-super-ultraschallbaeder/sonorex-super-rk-255-h-ultraschallbad-mit-heizung/.
[115] D. electronic.
[116] Praezitherm hot plate type PZ 2860-SR, https://profcontrol.de/Harry-Gestigkeit-PZ-28-1-Praezitherm-Praezisionsheizplatte-Precision-Hot-Plate_1.

[117] G. Faraji, H. S. Kim, H. T. Kashi, (Eds.: G. Faraji, H. S. Kim, H. T. Kashi), Elsevier, **2018**, pp. 1-17.
[118] Ankit Rohatgi, WebPlotDigitizer, https://automeris.io/WebPlotDigitizer.
[119] TGA - TG 209 F1 Iris https://analyzing-testing.netzsch.com/en/products/thermogravimetric-analysis-tga-thermogravimetry-tg/tg-209-f1-libra.
[120] A. W. Coats, J. P. Redfern, *Analyst* **1963**, *88*, 906-924.
[121] Four-point Probe, https://www.ossila.com/en-eu/products/four-point-probe-system.
[122] F. M. Smits, *The Bell System Technical Journal* **1958**, *37*, 711-718.
[123] L. B. Valdes, *Proceedings of the Institute of Radio Engineers* **1954**, *42*, 420-427.
[124] EddyCus® TF lab 2020 Series – Non-contact Sheet Resistance and Layer Thickness Measurement Device for Single Point Measurements, https://www.suragus.com/en/technology/eddy-current/, https://www.suragus.com/en/products/sheet-resistance/laboratory-devices/eddycus-tf-lab-2020/#sheet-resistance.
[125] Y. F. Dufrene, *Journal of Bacteriology* **2002**, *184*, 5205-5213.
[126] F. A. Stevie, C. L. Donley, *Journal of Vacuum Science & Technology A* **2020**, *38*.
[127] B. Muhsin, J. Renz, K. H. Drue, G. Gobsch, H. Hoppe, *Physica Status Solidi a-Applications and Materials Science* **2009**, *206*, 2771-2774.
[128] B. H. Hamadani, *Appl Phys Lett* **2020**, *117*.
[129] M. Burgelman, A. Niemegeers, *Sol. Energy Mater. Sol. Cells* **1998**, *51*, 129-143.
[130] M. Seeland, H. Hoppe, *Phys. Status Solidi A-Appl. Mat.* **2015**, *212*, 1991-2000.
[131] W. Shockley, H. J. Queisser, *J. Appl. Phys.* **1961**, *32*, 510-&.
[132] J. F. Guillemoles, T. Kirchartz, D. Cahen, U. Rau, *Nat. Photonics* **2019**, *13*, 501-505.
[133] S. Rühle, *Sol. Energy* **2016**, *130*, 139-147.
[134] D. C. Sun, D. S. Sun, *Mater. Chem. Phys.* **2009**, *118*, 288-292.
[135] A. Polman, M. Knight, E. C. Garnett, B. Ehrler, W. C. Sinke, *Science* **2016**, *352*, 10.
[136] R. Meitzner, U. S. Schubert, H. Hoppe, *Adv. Energy Mater.* **2021**, *11*, 7.
[137] C. S. Prakasarao, P. Hazarika, S. D. Dsouza, J. M. Fernandes, M. Kovendhan, R. A. Kumar, D. P. Joseph, *Curr. Appl. Phys.* **2020**, *20*, 1118-1124.
[138] E. Dauzon, Y. B. Lin, H. Faber, E. Yengel, X. Sallenave, C. Plesse, F. Goubard, A. Amassian, T. D. Anthopoulos, *Adv. Funct. Mater.* **2020**, *30*, 11.
[139] M. Vosgueritchian, D. J. Lipomi, Z. A. Bao, *Adv. Funct. Mater.* **2012**, *22*, 421-428.
[140] J. Y. Wan, Y. G. Xia, J. F. Fang, Z. G. Zhang, B. G. Xu, J. Z. Wang, L. Ai, W. J. Song, K. N. Hui, X. Fan, Y. F. Li, *Nano-Micro Lett.* **2021**, *13*, 14.
[141] F. Daneshvar, S. Tagliaferri, H. X. Chen, T. Zhang, C. Liu, H. J. Sue, *Acs Applied Electronic Materials* **2020**, *2*, 2692-2698.
[142] Z. K. Liu, P. You, S. H. Liu, F. Yan, *ACS Nano* **2015**, *9*, 12026-12034.
[143] D. H. Shin, C. W. Jang, H. S. Lee, S. W. Seo, S. H. Choi, *Acs Applied Materials & Interfaces* **2018**, *10*, 3596-3601.
[144] X. Huang, P. Sheng, Z. Y. Tu, F. J. Zhang, J. H. Wang, H. Geng, Y. Zou, C. A. Di, Y. P. Yi, Y. M. Sun, W. Xu, D. B. Zhu, *Nat. Commun.* **2015**, *6*, 8.
[145] X. Huang, H. Yao, Y. Cui, W. Hao, J. Zhu, W. Xu, D. Zhu, *ACS Applied Materials & Interfaces* **2017**, *9*, 40752-40759.

[146] F. Guo, N. Li, V. V. Radmilovic, V. R. Radmilovic, M. Turbiez, E. Spiecker, K. Forberich, C. J. Brabec, *Energy & Environmental Science* **2015**, *8*, 1690-1697.
[147] L. Cattin, A. El Mahlali, M. A. Cherif, S. Touihri, Z. El Jouad, Y. Mouchaal, P. Blanchard, G. Louarn, H. Essaidi, M. Addou, A. Khelil, P. Torchio, J. C. Bernède, *Journal of Alloys and Compounds* **2020**, *819*, 152974.
[148] L. Cattin, G. Louarn, M. Morsli, J. C. Bernède, *Nanomaterials* **2021**, *11*, 393.
[149] Y. Mouchaal, G. Louarn, A. Khelil, M. Morsli, N. Stephant, A. Bou, T. Abachi, L. Cattin, M. Makha, P. Torchio, J. C. Bernede, *Vacuum* **2015**, *111*, 32-41.
[150] A. Kim, Y. Won, K. Woo, S. Jeong, J. Moon, *Adv. Funct. Mater.* **2014**, *24*, 2462-2471.
[151] K. D. M. Rao, C. Hunger, R. Gupta, G. U. Kulkarni, M. Thelakkat, *Phys. Chem. Chem. Phys.* **2014**, *16*, 15107-15110.
[152] H. Wu, D. S. Kong, Z. C. Ruan, P. C. Hsu, S. Wang, Z. F. Yu, T. J. Carney, L. B. Hu, S. H. Fan, Y. Cui, *Nat. Nanotechnol.* **2013**, *8*, 421-425.
[153] C. P. Muzzillo, *Sol. Energy Mater. Sol. Cells* **2017**, *169*, 68-77.
[154] A. Anand, M. M. Islam, R. Meitzner, U. S. Schubert, H. Hoppe, *Adv. Energy Mater.* **2022**, *12*.
[155] A. Schoonderbeek, M. Bärenklau, R. Rösch, B. Muhsin, O. Haupt, H. Hoppe, D. Teckhaus, U. Stute, *International Congress on Applications of Lasers & Electro-Optics* **2010**, *2010*, 1226-1234.
[156] N. Koch, A. Vollmer, A. Elschner, *Applied Physics Letters* **2007**, *90*, 3.
[157] D. J. Yun, H. Ra, J. Kim, I. Hwang, J. Lee, S. W. Rhee, J. Chung, *ECS J. Solid State Sci. Technol.* **2012**, *1*, M10-M14.
[158] L. Biessmann, L. P. Kreuzer, T. Widmann, N. Hohn, J. F. Moulin, P. Muller-Buschbaum, *Acs Applied Materials & Interfaces* **2018**, *10*, 9865-9872.
[159] B. Friedel, P. E. Keivanidis, T. J. K. Brenner, A. Abrusci, C. R. McNeill, R. H. Friend, N. C. Greenham, *Macromolecules* **2009**, *42*, 6741-6747.
[160] B. Y. Lu, H. Yuk, S. T. Lin, N. N. Jian, K. Qu, J. K. Xu, X. H. Zhao, *Nat. Commun.* **2019**, *10*, 10.
[161] P. C. Jukes, S. J. Martin, A. M. Higgins, M. Geoghegan, R. A. L. Jones, S. Langridge, A. Wehrum, S. Kirchmeyer, *Adv. Mater.* **2004**, *16*, 807.
[162] I. Ivanko, J. Panek, J. Svoboda, A. Zhigunov, E. Tomsik, *J. Mater. Chem. C* **2019**, *7*, 7013-7019.
[163] P. Govindaiah, Y. S. Kim, J. K. Hong, J. H. Kim, I. W. Cheong, *RSC Adv.* **2015**, *5*, 93717-93723.
[164] E. S. Muckley, C. B. Jacobs, K. Vidal, J. P. Mahalik, R. Kumar, B. G. Sumpter, I. N. Ivanov, *ACS Appl. Mater. Interfaces* **2017**, *9*, 15880-15886.
[165] M. P. d. Jong, L. J. v. IJzendoorn, M. J. A. d. Voigt, *Appl. Phys. Lett.* **2000**, *77*, 2255-2257.
[166] F. Hossein-Babaei, T. Akbari, B. Harkinezhad, *Sens. Actuator B-Chem.* **2019**, *293*, 329-335.
[167] M. Kus, S. Okur, *Sens. Actuator B-Chem.* **2009**, *143*, 177-181.
[168] K. Kawano, R. Pacios, D. Poplavskyy, J. Nelson, D. D. C. Bradley, J. R. Durrant, *Sol. Energy Mater. Sol. Cells* **2006**, *90*, 3520-3530.

[169] J. J. Yeh, I. Lindau, *Atom. Data Nucl. Data Tables* **1985**, *32*, 1-155.
[170] C. W. T. Bulle-Lieuwma, W. J. H. van Gennip, J. K. J. van Duren, P. Jonkheijm, R. A. J. Janssen, J. W. Niemantsverdriet, *Appl. Surf. Sci.* **2003**, *203*, 547-550.
[171] G. Greczynski, T. Kugler, W. R. Salaneck, *Thin Solid Films* **1999**, *354*, 129-135.
[172] C. C. Lin, C. K. Huang, Y. C. Hung, M. Y. Chang, *Jpn. J. Appl. Phys.* **2016**, *55*, 6.
[173] E. Dauzon, A. E. Mansour, M. R. Niazi, R. Munir, D. M. Smilgies, X. Sallenave, C. Plesse, F. Goubard, A. Amassian, *Acs Applied Materials & Interfaces* **2019**, *11*, 17570-17582.
[174] H. Shi, C. Liu, Q. Jiang, J. Xu, *Adv. Electron. Mater.* **2015**, *1*, 1500017.
[175] L. V. Lingstedt, M. Ghittorelli, H. Lu, D. A. Koutsouras, T. Marszalek, F. Torricelli, N. I. Crăciun, P. Gkoupidenis, P. W. M. Blom, *Adv. Electron. Mater.* **2019**, *5*, 1800804.
[176] B. Vaagensmith, K. M. Reza, M. D. N. Hasan, H. Elbohy, N. Adhikari, A. Dubey, N. Kantack, E. Gaml, Q. Qiao, *ACS Applied Materials & Interfaces* **2017**, *9*, 35861-35870.
[177] A. Hu, L. Tan, X. Hu, L. Hu, Q. Ai, X. Meng, L. Chen, Y. Chen, *J. Mater. Chem. C* **2017**, *5*, 382-389.
[178] N. Kim, S. Kee, S. H. Lee, B. H. Lee, Y. H. Kahng, Y.-R. Jo, B.-J. Kim, K. Lee, *Adv. Mater.* **2014**, *26*, 2268-2272.
[179] Y. Shi, Y. Zhou, R. Shen, F. Liu, Y. Zhou, *Journal of Industrial and Engineering Chemistry* **2021**, *101*, 414-422.
[180] S. Kee, N. Kim, B. S. Kim, S. Park, Y. H. Jang, S. H. Lee, J. Kim, J. Kim, S. Kwon, K. Lee, *Advanced materials (Deerfield Beach, Fla.)* **2016**, *28*, 8625-8631.

List of publications

Published

First author papers:

1) **Aman Anand**, Md Moidul Islam, Rico Meitzner, Ulrich S Schubert, Harald Hoppe, "*Response to Christopher P. Muzzillo's Comments on* "*Introduction of a Novel Figure of Merit for the Assessment of Transparent Conductive Electrodes in Photovoltaics: Exact and Approximate Form*", *Adv. Energy Mater.* **2022**, *12*, 2200828.
2) **Aman Anand**, Md Moidul Islam, Rico Meitzner, Ulrich S Schubert, and Harald Hoppe, "*Introduction of a Novel Figure of Merit for the Assessment of Transparent Conductive Electrodes in Photovoltaics: Exact and Approximate Form*", *Adv. Energy Mater.* **2021**, *11*, 2100875.
3) **Aman Anand**, Jose Prince Madalaimuthu, Maximilian Schaal, Felix Otto, Marco Gruenewald, Shahidul Alam, Torsten Fritz, Ulrich S. Schubert, and Harald Hoppe, "*Why Organic Electronic Devices Comprising PEDOT:PSS Electrodes Should be Fabricated on Metal Free Substrates", ACS Appl. Electron. Mater.* **2021**, *3*, 929−943.

Co-author papers:

4) Zhuo Xu, Jose Prince Madalaimuthu, Josef Bernd Slowik, Rico Meitzner, **Aman Anand**, Shahidul Alam, Ulrich S. Schubert, and Harald Hoppe, "*Compatible Solution-processed Interface Materials for Improved Efficiency of Polymer Solar Cells*", A*dv. Mater. Interfaces* **2022***,* 2201740*.*
5) Rico Meitzner, Aurelien Sokeng Djoumessi, **Aman Anand**, Chikezie Ugokwe, Anastasia Sichwardt, Zhou Xu, Daria Miliaieva, Jan Čermák, Theo Pflug, Arthur Markus Anton, Shahidul Alam, Štěpán Stehlík, Alexander Horn, Ulrich S Schubert, Harald Hoppe, "*Transmission windows of charge transport layers and electrodes in highly transparent organic solar cells for agrivoltaic application*", AIP Conference Proceedings **2022**, *2635*, 080001.
6) Aurelien Sokeng Djoumessi, Jose Prince Madalaimuthu, Shahidul Alam, **Aman Anand**, Anastasia Sichwardt, Peter Fischer, Roland Rösch, Ulrich S. Schubert, and Harald Hoppe, "*Flash-Lamp Processing of Charge Extraction Layers for Polymer Solar Cells*", *Adv. Mater. Interfaces* **2022**, 2201150.

7) Shahidul Alam, **Aman Anand**, Md Moidul Islam, Rico Meitzner, Aurelien Sokeng Djoumessi, Josef Slowik, Zekarias Teklu, Peter Fischer, Christian Kästner, Jafar I Khan, Ulrich S Schubert, Frédéric Laquai, and Harald Hoppe, "*P3HT:PCBM polymer solar cells from a didactic perspective*", *J. of Photonics for Energy* **2022**, *12(3)*, 035501.
8) Rico Meitzner, Jose Prince Madalaimuthu, Shahidul Alam, Md Moidul Islam, Sebastian Peiler, **Aman Anand**, Johannes Ahner, Martin D Hager, Ulrich S Schubert, Yingping Zou, Frédéric Laquai, and Harald Hoppe, "*An effective method of reconnoitering current-voltage (IV) characteristics of organic solar cells*", *J. Appl. Phys*. **2022**, *132*, 015001
9) T Jesper Jacobsson, Adam Hultqvist, Alberto García-Fernández, **Aman Anand**, Amran Al-Ashouri, Anders Hagfeldt, Andrea Crovetto, Antonio Abate, Antonio Gaetano Ricciardulli, Anuja Vijayan, Ashish Kulkarni, Assaf Y Anderson, Barbara Primera Darwich, Bowen Yang, Brendan L Coles, Carlo AR Perini, Carolin Rehermann, Daniel Ramirez, David Fairen-Jimenez, Diego Di Girolamo, Donglin Jia, Elena Avila, Emilio J Juarez-Perez, Fanny Baumann, Florian Mathies, GS González, Gerrit Boschloo, Giuseppe Nasti, Gopinath Paramasivam, Guillermo Martínez-Denegri, Hampus Näsström, Hannes Michaels, Hans Köbler, Hua Wu, Iacopo Benesperi, M Ibrahim Dar, Ilknur Bayrak Pehlivan, Isaac E Gould, Jacob N Vagott, Janardan Dagar, Jeff Kettle, Jie Yang, Jinzhao Li, Joel A Smith, Jorge Pascual, Jose J Jerónimo-Rendón, Juan Felipe Montoya, Juan-Pablo Correa-Baena, Junming Qiu, Junxin Wang, Kári Sveinbjörnsson, Katrin Hirselandt, Krishanu Dey, Kyle Frohna, Lena Mathies, Luigi A Castriotta, Mahmoud Aldamasy, Manuel Vasquez-Montoya, Marco A Ruiz-Preciado, Marion A Flatken, Mark V Khenkin, Max Grischek, Mayank Kedia, Michael Saliba, Miguel Anaya, Misha Veldhoen, Neha Arora, Oleksandra Shargaieva, Oliver Maus, Onkar S Game, Ori Yudilevich, Paul Fassl, Qisen Zhou, Rafael Betancur, Rahim Munir, Rahul Patidar, Samuel D Stranks, Shahidul Alam, Shaoni Kar, Thomas Unold, Tobias Abzieher, Tomas Edvinsson, Tudur Wyn David, Ulrich W Paetzold, Waqas Zia, Weifei Fu, Weiwei Zuo, Vincent RF Schröder, Wolfgang Tress, Xiaoliang Zhang, Yu-Hsien Chiang, Zafar Iqbal, Zhiqiang Xie, and Eva Unger, "*An open-access database and analysis tool for perovskite solar cells based on the FAIR data principles*", *Nature Energy* **2022**, *7*, 107–115.
10) Aurelien Sokeng Djoumessi, Shahidul Alam, Jose Prince Madalaimuthu, **Aman Anand,** Josef Slowik, Theo Pflug, Rico Meitzner, Roland Roesch, Enrico Gnecco, Alexander Horn, Ulrich S Schubert, and Harald Hoppe, "*Improved Hole Extraction Selectivity of*

Polymer Solar Cells by Combining PEDOT:PSS with WO_3", *Energy Technol.* **2021**, *9*, 2100474.

11) Theo Pflug, **Aman Anand**, Sandra Busse, Markus Olbrich, Ulrich S Schubert, Harald Hoppe, and Alexander Horn, "*Spatial Conductivity Distribution in Thin PEDOT: PSS Films after Laser Microannealing*", *ACS Appl. Electron. Mater.* **2021**, *3*, *6*, 2825–2831.
12) Shahidul Alam, Vojtech Nádaždy, Tomáš Váry, Christian Friebe, Rico Meitzner, Johannes Ahner, **Aman Anand**, Safakath Karuthedath, Catherine SP De Castro, Clemens Göhler, Stefanie Dietz, Jonathan Cann, Christian Kästner, Alexander Konkin, Wichard Beenken, Arthur Markus Anton, Christoph Ulbricht, Andreas Sperlich, Martin D Hager, Uwe Ritter, Friedrich Kremer, Oliver Brüggemann, Ulrich S Schubert, Daniel AM Egbe, Gregory C Welch, Vladimir Dyakonov, Carsten Deibel, Frédéric Laquai, and Harald Hoppe, "*Uphill and downhill charge generation from charge transfer to charge separated states in organic solar cells*", *J. Mater. Chem. C* **2021**, *9*, 14463-14489.
13) Rico Meitzner, Juliette Essomba, Shahidul Alam, **Aman Anand**, Nora Engel, Kevin Fulbert, Krisna Kuma, Fernanda Ayuyasmin, Md Moidul Islam, Chikezie Ugokwe, Ulrich S Schubert, and Harald Hoppe, "*Performance and Stability of Organic Solar Cells Bearing Nitrogen Containing Electron Extraction Layers*", *Energy Technol.* **2020**, *8*, 2000117.
14) Rico Meitzner, Tobias Faber, Shahidul Alam, **Aman Anand**, Roland Roesch, Mathias Büttner, Felix Herrmann-Westendorf, Martin Presselt, Laura Ciammaruchi, Iris Visoly-Fisher, Sjoerd Veenstra, Amaia Diaz de Zerio, Xiaofeng Xu, Ergang Wang, Christian Müller, Pavel Troshin, Martin D Hager, Sandra Köhn, Michal Dusza, Miron Krassas, Simon Züfle, E Kymakis, Eugene A Katz, Solenn Berson, Filip Granek, Matthieu Manceau, Francesca Brunetti, Giuseppina Polino, Ulrich S Schubert, Monica Lira-Cantu, and Harald Hoppe, "*Impact of P3HT materials properties and layer architecture on OPV device stability*", *Solar Energy Materials and Solar Cells* **2019**, *202*, 110151.

Under Preparation:

15) **Aman Anand**, Oluwaseun Adebayo, Arthur Markus Anton, and Harald Hoppe, "*Generic strategy to yield highly conductive PEDOT:PSS electrodes for organic photovoltaics*".